Numerical and experimental investigations of tool-workpiece interaction in diamond turning of copper beryllium

By

ANUJ SHARMA

ENGG01201304013

Bhabha Atomic Research Centre, Mumbai

A thesis submitted to the
Board of Studies in Engineering Sciences

In partial fulfilment of requirements
for the degree of

DOCTOR OF PHILOSOPHY

of

HOMI BHABHA NATIONAL INSTITUTE

October 2019

Homi Bhabha National Institute[1]

Recommendations of the Viva Voce Committee

As members of the Viva Voce Committee, we certify that we have read the dissertation prepared by Anuj Sharma entitled "Numerical and experimental investigations of tool-workpiece interaction in diamond turning of copper beryllium" and recommend that it may be accepted as fulfilling the thesis requirement for the award of Degree of Doctor of Philosophy.

Chairman - Dr. B. K. Dutta — BK Dutta — **Date:** October 18, 2019

Guide / Convener - Dr. R. Balasubramaniam — **Date:** October 18, 2019

Co-guide - Dr. D. Datta — **Date:** October 18, 2019 — DDatta

Examiner – Dr. Shrikrishna N. Joshi — **Date:** October 18, 2019

Member 1- Dr. J. Chattopadhyay — J Chattopadhyay — **Date:** October 18, 2019

Member 2- Dr. T. A. Dwarakanath — **Date:** October 18, 2019

Member 3- Dr. I. A. Khan — **Date:** October 18, 2019 — Imran Khan

Final approval and acceptance of this thesis is contingent upon the candidate's submission of the final copies of the thesis to HBNI.

We hereby certify that we have read this thesis prepared under our direction and recommend that it may be accepted as fulfilling the thesis requirement.

Date: October 18, 2019

Place: Mumbai

DDatta
(Dr. D. Datta)
Co-guide

(Dr. R. Balasubramaniam)
Guide

[1] This page is to be included only for final submission after successful completion of viva voce.

STATEMENT BY AUTHOR

This dissertation has been submitted in partial fulfillment of requirements for an advanced degree at Homi Bhabha National Institute (HBNI) and is deposited in the Library to be made available to borrowers under rules of the HBNI.

Brief quotations from this dissertation are allowable without special permission, provided that accurate acknowledgement of source is made. Requests for permission for extended quotation from or reproduction of this manuscript in whole or in part may be granted by the Competent Authority of HBNI when in his or her judgment the proposed use of the material is in the interests of scholarship. In all other instances, however, permission must be obtained from the author.

(Anuj Sharma)

DECLARATION

I, hereby declare that the investigation presented in the thesis has been carried out by me. The work is original and has not been submitted earlier as a whole or in part for a degree / diploma at this or any other Institution / University.

(Anuj Sharma)

List of Publications arising from the thesis

Journals

1. **Sharma, A.**, Datta, D., Balasubramaniam, R., *An investigation of tool and hard particle interaction in nanoscale cutting of copper beryllium*, **Computational materials science** (2018), 145, 208–223.

2. **Sharma, A.**, Datta, D., Balasubramaniam, R., *Molecular dynamics simulation to investigate the orientation effects on nanoscale cutting of single crystal Copper*, **Computational materials science** (2018), 153, 241-250.

3. **Sharma, A.,** Datta, D., Balasubramaniam, R., A molecular dynamics simulation of wear mechanism of diamond tool in nanoscale cutting of copper beryllium, **International Journal of Advanced Manufacturing Technology** (2019), 102, 731-745.

4. **Sharma, A.,** Roy T., Ranjan, P., Datta, D., Balasubramaniam, R., Investigation of tool-workpiece interaction in nanoscale cutting: A Molecular Dynamics study, Accepted, **International Journal of Precision Technology** (2019), 8, 411-28.

5. **Sharma, A.,** Joshi S. S., Datta, D., Balasubramaniam, R., *Modeling Tool Wear Mechanisms in Diamond Turning of Copper Beryllium Alloy*, **Under review**, Journal of Manufacturing processes.

6. **Sharma, A.,** Joshi S. S., Datta, D., Balasubramaniam, R., *Effect of Hard Precipitates on surface quality in Diamond Turning of Copper Beryllium Alloy*, **Under review**, ASME-Journal of Manufacturing Science and Engineering.

7. **Sharma, A.,** Datta, D., Balasubramaniam R., *Numerical and Experimental Investigations on tool wear in diamond turning of CuBe*, **Submitted**, Journal of micro-manufacturing.

Conferences

1. Sharma, A., Ranjan, P., Datta, D., Balasubramaniam R., A comparative study on the reflectivity of metallic mirrors finished by deterministic and random processes, 5th International & 26th All India Manufacturing Technology, Design and Research Conference (AIMTDR 2014) / IIT Guwahati / December 12-14, 2014/ 178 (1-6).

2. Sharma, A., Roy, T., Ranjan, P., Datta, D., Balasubramaniam R., Investigation of tool-workpiece interaction in nanoscale cutting: A Molecular Dynamics study, Proceeding of 10th International Conference on Precision, Meso, Micro and Nano Engineering / IIT Madras / December 07-09, 2017 / 811-14..

3. Sharma, A., Datta, D., Balasubramaniam R., MD simulation study to investigate nanocutting process in Cu and CuBe, EUSPEN's 18th International Conference & Exhibition, Venice (ITALY) -2018.

(Anuj Sharma)

ACKNOWLEDGEMENTS

First and foremost I would like to express my deepest and heartfelt gratitude to my main supervisor, Dr. R. Balasubramaniam (Bala sir). Throughout the duration of the project, he not only provided strong technical guidance, background knowledge and invaluable feedbacks on my research at all times, but also provided strong encouragement and kind affection. He has given me all the freedom to pursue my research, while ensuring that I stay on course and do not deviate from the core of my research. Without his able guidance and constant motivation, this thesis would not have been possible and I shall eternally be grateful to him for his assistance. I am also indebted to Revathi madam (Bala sir's wife) who not only invited me at various occasions but also treated me as a family member.

I would like to express my sincere gratitude to my co-supervisor, Dr. D. Datta, who helped me out of the difficulties that I encountered during the research. I thank him for introducing me to the field of MDS. I extend my gratitude to Dr. Naveen who helped immensely in learning and carrying out MDS. My sincere indebtedness to Dr. Prabhat Ranjan, whose invaluable suggestions helped me a lot in simulation as well as in experiments. Many thanks to Mr. Ashwin Rathod who helped me in carrying out FFT. I am thankful to my lab mate and flat mate, Dr. Tribeni Roy, who motivated me to write more number of journal papers. I thank Mr. Shivam Mishra and Mrs. Shrinkhla Ghildiyal for their moral and technical support. I am deeply indebted to Mr. Arvind (Shrinkhla ma'am's husband) for proof-reading of the thesis. I wish to express my appreciation to Mr. Surenderan Ji, Mr. Chandan Behera, Mr. Ramravendra Nagar and Mr. Lalchand, who assisted immensely during my experiments. I also express my regards to Mrs. Sushma Joshi, Mr. Nandan and Mr. Shankar, who helped me a lot in official and administrative activities.

I greatly acknowledge the contributions of my doctoral committee members Dr. B. K. Datta, Dr. J. Chattopadhyay, Dr. T. A. Dwarakanath and Dr. I. A. Khan who spared their valuable time for periodical critical assessment of my work. Incorporation of their constructive suggestions has greatly enhanced the technical level of my research work. I am also thankful to Dr. B. K. Dutta (Dean HBNI), Dr. V. Kain (Academic dean, HBNI), Dr. D. K. Maity (Associate Dean HBNI), Board of Studies (Engg. Sciences, HBNI) and administrative staff for their constant support during my PhD research work. I appreciate the efforts of both the reviewers for their invaluable comments and suggestions.

I would like to thank Department of Atomic Energy, India, for providing me the generous financial support in the form of a highly prestigious award of DAE Graduate Fellowship Scheme (DGFS-Ph.D.). I would also like to acknowledge BARC for allowing me to use the necessary resources in this work.

I would like to appreciate Prof. Suhas Joshi for the research guidance at times and Prof. Rakesh Mote to allow me to use the facilities at IIT Bombay. I would like to acknowledge the suggestions given by Dr. Saurav Goel, Cranefield University. My sincere acknowledgement to Dr. Ramagopal (Ex-scientist, CSIO, Chd.) for his valuable suggestions.

I would like to take the opportunity to thank my M. Tech. Guide ‘Dr. Ravindera K. Saxena’. Without his guidance and support during M. Tech., I could not have made to this PhD programme. I would also like to express my deepest gratitude to all the teachers who have taught me at different levels of my education.

I extend my gratitude to my flatmates Dr. Shankar Rao, Mr. Abhishek Kaushik, Mr. Rahul Kumar and Dr. Tribeni Roy for several cheerful memories. I would also like to thank Dr. Vinod Belwanshi, Dr. Ashish Shelke, Dr. Ravi Dhawan, Ms. Deepa Khandekar (IIT B), Dr. Ashwini Kumar, Dr. Vinay Rastogi, Mr. Suryakant Gautam, Mr. Ganesan Guna (IIT B), Ms. Sonal (IIT

B), Dr. Neha Khatri (CSIR-CSIO) for their support and motivation during PhD. A special thanks to Ms. Naini Bajaj for pleasant memories and helping me in formatting the thesis.

Special thanks to my M. Tech. friends Mr. Bharat Chaudhary, Mr. Vivekanand Shukla, Mr. Prashant Tripathi, Mr. Aashish Saxena, Mr. Satnam Khangura, Mr. Pradeep Saini, Mr. Harish Chauhan and Mr. Apurav Singh. I would also like to mention my B. Tech. friends, school friends and childhood friends. I missed all of them and the joyful times spent with them, a lot during my Ph.D.

Words would be few to describe my gratitude towards my family, especially my beloved parents, Smt. Neelam Sharma and Sh. Chanderbhan Sharma for their endless patience, support and encouragement. Special thanks to my brother Mr. Abhishek Sharma and sister in law Mrs. Monika Sharma, who constantly supported me during the PhD tenure. Thanks to my little nephew 'Master Advik' for cheerful memories.

Contents

Synopsis

Ultraprecision diamond turning of difficult to machine materials has been increasing in recent years to cater the ever-expanding application areas in aerospace, energy, optical, electronics and bio-medical industries. Copper beryllium is one such material, which is heterogeneous in nature, and after diamond turning, it is extensively used in high speed bearing applications owing to its combination of properties like large strength, high hardness and resistance to wear together with good thermal conductivity and excellent seizing and galling resistance. While, there are sufficient studies which explain the tool and workpiece interaction in case of single point diamond turning of homogeneous materials, there is a lack of understanding in case of heterogeneous materials. Therefore, the present thesis work is carried out to understand the effects of tool and workpiece interaction on the tool wear and surface quality in ultraprecision diamond turning of CuBe alloy.

Molecular dynamics simulation (MDS) has been carried out to understand the tool-workpiece interaction in nano-regime machining of CuBe with a single crystal diamond tool. In MDS, availability of accurate interatomic potential energy functions decides the accuracy of simulation. Since, CuBe interaction potential was not available in the literature, Density Function Theory (DFT) calculations have been performed to obtain the interatomic potential energy and Morse potential function parameters have been fitted to the interatomic potential energy curve.

In MDS of nanoscale cutting of CuBe, ratio of uncut chip thickness ‘a’ to cutting edge radius ‘r’ has been selected as a parameter to analyse the underlying mechanisms. Results of MDS of nanocutting of CuBe showed that the mechanisms of material removal and tool wear differ from that of homogeneous materials viz. Cu. Since CuBe contains two phases, the material removal mechanism has been analysed for Cu phase and Be phase separately. In case of Cu phase, the mechanisms of cutting vary from shear plane cutting at higher a/r ratio to elastic plastic deformation at lower a/r ratio. Whereas, in case of Be, the material removal takes place by brittle mode machining at higher a/r ratio and ductile mode at lower a/r ratio. During the interaction between tool and workpiece while cutting CuBe, the wear mechanism is also found to differ due to the presence of hard particles. It is observed that the abrasion wear mechanism in the form of micro-chipping dominates when the tool is sharp, whereas, phase transformation in the form of amorphization of diamond is the governing wear mechanism for blunt tool edge. Particles from the tool edge subsequently get diffused into the machined surface and contaminate it.

The mechanisms observed through MDS results have been confirmed with the help of experimental investigations. Experimental investigations on tool wear while diamond turning reveal that there is a rapid diamond tool wear in case of CuBe and the tool life is observed to be 60 % lower than that of Cu. Raman Spectroscopy on the diamond tool as well as on the machined CuBe surface shows that microchipping in the initial phase of tool life and subsequently phase transformation on the diamond tool take place. With the help of experimental results of tool wear and MDS results of stresses and temperature, tool wear coefficients from a known tool wear model have been obtained for a diamond tool and CuBe workpiece combination.

In addition to tool wear, the tool-workpiece interaction during diamond turning affects the quality of the machined surface. Surface roughness, lay pattern and surface contaminations have been analysed with the help of different characterization techniques. The surface roughness value in case of CuBe is observed to be 48% higher than that of Cu at the end of tool life. The cutting mechanisms on Cu phase and Be phase are also confirmed with SEM which shows that ductile to brittle transition occurs when cutting takes place from Cu to Be. SEM, FFT, cutting forces and MDS results show that the lay pattern in case of CuBe is subjected to suppression of feed marks and due to which it leads to the transition from deterministic to near random lay pattern. XPS results confirm that diamond turned CuBe surface is contaminated by the tool wear particles and their oxides.

Based on the understanding from the results of this study, an interaction effect diagram depicting various effects of nanomachining of Cu and CuBe with diamond tool is constructed and presented.

List of Figures

List of tables

List of Symbols

E_{ij}	Cohesive energy
R	Position of cut-off region
S	Adjustable parameter from Pauling plot
V	Pair potential energy
F_i	Embedding energy
ρ_i	host electron density
D	binding energy
α	Elastic modulus in Morse Potential
D_o	Dimer energy
θ_{ijk}	Bond angle
μ	Fitting parameter
V_A	Attractive pair potential energy
V_R	Repulsive pair potential energy
W	Width of cut-off region
r_{ij}	Atomic separation distance
r_o	equilibrium atomic spacing
m_i	Mass of ith atom
a_i	Acceleration of ith atom
β	Bond order
χ_{ij}	Effective coordination number

$g(\theta_{ijk})$	Angular function
γ, c, d and h	Angular dependence parameters in ABOP potential
σ_t	Theoretical stress
b_{ij}	Bond order
f_c	Cut-off function
U_{tot}	Total potential energy in EAM potential
E	Young's modulus of elasticity
b	Burgers vector
G	Shear modulus
A, B	Tool wear coefficients

Abbreviation

ABOP	Analytical bond order potential
OFHC	Oxygen Free High Conductivity
OVITO	Open Visualization Tool
LAMMPS	Large-scale atomic/molecular massively parallel simulator
HV	Vickers Hardness
EDS	Electron Dispersive Spectroscopy
SEM	Scanning Electron Microscopy
MDS	Molecular Dynamics Simulation
EAM	Embedded Atom Method
NVE	No. of atoms; Volume; Energy in an ensemble
XPS	X-ray Photoelectron Spectroscopy
Cu	Copper
C	Carbon
CuBe	Copper Beryllium
Be	Beryllium
UPM	Ultra precision machining
DTM	Diamond turn machining
SPDT	Single point diamond turning

Chapter 1

Introduction

1.1. Relevance and Motivation

Ultraprecision machining techniques have gained prominence over last few decades owing to the increasing demands for ultraprecision components with close dimensional tolerance, high shape accuracies and excellent surface quality. Among the ultraprecision machining techniques, single point diamond turning (SPDT), otherwise known as Diamond turn machining (DTM) is one of the key technologies in the field of precision engineering to produce the components having complex shapes with high level of accuracies and surface finish [1]. The single point diamond turning technology was first explored in 1960s with the necessity of advancement in various sectors including defence, aerospace, computer, electronics and medical. Taniguchi plot published in 1983 for the evolution of machining accuracy with the passage of years and its prediction for the 21st century by extrapolation of the curve is shown in Fig. 1.1.

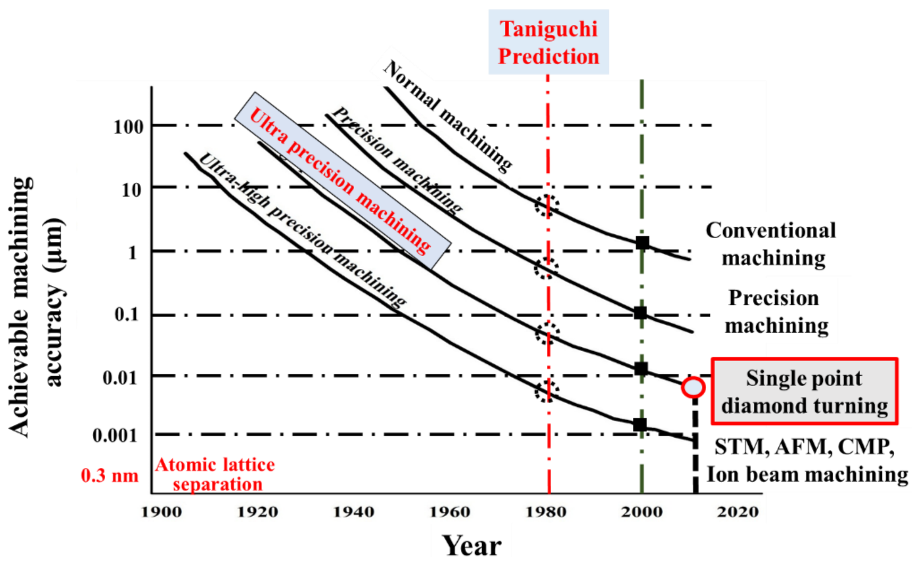

Fig. 1.1. Taniguchi's prediction of machining accuracies

Later on, other researchers have further extrapolated [2] and it appears to be true as we approach 2020. Taniguchi [3] indicated that in 21st century, single point diamond turning technique would be able to produce with machining accuracies up to 0.01 μm. To achieve this extreme level of precision, the processing scale should be extremely small and of the order of atomic dimensions which in turn depends on the accuracies of the machine tool and cutting tool being used. Various state-of-art technologies, such as monolithic granite bed, liquid cooled air bearing spindle, ultrastiff and ultraprecise hydrostatic bearings for slideways, linear motors, optical linear scale feedback system, computer numerical control (CNC) motion controller, etc. are integrated in ultraprecision diamond turning machine which enable it to realize the possibility of achieving extremely small material removal. Single crystal diamond, being the hardest naturally occurring material with an ability to possess sharp edge radius of the order of few nanometers, enables removal of the material from non-ferrous workpiece at nanoscale level and it is considered the best choice for the tool material in ultra-precision machining. In addition, cutting speed, feed and depth of cut are the major process parameters which govern the quality of the surface being generated. Thus, the combination of the ultraprecision machine tool and the cutting tool having nanometric edge radius with the optimized process parameters enables the material removal in a deterministic manner as well as machining components with size tolerances and shape accuracies of the orders of few tens to few hundreds of nanometers.

The driving force to employ the diamond turning technology is its use in applications which require extremely high level of form accuracy and surface finish. These applications can be found in number of industrial sectors including tribology, optics, electronics, biomedical, defence and aerospace. High speed bearing components for various applications, telescopic mirrors for astronomical purposes, substrate material for MEMS in electronics, micro-optics for telecommunication, contact lens as well as knee joint and hip joint implants in biomedical applications, thermal imaging cameras for defence and aerospace are some of the major application areas.

Initially, the diamond turning technology evolved with a limitation to machine nonferrous materials only as ferrous materials reacts with diamond tool. The diamond turning technology was later extended to machine brittle materials like Si, Ge, W, etc. through ductile mode machining. Concurrent developments in the field of modulated machining has led to the application of single crystal diamond tools to machine ferrous materials also. In recent years, the emphasis has been more to explore the possibility of heterogeneous materials like hybrid aluminium metal matrix composites, electroless Ni, CuBe etc. Among the heterogeneous materials, diamond turned copper beryllium (CuBe) is extensively used in high speed bearing applications owing to its combination of properties like high strength, high hardness and resistance to corrosion together with good thermal conductivity and excellent seizing and galling resistance. CuBe are used in optical industry for laser or infrared applications, because the materials exhibit the highest damage thresholds for long wavelength and high-energy beams [4]. CuBe is also used as highly precise optical moulds for making optical components. In addition, CuBe is used extensively in the electronics industry as connectors, springs, and so forth, for their high conductivity, modulus, and strength [5]. These applications require highly finished surfaces with highly accurate size and shape. Other ways to generate these surfaces are polishing, micro-grinding and other abrasive based finishing processes. It is difficult to produce highly precise components which satisfy size, shape and surface finish at the same time with very low cycle time. SPDT or diamond turn machining is a process which caters all these requirements in a very low cycle time and thus, it is a more economical and productive as compared to other processes. However, excessive tool wear and degraded surface quality are some of the issues in machining CuBe with a single crystal diamond tool.

Fig. 1.2 schematically shows the chip removal mechanism in diamond turn machining. Fig. 1.2 (b) shows the chip profile being generated with the uncut chip thickness varying from zero to some maximum value, depending upon the feed rate. This results in generating three distinct regions of cutting where the ratio between uncut chip thickness (a) and tool edge radius (r) varies from 0 to greater than 1. The material removal mechanisms at these three regions are shown in Fig. 1.2 (d-f). At a/r > 1, majority of the material flows along the rake face of the tool which ensures cutting. Bulk of the material removal lies in this portion of the chip. At a/r ~ 1, the tool edge and the uncut chip thickness become comparable and the material from the workpiece is subjected to hydrostatic pressure which squeezes and forces the material to move along rake and flank face of the tool.

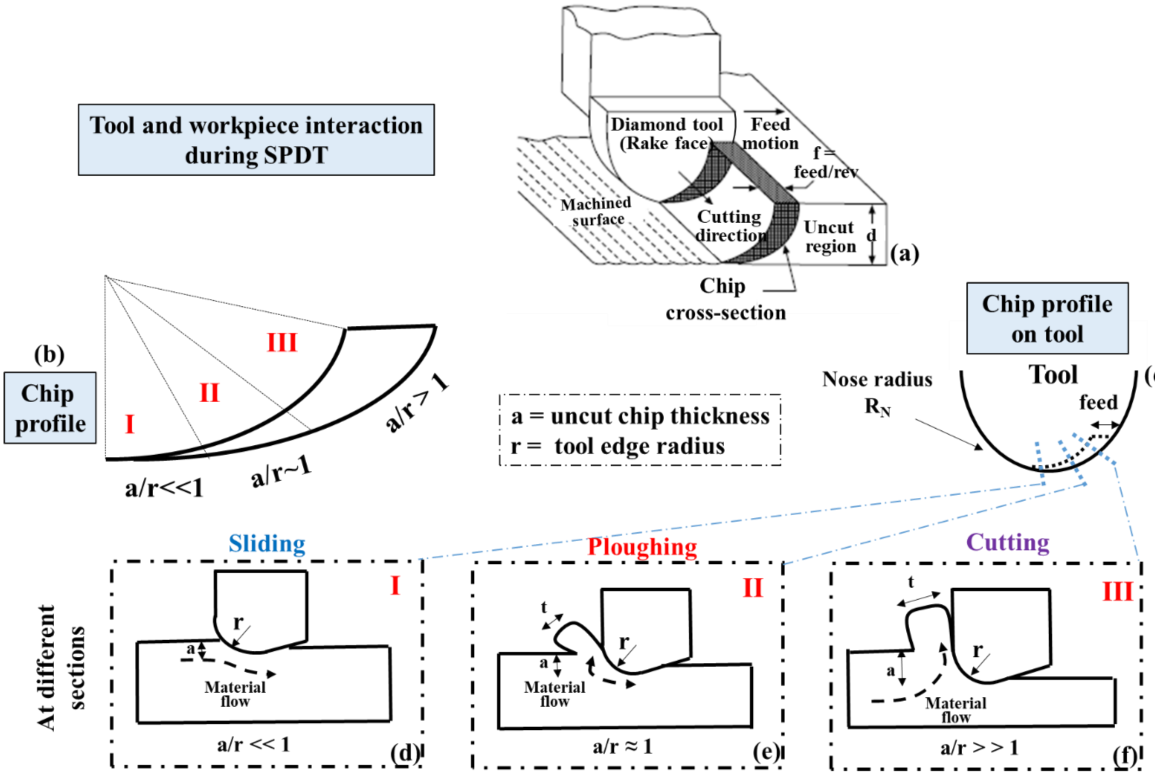

Fig. 1.2. Schematic of interaction between tool and workpiece in diamond turning

For a/r <<1, no material removal takes place and only sliding takes place. In addition to this, as the tool wears out, the tool edge radius at every section of the cutting edge interacting with the work material increases and it changes the a/r ratio which in turn alters the range of these regions. Therefore, it is not only the chip thickness which varies along the chip profile but the tool edge radius also continuously changes with increasing tool wear. In addition to this, the flank wear adds complexity to the cutting mechanisms. In case of machining with straight tool path like turning, facing and taper turning, localized flank wear also becomes predominant unlike contoured surface machining where, wear is distributed along the length of the cutting edge engaged for machining.

Fig. 1.3 (a-d) shows a schematic which represents the variation in cutting edge sharpness (r) at any uncut chip thickness (a) as the tool wear takes place. Fig. 1.3 (b-d) shows the condition of tool edge at three distinct instances of tool wear. During initial cutting stages when the tool is fresh, it possesses a sharp cutting edge with very small radius (r_1) for an uncut chip thickness '*a*' as shown in Fig. 1.3 (b). During the intermediate stages of cutting, when the tool wears and the edge becomes blunt, the cutting edge radius increases from 'r_1' to 'r_2' as shown in Fig. 1.3 (c). The increased edge radius causes a decrease in the a/r ratio. This is a stage where uncut chip thickness and edge radius become approximately comparable i.e. a/r ~1 at that section. With a further increase in cutting edge radius from 'r_2' to 'r_3', the a/r ratio decreases to a value less than 1. The material removal becomes difficult and thereby no chips are removed from the workpiece material at the final stages of cutting [Fig. 1.3 (d)].

Thus a/r ratio is dynamically varying and plays a major role in tool and workpiece interaction during the diamond turning process. It determines the material removal mechanism, tool condition and subsequently its influence on the machined surface. Therefore, it is important to understand the effect of a/r ratio on the above three aspects.

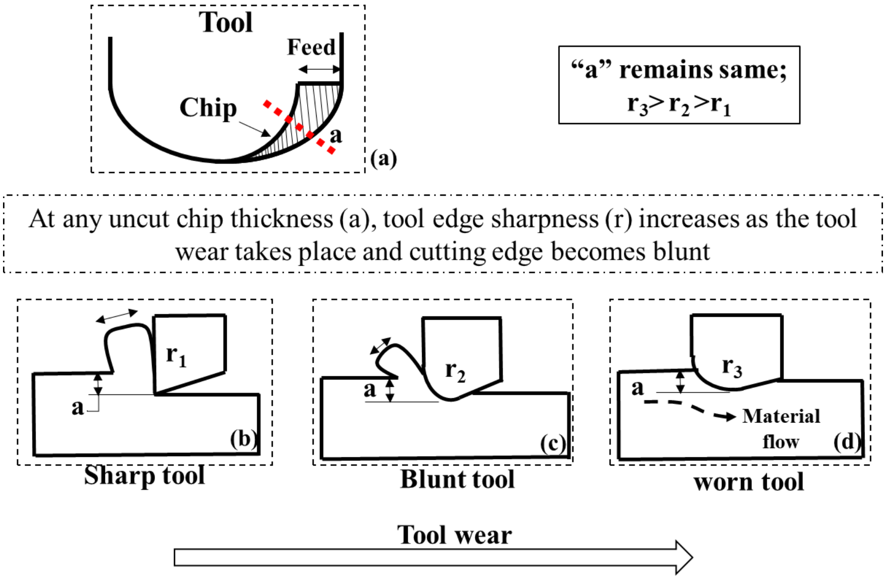

Fig. 1.3. Schematic of tool edge condition with an increase in tool wear

There are numerous studies which explain the tool-workpiece interaction in case of homogeneous materials, but there is lack of understanding in case of heterogeneous materials containing multiple phases. One of the popular material CuBe, which is used in this study, is a two phase material (i.e. hard and soft phase). Interaction of tool and workpiece affects both the cutting tool as well the work surface. Fig. 1.4 schematically shows the influence of heterogeneity in the form of hard particle on the cutting process. The cutting process is subjected to perturbations by the particle interaction with the cutting tool in the vicinity of the particle.

Heterogeneous nature of the CuBe workpiece due to the presence of hard particles tend to cause excessive tool wear and subsequently results in the degradation of work surface. It is envisaged that the mechanisms of tool wear and surface generation while machining CuBe material could be different from what is observed for a homogeneous Cu material.

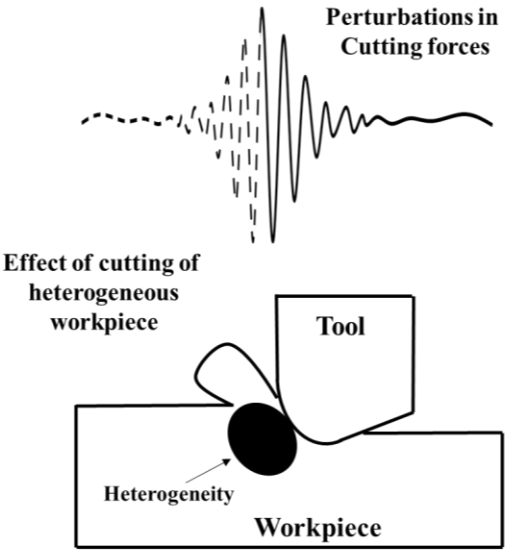

Fig. 1.4. Schematic of effect of machining of a heterogeneous material

While these mechanisms during diamond turning of homogeneous materials are well known, CuBe alloy containing hard beryllium precipitates has not been investigated elaborately so far. Therefore, understanding the effect of hard precipitates in the workpiece material on the tool wear and the reflection of tool wear on quality of the generated surface during ultra-precision diamond turning of CuBe alloy needs to be understood.

1.2. Objectives

CuBe is one of the high strength materials which are extensively used in precision engineering applications post diamond turning. The heterogeneous nature of the CuBe workpiece material affects the cutting mechanism, causes excessive tool wear and surface defects. Therefore, the primarily objective of this study is to understand the issues involved in tool and workpiece interaction which is rather different from the machining of homogenous material owing to the presence of hard particles. The investigation on tool and workpiece interaction in the present work has been carried out by studying the following three aspects:

- Mechanism of material removal, tool wear and surface quality by molecular dynamics simulation
- Tool wear and its mechanism by experimental investigation
- Experimental analysis of surface quality

Fig. 1.5 schematically shows various studies carried out in the present work. Identification of the cutting mechanism for a heterogeneous material (i.e. CuBe) while diamond turning is not well established, therefore, the first section of the study is dedicated to study the underlying mechanisms. Since diamond turning is also a nano-regime machining, molecular dynamics simulation (MDS) has been performed to study the cutting mechanism at nanoscale. In 2% CuBe material, 98% is Cu; still it behaves significantly different from Cu while machining due to the presence of hard particles. The tool-particle interaction is the main focus in the MDS study. As nanoscale cutting simulation involves extremely small cutting length, the cutting mechanisms and the tool wear mechanisms are not revealed for the whole tool life. Therefore, experiments were carried out to study tool wear and its mechanism for whole span of tool life and to a certain extent, validation of MDS results for different tool edge configurations was carried out.

Similarly, experiments were performed to study the lay pattern and morphology on the machined surface for the whole tool wear span from sharp edge to blunt edge conditions. These experimental results were also compared with the results of the MDS. Additionally, surface contamination was investigated to examine its effect on chemical, mechanical and optical properties. These studies were also performed on Cu for benchmarking purpose to analyse and understand the effect of hard particles in CuBe. This study is focussed on the effect of tool-workpiece interaction on tool and the workpiece material in terms of tool wear and surface degradation and therefore, investigation on chip morphology is not included.

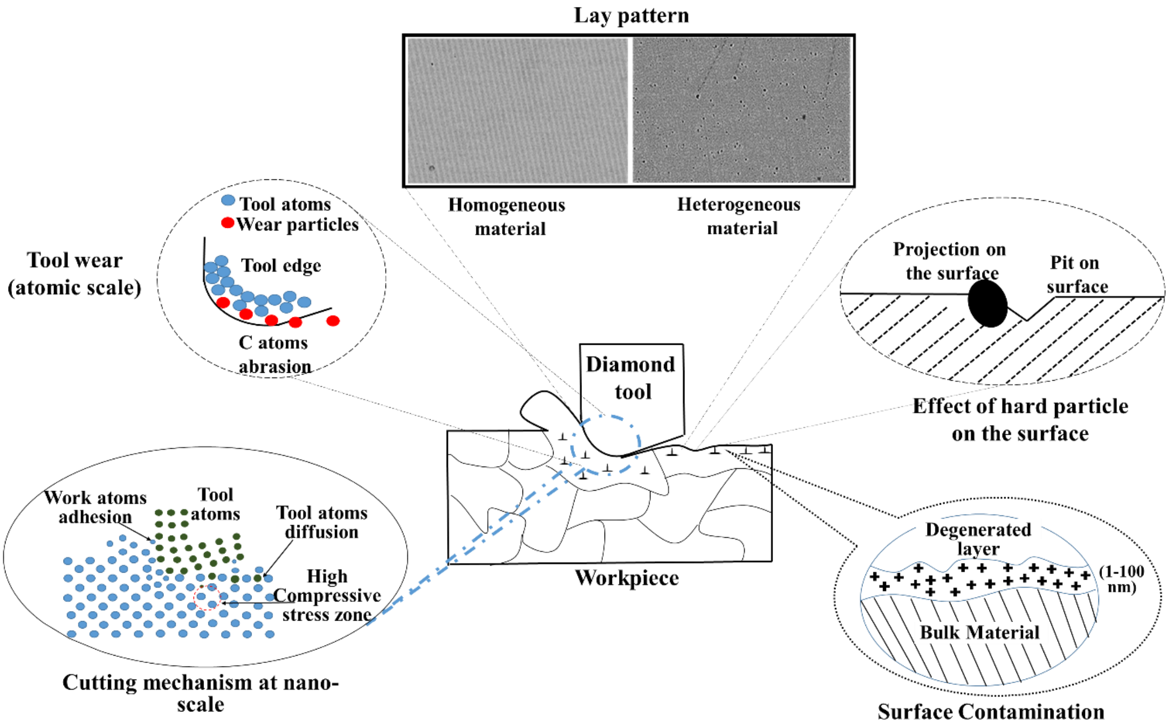

Fig. 1.5. Various aspects of study carried out on diamond turning of CuBe

1.3. Organisation of the Chapters

In **Chapter 1**, relevance and motivations are reported with objectives of present research work. Applications areas and need of single point diamond turning are clearly brought out in this chapter. In addition, issues and challenges of single point diamond turning of CuBe are also highlighted.

Chapter 2 is devoted for the literature survey which helps in understanding challenges in diamond turning process of heterogeneous materials. Application of MDS for nanocutting is covered in this chapter. It also discusses about the research gap and scope of this research work in theoretical and experimental aspects.

Chapter 3 describes the existing interatomic potential functions applicable to the MDS of nancutting of CuBe. Since multibody potential for nanocutting of CuBe is not available, development of interatomic potential function for determining parameters for Cu and Be interactions is carried out. These parameters are subsequently used in Chapter 4 for carrying out MD simulation of nanocutting process.

Chapter 4 is dedicated to MD simulation of nanoscale cutting of Cu and CuBe alloy. The material removal mechanism, subsurface deformation, variation of cutting forces and stresses are discussed. In addition, the identified wear mechanism of the diamond tool at atomic scale is discussed. The effect of tool wear observed on the machined surface in the form of surface contamination is presented in detail.

Chapter 5 explains the experimental study carried out on the wear mechanism of diamond tool for full span of tool life. Cutting forces and experimental characterization techniques like Raman spectroscopy, EDS, SEM are used to discuss the tool wear mechanism in detail. The chapter also presents the details of determining the tool wear coefficient for CuBe and diamond combination using the wear model from the literature with input from MDS results and experimental data for CuBe alloy.

Chapter 6 investigates the effect of tool-workpiece interaction on the diamond turned CuBe surface. Surface lay pattern and cutting mechanism are elaborately discussed in this chapter. The investigation of surface contamination through experimental techniques for full span of cutting distance is carried out. Furthermore, the experimental findings are validated with MDS results. Additionally, mechanical, optical and chemical properties of the diamond turned CuBe surface are discussed.

Chapter 7 summarizes the concluding remarks of overall thesis work. Further, the future scope is also projected in this chapter.

Chapter 2

Literature Survey

2.1. Introduction

This chapter presents an overview of the various micro/nano material removal processes with emphasis on diamond turning process. The present research status of diamond turning process is highlighted and the up to date chronological developments in the research aspects of diamond turning are reported for previous time spans. The reported aspects cover pioneering work in diamond turning, machine building, process mechanics, molecular dynamics simulation to comprehend the underlying physics, understanding of material removal and tool wear mechanisms. Previous research literature is also reviewed to highlight the gap area. Based on the gap areas, the scope of the research work is listed.

2.2. Review of Micro-/Nano-scale material removal processes

The material removal at micro and nanoscale can be broadly classified as mechanical, physical and chemical processes [Fig. 2.1] depending on the nature of the mechanism of material removal [6]. While physical and chemical machining processes are restricted to specific materials and applications, mechanical micro-machining is extended to a wide variety of materials and applications. Mechanical machining at micro and nano scale is classified into two types, viz. cutting and abrasive based machining. The difference between these two lies in the fact that cutting is deterministic in nature due to the tool path control whereas abrasive based material removal processes are stochastic, random in nature and are force controlled. Therefore, precision of the highest level in terms of size and shape control and surface finish is not achieved through abrasive based material removal process [7]. In addition, the cycle time is relatively higher [8].

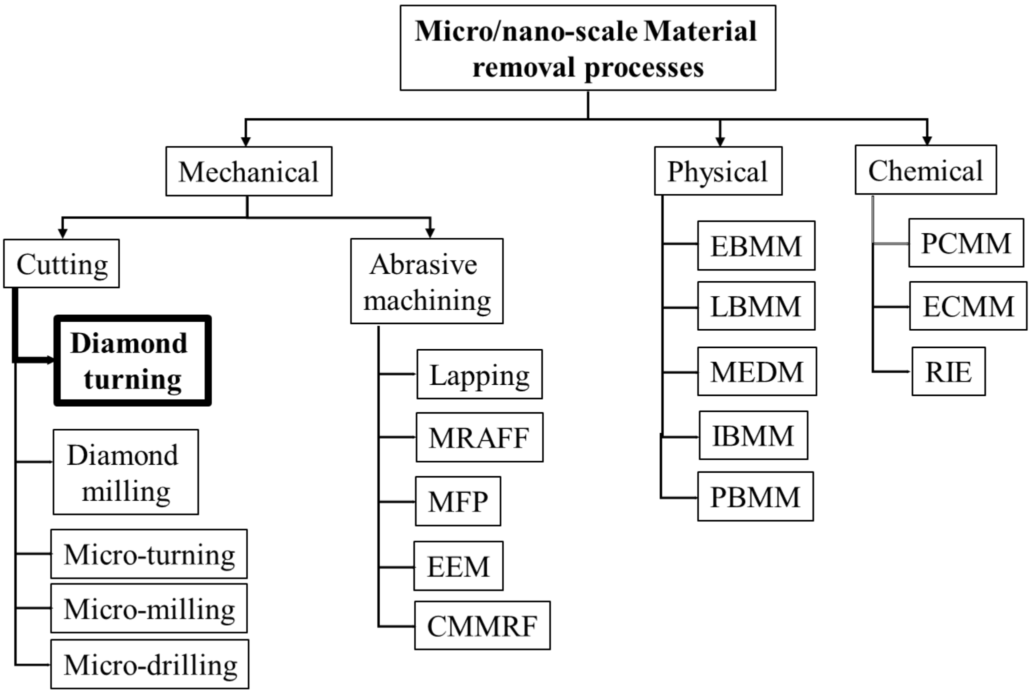

Fig. 2.1. Classification of various micro/nano scale material manufacturing processes

{MRAFF: magneto-rheological abrasive flow finishing; MFP: magnetic float polishing; EEM: elastic emission machining; EBMM: electron beam micromachining; LBMM: laser beam micromachining; MEDM: micro electric discharge machining; IBMM: ion beam micromachining; PBM: Plasma beam micromachining; PCMM: photo chemical micro-machining; ECMM: electro chemical micro-machining; RIE: Reactive ion etching}

Diamond turning (mechanical cutting technique) employs single cutting point and it is most efficient for machining flat to complex components with nanometre scale form accuracy and surface finish. Owing to its exceptional properties suitable for cutting tool, single crystal diamond tool with edge sharpness of the order of nanometers is extensively used in ultraprecision machining.

Taniguchi curve (1983) explained in “Chapter 1” indicates that the machining accuracy improves by one order in every twenty years. These significant and rapid improvements in ‘precision’ have come from the increasing demands of greater miniaturization, increased packing densities, better systems performance, reliable product, longer product life, and stricter quality control by higher machining accuracy. This improved level of precision in micro/nano scale machining is not simply achieved by scaling down the conventional machining processes. The major influencing factors which differentiate the micro/nano mechanical machining from the macro scale machining process are the uncut chip thickness, feature dimensions, cutting tool characteristics and mechanics of material removal. Among the various mechanical micro/nano-scale machining processes, diamond turning technology has brought a revolution in the world of precision machining by achieving submicron level accuracies in the size and shape of the machined component.

Till the 1970s, the diamond turning technology was limited to laboratories as it was in the initial stage of development. In the 1980s, the technology was spread out for use in various industrial purposes in 1980s like fabrication of Al scanner mirrors, substrate drums in photocopier machines and substrates of computer memory disks. During this period, efforts were made for the development of machine tool, understanding of process mechanism, material removal mechanism for various kinds of materials, enhancing the performance of the cutting tool, investigation of tool wear mechanism, study of diamond turned surface quality, application of MDS to understand the material removal and tool wear phenomenon at nanoscale, brittle to ductile transition mechanism etc. In the present era, various types of products rely on advanced manufacturing techniques to process high performance and cost-effective products. Such products include optics and components for television sets, video recorders, contact lenses, digital cameras, CD players, laptops, security systems, high quality optical components and high precision mechanical systems.

Table 2.1 shows the focus in the research area of diamond turning from its incipient stage. Initial few decades till 1970s were the years of growth of diamond turning in laboratories to bring about this technology to cater to the needs in defence and aerospace sectors. The span 1970-85 was dedicated mainly to the diamond turning machine building where highly accurate system of hydrostatic slides and aerostatic spindle bearing with nanometric feedback resolution were synchronized in the machine.

Table 2.1. Decade wise evolution of diamond turning process

Span	Primary Focus
Till 1970	Initial developments in diamond turning
1970-85	Diamond tuning machine tool building, Integration of precision technologies like air bearing spindle, hydrostatic bearings etc.
1985-2000	Machining aspects, Process Mechanics, Process improvement, Single crystal diamond tool, Understanding of material removal phenomenon
2000-15	Tool wear mechanism, MDS, Surface and subsurface damage, Fast tool and slow tool servo, wear mechanism, Ultrasonic machining, Micro-features generation, freeform machining
2015 onwards	Difficult to cut materials, Heterogeneous materials.

The time span from 1985 to 2000 was focussed on the machining issues and identification of process mechanisms for ductile and brittle materials. Various diamond tool configurations were also developed and optimized during this period. The era 2000-2015 saw significant developments which were mainly focused on enhancing the performance of the tool with respect to different crystal orientations. In addition, this period was devoted to understand the tool wear mechanism and its consequences on surface quality. The fast tool servo (FTS), slow tool servo (STS) accessories and ultrasonic machining methods were also integrated on the diamond turning machine to increase the flexibility and efficiency of the machine and cutting tool. Currently, the diamond turning is commonly used for various applications as listed below:

- cylinders for video tape recorders [9]
- substrates for magnetic discs in computers [10]
- convex mirrors for high output carbon dioxide laser resonators [11]

- infra-red lenses of germanium for thermal imaging systems [12]
- Contact lenses for human vision [13]
- scanners for laser printers and drums for photo copiers [10]
- elliptical mirrors for YAG (yttrium aluminium garnet) laser beam collectors [10]
- X-ray and ultraviolet optics [14]
- moulds for Compact Disc lenses [14]
- AIRS for missile guidance system [14]
- Aircraft windscreens [14] [15]
- Computer disk; photocopying application [9]

The recent trends indicate that the thrust area in the present decade is to explore the machining of difficult to cut advanced and heterogeneous materials to cater the needs of expanding ultra-precision manufacturing applications. CuBe is one such heterogeneous material which finds its usage primarily in tribological applications after ultraprecision machining.

2.3. Initial developments in diamond turning

The need of diamond turning technology emerged during world war II to fabricate optical components at Polaroid Corporation, in USA [16][17]. The 1960s was an important period for the development of diamond turning to cater the increasing demands of highly accurate parts required for energy, electronics and defence application [18–20]. This led to the construction of the first diamond turning machine which was attempted by Y-12 at Union Carbide Nuclear Division, Oak Ridge, Tennessee in USA. The machine was capable of generating hemisphere component with shape accuracy and surface roughness of ± 0.6 μm and 25 nm, respectively. This established its potential for fabricating reflective optics for use in the infrared and for high power, cooled laser optics. From the 1960'-s to 1970'-s, the ultraprecision diamond turning technology was mostly developed in national laboratories such as Lawrence Livermore

National Laboratory (L.L.N.L.) and defence builders like Bell and Howell and Perkin Elmer; and the products were used for advanced science and technology such as the optical components for NASA, grazing-incidence x-ray space telescopes etc. In the early phases of diamond turning development, hydrostatic bearings were used for the spindle, to operate at submicron rotational accuracy [19]. With the development and integration of air bearing spindles, the diamond turning technology was significantly improved in the early 1970s in terms of accuracy achieved. The pioneering work of Bryan, J.B. at Lawrence Livermore National Laboratory extended the application of diamond turning to optical components with complex shapes [21].

2.4. Development of machine tool (1970-1985)

Significant developments took place in the USA and the UK in diamond turning technology in the beginning of 1970s. Bryan et al. [21] successfully carried out diamond turning of parabolic mirror for high power laser beam applications.

In this period, the key technologies used in diamond turning machine tool included air spindle, laser interferometer position feedback, capacitance gauge, numerical control, three-axis machining, brushless DC motor, pneumatic vibration isolators, and temperature control [22].

In the early 1970s, other key technologies integrated with diamond turning were stepper motors to drive the lead screws, roller ways, precision air bearing LVDT [21] [23]. The inaccuracies of conventional drive were eliminated by the development of a linear motor. Barkman W. E. [22] implemented a linear induction motor slide drive system which avoids any mechanical coupling between the motor's stationary and moving members. The use of linear drive motion significantly reduced the slide positioning errors in diamond turning. Saito T. T. [14] reduced the slope error problem by incorporating the linear motor in the machine tool.

Smooth and precise motion are the essential requirements for maintaining the uniform contact between the tool and workpiece system. Rigid machine base, air bearing spindle and pneumatic isolation eliminated the external as well as most of the machine tool vibrations. However, the slide drive mechanism governed by ball nut/lead screw remained a source of vibrations and slide positioning errors due to errors in gear train viz. lead errors, screw whipping, stick-slip etc. resulted in periodic and aperiodic disturbances that caused undesirable slide motions.

Casstevens J. M. [24] emphasized the need of submicron accuracy spindle in diamond turning to generate large optics with high accuracy. He further showed that by upgrading the existing air bearing spindle, the radial motion error was improved from ~ 0.15 µm to ~0.04 µm and the axial motion error was reduced from ~0.15 µm to ~0.02 µm.

Bryan J.B. [25], in the year of 1979, suggested the design of the most accurate diamond turning machine of that period and it was capable of securing components having maximum of 84 inch diameter and 4500 kg of weight on the machine. It was diamond turning machine number 3 in the history of LLNL and it was anticipated that it would be the world's most accurate lathe machine, 10 times more accurate than the second diamond turning machine. This machine was equipped with hydrostatic slides, hydrostatic spindle, eddy current motor for spindle, friction drive system was chosen for drives rather than lead screw and linear motor to avoid backlash, granite bed, linear variable differential transformer based correction system and laser interferometers based nanometric measurement system. This machine was supposed to possess straightness errors of less than 0.025 µm and displacement error of less than 0.013 µm.

A small variant of the above machine was created where 100 mm diameter could be held. It was a two axis machine with T- configuration and it was furnished with air bearing spindle, brushless dc servo motor for the spindle, granite machine base, laser interferometer, encoders for feedback etc. One major improvement on this machine was the localized temperature control which was provided in the spindle drive motor unit due to high heat generation in this unit. Earlier versions of the diamond turning machine were provided with temperature controlled oil flow throughout the machine, which was not effective and it was ruled out in this machine due to its contamination with some of the parts in the machine. The X and Z slide errors were found to be ~ 1.25 and 1 µm respectively over their full travel. The machine was able to generate a hemispherical component of Al with size accuracy of 250 nm and surface finish of 25-40 nm rms [26].

The other improvements in the machine tool were piezo microfeed devices for nanometric tool Positioning [27] and the error Compensation of hydrostatic bearings [28].

The accuracy and finish of the component depends on the uniform contact between the tool and the workpiece during the course of machining. This requires a feedback system which rectifies the slide error and does the correction with quick response. The servo control mechanism takes the input from laser interferometers and subsequently activates the actuators to compensate for any slide errors. The bandwidth of the servo system should be sufficiently high to accommodate the disturbances that emerge from the machine tool as well as external environment [21][29]. Taniguchi [3], in the year 1983, reported the feedback resolution of ultraprecision motion control servo system of 10 nm through the use of piezoelectric system.

Accuracy of the slide travel was still a limitation as the slide bearings were cross rollers producing 1 µm of straightness error. Moreover, the slide drive was a leadscrew with a plain nut driven by a DC motor and tachometer. Donaldson and Maddux [30], utilized oil hydrostatic bearings with a capstan roller drive driven by a DC motor and tachometer in diamond turning. Both the hydrostatic bearings and capstan roller drive are free from frictional contact.

Hydrostatic bearings have the advantages of better damage resistance, and higher viscous damping which improve the dynamic characteristics of the diamond turning machine. The straightness error was improved to 200 nm over a travel of 100 mm in the form of a smooth arc.

With the evolution of diamond turning technology, the open loop structure previously used with stepper motors was not suitable as any errors in the drive train are not corrected and fed back. The advancement in the controller of the diamond turning machine was the need of the hour to strive for ultimate accuracy. Burleson R.R. [31], in the year 1983, highlighted the need for an upgraded processing unit which can simultaneously perform interpolation and federate override calculations, reading feedback sensors and evaluate the equations of motion, monitoring and updating the control panel, communicating with control panel and reading part programs stored in the disk. However, though majority of developments in diamond turning took place in this period till 1985, it continued to evolve during subsequent eras with improvement in the accuracies of the machine tool components.

2.5. Initial machining challenges and machinability aspects

In this era, the machinability aspects of diamond turning were explored for variety of materials to extend the areas of applications of diamond turning technology. In some of the very first works reported in the field of diamond turning, Arnold et al. [32], in 1975, machined several materials in Y-12 laboratory with diamond tool to investigate the machinability for optics application and noticed that pure and soft metallic materials with face centred cubic lattice structure like gold (Au), silver (Ag), copper (Cu), lead (Pb) and Aluminium (Al) are easy to machine whereas pure metallic materials such as iron (Fe), platinum (Pt) and nickel (Ni) are difficult to machine which limited their application in optics.

Saito T. T. [14] listed the metals compatible for diamond turning as copper, gold, silver, aluminium, platinum, lead, etc. Other materials, which are diamond turnable, are ZnS, ZnSe, NaCl, KCl, KCl (RbCl doped), MgF_2 , KCl ($EuCl_3$ doped), CaF_2 SrF_2 germanium, silicon, lithium niobate, and plastic. He reported that the polycrystalline materials are prone to inferior surface finish than that of single crystal materials owing to grain boundary effect.

Bennett J. M. [33], in 1976, categorized surface errors into three divisions: surface figure, surface waviness, and surface roughness. Figure error on the machined component is influenced by a number of factors including low order tool path errors, machine tool errors, spindle growth owing to temperature variation, tool forces causing dynamic flexures of the workpiece during machining, and faulty design of fixture that can generate a warped or astigmatic part. Surface roughness is a measure of low frequency variations in surface heights and it depends on tool feed rate, workpiece material properties, tool-workpiece vibrations, and diamond tool edge quality. Lying between these two extremes is surface waviness and is attributed to straightness and angular errors in the machine slide ways.

As the diamond turning process evolved with time, the measurement of ultraprecision diamond turned surfaces in terms of size, shape and surface finish became a challenge. Therefore, surface characterization techniques were developed parallel to the advancement in diamond turning technology. Bennet and Decker [34] highlighted the importance of surface characterization to understand the physical significance of surface texture. They represented the suitability of various surface characterization techniques with the help of a bar chart plotted with respect to range of their spatial wavelengths as shown in Fig. 2.2.

Further, they compared four microroughness measuring techniques (viz. Stylus profiling instrument, FECO (fringes of equal chromatic order) interferometer, Heterodyne interferometer, Stereo microscopy) based on height sensitivity, lateral resolution, and maximum profile length and reported that the stylus profiling instrument showed excellent height sensitivity and lateral resolution over maximum length of travel.

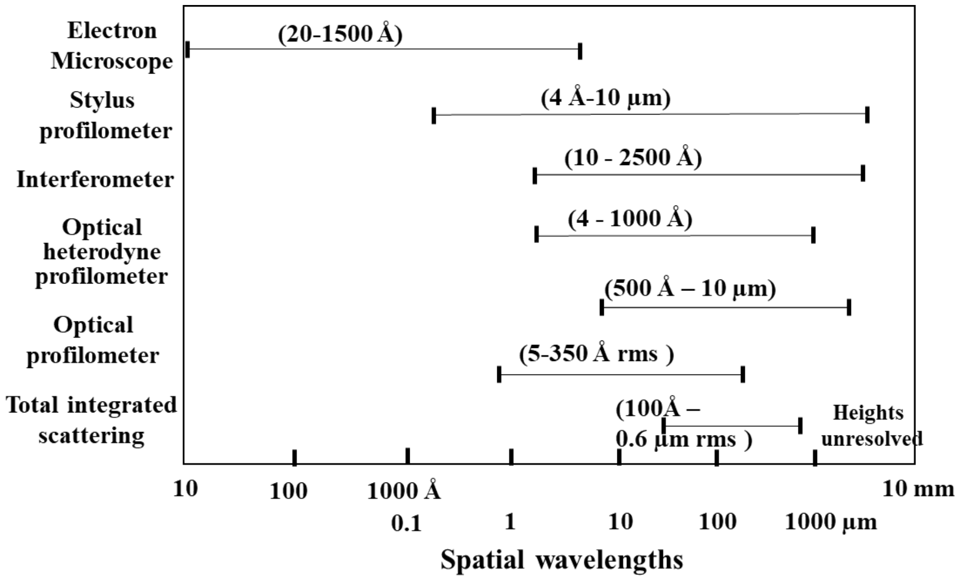

Fig. 2.2. Different techniques for surface measurement

Stover J. C. [35], in 1976, reported that spectral distribution function (SDF) is a more powerful tool in comparison to surface roughness value in order to reveal the surface characteristics which is a result of various parameters such as feed rate, groove shape and chattering effects. In addition, SDF can also be used as a way of comparing various systems with different spatial frequency bandwidths.

Shagam et al. [36], in the year 1977, suggested that the figure measurement of the diamond turned mirror surface is best achieved by interference based measurement techniques and not by wavefront slope methods. Brodmann et al. [37] endorsed the use of optical measuring techniques to circumvent the shortcomings of the stylus method of measurement in fine machining. According to them, the limitations of using a stylus based measurement method are: 1) Surface degradation takes place due to stylus pressure and stylus also wears; (2) Large measurement time from several seconds to minutes; (3) two dimensional details of a surface topography are not sufficient for describing three dimensional details of a machined surface.

In contrast, optical measurement has the advantage of its noncontact nature, faster measuring rate and area sampling.

Taylor et al. [38] carried out diamond turning tests on electroless-nickel samples and on measuring with Talysurf stylus profilometry, they revealed that diamond tool edge irregularities are reflected on the machined surface and the spatial frequency amplitudes depend on these irregularities.

Chaloux L. E. [39] suggested the need of proper fixturing to successfully diamond turn the components. He reported that distortion in the component takes place due to: (1) inaccurate chucking surface or workpiece mounting surface; (2) residual stresses from excess clamping force; (3) faulting mounting; (4) centrifugal forces during spindle rotation.

Hannah P. R. [40] reported the complete oil shower system for the diamond turning. Further, he indicated that the diamond turning machine is truly an optical element fabrication scheme owing to is capability of generating any optical surface from flats to spheres and aspheric from simple conics to high order polynomials.

Cooke et al. [41] brought about the comparisons between diamond turning and conventional polishing technique and showed that the diamond turning process is much more efficient and economical than the conventional techniques. Table 2.2 shows the comparison between the conventional polishing and diamond turning for different parameters.

Table 2.2. Comparison of conventional polishing and diamond turning

Parameter	Polishing	Diamond turning
Accuracy (p-v)	3 μm	0.6 μm
Cost per mirrror	$50,000	$4,000
Fabrication time	12 months	3 weeks

Miller et al. [42] employed special thermally stabilized air bearing spindle and machine calibration equipment in diamond turning and found that the generated Cu surface achieved contour accuracy of 75 nm and surface finish of 1.23 nm rms.

Although diamond turning of optics had been performed in the 1960s, the machining of various materials have been reported since 1970s. Owing to the very close tolerances, extremely high level of surface finish achievable in diamond tuning and reduced cycle time, the usage of lapping process became insignificant in generation of precision spherical or aspherical surfaces [43] [44][12].

2.6. Developments in diamond turning from 1980 onwards

As the diamond turning technology reached acceptable level of precision in the beginning of early 1980s, it necessitated the shift of focus from machine tool development to machining aspects and cutting behaviour. Various studies were carried out in this direction to understand the process, optimize the process parameters, strive for higher cutting efficiency and consequently reduce the energy requirements. Most of the studies initially were performed on the ductile materials. Since the cutting zone in diamond turning is extremely small, efforts were made to understand the physics behind the material removal. This would extend the range of diamond turnable materials namely to brittle materials such as ceramics and glass. The following sections deal with various aspects of post 1980s developments in diamond turning.

2.7. Machinability in diamond turning

Jeanmichael and Prevost [45], in 1986 reported the diamond turnability of various materials. Table 2.3 shows the different class of materials which are diamond turnable**.**

Table 2.3. List of diamond turnable materials

Pure metals	Alloys	Infra-red materials	Glasses	Crystals	Plastic materials
Aluminum Copper Tin Zinc Nickel	Al Alloy Brass Bronzes	Germanium Silicon Zinc sulphide Zinc selenide Amtir (Ge-AS-Se) IRG 100 (Ge-Sb-Se) Magnesium fluoride Calcium fluoride	Optical fibre plates	Potassium dideuterium phosphate (K D P)	Acrylic Polycarbonates Polyamides Epoxies

In diamond turning, the scale of tool and workpiece interaction is substantially smaller than that of conventional machining which raises a number of issues. The main difference between the macroscale machining and diamond turning lies in the size of uncut chip thickness. Ikawa et al. [46] suggested that below certain minimum chip thickness, no stable chip would form. They reported that minimum uncut chip thickness of 1 nm could be achievable for an electroplated copper workpiece material machined with a specially designed diamond cutting edge.

2.7.1. Size effect

Reducing the scale of machining brings the size effects into picture. Unlike conventional machining process, single point diamond turning process with a highly sharp diamond tool exhibits the size effect due to its reduced scale of material removal. Cutting tool edge radius (r) becomes significant with respect to uncut chip thickness (a) during diamond turning process as a result of size effect. Lucca et al. [47] expressed the need to examine the energy dissipation in ultraprecision machining owing to the fact that the characteristic length scale of cutting is much smaller in diamond turning than in case of conventional cutting [Fig. 2.3 [48]]. They carried out machining trials at various uncut chip thicknesses in plunge cutting. They showed that the resisting shear strength increases significantly as the chip thickness is lowered as shown in Fig. 2.4. They highlighted the role of sliding and ploughing in ultraprecision machining in terms of increase in specific cutting energy.

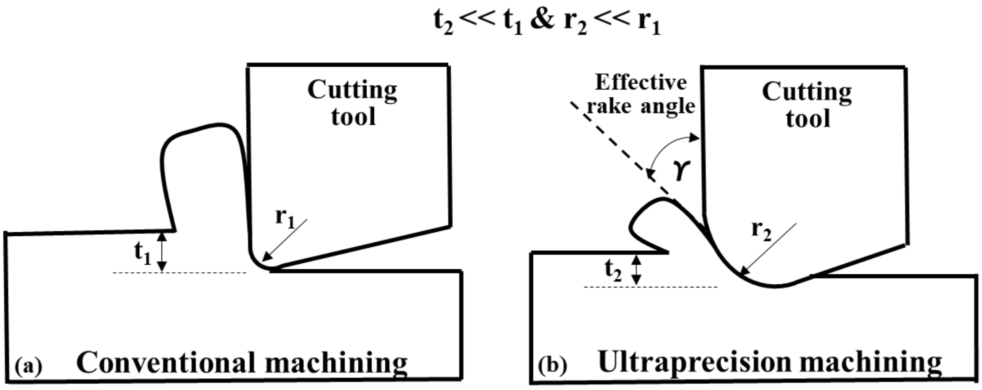

Fig. 2.3. Schematic of conventional and ultraprecision machining

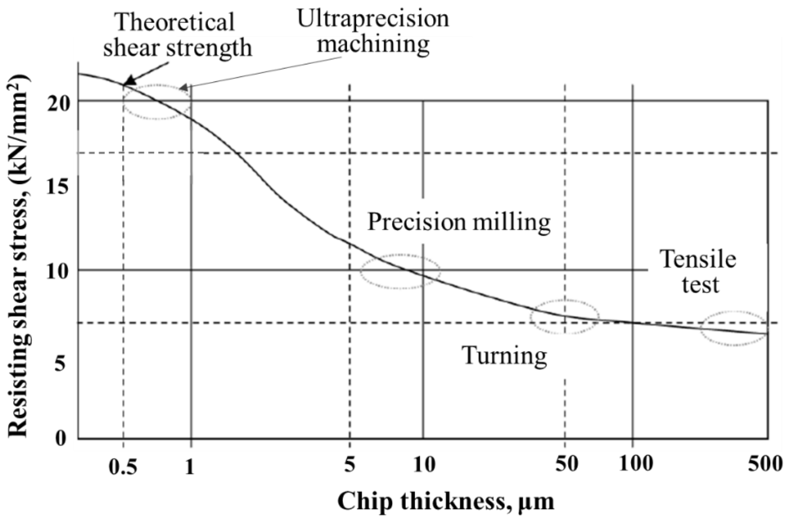

Fig. 2.4. Size effect in ultraprecision machining

Moriwaki and Okuda [49] observed that when the cutting depth is reduced from few microns to a few nanometres, sub grain cutting takes place and the specific cutting resistance increases significantly. They also emphasized that the finished surface is generated in the cutting region of very small effective cutting depth even with large nominal feed rate and depth of cut and plastic deformation viz. rubbing and burnishing are more dominant than cutting at very small effective cutting zone.

It is reflected here that size effect becomes more prevalent with the size of uncut chip thickness as compared to tool edge radius. In diamond turning, the tool edge radius is continuously degraded and increased with constant uncut chip thickness, which in turn deteriorates the machining process.

2.8. Cutting mechanism

The cutting edge radius in ultraprecision diamond turning affects the cutting mechanism. The tool edge radius tend to be of the same order as uncut chip thickness in diamond turning and their ratio governs the cutting mechanism such as shear plane cutting, ploughing and sliding. These mechanisms in turn control the resulting surface quality. A few researchers have investigated the minimum uncut chip thickness, below which no material removal takes place due to cutting, in order to ensure efficient cutting and to suppress ploughing and sliding [50].

Kim and Kim [51] showed that at very small uncut chip thickness of a micron or less, the mechanism of material removal changes from shear plane cutting to shear zone cutting when tool cutting radius increases [Fig. 2.5].

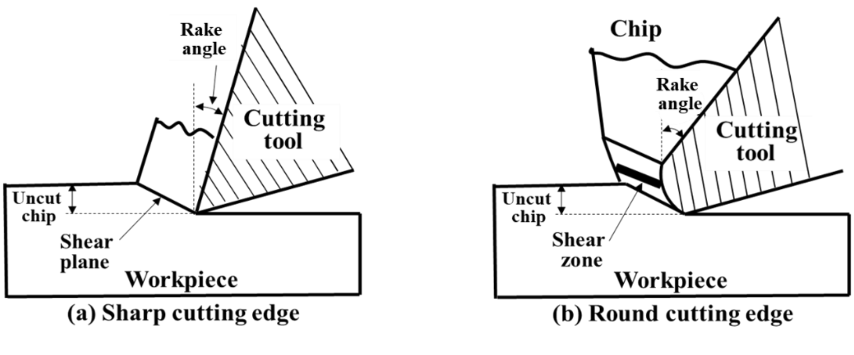

Fig. 2.5. Schematic of shear plane cutting and shear zone cutting

Sliding at the flank face due to elastic recovery of the workpiece material and ploughing due to edge radius of the tool become dominant in ultraprecision diamond turning.

With the help of a simulation study, Shimada et al. [52] deduced the attainable extreme level of accuracy and observed that the minimum uncut chip thickness is approximately 5% of the tool edge radius for Cu and Al work materials. However, Yuan et al. [53] observed that the minimum uncut chip thickness should lie between 20-40% of the tool edge radius.

During ultraprecision diamond turning of Cu with single crystal diamond tool, Moriwaki and Okuda [49] varied the uncut chip thickness from 3 μm to 2.5 nm and showed that the surface generation occurs at a very small effective depth of cut even when the feed rate and depth of cut are very high. While machining with lesser uncut chip thickness, thrust force to cutting force ratio increases and plastic deformation such as rubbing and burnishing becomes dominant. Moreover the specific cutting resistance increases as the uncut chip thickness is reduced.

Similarly, Furukawa and Moronuki [54] noticed a significant increase of specific cutting energy during the diamond turning experiments in submicron cutting scale. The increase in specific energy occurs as a result of: (1) one part of energy being used in material ploughing and (2) the other part being used by the sliding mechanism. Both of these mechanisms become prevalent at lower uncut chip thicknesses where the tool edge appears as blunt and contributes to increase in specific cutting energy. Lucca et al. [55] showed that the specific cutting energy is closely correlated to uncut chip thickness.

Taminiau and Dautzenberg [56] investigated the effect of tool edge roundness on the cutting forces in ultraprecision diamond turning. They suggested that there exists a small stagnation zone ahead of the tool edge below which the plastic deformation occurs causing rubbing, whereas material flows in the form of chips above this zone.

Lucca et al. [57] presented tool-workpiece contact length as the characteristic length when machining at submicron scale of uncut chip thickness and suggested that the ultraprecision diamond turning process can be considered as a transformation for cutting to sliding/ploughing process. Apart from the machine and cutting tool inaccuracies, the machining accuracy is governed by the uncertainty of the thickness of cut.

The mechanism of material removal in diamond turning, thus, primarily depends upon the uncut chip thickness and tool edge radius. Since, the uncut chip thickness along the chip profile varies, the mechanisms tend to vary along it. The tool edge sharpness also degrades during the course of machining, which also affects the cutting mechanisms.

2.8.1. Ductile regime machining of brittle materials

During conventional machining of brittle materials, the material removal takes place by brittle fracture. Fracture in the brittle materials occurs as a result of median and lateral cracks similar to indentation process used in brittle materials [58]. This brittle failure can be avoided by using low uncut chip thickness to avoid the nucleation and propagation of microcracks [59]. This is called ductile regime machining of brittle materials.

Ductile regime machining is necessary for obtaining mirror surfaces in brittle materials. In diamond turning of a brittle material, ductile response takes place at the tool nose apex where the uncut chip thickness approaches to zero. Smooth, damage free and optical quality surface is generated if the uncut chip thickness along the tool nose is below critical chip thickness. Tool feed rate, thus, becomes an influential factor in deciding the nature of the generated surface [60].

Blackley and Scattergood [61] proposed a machining model based on critical depth of cut and subsurface damage depth which suggested that fracture is initiated at the critical uncut chip thickness (d_c) and is subsequently propagated in the material. The chip thickness varies from zero at the tool centre to a maximum at the top of the uncut shoulder as shown in Fig. 2.6. As long as the fracture does not penetrate into the cut surface plane, ductile regime conditions are achieved. If the fracture penetrates into the surface, the machining mode will be in brittle regime. The critical chip thickness separates these two machining modes.

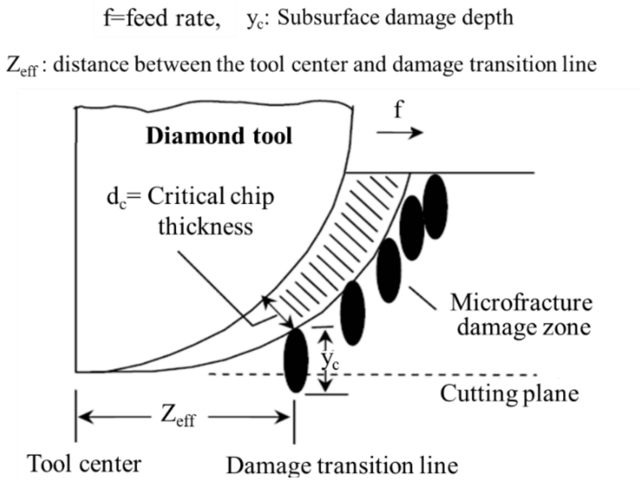

Fig. 2.6. Schematic of brittle to ductile transition

This transition of mechanism is also known as brittle - ductile transition. Blackley and Scattergood [62] showed the brittle - ductile transition with the help of chip topography. The frequency of occurrence of serrations on the chip correlated with the pits on the cut surface. According to Nakasuji et al. [63], brittle-ductile transition takes place in the diamond turning process of brittle materials. This is a mechanism shift from tensile cleavage fracture to large-strain plastic deformation owing to the stress state in the cutting region. When uncut chip thickness is large, as shown in Fig. 2.7, there exists a concentration region of tensile stress in the vicinity of the cutting edge.

Since the chip region is large, it contains number of defects which can nucleate to expand the cracks and cause brittle fracture. Whereas in the extremely small uncut chip thickness, there are too few defects to nucleate and to form cracks and hence it enables to remove the material in ductile mode.

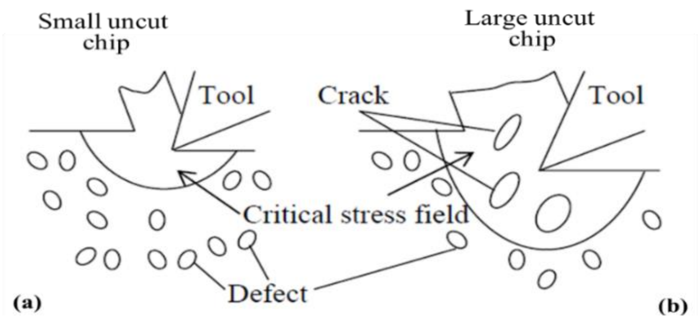

Fig. 2.7. A model of chip removal with a size effect in terms of defects distribution

Shimada et al. [64] used a different model to elaborate the brittle-ductile transition. They suggested that there are two ways of material removal: one is the ductile machining due to plastic deformation in the slip direction on the characteristic slip plane and the other is the brittle mode machining owing to cleavage fracture on the characteristic cleavage plane. When the resolved shear stress τ_{slip} in the slip direction on the slip plane exceeds a certain critical value τ_c inherent to the workpiece material, plastic deformation occurs in a small stressed field in the cutting region of a specified scale. On the other hand, a cleavage occurs when the resolved tensile stress normal to the cleavage plane σ_{cleav} exceeds a certain critical value σ_c. The mode of material removal depends on which criteria dominates or precedes $\tau_{slip} > \tau_c$ or $\sigma_{cleave} > \sigma_c$ for the stress state under a particular machining condition.

Fang et al. [48] observed ductile response of glass and reported that hydrostatic compressive stresses are responsible for the ductile nature of brittle materials in a very small cutting region. They further suggested that a negative rake tool gives rise to required hydrostatic stress which enables the ductile regime machining.

The critical values of stress for plastic and cleavage deformation are controlled by density of defects/dislocations in the work material. Thus size effect plays a lead role. With the smaller uncut chip thickness, the size of the resultant critical stress field is small enough to avoid a cleavage initiated at the defects. With larger uncut chip thickness, the critical stress field acts as a nuclei for crack propagation as shown in Fig. 2.8. Leung et al. [65] stated that there exists a critical depth of cut above which fractured surface is generated and below which smooth surface is produced i.e. ductile regime conditions are achieved.

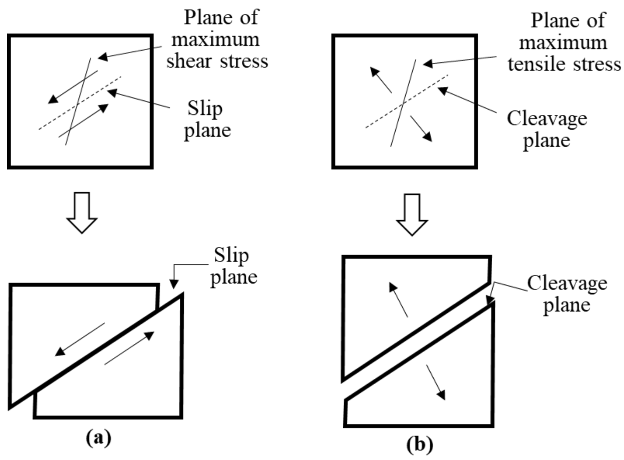

Fig. 2.8. Ductile and brittle regime models of chip removal

It has been noticed that the cutting mechanism is different for ductile and brittle material and at small length scale of cutting, the mechanism occurs in the same way for both the class of materials. However, literature does not report to the class of heterogeneous materials where hard phase particles are embedded into soft base material. It is anticipated that mechanisms of material removal would differ in the heterogeneous materials.

2.9. Material anisotropy

While the polycrystalline material in conventional cutting process is assumed to be homogeneous, continuous, and isotropic, it behaves as anisotropic in nature in the ultraprecision machining as the cutting takes place within the grain [66].

Lee W. B. [67] suggested that to carry out ultraprecision machining, an uncut chip less than the size of average grain is a prerequisite. The subgrain cutting of polycrystalline material resembles to the cutting of single crystals. The mechanics of cutting is affected by the crystal plane orientation which in turn introduce anisotropy. They found that the chip formation is affected by the crystal orientation due to the difference in shear angle for each orientation.

In the investigation of the effect of workpiece material properties in ultraprecision cutting, Moronuki et al. [68] revealed that for a depth of cut less than a micron, polycrystalline workpiece acts as a discrete and heterogeneous material whereas single crystal workpiece acts as a continuous and homogeneous material but it is anisotropic in nature which affects the material removal as well as surface quality. It was noticed in the case of cutting of single crystal Al, where a difference in cutting forces was evident in different crystal orientations. Furthermore they suggested that the polycrystalline materials should be considered as discrete and heterogeneous materials for a cutting depth less than 2 µm**.**

Sato et al. [69] observed the variation in surface roughness and flatness in the cutting direction in diamond turned single crystal Al and suggested that the workpiece orientation should be controlled to improve the machining accuracy.

Zhang et al. [70] during the nano cutting simulation of single crystal Cu with the crystal orientation $(111)[11\bar{2}]$ found out that the material undergoes severe plastic deformation. Nanoindentation simulation results showed there exists a critical stress which decreases with increasing machining depth.

Zhu and Fang et al. [71] suggested that it is difficult to remove a single layer of atoms while carrying out nanoscale machining on single crystal Cu on three different planes namely (001), (110), and (111) planes.

Shimada et al. [52] conducted MD simulation using morse potential to analyze the chip removal in the cutting of single crystal copper with crystal orientation (111)[1$\bar{1}$0] and proposed that a minimum of 1 nm chip thickness could be achieved. Pei et al. [72] compared Morse pair potential and EAM potential during nanometric cutting of Cu with the crystal orientation (100)[100] and observed that tool forces can be precisely calculated with EAM potential. Further, they showed that the machined surface integrity depends on rake angle. Ye et al. [73] carried out MD simulation of nanoscale machining of Cu on its crystal orientation (001)[100] at two different speeds and observed the presence of dislocations at a lower speed.

Wang et al. [74] studied the subsurface plastic deformation and defects during nanoscale cutting of copper on (010)[100] orientation. They observed the presence of stacking faults, dislocations, and point defects in the primary shear zone. Li et al. [75] investigated subsurface damage and surface integrity of copper (001)[100] surface containing the pores and second phase particles and found that machining forces and friction coefficient are affected by the presence of pores while second phase particle leads to work hardening phenomenon. Hosseini and Vahdati [76] performed MD simulation on single crystal copper having (001)[100] crystal orientation and observed that there exist a stagnant zone in the tool tip that dictates the mechanism of material removal. They further found that cutting mechanism is changed to sliding mechanism when the stagnant point lies above the uncut chip thickness.

Thus, it is apparent that most of the studies available on Cu in the literature are based on the single orientation of the workpiece material namely {100} family of cutting planes and <100> family of cutting directions and the studies were mostly performed with single cutting depth. It is likely that the cutting process will be affected in terms of material removal and deformation mechanism, cutting forces, surface and subsurface deformation while cutting along different cutting orientations and at various cutting depths.

2.10. Surface characteristics

The tool-workpiece interaction affect the surface mainly in the form of surface roughness. The surface texture is a result of process, machine tool characteristics, tool wear, tool workpiece vibrations, material properties, etc. Surface roughness is a significant parameter to evaluate the quality of the surface in the optical and tribological domain. Various researchers in the 1980s and 90s focused on the surface generated by the diamond turning process.

Taylor et al. [38] investigated the surface roughness of diamond turned electroless Ni and observed that the surface after material removal contains periodic marks corresponding to the tool edge fidelity. They pointed out that low wavelength spectral components can be reduced by improving the tool edge waviness.

While machining with a diamond tool, Syn et al. [77] revealed that the tool edge configuration is reflected in the feed marks and the height of these feed cusps increases with the wear of the tool. With the progression of tool wear, the cutting mechanism transforms into burnishing.

While diamond turning of Aluminum alloy, Sugano et al. [78] summarized that with the increase in tool nose radius and reduction in feed rate, the surface finish improves. The tool wear in the form of flank wear occurs that in turn increases the thrust force which consequently results into the degradation of surface finish. As the tool wear occurs, compressive residual stress on the surface increases due to burnishing action.

Mckeown P.A., [79] defined the zone band of tolerance between 0.05 µm and 0.005 µm in ultraprecision machining.

Asai and Kobayashi [80] concluded that the surface generation takes place at a very small cutting zone which is even smaller than the cutting edge sharpness of the tool while diamond turning of Al alloy. They further revealed that the temperature generated was higher than the melting point of the alloy.

Myler et al. [81] reported the primary causes of degradation of surface form accuracy are X-center error, progressive tool wear, induced stress, machine tool vibration.

Puttick et al. [82] compared the surface finish results obtained by diamond turning and ground specimen. They observed that diamond turned surface produces a very high surface finish with R_{max} of 6 nm whereas it lies in the range of 64-148 nm for ground specimen. Mean damage depth for both the processes was found to lie in 200-400 nm, however, diamond turned surface consisted of dislocations and ground surface were subjected to permanent subsurface damage with cracks and high density of dislocations.

To et al. [83] carried out ultraprecision diamond turning on single crystal Al and suggested that the surface finish is affected by the crystallography of the substrate materials. The (100) cutting plane gives the best surface finish and (110) results in poor surface finish.

In the previous studies till the year of 2000, surface finish and shape accuracy were focused upon without giving much attention to other aspects like the surface morphology, subsurface damage, effect of tool-workpiece vibrations etc.

Cheung and Lee [84] carried out power spectral density analysis of a surface roughness profile and revealed that the surface roughness in the diamond turning is generated as a result of various periodical components such as feed rate, tool configuration and relative tool-workpiece vibrations. In addition to this, tool interference and materials swelling also affect the surface roughness in diamond turning.

Revel et al. [85] experimentally characterized the diamond turned pure Al and Al alloy and found that the precipitates in Al alloy affect the machined surface and preferential damage is induced by the hard precipitates.

Zhang et al. [86] reported that surface topography or surface roughness is one important feature parameter in estimating components' surface quality. In diamond turning, surface topography is determined by multiple factors: cutting conditions [87][88][89], such as tool tip geometry, spindle speed, depth of cut and feed rate; material pile-up [90]; material swelling and recovery [91] [92]; crystal orientation [93]; the relative vibration between tool and work-piece [94] ; material- induced vibration [95]; tool tip vibration [96] and tool shank vibration. But the effects of the spindle-induced vibration on surface topography in the diamond turning have been little studied.

Zhang et al. [97] carried out the ultra-precision cutting of Cu alloy (CuZn30) and found that as the cutting process progressed, burrs were generated on the surface, which caused the degradation in surface finish.

While machining on single crystal silicon (Si), Yan et al. [98] noticed that the surface roughness was gradually increasing up to a cutting distance of 5 km, and after that it increases significantly. Peak to valley roughness before 5 km was observed to be well below 200 nm, however, it is increased to 1000 nm in the next 6 km of cutting distance. They further suggested that ductile to brittle transition is responsible for the increased surface roughness.

Hung et al. [5] observed excessive tool wear and its consequences on surface finish during precision machining of CuBe. It was noticed that the beryllium inclusions reduced the machinability of CuBe workpiece as a result of tool chipping and surface smearing. The hard particles were either dislodged from the surface or they were smeared along the surface which in turn deteriorated the surface finish. They recommended to avoid the use of mist coolant as it degraded the machined surface by chemically reacting to it. The material removal was noticed to be by shearing action. The study investigates the surface degradation, but subsurface deformation and nature of machined surface for full span of cutting were not addressed. Although tool wear was significant, physical and chemical contamination of the machined surface were not examined.

With the help of MD simulation in nanocutting of Si, Han et al. [99] revealed that under the effect of cutting tool, the workpiece atoms are subjected to great hydrostatic stress that causes crystal imperfections, dislocations and fracture of the atomic bonds in the cutting region. Further they observed that the amorphous layer is generated on the machined surface.

Yingfei et al. [100] noticed that with the increase in tool wear, surface defects in the form of scratches and craters started appearing in diamond machining of SiCp/2009Al. As the tool wore significantly, it was observed that the plastic side flow of the workmaterial around the tool was increase significantly and in turn caused material swelling. It was found that flank wear width of round edge single crystal diamond was five times that of polycrystalline diamond or straight nose single crystal diamond.

Zareena and Veldhuis [101] showed that the adhesion of workpiece material with the diamond tool caused wear on the tool which eventually resulted in increase in surface roughness. They suggested that the use of Perfluoropolyether (PFPE) coating on the tool is helpful in reduction of surface roughness and tool life enhancement. They observed that subsequent to PFPE coating on the tool, the surface roughness was decreased from 11.25 nm to 7.718 nm at a cutting distance of 4.7 km.

Zong et al. [102] investigated the effect on machining single crystalline Si (111) wafers with the diamond tools and observed that following the tool wear, C atoms removed from the tool are diffused on the machined surface. This leads to the formation of SiC on the machined surface.

Zong et al. [103] plotted average roughness value of diamond turned Si surface with respect to cutting distance for four orientations of diamond and showed that the average surface roughness values (Ra) were less than 10 nm up to a cutting distance of 4.5 km and vary within a surface roughness of 5 nm for different tool orientations. Subsequently as the cutting distance increases, it shows a wide variation of ~50 nm between the different orientations.

Yue et al. [104] related the surface quality of ceramic workpiece material to the cutting edge configuration and showed that sharp edge configuration of the diamond tool yielded better surface. The sharp edge caused surface average roughness (Sa) of 55.8 nm whereas the blunt edge led to surface average roughness (Sa) of 82 nm. He et al. [105] considered the kinematic roughness, plastic side flow, material elastic recovery and uncontrollable factors in a prediction model in order to obtain the surface roughness. The model reveals that with the decrease in feed rate, the kinematic component of the surface roughness reduces while the side flow increases. They showed that the contribution of these factors depend on the grain structure of the workpiece and tool nose radius.

Chen and Zhao [106] proposed the surface roughness model based upon the tool-work relative vibration and the swelling effect based on the elastic-plastic deformation and showed that model values lie within 6.5 % of the experimentally obtained average surface roughness values. Zeqin et al. [107] developed a surface roughness prediction model by considering the influences of tool-work vibration components in feeding, cutting and in-feed cutting direction and found that the predicted surface roughness agrees well with the experimentally obtained roughness values. Zhang et al. [108] reviewed the effect of ultraprecision machining on surface roughness generation and suggested that the factors which influence surface generation, include cutting parameters, workpiece materials, tool wear, machine tool vibration, thermal effects and elastic plastic deformation etc.

Mukaida and Yan [109] carried out diamond machining of microlens arrays on (100) plane of single crystal silicon and found that at higher feed rate than 5 μm/rev, brittle fracture takes place along certain direction. They further observed that the diamond cubic structure of Si workpiece transforms to amorphous. Rahman et al. [110] observed that the variation of machined surface integrity is influenced by the tool edge radius effect in ultra-precision machining of Cu and Mg alloy. Based upon the machined surface integrity and surface roughness, they identified four distinct machining zones viz. shearing, extrusion, ploughing and rubbing. Tauhiduzzaman and Veldhuis [111] associated the surface roughness to material side flow, grain boundary and inclusions in the material while diamond turning of Aluminium alloy.

In addition to surface roughness degradation, tool wear affects the surface quality in the form of shape inaccuracies and size tolerances. Zhou and Ngoi [112] reported that the cutting point changes continuously along the cutting edge during the machining of curved surfaces and leads to different rate of wear at distinct cutting points due to change in cutting velocity which in turn affects the form accuracy of the machined curved surface.

Tool workpiece interaction affects the machined surface not only in the form of roughness, waviness, shape and size error, it also causes the chemical contamination on the machined surface due to tool wear and surrounding conditions. Physical as well as chemical degradation of diamond turned surface mainly depend on the work material properties, mechanism of material removal, and tool wear.

2.11. Single crystal diamond tool

Single crystal diamond tool is used in ultraprecision diamond turning of nonferrous materials because of its ability to maintain an extremely sharp cutting edge owing to its wear resistance property. Single crystal diamond tool has a round nose with rake angle ranging from 0^o to highly negative and suitable clearance angle [Fig. 2.9] enough to avoid the contact between clearance face and the machined surface.

Sharp edge of the tool possess radius in the order of tens of nanometers with controlled waviness along whole edge. It possesses the highest thermal conductivity which makes it suitable in efficiently cutting various materials and capable of withstanding higher temperatures (i.e. up to 1000 K) during cutting. However, above 1000 K, the tool wear becomes rapid and results in degrading the surface integrity and machining accuracy [113]. The performance of single crystal diamond tools depends on the quality of the diamond, its crystal orientation, edge radius/sharpness [Fig. 2.9 (b)], and edge irregularities [Fig. 2.9 (c)]. Of these, measurement of tool edge radius is a challenge due to the fact that the tool edge is extremely sharp.

Diamonds are categorized into four types based on the presence of nitrogen as an impurity in their crystals. These are: Ia, Ib, IIa, IIb. Majority of natural diamonds (~99 %) come in type Ia. Type Ia consists of nitrogen in the form of aggregates in the crystal. All synthetic diamonds are of type Ib with an even distribution of nitrogen atoms in the crystal. Types IIa and IIb are very rare in nature but can be synthesized for industrial purposes. In all natural diamonds, there exist many impurity elements such as nitrogen, hydrogen, boron and oxygen [114].

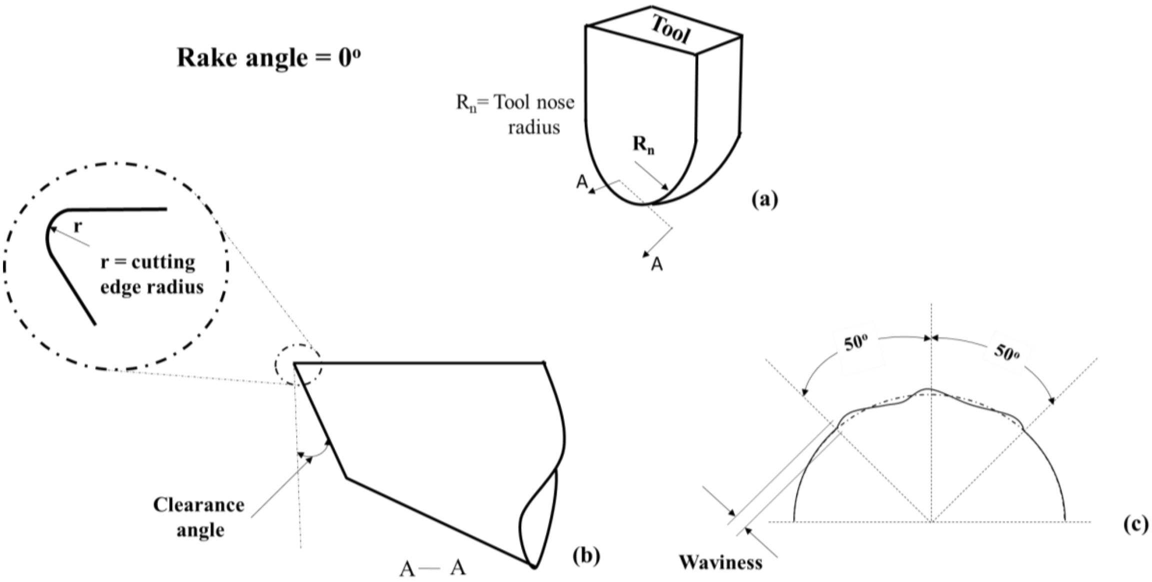

Fig. 2.9. Cutting tool geometry

Asai et al. [115] proposed a measuring method for diamond tool edge sharpness. They developed the conventional SEM by incorporating two secondary electron detectors. The signals from these detectors were processed to generate the fine cutting edge by the approximate curve obtained by simplex method of approximation. This technique of measurement was suitable for diamond tool with edge radius even below 45 nm.

Apart from the edge sharpness, diamond tool is required to have controlled waviness (i.e. < 1 μm) on its edge. The waviness on the tool edge results from the manufacturing inaccuracies related to its method of fabrication [Fig. 2.9 (c)]. There are two popular methods viz. grinding and ion beam milling. Grinding is frequently used to fabricate the diamond tool and the achievable waviness with this process is ~50 nm or better. Obata Kazushi [116] reported that the cutting tool with a waviness error causes deterioration in accuracy of a machined component.

Yuan et al. [117] conducted experiments on different orientations of single crystal diamond tool to find out the optimum crystal plane for ultraprecision machining. They performed the friction tests on rake and flank face of the tool, found out the friction coefficients and saw the effect on shear deformation, tool wear and the machined surface quality. Based on the friction coefficients value on different directions of crystal orientation of (100), (110) and (111), it was found that the (100) plane shows highest anisotropy.

Results of actual ultraprecision machining tests including the shear deformation, tool wear and surface quality showed that the (100) plane is most suitable for rake as well as flank surfaces. However, Uddin et al. (2007) recommended {100) as rake plane and {110} as flank plane for the diamond tool while machining of Si. With theoretical calculations, Zong et al. (2007) suggested that it is possible to achieve 1 nm sharp edge radius for the (110)(100) crystal orientation.

2.11.1. Wear characteristics of the diamond tool

The tool and workpiece interaction in ultraprecision diamond turning affects the tool in terms of tool wear. Tool wear in diamond turning of ductile and non-ferrous materials is found to be substantially low whereas it is rapid in case of hard and brittle materials. Early studies in case of tool wear were more related to examining the diamond suitability to machine the material. In 1990s and post 2000, attempts were made to understand the tool wear mechanism for various diamond turnable materials.

Hurt and Showman [118] investigated the tool wear and its effect on Cu and found that the tool wear is very slow while machining Cu and it takes place at the location where diamond contains defects and voids. The (111) plane, the weakest plane, is found more prone to tool wear. Yeo et al. [119] carried out the tool wear study while diamond turning of glass and with the help of the worn tool, they observed that cleavage and microchipping were dominant.

Paul et al. [120] proposed a hypothesis that suggested that the wear of diamond tools is associated with the unpaired ‘d’ electrons in the outermost shell of a workpiece material. Nonferrous metals do not have unpaired ‘d’ electrons, therefore the wear rate is slow. Whereas, the materials with outermost shell containing unpaired ‘d’ electrons cause the tool to wear rapidly.

Lin et al. [121] studied the effects of tool wear on the process as well as on the machined surface. They showed that the maximum temperature occurs for the largest flank wear length. Further, it was observed that there is compressive residual stress around the tool tip and it increases with the flank wear length. However, this compressive stress turns into tensile stress as the distance from the tool tip increases.

Evans and Bryan [122] classified tool wear in four categories namely: (i) Adhesion; (ii) Abrasion, microchipping and fatigue; (iii) tribothermal; and (iv) tribochemical wear. They suggested that these tool wear phenomena can occur either simultaneously or one mechanism may dominate the other.

Wada et al. [123] observed cleavage due to micro-fracture on the tool during diamond machining of nylon with a filler material and attritious wear while machining of pure nylon and aluminium. Similar observations were noticed by Zhou et al. [124], while machining glass with the diamond tool. On the basis of tool wear zone and machined surface topography, they showed that cleavage as well as microchipping are the dominant wear mechanisms.

Hung et al. [5] suggested that the hard precipitates in CuBe prompt excessive wear of diamond tools in diamond turning. Tool chipping by the impact of hard beryllium particles was the dominant mode of wear mechanism. They proposed to decrease the size and distribution of the particles in order to reduce the tool wear. However, their study did not involve the investigations on wear measurements and wear mechanism for full life of the cutting tool. The effect of single particle on the tool by experimental or simulation study was not considered. CuBe is a heterogeneous material and cutting forces are supposed to vary in the vicinity of the particle, but the study lacked the analysis of forces.

Zhang et al. [97] found that in ultra-precision cutting, cutting edge fracture and workpiece material welding to the diamond tool in the contact zone lead to the formation of wear land on the tool flank. Uddin et al. [125] found a gradual wear with smooth pattern on tool flank surface during diamond turning of silicon. Yan et al. [126] observed micro chipping on cutting edge for a tool with zero rake angle, and micro-grooving on flank for a tool with negative rake angle during machining of reaction bonded silicon carbide with diamond tool.

Li et al [127] reported generation of micro/nano-grooves at the tool flank surface. They observed that these micro grooves in turn lead to formation of sub-cutting edges on the main cutting edge itself. These grooves become deeper and extend towards the tool rake face and eventually become the leading cutting edge. Zareena and Veldhuis [101] reported the adhesion of the workpiece material to the diamond tool after initial graphitization, thereby, leading to the formation of a built-up edge on the tool, which subsequently wears out the tool.

Shimada et al. [128] put forward two mechanisms of tool wear connected to ferrous metals depending on the machining temperature. At a temperature higher than 1000 K, dissociation of carbon atoms on the diamond tool takes place while interacting with work surface atoms and they get simultaneously removed from the surface. At a temperature lower than 900 K, the mechanism involves the removal of carbon atoms due to oxidization of diamond accompanied with deoxidization of oxide layer present over the surface. Zong et al. [102], while machining single crystalline Si wafers with diamond tools having different rake and flank face orientation, have observed diffusion as a prominent mechanism, which in turn leads to the formation of SiC. With the help of Molecular Dynamics Simulation (MDS) on monocrystalline Si, Goel et al. [129] attributed tool wear to the temperature between the interface of tool edge and work surface. They showed that the temperature is an influential factor in carbide formation with simultaneous conversion of sp^3 structure of diamond to sp^2 (graphite).

Brinksmeier et al. [130] observed low tool wear at high cutting speed and high tool wear at low cutting speed while diamond machining of electroless nickel and brass. They further analysed that the reduced contact time between tool and workpiece at high speeds leads to less chemical activity. With further investigation, they showed that high speed machining of OFHC Cu and brass leads to better surface finish. Kumar et al. [131] suggested that heat generation is the dominant mode of tool wear during the diamond turning of polycarbonate lens. With the help of a mathematical model, they analysed and reported that the temperature of the machined surface layer as well as the successive underneath layers increases which further degrades the surface profile accuracy and surface finish.

Heidari and Yan [132] observed microchipping as the wear mechanism while machining porous silicon with the diamond tool. They further observed that the micro chipping gradually leads to larger edge chipping. In addition, they demonstrated that high flatness of the order of 13 nm could be achieved on diamond machined porous silicon by using wax and controllable parameters. Yingfei [100], in diamond machining of SiCp/2009Al, found that both mechanical and chemical wear are the dominating wear mechanisms on a diamond tool.

Zhou and Ngoi [112] reported that the cutting point changes continuously along the cutting edge during machining of curved surfaces, which leads to a different rate of wear at distinct cutting points due to change in cutting velocity. Yan et al. [98] suggested that the presence of microgrooves on the tool's flank surface is the major cause of higher surface roughness on the machined Si surface.

Studies on diamond tool wear show that mechanism of tool wear are material dependent. It is noticed that various wear mechanisms of tool take place simultaneously while machining any given material. However, one wear mechanism dominates over others while machining different materials. Moreover, tool wear affects the surface quality in terms of its surface finish and level of contamination.

2.12. Copper Beryllium

Copper beryllium is a potential heterogeneous material which has been used in electronic, optical and nuclear industries because of high strength, nonmagnetic, good wear resistance, corrosion resistance, high fatigue strength and non-sparking qualities. Conventional and nonconventional techniques are able to machine CuBe for the required applications. Few literatures on the tool-workpiece interaction during machining of CuBe have been surveyed here. Initially, Arnold et al. [133] explored the machining of CuBe with diamond tool and made an effort to determine its machinability.

Mehfuz and Ali [134] used response surface methodology for analysing the experimental data on micromilling of CuBe alloy and observed that the interaction effect of depth of cut and feed rate is effective in obtaining better surface finish.

Sudhakar et al. [135] employed dry and wet machining of CuBe using polycrystalline diamond and found that though machinability of CuBe under wet conditions is suitable for achieving better surface finish, dry-machined samples showed relatively higher hardness values as a result of excessive work hardening effects during the machining process.

Hung et al. [5] investigated the machinability of CuBe with a single crystal diamond and compared with precision grinding and observed that the diamond turn machining generates surface with better finish. Be particles were found to be responsible for degraded surface in both the processes. They, however, suggested to carry out dry machining in order to avoid chemical attack on the mirror finished surface as a result of coolant.

It is noticed that earlier studies on machining of CuBe either at micro/nano or macro scale are very limited and it is required to carry out the investigation in ultraprecision machining of CuBe.

2.13. Molecular Dynamics (MD) Simulation in diamond turning

Due to its extremely small cutting zone in the order of nanometers at the region where surface generation takes place, the diamond turning process is also called nanoscale cutting/machining process. Nanomachining involves material deformation in only a few atomic layers. At such a small length scale, the traditional continuum theory, such as finite element methods (FEM), becomes questionable. Furthermore, the effect of temperature and defect structures during nanomachining process becomes more important, while these effects are hard to capture by experiment. So, nanomachining simulation should be based on discrete atomistic analysis. Hence, molecular dynamics (MD) simulation technique has been generally applied in the study of machining processes at nanoscale. Molecular dynamics simulations are a microscopic approach to trace the behavior of atoms at every short time step and by the time integration of

Newton's second law. The force acting on each atom is obtained by the summation of interactions from the surrounding atoms in the model assuming an interatomic potential. There is a long list of interatomic potential functions for different materials depending upon their nature of bonding. Table 2.4 lists various interatomic potential functions.

Table 2.4. Interatomic potential functions

Potential Function	Model	Application
Lennard-Jones Potential	$\boldsymbol{V_{ij} = 4\varepsilon \left[\left(\frac{\sigma}{r}\right)^{12} - \left(\frac{\sigma}{r}\right)^{6}\right]}$ $\boldsymbol{\sigma}$ and $\boldsymbol{\varepsilon}$ are constants which are dependent on the physical property of the materials.	Mostly suitable for rare gases
Morse Potential	$\boldsymbol{\phi(r_{ij}) = D\left[exp\left(-2\,\alpha(r_{ij} - r_0)\right) - 2\,exp\left(-\alpha\,(r_{ij} - r_0)\right)\right]}$ $\boldsymbol{r_{ij}}$and $\boldsymbol{r_0}$ are instantaneous and equilibrium distances between atoms i and j respectively $\boldsymbol{\alpha}$ and D are constants determined on the basis of the physical properties of the material	Mostly suitable for cubic metals
Born-Mayer Potential	$\boldsymbol{\phi(r_{ij}) = A\left[exp\left(-2\,\alpha(r_{ij} - r_0)\right)\right]}$ A and $\boldsymbol{r_0}$are constants dependent on the material.	Mostly suitable for ceramics
Embedded-Atom Potential (EAM)	$\boldsymbol{U_{metal} = \frac{1}{2}\sum_{i=1}^{N}\sum_{j=1}^{N} V_{ij}(r_{ij}) + \sum_{i=1}^{N} F\,(\rho_i)}$ $\boldsymbol{\rho_i}$ is the total electron density at atom i due to the rest of the atoms in the system. F is the embedding energy for placing an atom into the electron density V_{ij} is the short range pair interaction representing the core-core repulsion r_{ij} is the separation of atoms i and j	Applicable to a wide range of metals
Tersoff Potential	$\boldsymbol{V_{ij} = V_r(r_{ij}) - B_{ij}V_a(r_{ij})}$ $\boldsymbol{V_r}$ and $\boldsymbol{V_a}$ are the potentials due to repulsive and attractive forces between atoms i and j and $\boldsymbol{B_{ij}}$ is a parameter that provides the information for the direction and the length of the bond.	Significant for covalently bonded materials

The Molecular dynamics (MD) simulation is a very effective numerical method for analyzing various phenomena at the atomistic scale. Currently, MD is playing an increasingly prominent role in the analysis of the behaviour of materials at an atomistic level that cannot be readily obtained either by other theoretical methods or by experiments. The MD technique was first applied in the study of statistical mechanics in the late 1950s at the Lawrence Radiation Laboratory by Alder and Wainwright [136]. Since then, the simulation method has been used in a broad range of fields which include material science, physics, chemistry, micro-biology, tribology and engineering.

MDS was introduced in 1980s for modelling the nanometric cutting. It is helpful in addressing a number of machining and finishing problems at atomic scale. Atomistic simulation provides the information about the various mechanisms taking place in few nanometres of atomic layers. The pioneering work of Belak and Stowers et al. at the Lawence Livermore National Laboratory in the field of metal cutting led to the success in modelling various aspects of nanometric cutting [137].

MDS is deterministic i.e. once the positions, velocities and accelerations of the particles are known, the state of the system can be predicted. MD simulation method presents higher temporal and spatial resolution of the cutting process than by other simulation technique. As the process is reduced to its fundamental units, MD simulation throws more light on the understanding of mechanism and mechanics undergoing at nanoscale cutting. There are different interatomic potentials which are used for the simulation purposes depending upon the material properties. Belak and Stowers [137], Shimada and Ikawa [52] pioneered the concept of MD in the framework of nanometric cutting. Shimada and Ikawa [52], and Komanduri et al. [58,138–143] have contributed significantly to this area and set a foundation for the study of nanometric cutting processes using MD simulation. The typical works among them are those by Komanduri et al. [58,138–143], who carried out MD simulations of the nanometric machining of single crystal copper and aluminium to study the chip formation, material deformation, cutting forces, atomic scale friction and exit failure during nanometric machining process. They investigated the effects of crystal orientation, cutting direction and tool geometry on the nature of deformation and machining anisotropy of the material.

Ikawa et al. [50] performed atomistic analysis of nanometric cutting to examine the minimum chip thickness of cut for a given edge radius. It was concluded that while the minimum thickness is affected by the tool-work material interaction to a certain degree, it is strongly affected by the sharpness of the cutting edge. Shimada et al. [52] conducted molecular dynamics simulation to investigate the ultimate accuracy that can be achieved in ultra-precision machining of aluminium and copper using a hypothetically perfect machine tool. They observed the minimum thickness of cut to be about 1 nm or less. Komanduri et al. [144] investigated the effect of tool geometry in nanometric cutting in terms of rake angle and tool edge radius using pair-wise Morse potential function. Komanduri et al. [145] also investigated the effect of different tool rake angles on nanoscale cutting of monocrystalline silicon with perfectly sharp tool edge. They observed that the negative rake angle and/or large edge radius provide high hydrostatic pressure required for the formation of a small plastic deformation zone in workpiece immediately beneath the tool instead of initiating brittle fracture in brittle material like silicon.

Pei et al. [146] studied the effect of tool rake angle on cutting process of copper single crystal. They observed that as the rake angle changed from -45 to 45, the machined surface became smoother. They also compared pair-wise Morse and metallic EAM potential and showed there was no big difference in the simulated chip formation and machined surface under these different potentials. However, EAM potential was better in calculating tool forces precisely.

Pei et al. [147] also carried out large scale MD simulation of copper nanomachining with rounded tool edge in different cutting depths, speeds and crystal orientation. They elaborated that dislocations and other lattice defects were produced in cutting region near the tool edge and some of them glided deep into the workpiece. Lucca et al. [148] studied the effect of single crystal diamond tools with negative rake angles on tool forces for Germanium. Also, tool edge geometry and the new machined surfaces were characterized with atomic force microscopy. They concluded that a significant increase in thrust force to the cutting force ratio occurs for decreasing depth of cut and for increasing negative rake angle.

Cai et al. [149] used molecular dynamics method to simulate crack initiation in the ductile–brittle mode of cutting for depths of cut ranging from smaller than tool cutting edge radius to larger in Si material. They observed that when the uncut chip thickness becomes larger than the tool edge radius, cracks may be initialized due to a peak deformation. As the uncut chip thickness is smaller than the cutting edge radius, there is no peak in the chip formation zone, and thus there is no crack initiation zone in the undeformed workpiece material. Hosseini and Vahdati [76] performed MD simulation on single crystal copper considering diamond tool as a rigid body and observed that there exist a stagnant zone in the tool tip that dictates the mechanism of material removal. They further found that cutting mechanism changes to sliding mechanism when the stagnant point lies above the uncut chip thickness.

MD simulation has been an indispensable technique for understanding the science behind the machining of various materials. However, most of the studies have been focussed on single crystal orientations of the workpiece materials and these studies were confined to defect free materials. Inhomogeneities in the materials have not been considered which may affect the cutting behaviour during nanoscale cutting.

2.14. Gap areas

Following research areas have been identified as gap areas at the end of this literature survey.

1. Machining of heterogeneous materials (i.e. CuBe, electroless Nickel (NiP), Si reinforced Al matrix composites (Si/Al)) with SCDT has received a little attention.
2. Material removal mechanisms in nanoscale cutting of heterogeneous materials have not been addressed.
3. Molecular dynamics simulation of nanoscale cutting of heterogeneous materials (like CuBe) has not been attempted to investigate the interaction effects of tool and workpiece.
4. Tool wear mechanisms have not been established while machining CuBe, NiP, Si/Al materials with a single crystal diamond tool.
5. Effect of work material, mechanism of material removal, and the effect of tool wear on the diamond turned surface have not been comprehensively studied for any of the engineering material.
6. Apart from the physical degradation, chemical and metallurgical changes on the diamond turned surfaces have not been studied for CuBe machined surfaces.
7. The multiscale simulation has not been explored for the nanocutting process.
8. Tool wear models have not been well established in case of diamond tool and different workpiece materials in ultraprecision machining.
9. Studies related to the prediction of diamond tool wear and compensating it on tool path to get consistent dimension on the product are still in incipient stage.
10. Cutting mechanics and tool wear modeling in case of ultraprecision diamond turning are not derived for different class of materials.

Based on the research gap areas, scope of the present work has been devised and proposed.

2.15. Scope of research work

Among the research gaps, few areas are considered for investigations in this research work. To understand the mechanisms involved in a heterogeneous material, CuBe, which has wider application area, is considered as a workpiece material for this study. Following areas of research activities are identified as a scope for this research work and investigations are carried out:

1. There is a need to study the interaction between the diamond tool and hard particles while machining of CuBe alloy. Since the cutting zone, where the actual surface generation takes place is extremely small, it requires discrete mechanics approach to investigate the underlying mechanisms. Therefore, the following are defined as the scope of this research work:
   - **Molecular dynamics simulation** (MDS) at nanoscale cutting zone to understand the material removal mechanism, tool wear mechanism and effect of tool condition on the quality of generated surface.
   - Since MDS of nanocutting of CuBe requires interatomic potential for Cu and Be atoms, development of an interatomic potential for Cu-Be is essential.
2. **Wear Mechanism**: It is important to understand the wear mechanisms of the diamond tool while machining a heterogeneous CuBe workpiece material. Hence, both MDS and experimental investigations are necessary.
3. **Surface Quality:** As the condition of the tool affects the quality of the machined surface, it is necessary to comprehend the nature of generated surface while diamond turning of CuBe both by MDS and experimental study.

Chapter 3

Molecular dynamics modelling and development of interatomic potential for Cu-Be interactions

3.1. Introduction

The phenomenon underlying in a very small cutting zone in a diamond turning process can be understood with the help of molecular dynamics simulation (MDS) technique, owing to the fact that the conventional continuum approach does not hold good at this scale. At nano scale, discrete effects of the material come into picture and these are aggravated by the presence of beryllium particles in CuBe. Thus, MDS is carried out to understand the mechanisms in nanoscale cutting of CuBe with single crystal diamond tool and Cu is considered for benchmarking purposes. CuBe alloy with 2% Be is considered as the workpiece material for this study. During MDS of nanocutting of CuBe with a single crystal diamond tool, there are multiple interactions which take place between Cu, C and Be. Since, a single multibody potential for defining Cu-C-Be interactions does not exist, it is essential to define the intra- and inter-atomic interactions. Although there are interatomic potentials for Cu-Cu, C-C, Be-Be, Cu-C, and Be-C interactions, the potential function parameters for Cu-Be interactions is not available. In this chapter, nanoscale cutting simulation is modeled for CuBe based on the basis of experimental characterization of the specimen. The potential functions for each atomic interaction are defined with their parameters. Further, calculations and determination of interatomic potential parameters of Cu and Be atomic interactions are carried out.

3.2. Characterization of CuBe alloy

Since CuBe is an alloy and is a heterogeneous material consisting of different phases, it is essential to characterize the CuBe workpiece prior to carrying out the simulation model for nanocutting simulation and experiments. In the characterization of CuBe, its microstructure with optical microscope, chemical composition with electron dispersive spectroscopy (EDS) and X-ray photoelectron spectroscopy (XPS), and hardness with Vickers micro hardness tester were evaluated.

3.2.1. Microstructure of CuBe

To reveal the microstructure, the CuBe specimen was cold mounted in an epoxy. The specimen was hand ground followed by fine polishing with 1µm diamond paste. The polished CuBe specimen was then etched with an etchant [7 ml H_2O + 13 ml NH_4OH + 12 ml $(NH_4)_2S_2O_8$] to reveal the particle distribution over the workpiece. The specimen was etched for 5 seconds and then viewed under a microscope to display the particle distribution on the workpiece. The microstructure of CuBe is shown in Fig. 3.1. It is noticed that the particles are distributed over the specimen within the grains as well as at the grain boundary. There are two phases present on the workpiece: (1) Cu rich phase (α-phase) and (2) Be rich phase (ϒ-phase). The ϒ-phase or the granular particles distributed over the workpiece are hard precipitates which are enriched with Be. The hardness and strength of CuBe alloy are significantly increased by Be precipitates.

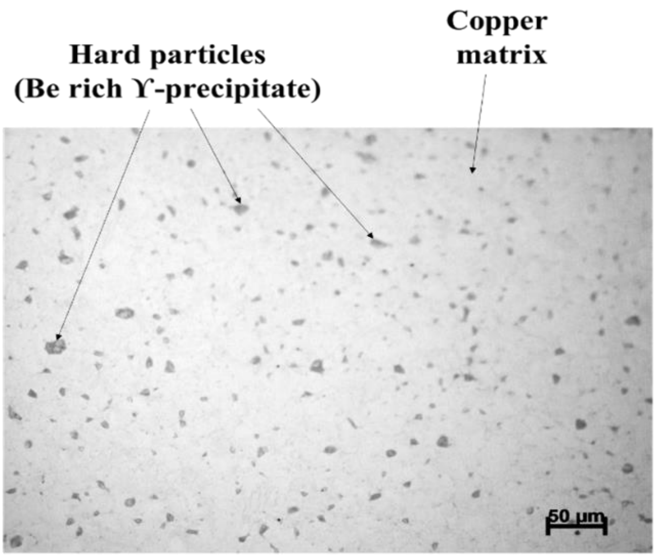

Fig. 3.1. Microstructure of copper beryllium (300 X magnification)

Fig. 3.2 reveals the formation of Be precipitates with the help of a schematic. Be atoms as solute particles are distributed randomly initially before the age hardening process [Fig. 3.2 (a)]. In the age hardening process, Be atoms tend to coalesce together and forms a Be rich phase or precipitates [Fig. 3.2 (b)]. Similarly, the remaining substrate material become Cu rich as the Be atoms tend to form a concentrated granular particle [150]. These precipitates are hard in nature and hinder any deformation. Due to this, the CuBe alloy possesses strength as well as hardness. The ‘hard Be precipitates’ are interchangeably called ‘hard Be particles’ or simple ‘hard particles’ in the current study. The CuBe workpiece is interpreted as hard Be particles embedded in a soft Cu matrix.

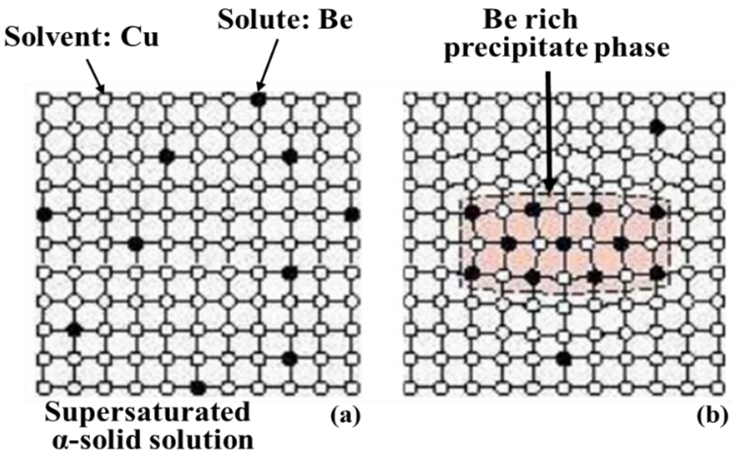

Fig. 3.2. Schematic showing the formation of Be rich phase

The cutting behaviour and mainly tool wear depend upon the hardness of the workpiece material. Therefore, Vickers hardness test was performed on Cu and CuBe workpieces to determine the bulk hardness. The value of hardness for the Cu workpiece is ~ 0.85 GPa and for CuBe workpiece, it is ~ 3.5 GPa. Since CuBe is a heterogeneous material, which contains two phases, its hardness is expected to vary within the material.

3.2.2. Chemical analysis of CuBe

The Cu and Be rich phases are characterized for composition to have better understanding before modelling and machining. For the chemical analysis, EDS and XPS was performed.

Chemical composition of the Cu rich phase and Be rich phase is required to be identified prior to analyse the tool and workpiece interaction. Therefore, EDS was performed to evaluate the composition of CuBe workpiece and the results are shown in Fig. 3.3.

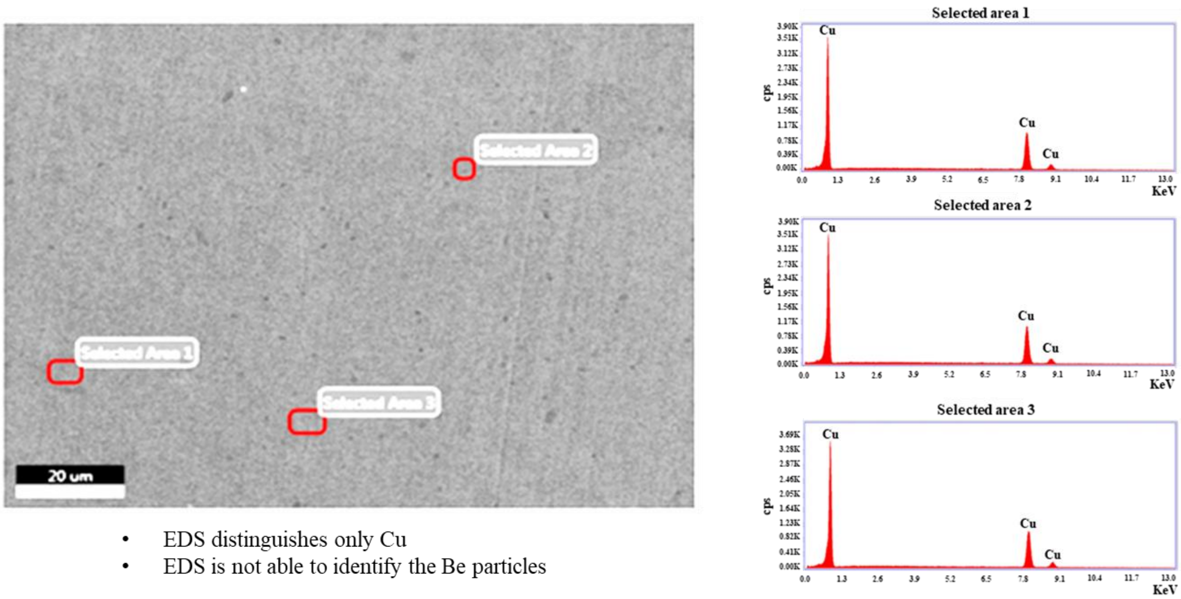

Fig. 3.3. EDS spectrum of CuBe sample (1000 X magnification)

As Be has a very small atomic number (*i.e.* Z=4) and contains only two shells very close to the nucleus, it usually does not emit sufficient characteristic X-rays to detect the Be present in the workpiece. The EDS spectrum shows only the presence of Cu in the workpiece. Beryllium (Be) being a small atomic number element is very less sensitive to X-rays and it is present in a very small amount (2%). To reveal the presence of Be, X-rays were utilized on CuBe sample with multiple scans while conducting the X-ray photoelectron spectroscopy [Fig. 3.4]. X-ray photoelectron spectrum shows a small peak around the Binding energy of Be (~113 eV) owing to its very less sensitivity, revealing the presence of Be particles in the sample. The chemical analysis shows that the sample contains Cu and Be as the constituent elements. Be is assumed to exist as a hard particle in the Cu base material for the modelling purpose.

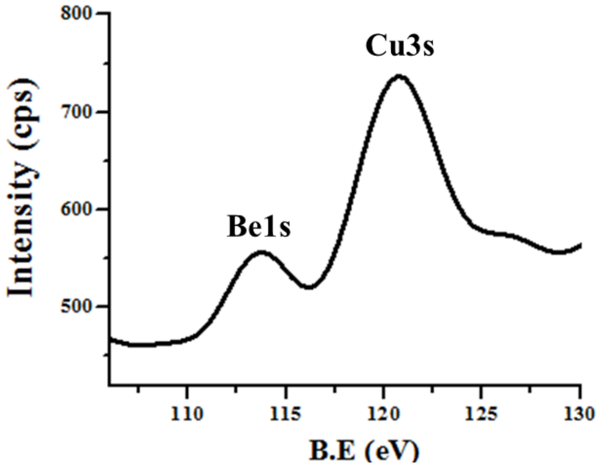

Fig. 3.4. XPS spectrum of CuBe

It is indicated by the microstructural and chemical analysis that the CuBe contains Be rich phase as a precipitate in Cu rich base material. Based upon these observations, the simulation model is created and interatomic potentials are defined in the following sections. For modelling of nanomachining, Be is assumed to exist as a hard particle in Cu matrix.

3.3. Material description in Molecular dynamics modelling

The key to computational efficiency of atomic-level simulations (barring electronic interactions) lies in the description of the interactions between the atoms at the atomistic instead of the electronic level. The atomistic description of the system eliminates the complex many body interactions arising due to the presence of electrons and nuclei as it occurs in quantum mechanics [151].

A homogeneous and continuous macro system when considered at atomic scale apparently behaves like a discrete material characterized by chemical elements and their coordinates. The coordinates describe the atomic arrangement based on known lattice structures and lattice constants for a metallic, covalent or ionic system [151]. The atomic arrangements for the tool and the workpiece material is shown in Fig. 3.5.

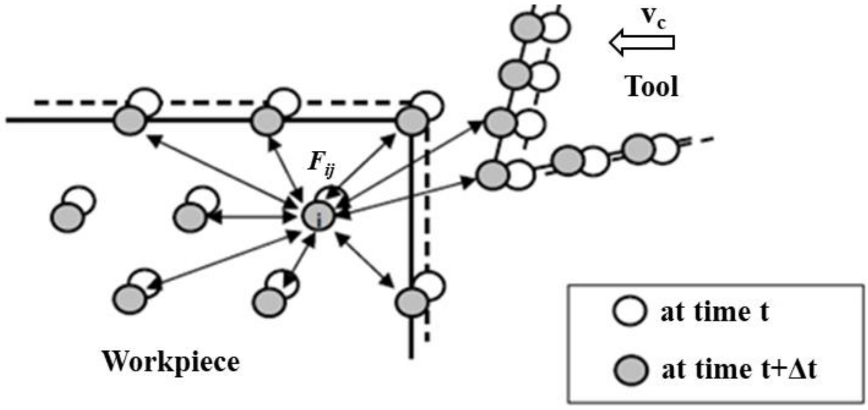

Fig. 3.5. Schematic of atomic description of tool and workpiece

The tool in actual diamond turning possesses single crystal structure while the workpiece possess polycrystalline structures. The crystal size of metallic workpiece represent realistic material structures for nanoscale cutting simulations as the highly sharp edge of the tool will have to cut at least 30, 000- 50,000 unit cells before reaching a grain boundary [152].

Moreover, the effect of various defects in crystalline structures, like inclusions, precipitates and particles, grain boundaries and dislocations can also be studied through MD simulation. In nanoscale cutting, for an uncut chip thickness less than 1 μm, the workpiece behaves as discrete and heterogeneous [68].

For each time increment (Δt), every atom changes its position and interacts with its surrounding neighbor atoms in a manner that can be determined from the interatomic potential function which is described in the next sub-section.

3.3.1. Atomic interactions

The central part of MD method is the computation of the atom-atom interactions. It determines the whole structure of the system at every timestep and thus it is the most time consuming part in MD program. Various algorithms have been developed for the efficient calculation of the system's structure in every time step.

The interactions between atoms are specified by the functions that describe the potential energy. While the accuracy of the interatomic potential function dictates the quality of the simulation results, its functional complexity governs the computational time required for a given system. The potential functions vary in their mathematical description depending on the type of material and the same function does not apply accurately for two different class of materials. Therefore, it is essential to develop a potential for each type of material. Empirical potentials are employed to define the pairwise interaction between two atoms. Validity of the function as well as the stability of the crystal for a given material are checked for various properties including cohesive energy, lattice constant, compressibility and elastic constants as well as the equation of state. Some commonly used potentials are described in the following sections for completeness.

3.3.1.1. Interatomic potential functions

Interatomic potential functions are mathematical expressions for calculating the potential energy of a system of atoms. The heart of the MD simulations is these interatomic potentials. The interatomic potential function and parameters give a complete information about the system energy and about the forces acting on each particle. They are classified into two types: pair potential and many-body potential. The most common pair potentials are Lennard-Jones (LJ) potential [153] and Morse potential [154]. In the many-body potentials, Embedded atom method (EAM) based function for metallic bonded materials [155] and analytical bond order potential (ABOP) for covalent bonded materials [156] are most popular. The mathematical description for these potential functions is provided as below:

i. **Lennard-Jones (LJ) potential**

LJ was mainly devised to simulate inert gases and liquids. Fig. 3.6 (a) and (b) shows the dependence of attractive, repulsive and net forces and potential energies, as a function of the interatomic separation, ‘r’, for two isolated atoms. The attractive force binds the atoms together while the repulsive force prevents them from coalescing. The curvature of the potential energy function is determined mainly by the repulsive force, which therefore dictates the elastic behavior of the solid. The length of the bond ‘r’ is the centre-to-centre distance of the bonding atoms. Strong bonds pull the atoms closer and so have smaller bond lengths compared with weak bonds. At ‘r_o’, the attractive and the repulsive forces exactly balance and the net force is zero. This corresponds to stable equilibrium with a minimum potential energy, the magnitude of which is the bond energy as expressed by equation 3.1.

$$V_{ij} = 4\varepsilon\left[\left(\frac{\sigma_0}{r_{ij}}\right)^6 - \left(\frac{\sigma_0}{r_{ij}}\right)^{12}\right] \quad \textbf{(3.1)}$$

Where V_{ij} is the potential energy of all the atomic bonds, r_{ij} denotes the distance between particle i and particle j, ε is the minimum of potential, which occurs when the distance r_{ij} is equal to $2^{1/6}\,\sigma_o$, where σ_o is determined by the physical property of the material.

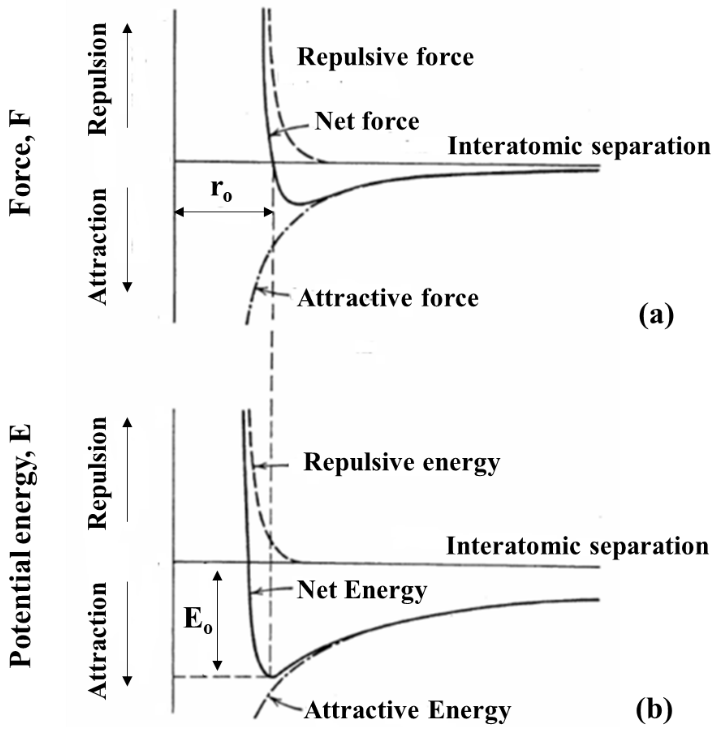

Fig. 3.6. Variation of interaction force and potential energy in LJ potential

ii. Morse potential

Morse potential is a popularly used empirical pairwise potential energy function which produces repulsive force in the short range, attractive force in the medium range and decays smoothly to zero in the long range. The potential explains chemically active materials as bonds that can be established or cut at the long-range part. The Morse potential represents realistic descriptions for two-body interactions in such a way that they account for the repulsion due to overlapping electron clouds at close distances and for attraction at large distances due to dispersion effects. Generally, in solids a shielding effect is created that make interactions beyond the first few neighbors of limited physical interest. Thus, potential functions are commonly truncated at a certain cutoff distance, preferably with a smooth transition to zero and result in so-called short-range forces [154].

The Morse potential energy function is given by

$$V(r_{ij}) = D[\exp(-2\alpha(r_{ij} - r_o)) - 2\exp(-\alpha(r_{ij} - r_o))] \tag{3.2}$$

where, D, α, r_{ij} and r_o are the binding energy, elastic modulus, arbitrary distance between ith and jth atoms and equilibrium atomic spacing respectively. The cutting simulation in this thesis involves the interactions of diamond tool and Cu workpiece defined by Morse potential.

iii. Embedded atom method

Embedded atom method (EAM) based potential energy precisely describes the interaction between atoms in the metallic system. The embedded-atom method is a semi-empirical method which is employed to perform calculations of metallic defects. The EAM potential provides a very robust means of calculating approximate structure and energetics. The energy based on EAM potential [155] is expressed as:

$$U_{tot} = \frac{1}{2}\sum_{j \neq i} V(r_{ij}) + \sum_{i} F_i(\rho_i) \tag{3.3}$$

Where V is a pair potential and is a function of the separation distance r_{ij} between atom i and surrounding atom j. And F_i denotes an embedding energy that is required to place an atom i in a host electron density (ρ_i) at the position of the atom i, induced by all other atoms in the system. ρ_i is expressed as:

$$\rho_i = \sum_{j \neq i} \phi_j(r_{ij}) \qquad r_{ij} < r_c \tag{3.4}$$

iv. Analytical Bond order potential (ABOP)

The analytical bond order potential (ABOP) is a multi-body potential function which permits formation and breaking of bonds during the machining simulation which is essential to analyse the tool wear. The ABOP function was proposed by Erhart and Albe [156] which precisely gives the description of both dimer and bulk properties of materials and therefore is more consistent for the covalent bond interactions. Total energy using ABOP function is a sum over each bond energies and is expressed as

$$E = \sum_{i > j} f_c(r_{ij}) \left[V_R(r_{ij}) - \frac{b_{ij} + b_{ji}}{2} V_A(r_{ij}) \right] \tag{3.5}$$

where, E is the cohesive energy which is the sum of individual bond energies which has pairwise repulsive (V_R) and attractive (V_A) contributions, b is the bond order parameter.

$$V_R(r) = \frac{D_0}{S-1} \exp\left[-\beta\sqrt{2S}(r - r_0)\right] \tag{3.6}$$

$$V_R(r) = \frac{SD_0}{S-1} \exp\left[-\beta\sqrt{2/S}\,(r - r_0)\right] \qquad \textit{(3.7)}$$

Where, D_o and r_o are the dimer energy and bond length, the parameter S determines the slope of the Pauling plot, β is the parameter which can be obtained from the ground state oscillation frequency of the dimer. The cut off function is defined as:

$$f_c(r) = \begin{cases} 1 & \mathrm{r < R - W} \\ 0 & \mathrm{r > R + W} \\ \frac{1}{2} - \frac{1}{2}\sin\left(\frac{\pi}{2}\frac{r-R}{W}\right) & |\mathrm{R - r}| \le W \end{cases} \qquad \textbf{(3.8)}$$

where, parameters R and W states the position and the width of the cut-off region. The bond order b_{ij} is given by:

$$b_{ij} = (1 + \chi_{ij})^{-\frac{1}{2}} \qquad \textbf{(3.9)}$$

$$\chi_{ij} = \sum_{k(\neq i,j)} f_c(r_{ij}) \exp[2\mu(r_{ij} - r_{ik}) g(\theta_{ijk})] \qquad \textbf{(3.10)}$$

where, μ is a fitting parameter, θ_{ijk} is the angle between ij and ik bonds, χ_{ij} represents effective coordination number and angular momentum $g(\theta)$ is given by:

$$g(\theta) = \lambda\left(1 + \frac{c^2}{d^2} - \frac{c^2}{d^2 + (h + \cos\theta)^2}\right) \qquad \textbf{(3.11)}$$

where, λ, c, d and h are angular dependence parameters in ABOP potential.

3.3.2. Calculation of forces and acceleration based on interatomic potential energy

Interaction force can be obtained by differentiating the potential energy. The interaction force between the interacting atoms is given by:

$$F_{ijx} = -\frac{\partial V_{ij}}{\partial x_i} \tag{3.12}$$

where, F_{ijx} is the interaction force acting on the i^{th} atom by the j^{th} atom in the x direction, and x_i indicates the i^{th} atom's coordinate in the x direction. Similarly, F_{ijy} and F_{ijz} can be obtained. The resultant force F_{ix} on the i^{th} atom in the x direction is given by the sum of all the forces arising from the interactions with every j atom within the cut off region.

$$F_{ix} = \sum_{j=1,\, j\neq i}^{N} F_{ijx} \tag{3.13}$$

The atoms in the system then follows the Newton's equation of motion.

$$a_{ix} = \frac{d^2 x_i}{dt^2} = \frac{F_{ix}}{m_i} \tag{3.14}$$

where, a_{ix} represents the i^{th} atom's acceleration in the x direction, m_i is the mass of the i^{th} atom. In the similar fashion, forces are evaluated in Y and Z directions at every time step.

3.4. MD simulation methodology for nanocutting of Cu and CuBe

3.4.1. Cutting simulation geometry and conditions

As Be rich phase exists as a hard precipitate in Cu rich base material, it was assumed that the workpiece in a nanocutting simulation model consists of a spherical particle in Cu. In the simulation, it was assumed that the hard particle is made of Be atoms and the base material consists of Cu atoms. To have a better comparison, nanocutting of Cu was also simulated for benchmarking. Fig. 3.7 shows the MD simulation model of nanocutting of both Cu and CuBe.

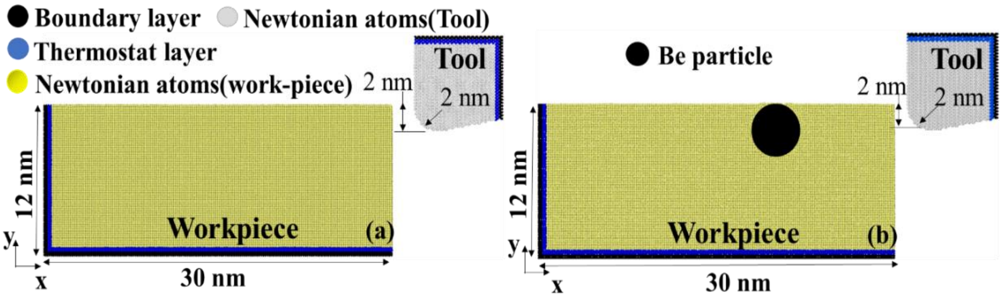

Fig. 3.7. MDS model for nanoscale cutting of Cu and CuBe

Both the tool and workpiece were composed of three layers viz. Newtonian layer, thermostat layer and boundary layer. There are certain assumptions considered for the modelling the nanocutting process:

(1) Be rich phase consists of pure Be and base material is made of pure Cu.

(2) Hard particle is spherical in shape.

(3) Simulation is carried out at 293 K.

(4) Cutting speed is 1 Å/ps.

(5) The system follows NVE dynamics.

Thermostat and Newtonian layer together forms a mobile layer in which atoms' positions and velocities were calculated based on Newton's second law of motion. Boundary layer atoms were fixed and served as rigid bases to support the mobile layer atoms and also to reduce the boundary effects. Thermostat atoms were kept at constant temperature (293 K) by rescaling the atoms velocities to the desired temperature. It assisted in dissipating the heat generated during machining. In actual machining process, it was carried away either by chips, lubricants and dissipated into the bulk material due to conduction. In order to minimize the size effects and to realize the bulk material conditions, periodic boundary conditions (PBC) were applied to z-direction. Shrink wrapped conditions were applied to x and y-directions. Though, the cutting velocity was selected at 100 m/s to minimize the computational effort, it does not affect the machined surface quality [147]. The computational parameters used in the MD simulation are presented in Table 3.1. In actual cutting practice, 2 nm cutting edge radius in single crystal diamond tool is not possible. According to Ding and Rahman [157], cutting edge radius of 15 nm is the least possible. In actual practice, 200 nm cutting edge radius is extensively used. The cutting edge radius of 2 nm is employed in this study for carrying out molecular dynamics simulation to understand the underlying mechanisms.

Table 3.1. Computational parameters used in the MD simulation

Workpiece material	**Dimensions**	**Tool**	**edge rad. (R)**	**Uncut chip (a)**	**Cutting velocity**	**Equilibration Temperature**	**Time step**
Cu and CuBe	300 Å x120 Å x181.6 Å	Single crystal diamond	20 Å	20,10, 5, 2.5, 1 & 0 Å	1 Å/ps	293 K	0.001 ps

3.4.2. Selection of Potential energy function

Accuracy of atomic trajectories and thermodynamic output properties in MD simulation of a system is based on the selection of appropriate interatomic potential energy functions. Since the tool and the workpiece materials are different in their chemical bonding and crystal structure, separate potential energy functions need to be defined. Moreover, the interaction between tool and workpiece will take place through a pair potential function. Table 3.2 tabulates the potential functions employed for various atomic interactions in nanocutting of Cu and CuBe.

Copper is a metallic material and possesses FCC lattice structure. The interaction between the copper atoms is well described by potential function based on Embedded Atom Method (EAM)

[155]. The EAM potential evolved from the density functional theory is a multi-body potential and effectively elucidates the behaviour of metal atom surrounded by a sea of electrons.

Table 3.2. Interatomic Potential Energy function

S. No.	Interactions	Potential function
1	Cu-Cu	EAM potential
2	Be-Be	ABOP function
3	Be-C	ABOP potential
4	Cu-C	Morse potential
5	C-C	ABOP potential

A 3-body potential based on ABOP formalism was used to describe the Be-Be, C-C and Be-C interaction [156]. Goel et al. [129] suggested that the analytical bond order potential (ABOP) formalism based potential energy function suggested by Erhart and Albe [156] can precisely describe both dimer and bulk properties. Table 3.3 lists the ABOP function parameters used in the simulation for Be and C interactions.

Table 3.3. ABOP Potential function parameters for Be and C interaction

Parameters	Be-Be	C-C	Be-C
D_0	1.03571	6	3.9093330
r_o (Å)	2.0788	1.39	1.724299
B (Å^{-1})	1.3	2.1	1.586761
S	1.88982	1.22	2.766724
γ	8.19587×10^{-7}	2.0813×10^{-4}	3.00184×10^{-5}
c	89.3894	330	57.004094
d	0.27443	3.5	0.358304
h	0.7606934	1	0.5599960
R (Å)	2.535	1.85	2.60
D (Å)	0.15	0.15	0.20

Morse pair potential function is well applicable for the elucidating the tool and workpiece interaction [158]. Morse potential parameters for Cu and C interactions are listed in Table 3.4. It is clearly mentioned here that while the interatomic potential parameters for Cu, C and Be are available, the same does not exist for Cu and Be interactions. It requires a quantum mechanical solution to develop the interatomic potential parameters for Cu and Be interactions.

Table 3.4. Morse potential parameters for Cu and C

Element	D (eV)	α (Å^{-1})	r_0(Å)
Cu-C	0.1	1.7	2.2

3.5. Interatomic Potential Energy function for Cu and Be

In the MD model of nanocutting, it was assumed that the Be rich phase or hard precipitate is made of spherical particle of Be atoms and this granular particle undergo surface to surface interactions with the Cu rich base material. The Cu rich phase was modelled by pure Cu atoms with a FCC structure. As surface interactions are dominant between Cu and Be phases, a Morse potential energy representation is appropriate to describe the interactions between them.

The Density Functional Theory (DFT) approach was employed to compute the potential parameters. As suggested by Romanowski et al. [159], DFT calculations were performed with B3LYP method and Cu and Be atom interactions were calculated at electronic scale by numerically solving simplified Schrodinger equation at various interatomic distances. CuBe dimerization energy was calculated on the basis of internuclear distance (r) which ranged from 1 to 5 Å [Fig. 3.8(a)].

At very large atomic separation, no force acts and therefore potential energy is zero. As the interatomic distance is decreased, force of attraction start acting and thus energy gets decreased. When the equilibrium distance is reached, energy becomes minimum. This is the equilibrium condition for the CuBe system which shows the binding energy of this system (i.e. D) marked by red line in the Fig. 3.8(b).

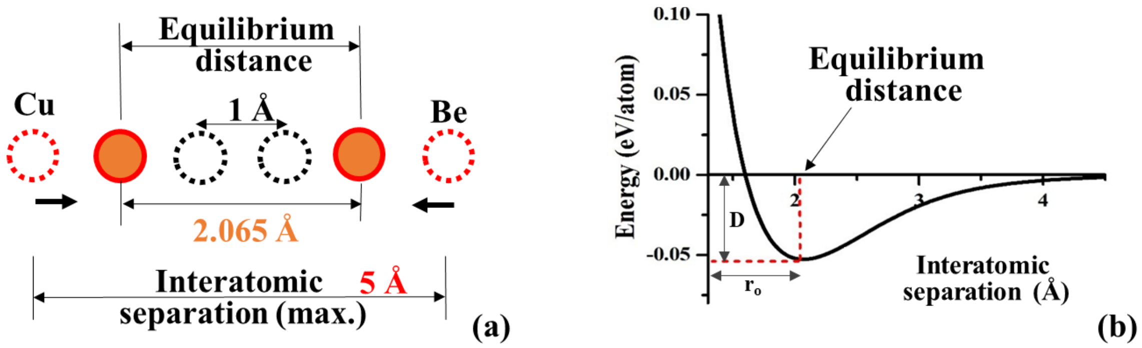

Fig. 3.8. Variation of potential energy with varying interatomic distance for CuBe dimer

On further decreasing the interatomic distance, the repulsive forces start acting and the potential energy start increasing. The interatomic distance cannot be decreased after a certain minimum distance as explained by the Pauli exclusion principle, which states that no two electrons can have same position at a particular instant. Interaction energy between Cu and Be (E_{int} (r)) was computed by subtracting interaction energy of individual Cu and Be atoms from the total energy of CuBe dimer.

$$E_{\text{int}}(r) = E_{CuBe}(r) - (E_{Cu} + E_{Be}) \quad \textbf{(3.15)}$$

Binding energy corresponding to equilibrium interatomic distance was calculated. It was found that Morse potential $\{ V(r_{ij}) = D[\exp(-2\alpha(r_{ij} - r_o)) - 2\exp(-\alpha(r_{ij} - r_o))] \}$, where, D, α and r_o are binding energy, damping parameter and equilibrium atomic spacing respectively fits very well to the results of DFT calculations. The fitted values are listed in Table 3.5.

Table 3.5. Morse potential parameters for Cu-Be

Element	**D (eV)**	**α (Å^{-1})**	**r_o (Å)**
Cu-Be	0.0563	5.042	2.065

3.6. Equilibrium lattice parameter

Inappropriate selection of lattice parameter can lead to erroneous interpretation of MD simulation results. Therefore, equilibrium lattice parameter was computed at the required temperature. Since the actual diamond process takes place at 293 K, a small system containing number of tool and workpiece atoms (N) were taken separately and constant temperature (T) and pressure (P) were applied to impose the NPT ensemble conditions for 20 ps. Fig. 3.9(a) and (b) show the variation in lattice constant and cohesive energy w.r.t. time provided for equilibration for Cu, Be and C respectively. It is observed that following an initial jump in the curves, lattice constant and energy for both the materials show slight fluctuations around a constant value which reveals equilibrium state of the system. Values after initial unstable region were averaged to give the equilibrium lattice constant. Table 3.6 shows experimental values from literature as well as equilibrium lattice parameter values at 293 K respectively.

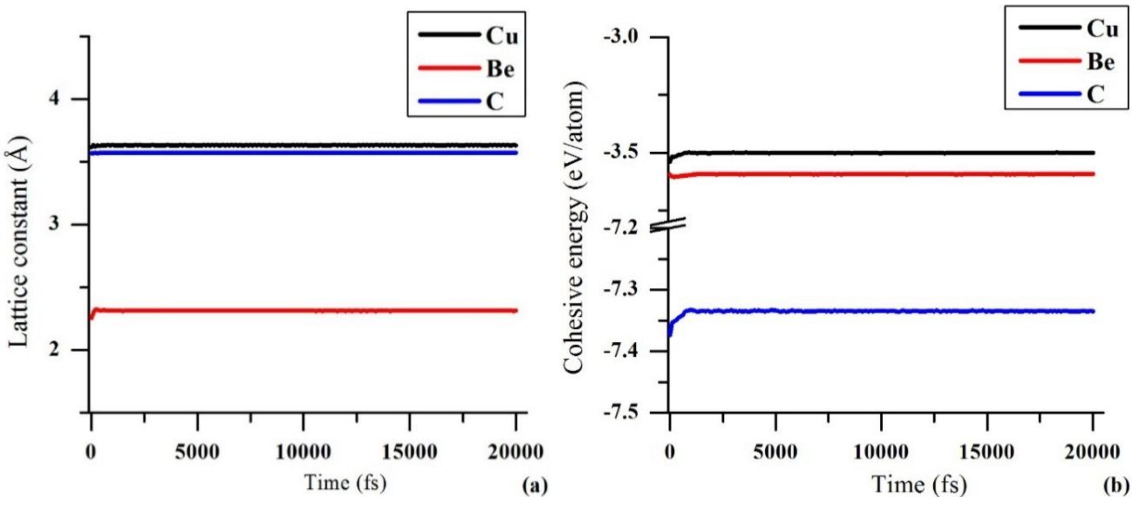

Fig. 3.9. Variation of lattice constant and cohesive energy for Cu, Be and C at 293 K

Table 3.6. Experimental and Equilibrium lattice parameter at 293 K

Material	Lattice constant (Å) (Experimental)	Equilibrium Lattice constant (Å)
Copper	3.6149 [160]	3.6323
Carbon	3.56683 [160]	3.571668
Beryllium	2.2866 [161]	2.2568

3.7. MD Simulation structure

The schematic of tool-workpiece with initial and boundary conditions and procedure of MD simulation steps are as shown in Fig. 3.10 and Fig. 3.11 respectively. Initial conditions were applied on the system of atoms defined by their crystal structures and lattice constants. Periodic boundary conditions along z-direction were assigned to realize plain strain conditions. Appropriate interatomic potentials were applied to the atoms in the system. Subsequently, tool and workpiece atoms were provided with initial velocities according to Maxwell-Boltzmann distribution at 293 K and equilibration was carried out for the whole system at same temperature under the micro canonical ensemble (i.e. constant *NVE*; *N: number of atoms in a system; V: volume of the system; E: energy of the system*) for appropriate number of time steps (t_E). Once the equilibration cycle was completed, velocity scaling was removed from the system and was applied to thermostat atoms of the tool and workpiece in order to dissipate the excess heat generated from the cutting zone.

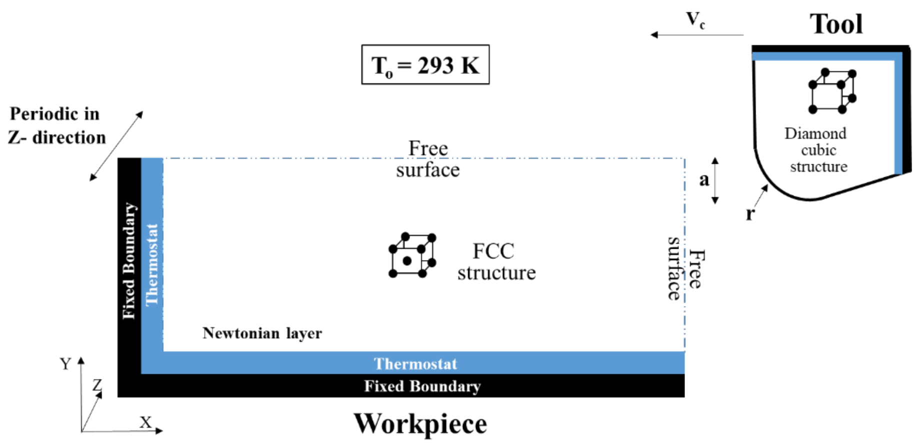

Fig. 3.10. Schematic of tool and workpiece for nanocutting simulation by MDS

To begin the cutting process, tool was given a cutting speed of 1 Å/ps and the whole system was imposed with NVE dynamics. NVE ensemble enabled the Newtonian and thermostat layer atoms to follow classical Newton's second law of motion. The finite difference method namely Velocity-Verlet algorithm [162] with a time step of 1fs was employed to update the atoms positions and velocities. The thermodynamic properties (like Number of atoms, volume, pressure, kinetic energy, potential energy, Temperature etc.) were taken as output and are then averaged over a few hundreds of timesteps.

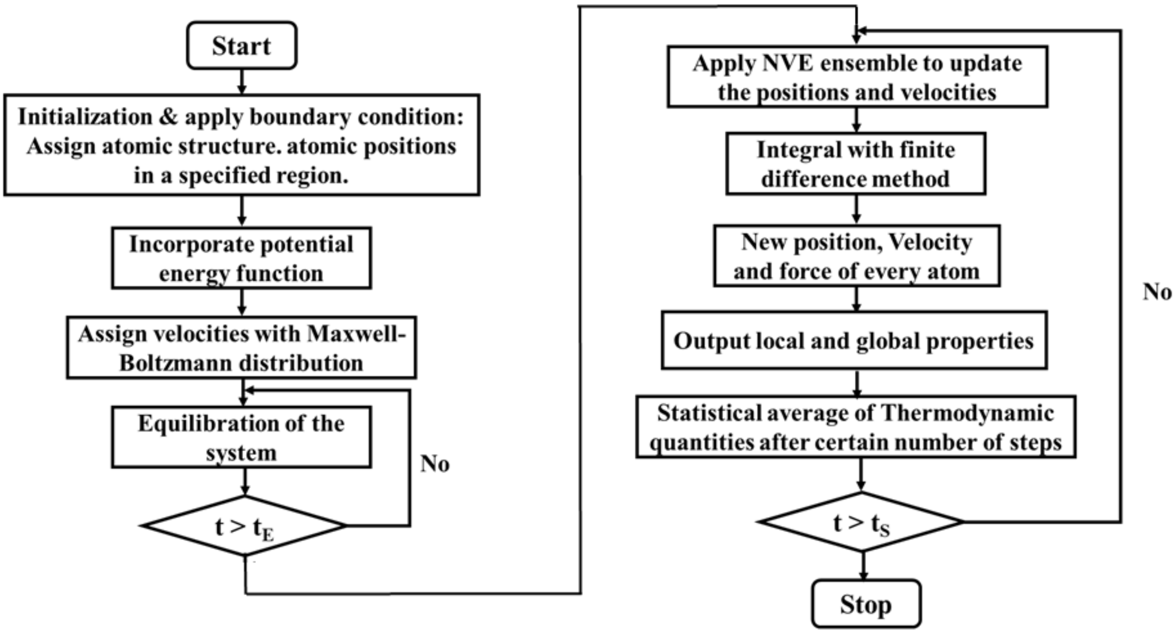

Fig. 3.11. Flowchart to conduct MD simulation

MD simulation was carried out with the help of Large-scale atomic/molecular massively parallel simulator (LAMMPS) [163], and OVITO [164], a 3D visualization software, was used for the visualization and analysis of atomistic data obtained from the LAMMPS. High performance computing facility was used for MD simulations. The simulation work has been carried out on four nodes in a supercomputing facility. Each node contains two Xeon quad-core processor at 2.5 GHz, 6 MB cache each, shared 16 GB memory and twin 750 GB SATA hard disks in a RAID-1 configuration. Common neighbour analysis (CNA) was carried out to notice the structural changes in workpiece material from FCC to BCC, HCP or amorphous phase. Dislocation extraction analysis (DXA) was performed to analyze the deformation and dislocation evolution in workpiece material during nanocutting.

3.8. Summary

The present chapter primarily deals in preparing a simulation model for CuBe and defining necessary interatomic potential energy functions for the interaction of different elements in the simulation system. The main findings from this chapter are summarized here:

- Interatomic potential parameters are determined for Cu and Be interactions which will be used in next section.
- Equilibrium lattice constant is found out for all three elements Cu, C and Be employed in nanocutting at 293 K.

Chapter 4

Molecular dynamics simulation of nanoscale cutting of CuBe

4.1. Introduction

In this chapter, the effect of ratio of uncut chip thickness to edge radius (i.e. a/r ratio) on the mechanisms of material removal, tool wear and surface contamination in nanoscale cutting of Cu and CuBe is analysed. MD simulation is performed to understand the underlying mechanisms in tool-workpiece interaction during nanoscale cutting. Cu is employed as a benchmarking material to understand the cutting behaviour in CuBe. Various combinations of a/r ratios for constant 'a' as well as constant 'r' are considered. To understand the material removal mechanism, force ratio is calculated and analysed whereas, stress and temperature are evaluated for understanding the diamond tool wear mechanism.

4.2. Variation of a/r in nano-regime diamond machining

In diamond turning, chip profile varies from zero to some maximum value of uncut chip thickness depending upon the feed rate [Fig. 4.1 (a)]. Owing to this variation in chip thickness (a), cutting mechanism tends to vary along the chip profile for the same cutting edge radius (r). Similarly, as the tool wear occurs at a particular uncut chip thickness (a), edge radius (r) tends to increase during the course of machining which in turn affects the cutting mechanisms. Thus, the relative magnitudes of 'a' and 'r' determine the cutting behaviour. In other words, a/r ratio is an important parameter to describe the cutting mechanisms. The minimum uncut chip thickness (a) and cutting edge radius (r) are in nanometric range and the surface generation takes place in the nanometric cutting zone at the tool-workpiece interface. Although the feed rate is in microns, maximum uncut chip thickness comes out to be in nanometers [Fig. 4.1 (b)].

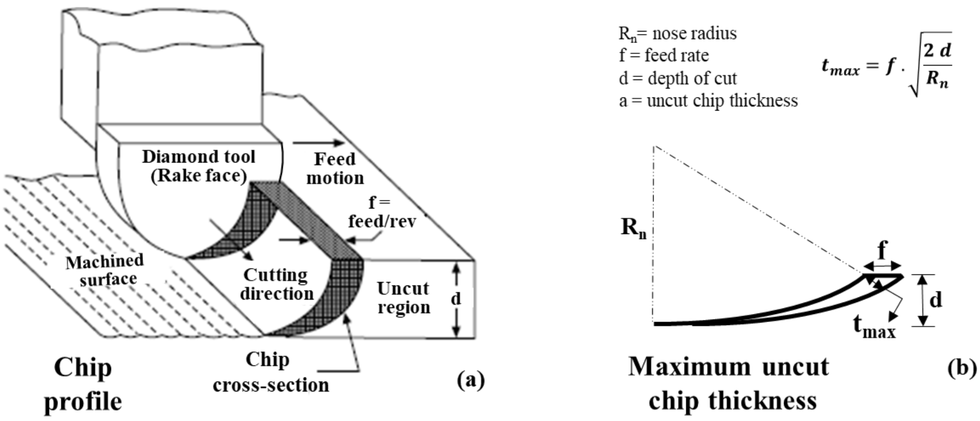

Fig. 4.1. Chip profile in diamond turning

Therefore, a nanoscale cutting model is preferred to simulate the tool-workpiece interaction in diamond turning.

4.3. Material removal mechanism in nanocutting of Cu and CuBe

Cu and CuBe are homogeneous and heterogeneous materials respectively. Their mechanisms of material removal are expected to differ owing to the presence of hard particles in CuBe. In nanoscale cutting process, the uncut chip thickness is very small. It can be considered that nanoscale cutting takes place within a single crystal, which involves processing of a few numbers of atomic layers on the work-piece surface. At such a scale, through experiments, it is very difficult to perceive the process mechanics and mechanisms like chip formation, material deformation, tool-workpiece interaction and subsurface defects etc. In addition, crystallographic orientations of the workpiece that affect the forces and specific cutting energies involved during the process cannot be observed through experiments.

The tool edge radius (r) in conjunction with uncut chip thickness (a) plays a major role in the mechanisms of material removal at nanoscale cutting. Therefore, various a/r ratios were considered here for simulation and to understand the material removal mechanism in nanoscale cutting of Cu and CuBe.

4.3.1. Material removal mechanism in nanocutting of Cu

Material removal and deformation of material depend on the crystallographic orientation of the workpiece undergoing a nanoscale processing. Similarly, cutting mechanism during nanocutting of crystalline materials depends on the crystal plane and the direction along which the cutting takes place. There are a set of crystal planes and directions which predominantly occur and find applications in various optical and engineering domains. Typically in a crystal, **(hkl)** shows a crystal plane which is represented by the normal and **[h*k*l*]** represents a direction on that crystal plane which means the direction and the normal are perpendicular to each other. There is one condition which should be fulfilled for modelling the crystal orientations: $hh^* + kk^* + ll^* = 0$.

Various crystal orientations viz. $(010)[\bar{1}00]$, $(\bar{1}10)[110]$, $(111)[1\bar{1}0]$, $(001)[\bar{1}10]$, $(01\bar{1})[100]$, $(111)[11\bar{2}]$ are considered in nanocutting simulation at different a/r ratios namely 2, 1, 0.5, 0.25 and 0.1. [( ), [ ] are referred to as crystal plane and direction respectively. { } and < > have been used for a family of crystal planes and directions]. Three types of investigations have been performed here to understand:

- Cutting force and specific cutting energy for 6 orientations with different a/r ratios
- Cutting mechanism for various orientations with a single a/r ratio
- Cutting mechanisms with different a/r ratios for the selected orientation

In order to select the crystal orientation for simulation and to understand the cutting mechanisms, cutting forces and specific cutting energies were evaluated for various crystal orientations. Cutting forces were plotted for all the orientations at different a/r ratios as shown in Fig. 4.2. Cutting forces are noticed to be decreasing with decreasing a/r ratios. Cutting forces are found to be minimum for the $(111)[1\bar{1}0]$ orientation and maximum for the $(01\bar{1})[100]$ orientation. The cutting force on $(111)[1\bar{1}0]$ orientation is observed to be minimum because the (111)[110] crystal orientation is an easy slip orientation, which requires least force to displace the atoms. Maximum cutting force occurs on the $(01\bar{1})[100]$ orientation owing to the least number of dislocations generated. As the cutting forces required are high, cutting energy requirements also increase significantly. Komanduri [58] also observed that the cutting force decreases as the uncut chip thickness reduces.

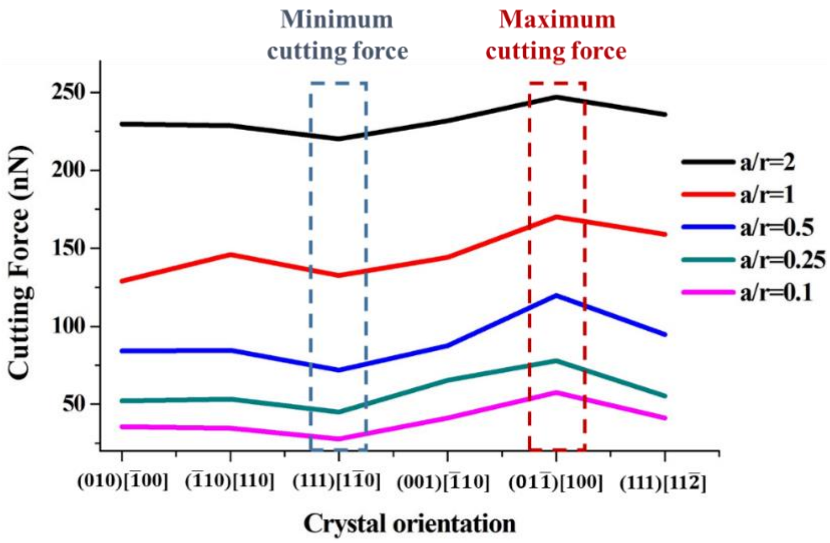

Fig. 4.2. Variation in cutting forces for nanocutting of Cu on different orientations

Fig. 4.3 shows the variation in specific cutting energy (i.e. cutting energy per unit volume) with respect to different orientations. On contrary to cutting forces, specific cutting energy is found to be increasing for decreasing a/r ratios. At lowest a/r ratio, specific cutting energy shows highest value as a result of size effect. Similar to the cutting forces, specific cutting energy is found to be minimum for the $(111)[1\bar{1}0]$ orientation and maximum for the $(01\bar{1})[100]$ orientation. However, it is observed that specific cutting energy is nearly same for a/r >=1 and it is different for each orientation for a/r<1.

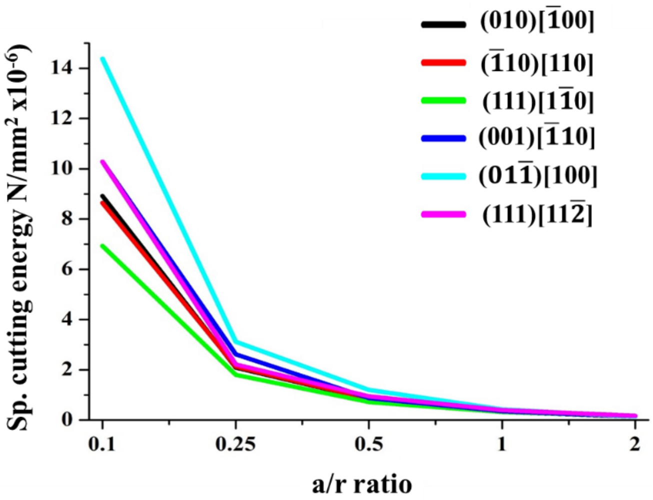

Fig. 4.3. Variation in cutting energy during nanocutting of Cu on different orientations

It indicates that in ultraprecision machining which is done at lesser cutting edge radius, decreasing uncut chip thickness requires more specific cutting energy and it tend to accelerate the tool wear due to intense stresses at the cutting edge.

From the cutting force as well as specific cutting energy plots, it is observed that the crystal orientations family {110}<100> is difficult to cut (*i.e. cutting force ~ 247 nN for a/r =2 and specific cutting energy ~ 14x10^{-6} N/mm^2 for a/r =0.1*), whereas crystal orientations family {111}<110> is easier to cut (*i.e. cutting force ~ 220 nN for a/r =2 and specific cutting energy ~ 6.9 x10^{-6} N/mm^2 for a/r =0.1*) in nanoscale cutting of Cu. As the (010)[$\bar{1}$00] crystal orientation shows an average behaviour among all the orientations, it will be considered further for the understanding of cutting mechanisms.

4.3.1.1. Effect of various crystal orientations on cutting mechanism

It is well known that the material removal and deformation is caused by the flow of dislocations. The shear slip induced dislocation flow is highly dependent on the crystal orientations. In order to observe the flow of dislocations in nanocutting of various crystal orientations of Cu, the CNA tool in the LAMMPS software was used to reveal the structure [Fig. 4.4(a-f)]. Table 4.1 lists the computational parameters used for nanoscale cutting in Cu.

Table 4.1. Computational parameters used in the MDS of nanoscale cutting of Cu

Workpiece material	Single crystal copper (FCC)
Dimensions	30 nm x12 nm x 18.16 nm
Tool	Single crystal diamond
Cutting edge radius (R)	2 nm
Uncut chip thickness (a)	4 nm
Cutting velocity	0.1 nm/ps
Equilibration Temperature	293 K
Time step	0.001 ps

During the cutting simulation, the mechanisms were interpreted from the snapshots from OVITO after the CNA analysis. The CNA tool analyses the crystal structure and based upon the structural analysis, it shows the shearing action by revealing the flow of dislocations in the workpiece material. Dislocation flow represents deformation in the material.

The orientation (010)[$\bar{1}$00], during cutting, shows the shear slip at an angle of 45 degrees to the horizontal direction as shown in Fig. 4.4(a). This represents a <110> direction. Tool has a cylindrical configuration and poses both tangential and normal load on the workpiece. Therefore, the slips propagate dislocations ahead and beneath the cutting tool. Slip induced dislocations are mainly represented by HCP structure. The HCP structure arises due to stacking faults created in workpiece material while cutting. Subsurface damage takes place in the form of dislocations.

Fig. 4.4(b) shows the cutting phenomenon in ($\bar{1}$10)[110] orientation. In this orientation, the cutting direction is itself a slip direction and both tangential and thrust loads are applied in slip directions. As a result of material being cut in slip directions, slips propagate to larger distance tangentially and vertically than in case of (010)[$\bar{1}$00]. Since <110> is oriented in vertical direction, slip can propagate easily in this direction and thus causes *substantial subsurface damage in the material*.

The (111)[1$\bar{1}$0] orientation itself denotes a slip system and therefore the deformation in the form of shear slips is easier. Since (111) is the cutting plane and [1$\bar{1}$0] is the cutting direction, deformation in the form of slip induced dislocations occur only in the upper region where the tool and workpiece interact and travel in the horizontal direction [Fig. 4.4(c)]. The slips do not occur in the vertical direction as a result of which *subsurface damage is quite low*.

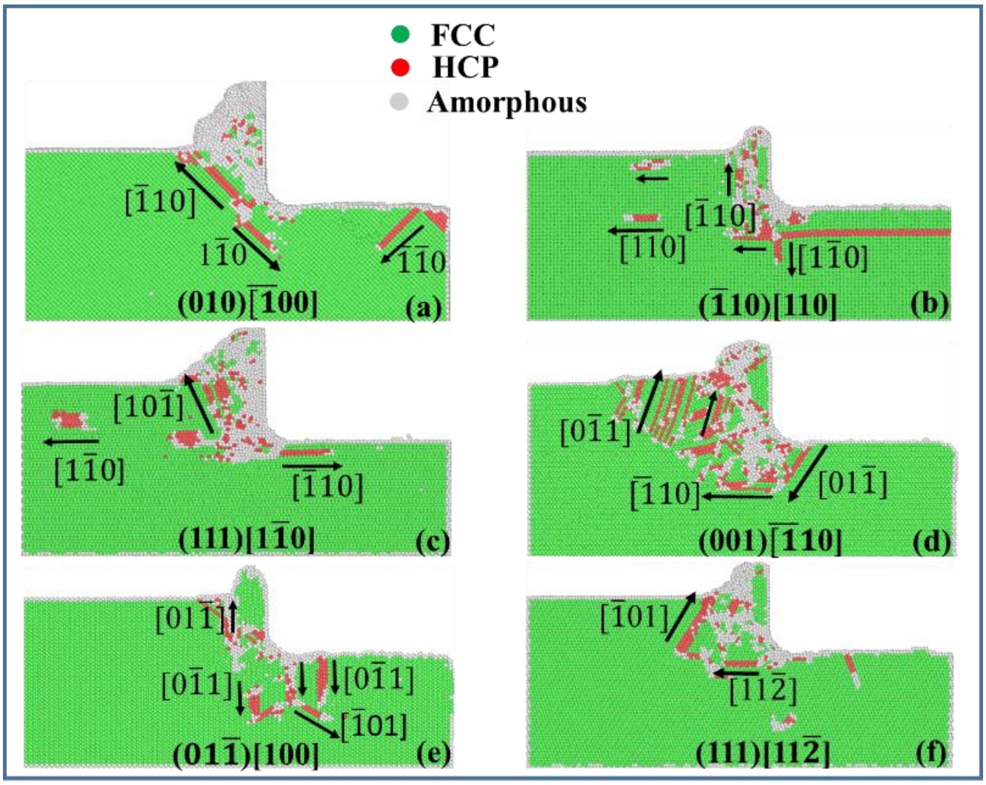

Fig. 4.4. Material deformation during nanocutting of Cu in various orientations

For orientation, (001)[$\bar{1}$10] slip movement takes place in the cutting direction owing to easy slip in [$\bar{1}$10]. Vertical slips are not noticed in this case, however some slips are observed at an angle of 120^o to the cutting direction [Fig. 4.4(d)].

It is seen that a lot of dislocations generated slips interfere with each other in a cutting zone ahead of the tool. Since cutting takes place in <110> slip direction, it is observed that the deformation does not penetrate deeper into the material which suggest that there is *less subsurface damage* in this cutting orientation.

For a $(01\bar{1})[100]$ orientation, the cutting mechanism is just opposite to orientation $(010)[\bar{1}00]$. Since {110} is the cutting plane and the direction normal to it is <110>, the dislocations are generated and propagated in the vertical downward direction to the tool [Fig. 4.4(e)]. Owing to slips occurring beneath the tool, the *subsurface deformation in this case is higher* as compared to {100} cutting plane orientation.

The $(111)[11\bar{2}]$ orientation shows high deformation in {110} directions aligned at 60^o to the cutting direction as shown in Fig. 4.4(f). Therefore, slip deformation takes place ahead of the tool at an angle of 60^o to the cutting direction. The *subsurface deformation in this case is less* as compared to {100} cutting plane orientation.

It is observed from all the cutting orientations that material deformation during cutting occurs only along the slip directions. Slip induced dislocations are propagated in the <110> family of directions.

4.3.1.2. Cutting mechanism at different a/r ratio and the amount of material removal

The material removal mechanism was observed for various ratios of uncut chip thickness (a) to cutting edge radius (r) viz. 2, 1, 0.5, 0.25, 0.1, 0 with constant cutting edge radius of 2 nm. Crystal orientation of $(010)[\bar{1}00]$ for Cu was selected for conducting nanoscale cutting based on the results of specific cutting energy.

At a/r equals to 2 [Fig. 4.5(a)], shear slip occurs along the [$\bar{1}$10] direction. As the shear slip occurs, crystal structure of the atoms along shear plane changes from FCC to HCP. Since stacking fault energy for Cu is quite low, a deformation along shear plane transforms the FCC structure along shear plane. Stacking faults are generated by motions of Shockley partial dislocations [165].

This transformed structure in Cu manifests as twin boundary characterized by HCP structure. A twin boundary separates two crystals in a symmetrical manner. High stresses and low stacking-fault energy facilitate deformation twinning. During steady state cutting conditions, material removal takes place through well-defined shear plane with additional small deformation zone near the tool edge owing to the round cutting edge of the tool.

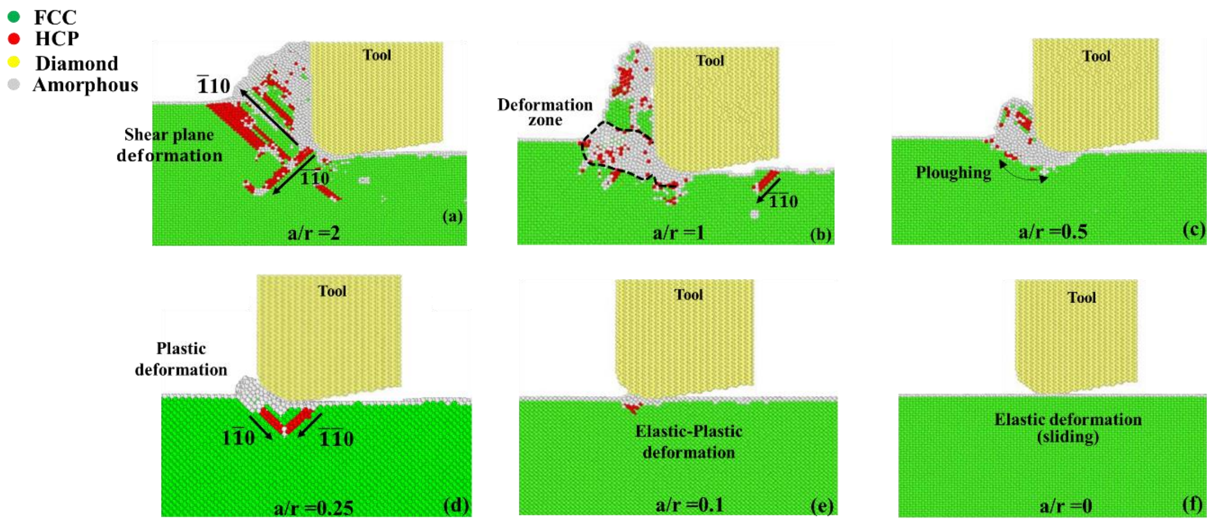

Fig. 4.5. Material removal and structural changes in nanocutting of Cu

In case of a/r ratio equals to 1, the round cutting edge compresses material ahead of it and squeeze it to flow through either ahead or beneath the tool edge. Material removal takes place by a thick shear zone ahead of the cutting tool instead of a well-defined shear plane and this is indicated by non-crystalline phase as shown in Fig. 4.5(b). Roundness of cutting edge does not enable removal of entire uncut chip thickness and some of the deformed material flows underneath the tool and becomes a part of the machined surface. HCP layer is formed ahead of the non-crystalline zone as well as beneath the tool. For a/r ratio equals to 0.5 [Fig. 4.5(c)], material flow during deformation occurs through either ahead or beneath the cutting tool edge. This is similar to the squeezing/extrusion action when a soft material is compressed under a load. When a chip comes out of the high pressure zone, it expands to release the strain energy stored during deformation. Due to high pressure, non-crystalline structure exists in the deformation zone in front of tool edge.

As a/r ratio is further reduced to 0.25, more and more material flows beneath the tool edge rather than flowing in chip direction as shown in Fig. 4.5(d). This is due to increased normal interaction of tool with the work-piece which pushes the material downwards. However, small chip still seems to be removed due to the ploughing action of tool on the work-piece. When a/r ratio becomes 0.1 [Fig. 4.5(e)], work-piece material is deformed in a few atomic layers, however, chip removal does not take place as whole of the deformed material is pushed beneath the tool. Only rubbing action takes place. When cutting depth approaches to zero, centre of the top atoms on the workpiece coincides with the centre of the bottommost atoms of the tool and elastic deformation of workpiece material takes place as shown in Fig. 4.5(f). There are no subsurface structural changes observed in case of a/r equals to 0.

Table 4.2 lists the observed mechanism in MDS of nanocutting of Cu. Thus, the material removal mechanism changes from shear slip to shear zone deformation when a/r ratio changes from 2 to 1 and then to ploughing when a/r ratio approaches to 0.5. Below 0.25, only plastic deformation occurs without any significant chip formation. Elasto-plastic and elastic deformation takes place for the a/r = 0.1 and 0 respectively without any material removal. *For a given cutting edge radius, as the uncut chip thickness reduces, the cutting mechanism changes from shear plane cutting to ploughing to sliding in Cu.*

Table 4.2. Cutting mechanism in nanocutting of Cu (010)[$\bar{1}$00]

a/r	a (nm)	Observation/ mechanism
2	4	Chip removal along shear plane
1	2	Chip removal through shear zone
0.5	1	Ploughing (extrusion like deformation)
0.25	0.5	Plastic deformation
0.1	0.2	Elastic-plastic deformation
0	0	Elastic deformation (sliding)

Fig. 4.6 shows number of atoms removed during chip formation with respect to time for different a/r ratio. Amount of material removal was computed by counting number of atoms that are coming out of a defined workpiece region either as a chip or as a ploughed material. It can be noticed that small fluctuations take place.

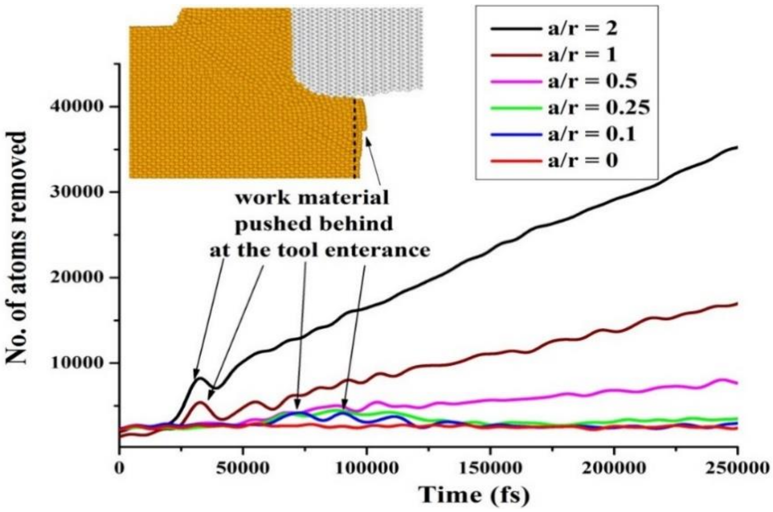

Fig. 4.6. Amount of material removal in terms of number of atoms removed

This is due to atomic vibrations that causes centres of surface atoms on the workpiece to move in and out, which are correspondingly counted as either removed material or unremoved material. Atoms removed during the cutting process show almost a linear relationship with the time with decreasing slope as the a/r ratio reduces. However, the graph shows initial sudden increase and then decrease in material removal which happen due to the fact that as tool contacts the workpiece, some of the workpiece atoms beneath the tool are pushed behind due to round cutting edge and subsequently comes out of the defined region of the work-piece and counted as removed material.

With further movement of tool, they again recover to the extent possible and return in their defined region and become unremoved material. From the graph, it is clearly seen that material removal is highest when a/r is equal to 2 and decreases for remaining a/r ratios. Material removal is quite low for the a/r ratios after it becomes equal to 0.5, as most of the material after deformation flows underneath the tool. For a/r ratio lower than 0.25 (i.e. a/r= 0 & 0.1), though amount of material removed is almost equal to zero as there is no cutting achieved, plastic deformation occurs for a/r > 0.1 and elastic deformation takes place for a/r = 0. Thus, *a/r of around 0.25 is the minimum ratio below which no material removal takes place*.

4.3.2. Discussion on results of nanocutting of Cu

Using the output of MDS results, cutting forces and specific cutting energy were calculated for various a/r ratios and orientations. These results are discussed in the following sections:

4.3.2.1. Mechanism based on Force ratio

The principal cutting and thrust forces during cutting in a single crystal orientation (010)[$\bar{1}$00] are presented in Fig. 4.7(b). In general, there are three type of forces involved in the cutting process: Tangential cutting force denoted by F_x; Normal thrust force represented by F_y; and lateral feed force designated by F_z [Fig. 4.7(a)]. Initial unsteady period for calculating the average force is neglected. Only the steady period, where the forces fluctuate around an average value, is considered. Since it was an orthogonal cutting, only thrust and cutting forces were taken into account. The calculated values of cutting and thrust forces during nanocutting of Cu at a/r ratio equal to 1 are shown in Fig. 4.7(b). Based on the computed force values, the force ratio, which is a ratio of thrust to cutting force, is evaluated and plotted at various a/r values.

The force ratio indicates size effect; as the a/r decreases, the force ratio increases considerably. Based on the force ratio (i.e. thrust / cutting) plot w.r.t. a/r ratio, material removal mechanism is specified in three regions [Fig. 4.7(c)]. Region I, associated with high force ratio, is referred to sliding mechanism which is an elastic-plastic deformation; region II, connected with reduction in force ratio, denotes ploughing mechanism; and region III, related to lower force ratio, presents the shear plane cutting mechanism. The region I shows a higher force ratio at lower uncut chip thickness. The high thrust force results in a large hydrostatic pressure which leads to the sliding mechanism. In sliding mechanism, no material is removed and only elastic-plastic deformation takes place. The region II belongs to a ploughing regime, where a large plastic deformation takes place without significant amount of material removal. The magnitude of thrust and cutting forces become comparable, which leads to the material flow simultaneously along the top rake and flank sides of the tool edge. The region III represents a shear plane cutting, where the principal cutting force is higher than the thrust force as it occurs in conventional cutting. The high principal cutting force enables large material removal from the workpiece.

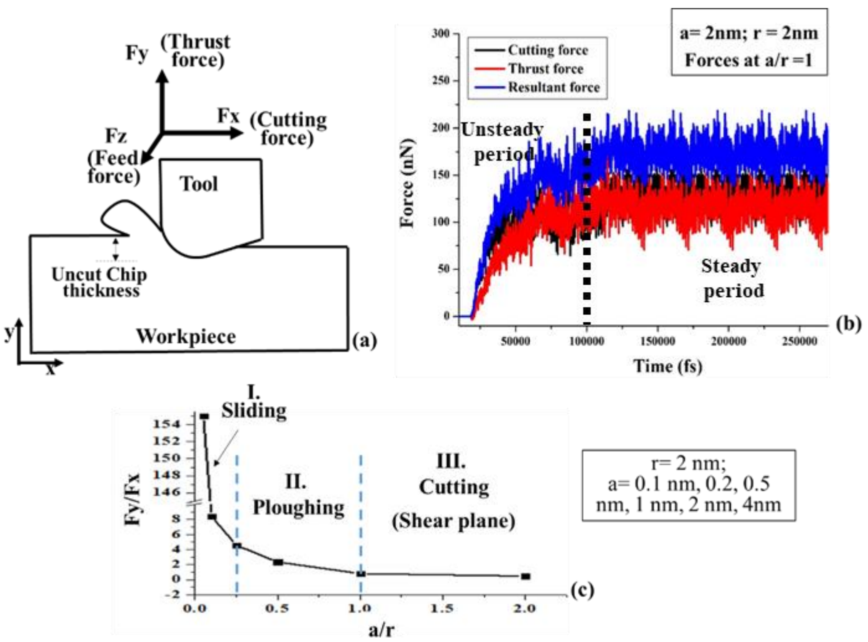

Fig. 4.7. Cutting forces during nanocutting of Cu

4.3.2.2. Influence of nanocutting on deformation

Since cutting orientations in all the cases are different, the amount of deformation in all of them was found to differ. The dislocations mobility enables the deformation in the workpiece material and thus actuates the material removal process. Dislocation length is one of the parameters, which measures the amount of deformation. Therefore, dislocation length for all the cutting orientations is plotted in Fig. 4.8.

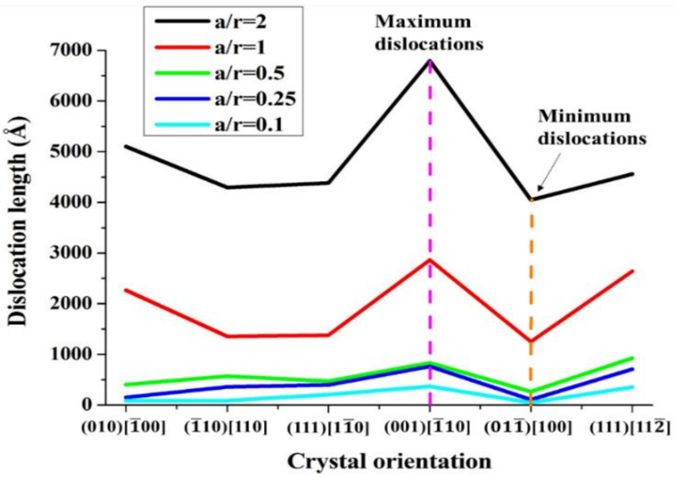

Fig. 4.8. Variation in dislocation density for nanocutting on different orientations of Cu

It is observed that for higher uncut chip thicknesses and higher a/r ratio (i.e. a/r >=1), the dislocation density is quite high owing to larger deformation compared to that of lower a/r ratio (i.e. a/r <= 0.5). For (001)[$\bar{1}$10] cutting orientation of workpiece material, the dislocation density is maximum, whereas in case of (01$\bar{1}$)[100] cutting orientation, it is minimum. The dislocation density in (001)[$\bar{1}$10] cutting orientation is approximately 70% higher than that in case of (01$\bar{1}$)[100] orientation for a/r equal to 2. This is also observed from the Fig. 4.4(d) and (e), where region of deformation ahead of the tool show large variation in size for these orientations. At lower a/r ratios, the difference in the amount of dislocations become even larger. At a/r equal to 0.1, dislocations in (001)[$\bar{1}$10] cutting orientation are 86% higher than in case of (01$\bar{1}$)[100] cutting orientation. The amount of dislocations also shows the extent of cutting resistance and as the dislocation length varies significantly in all six cutting orientations, it is expected that the cutting resistance would also differ for all these orientations.

It is observed that for higher uncut chip thicknesses and higher a/r ratio (i.e. a/r >=1), the dislocation density is quite high owing to larger deformation compared to that of lower a/r ratio (i.e. a/r <= 0.5). For $(001)[\bar{1}10]$ cutting orientation of workpiece material, the dislocation density is maximum, whereas in case of $(01\bar{1})[100]$ cutting orientation, it is minimum. The dislocation density in $(001)[\bar{1}10]$ cutting orientation is approximately 70% higher than that in case of $(01\bar{1})[100]$ orientation for a/r equal to 2. This is also observed from the Fig. 4.4(d) and (e), where region of deformation ahead of the tool show large variation in size for these orientations. At lower a/r ratios, the difference in the amount of dislocations become even larger. At a/r equal to 0.1, dislocations in $(001)[\bar{1}10]$ cutting orientation are 86% higher than in case of $(01\bar{1})[100]$ cutting orientation. The amount of dislocations also shows the extent of cutting resistance and as the dislocation length varies significantly in all six cutting orientations, it is expected that the cutting resistance would also differ for all these orientations.

Fig. 4.8 clearly indicates that lesser uncut chip thickness is essential requirement for ultraprecision machining, wherein subsurface damage need to be minimal.

4.3.3. MD simulation of nanocutting of CuBe

The deformation in a cutting process is expected to be affected, when some impurities or inhomogeneities are encountered during interaction of the tool and workpiece. In nanoscale cutting, even few nanometres sized impurity cause significant effect on the cutting process.

In the following sub-sections, effect of single particle representing Be particle in copper base workpiece material having $(010)[\bar{1}00]$ crystal orientation is examined on the cutting process.

Fig. 4.9 shows the schematics of various locations of hard particle in CuBe workpiece with respect to cutting planes. Four different cases were considered for further simulation.

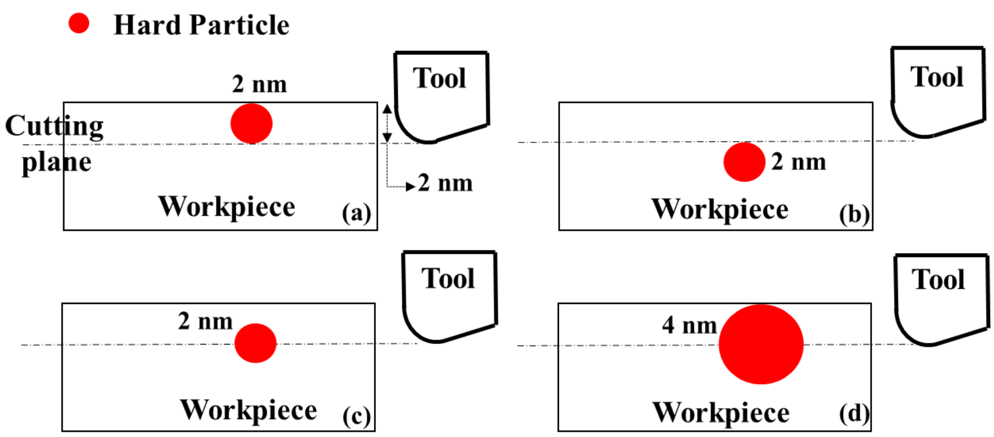

Fig. 4.9. Schematic of location of hard particle with respect to cutting plane

4.3.3.1. Effect of hard particle interaction with tool

A hard particle containing Be atoms was introduced to the Cu base material at different depths from the free surface of the workpiece to study different cases. Since the γ-phase in CuBe alloy is enriched with Be atoms, therefore, the hard particle employed in the simulation was considered to be Be atoms only. The particle shape was also assumed to be spherical. Table 4.3 shows the computational parameters that are used for the MD simulation of cutting. The orientation of Be particle is taken as similar to the Cu matrix i.e. (010) cutting plane and $[\bar{1}00]$ cutting direction.

Table 4.3. Computational parameters used in the cutting simulation

Workpiece material	Copper with Be as hard particle
Cutting plane and direction	(010) and $[\bar{1}00]$
Workpiece dimensions	30 nm x12 nm x18.16 nm
Cutting tool (Deformable)	Single crystal diamond
Tool edge radius (r)	2 nm
Uncut chip thickness (a)	2 nm
Hard particle size	2 and 4 nm (spherical)
Cutting speed	1 Å/ps (100 m/s)
Equilibration Temperature	293 K
Time step	0.001 ps

Table 3.2-3.5 presented in Chapter 3 show the interatomic potential energy functions for all the atomic interactions. For understanding the tool and workpiece interaction and especially the tool-particle interaction, four cases were considered where the particle position was varied about the cutting plane and reflection of their interactions was observed on the workpiece surface. Initial unsteady period for calculating the average force is neglected in all the cases. Only the steady period where the forces fluctuate around an average value is considered.

i. Case-1: When the particle is above the cutting plane (2 nm particle size)

Fig. 4.10(a) shows the snapshot of cutting simulation when the particle is located above the cutting plane in the workpiece. As the particle is above the cutting plane, the diamond tool when interacts with it, the particle is carried away along with the chips. In the vicinity of the particle, there are lot of compressed atoms owing to the cutting led deformation. Examining the snapshot (i) shows initial phase of cutting when the tool starts cutting only the base material. During the initial phase, tool shears the workpiece material at an angle of 45^{o} along the cutting direction which in turn facilitates the material removal. It is also observed that in the chip thickness in this phase is also uniform. In contrast, snapshot (ii) shows the non-uniform chip thickness due to the particle exerted deformation on the base material. In addition, the compressed atoms are left under the initial location of the particle causing alteration of surface layers. Once the particle is removed along with the chips, shear deformation occurs along the base material. Fig. 4.10(b) shows the variation of cutting forces with respect to time.

Since the particle lies above the cutting plane and moves up along with the chip, the direct interaction of tool and particle does not take place and thus the cutting forces are not much perturbed by the particle. However, forces are indeed higher when compared to that of cutting in Cu. The particle hinders the deformation process to an extent and thus increases the cutting forces. The average cutting force observed in this case is ~8.87% larger than that of cutting of Cu.

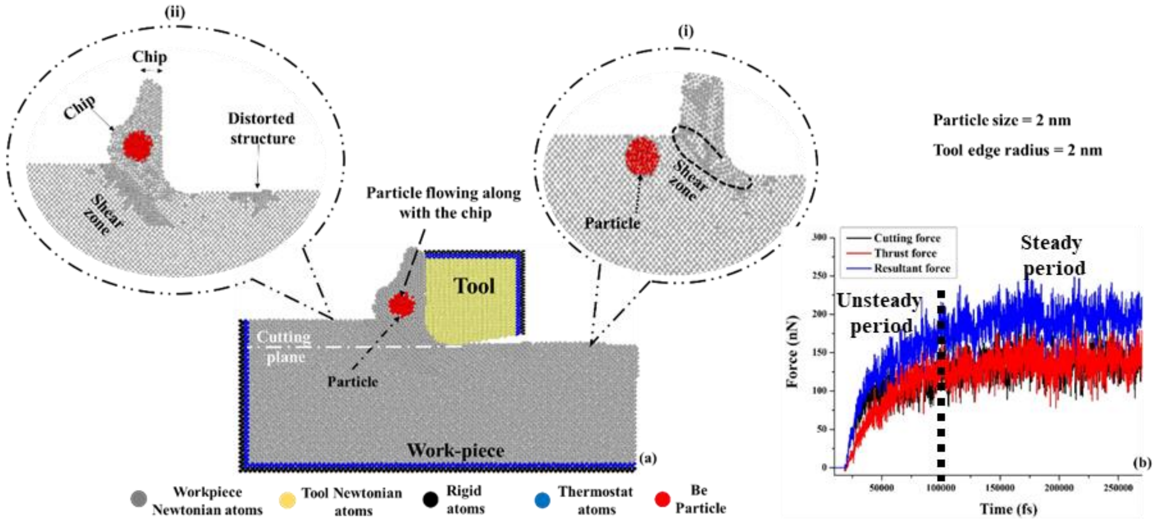

Fig. 4.10. Nanocutting of Cu and variation of forces for a particle above the cutting plane

ii. Case-2: When the particle is below the cutting plane (2 nm particle size)

Fig. 4.11(a) shows the snapshot of cutting simulation when the particle is located below the cutting plane in the work-piece. As the particle is below the cutting plane, the material removal is not affected by the presence of particle. However, the workpiece surface is slightly deteriorated in two atomic layers by the tool sliding over the particle. In this case, the particle is left behind at its location. The particle is rather pressed by the tool edge in few atomic layers as shown in (i). The chip thickness remains uniform during the cutting process and shear plane deformation continues to enable the material removal [view (ii) in the Fig. 4.11(a)]. The forces observed in this case are smaller than that of the case-1, however greater than that in case of Cu (~1.6%). The forces increase and then gets stabilized and fluctuate around a constant value after the tool passage over the particle [Fig. 4.11(b)].

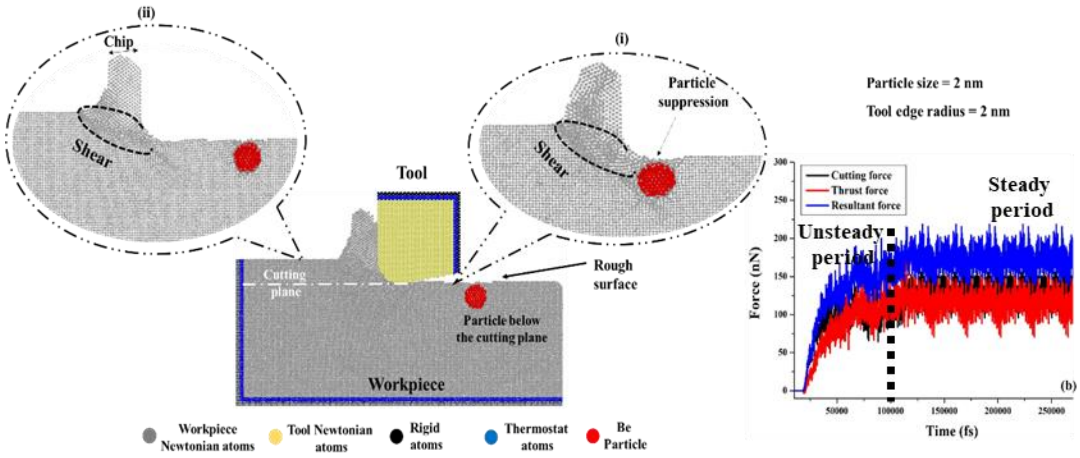

Fig. 4.11. Nanocutting of Cu and variation of forces for a particle below the cutting plane

iii. Case-3: The particle centre lies at the cutting plane (2 nm particle size)

In this case, the cutting process shows similar behaviour to case-1 at the initial stages of cutting. Fig. 4.12(a) and (b) show the cutting phenomenon for particle location at the cutting plane axis. In this case, the tool poses a high negative rake angle towards the particle. Because the base material (Cu) is much softer than the particle (Be), it offers a very small resistance to particle movement, and the particle is pushed against the Cu atoms. Thus, the hard particle undergoes a drag due to the simultaneous movement of the cutting tool.

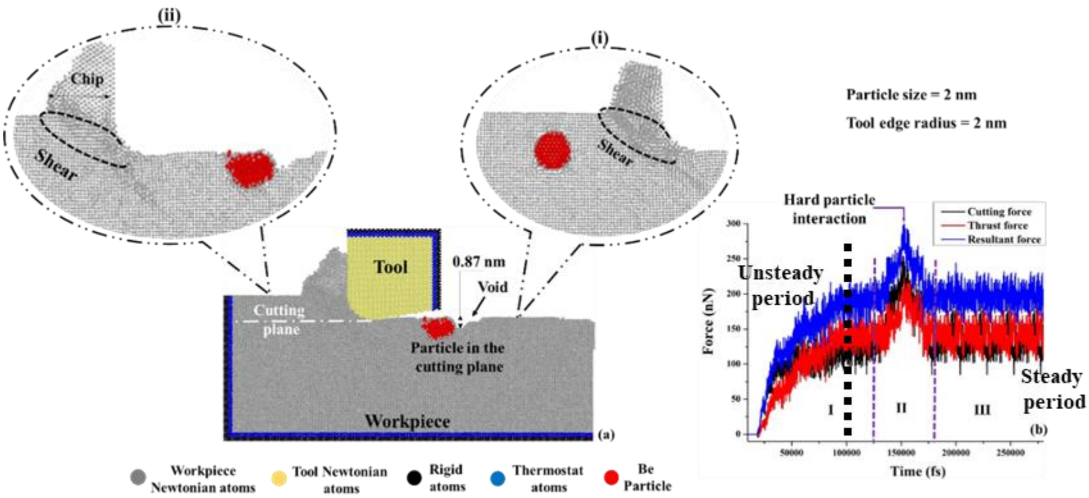

Fig. 4.12. Nanocutting of Cu and variation of forces for a particle in the cutting plane

The drag experienced by the hard particle causes the position of the particle gets shifted and a dig on the machined surface up to a ~0.87 nm of cutting distance, as shown in Fig. 4.12(a). When the tool passes over the particle, the particle springs back because of the difference in the elastic modulus of Cu and Be. Thus, the generated surface is left with a void behind the particle. Fig. 4.12(b) shows the variation in cutting forces which reveals that there exist three regions. The average cutting force observed in this case is ~57.14% larger than that of cutting of Cu.

Region 1 belongs to the initial phase of cutting where the tool starts cutting in Cu atoms and the forces begin to increase gradually as the engagement of tool and workpiece increases. Once the full contact between the tool and the workpiece is achieved, the forces become stable. In Region II, the tool starts cutting in the vicinity of the particle, due to which the graph witnesses a small increase in the cutting forces for a time period in which the tool and the particle were interacting. Region III does not reflect much change in the forces as the cutting takes place only in Cu.

iv. Case-4: The particle centre lies at the midplane and the size of the particle is 4 nm

Since particle position in case-1 does not affect significantly surface generation and tool-particle interaction showed a void on the machined surface in case-2, larger size of particle was considered here to see the effect on surface generation as shown in Fig. 4.13(a). In this case, similar behaviour is shown by the particle as in case-2, however, bigger size of the particle affects deformation in base material. Tool due to its round edge poses high forces on the hard particle which in turn compresses the base material below it as shown in extended view (ii) in Fig. 4.13(a), where a large amount of shear zone has been formed owing to particle induced deformation. The extended view (i) and (iii) however reveals shear deformation, where the particle effect is not reflected on the material deformation. As the particle is compressed by the tool it springs back after the tool passage over the particle. The compression of the particle and the tool's simultaneous movement during cutting leaves a large void of ~2.7 nm on the surface. Fig. 4.13(b) reveals that there are three regions of cutting depending upon the variation of cutting forces similar to the case III. Region I and Region III displays the cutting of Cu before and after the particle location respectively. They show similar magnitude of forces as in case 3. However, Region II witnesses the large increase in cutting forces during the tool interaction with the particle. As the particle is of bigger size, it causes a higher cutting resistance and simultaneously large thrust force is caused by the tool flank face on the particle which presses the particle on the Cu atomic layers which when sprung back, lifts the particle up. Maximum resultant force of ~375 nN is observed, which is ~36% higher than that of case 3.

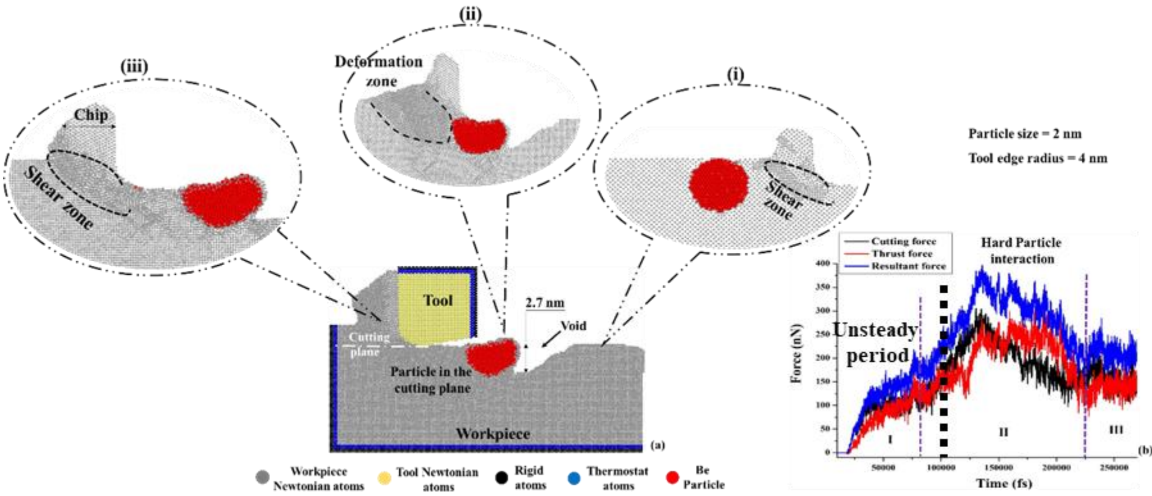

Fig. 4.13. Nanocutting of Cu and variation of forces for a particle in the cutting plane

4.3.3.2. Cutting mechanism in Cu phase and Be phase

MDS shows that the presence of hard particle affects the nanocutting process. It is observed that the cutting mechanism in soft Cu phase and hard Be phase (i.e. hard particle) are different. As tool initiates cutting, it first contacts Cu atoms and displaces the atoms causing a shear slip as shown in Fig. 4.14(a). Shear deformation occurs along <110>, since it is the dominant slip direction for Cu. Dislocations are generated through shear slip that cause either addition or subtraction of extra plane of atoms in the crystal. Dislocations propagate in the workpiece crystal and are finally annihilated at free surface, grain boundaries or at rigid boundaries which restrict their flow.

In nanocutting, shear deformation occurs and dislocations start nucleating and propagating through workpiece material in the initial phase. As the tool contacts with the particle, the tool tends to push the particle against the soft Cu phase. Extensive deformation occurs around the hard particle as revealed by slips shown in Fig. 4.14(b).

Since, base material (Cu) is much softer than the particle (Be), it shows a small resistance to the particle movement. As a result, hard particle experiences a drag due to simultaneous movement of cutting tool. Drag experienced by hard particle causes the shift in the position of the particle and a dig on the machined surface up to a few nanometers of cutting distance as shown in Fig. 4.14(c).

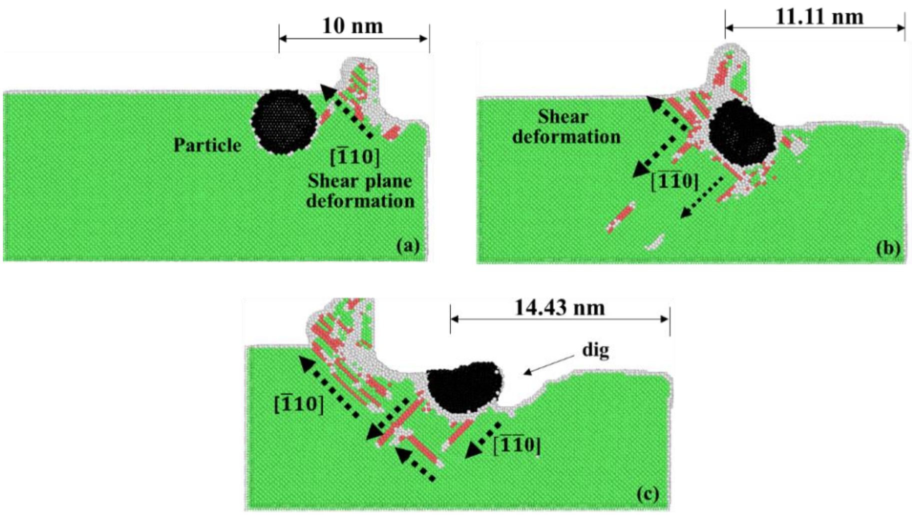

Fig. 4.14. Material removal and structural changes in nanocutting of CuBe

Following the tool passage, the particle springs back owing to the difference in elastic modulus of Cu and Be. Thus, the generated surface is left with a void behind the particle. Since the presence of the particle affects the cutting process, it is essential to identify the cutting behaviour of the hard Be particle. Fig. 4.15 reveals the nature of cutting in the hard particle.

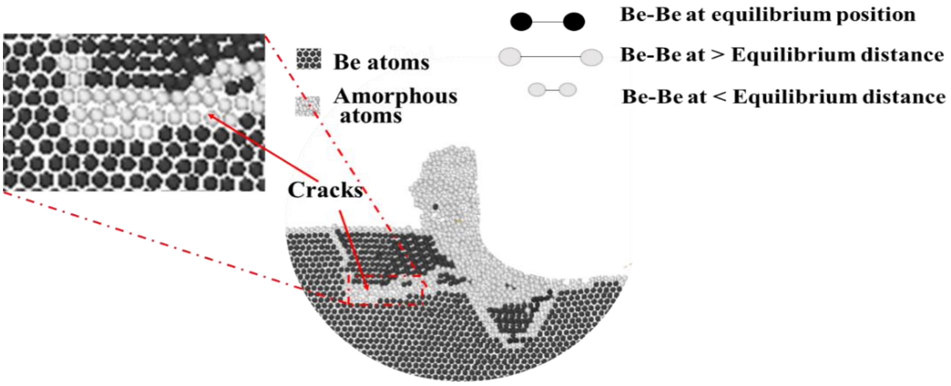

Fig. 4.15. Crack formation in Be particle revealed by MDS

As the tool is traversed across the Be workpiece, Be being a hard and brittle material shows crack formation. The crack propagates and expands ahead as well as beneath the tool. A zoomed view at the crack location in Be shows that there is an increase in interatomic distance which represents dissociation of atomic bonds between Be atoms and consequently leads to amorphous structure. Rest of the atoms in the hard particle remains in the ordered state. This crack formation reveals that as the tool travels from Cu rich phase to Be rich phase, the cutting mechanism shows transition from ductile to brittle machining. At lower a/r ratios, a high hydrostatic pressure in the cutting zone suppresses the crack and chips are produced without causing cracks in the bulk material [Fig. 4.16 (a) and (b)].

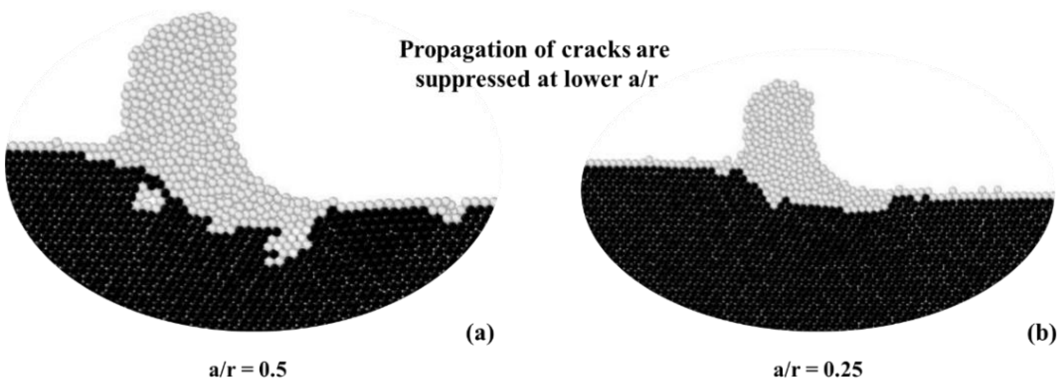

Fig. 4.16. Snapshot showing suppression of cracks in Be particle at lower a/r ratio

4.3.3.3. Subsurface deformation

Dislocation extraction analysis (DXA) tool in LAMMPS was used to observe the dislocation flow during nanocutting of Cu and CuBe. Both Cu and CuBe are metallic material and material deformation in metallic materials takes place due to the flow of dislocations. Fig. 4.17(a-d) and Fig. 4.18(a-d) show the snapshots of development of dislocations during cutting simulation in Cu and CuBe respectively.

As the cutting begins in Cu, dislocations form and workpiece material deforms plastically in the cutting zone [Fig. 4.17(a)]. The dislocations formation take place by three ways namely edge, screw and mixed character. Usually pure edge and screw dislocations are rare to exist during deformation. The mixed dislocations with certain percentages of screw and edge character in them form during deformation in cutting. With the progress in cutting, a number of dislocations forms ahead and below the tool [Fig. 4.17(b) and (c)].

Since the tool moves in cutting direction, the dislocations also propagate in the same direction. As the tool moves ahead, few dislocations remain underneath the machined region as residuals [Fig. 4.17 (d)]. The dislocations are immobile at room temperature and therefore, after machining process, they remain beneath the machined surface. This results in hardening of the machined surface layers. In case of CuBe, dislocations form and start propagating in the beginning of cut similar to that of Cu [Fig. 4.18(a)].

As the cutting progresses and encounters the particle, there is a decline in the number of dislocations [Fig. 4.18(b)]. This is due to the obstruction to the dislocation flow, caused by the presence of the particle. As the tool starts cutting in the hard Be particle, the particle is also pushed against the soft base material owing to the difference between their hardness. Due to this, large deformation takes place and dislocation density rises [Fig. 4.18(c)].

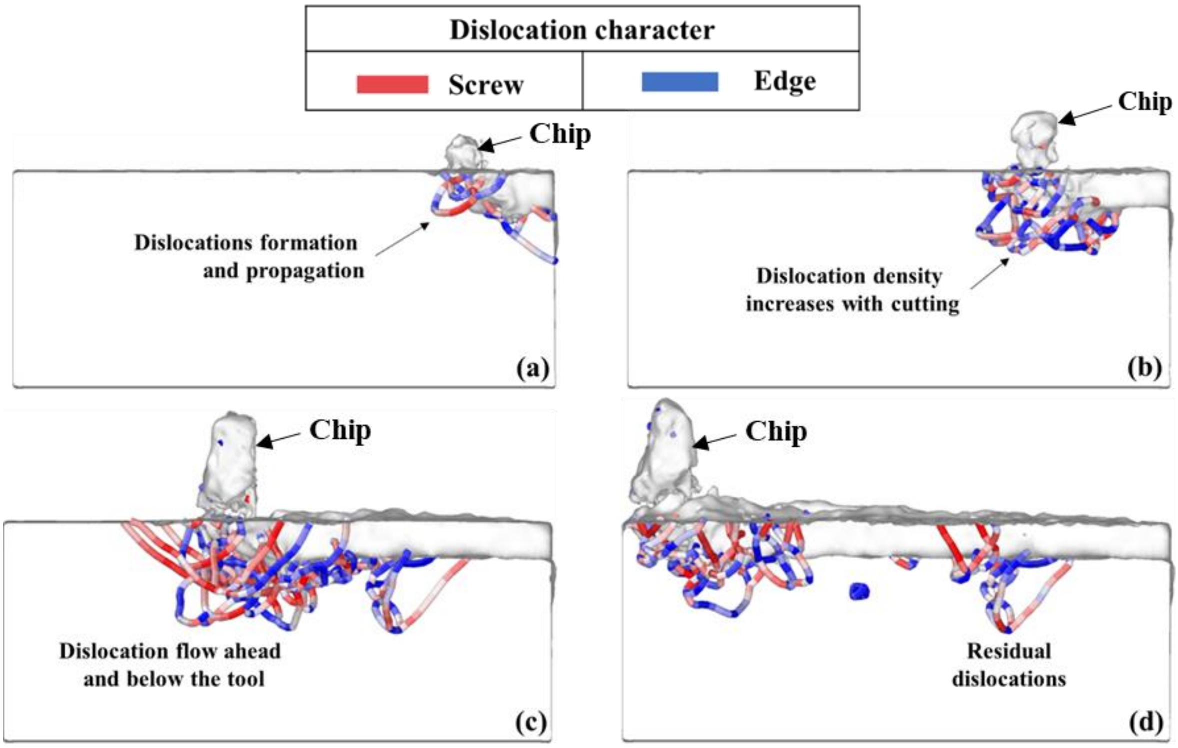

Fig. 4.17. Dislocation formation and propagation in nanocutting of Cu

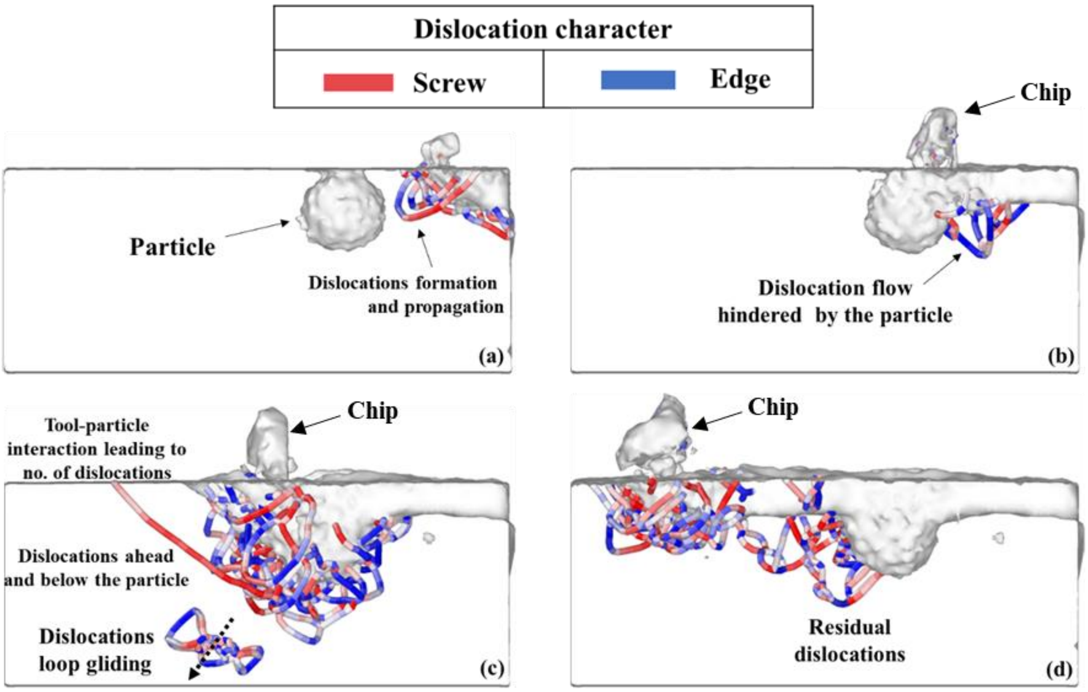

Fig. 4.18. Dislocation formation and propagation in nanocutting of CuBe

This leads to particle induced dislocation formation. Similar to Cu, the residual dislocations remain in the workpiece after the cutting [Fig. 4.18(d)]. Experimentally researchers have shown the formation of dislocation lines and loops in diamond turned surfaces with the help of transmission electron microscopy [166–169].

4.3.4. Analysis of material removal mechanism in CuBe

Material removal mechanism in nanocutting of CuBe is further analysed by plotting specific cutting energy and force ratio at different a/r ratios. In actual practice, the Be particle is bigger than the uncut chip thickness (a) and cutting edge radius (r), therefore, for the subsequent analysis, particle size of 4 nm i.e. bigger than both the uncut chip and cutting edge was considered. Particle was considered to be positioned at the cutting plane.

4.3.4.1. Specific cutting energy

To further analyze the cutting process with varying uncut chip thickness, simulations with varying a/r ranging from 2 nm to 0.1 nm were carried out with cutting radius of 2 nm. Specific cutting energies at the locations of precipitate were calculated for six different crystal orientations of Cu and plotted as shown in Fig. 4.19. The nature of the graph is similar to that of Cu [Fig. 4.3], however, the magnitude is quite high in case of CuBe [maximum of $60*10^{-6}$ N/mm^2 for CuBe against $14.5*10^{-6}$ N/mm^2 for Cu]. This is because of the higher cutting resistance caused by the particle.

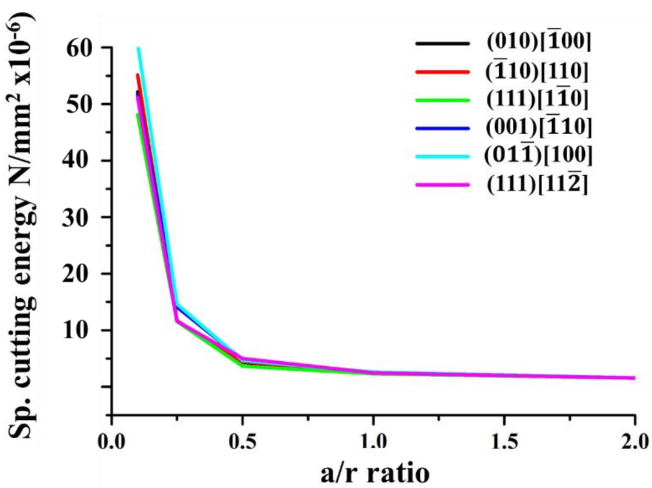

Fig. 4.19. Variation of specific cutting energy with respect to a/r ratio for CuBe

At a/r ratio less than or equal to 1, cutting energy significantly increases. Specific cutting energy for all the orientations show nearly similar value at various a/r ratio. This suggests that the presence of hard particle overcomes the effect of grain orientations and thus, the hard particle governs the cutting behavior. Therefore, further analysis is carried out for cutting in one orientation i.e. (010)[$\bar{1}$00].

4.3.4.2. Force ratio

In nanocutting, the force ratio (Fy/Fx) is indicative of cutting mechanisms. Higher thrust force reflects plastic deformation and ploughing mechanisms, whereas higher cutting force indicates shear mechanism in nanocutting. Here, the a/r ratio was varied keeping either ‘a’ or ‘r’ constant at a time. The force ratio plot in case of cutting in Cu phase of CuBe [Fig. 4.20 (a)] is similar to that revealed by Fig. 4.7 when cutting takes place in pure Cu. Similar findings were also noticed by Hosseini and Vahdati [76] where it was found that the thrust to cutting ratio decreases exponentially as the a/r reduces.

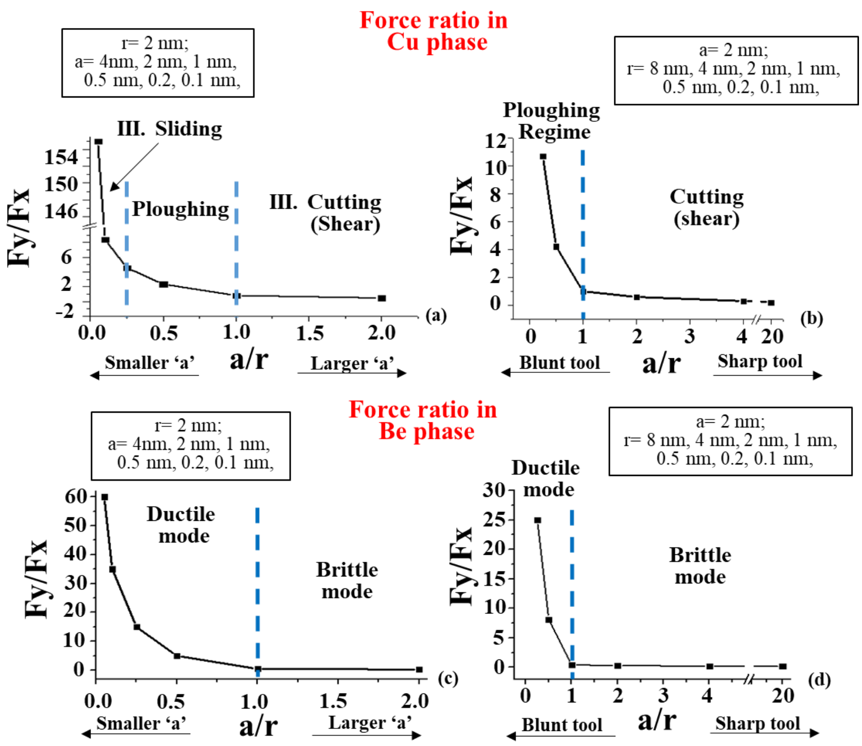

Fig. 4.20. Cutting mechanisms in case of CuBe for Cu and Be phase

It shows similar mechanisms from shear cutting to ploughing and then to elastic plastic deformation as the a/r ratio decreases. For constant uncut chip thickness (a) for varying cutting radii (r) also, the nature of curve shows similar behavior [Fig. 4.20(b)]. Both the curves indicate that at a/r ratio above 1 is suitable for cutting with the value of uncut chip thickness ‘a’ equals to 2 nm.

Since Be acts as an inhomogeneity, force ratios were calculated and plotted while nanocutting the Be particle in the workpiece for various a/r. In case of Be particle, material deformation does not occur with the flow of dislocations. Cracks are generated and propagated as the tool moves ahead. When the cutting edge radius (r) is constant and uncut chip thickness (a) is changing, a/r ratio higher than 1 causes brittle machining of the Be precipitate whereas lower a/r ratio than 1 leads to ductile regime machining [Fig. 4.20(c)]. This is also true when the cutting is carried out at constant chip thickness and varying edge radii [Fig. 4.20(d)]. These results indicate that a/r equal to 1 is suitable for cutting Cu phase and for ductile regime machining conditions.

4.4. Mechanism of plastic deformation during nanocutting of Cu and CuBe

It is already explained that the dislocations are responsible for the material deformation during nanocutting in the workpiece material. Predominantly Shockley partial dislocations have been observed during nanocutting of Cu and CuBe. These dislocations are observed in Cu base and not in the hard particle. It happens due to the fact that the particle is hard in nature and thus restrains the flow of dislocations within it. However, the hard particle intensifies the number of dislocations in Cu base material in its vicinity during cutting. This section describes about the mechanism of formation of Shockley partial dislocations in nanocutting.

During deformation in nanocutting process, HCP layer is first observed as the cutting begins. This is due to the fact that HCP crystal tends to have a slightly lower free energy than FCC crystals which leads to negative stacking fault energy (γ_{SFE}). Therefore a stacking fault, which is more stable in sheared state, is caused [170]. Another explanation is Cu assumes low stacking fault energy, so on shearing, the perfect dislocation is split into two well separated Shockley partial dislocations connected by stacking fault. For FCC crystals, slip plane and corresponding slip directions are {111} and <110> respectively. The HCP layer due to deformation by slip occurs in the <110> direction on {111} plane with a Burgers vector (a/2)[110]. The {111} planes are stacked on a closed packed sequence ABCABCABC and Burgers vector b= (a/2)[110] defines one of the slip directions, which can decompose into energetically favourable two partial dislocations (i.e. Shockley partial dislocations).

Shockley partials are created because of a stacking fault ABCACABC [Fig. 4.20]. Fig. 4.21(a-c) show the mechanism of formation of partial dislocations with stacking faults. Blue colour atoms represent A set of atoms, above which the B set of atoms are arranged. The B atoms are placed over those gaps in two adjacent layers of A set of atoms, where they are completely above the second layer of A set of atoms. Similarly, C atoms are placed on the gaps in B set of atoms. Fig. 4.21(a) shows translation of atoms in layer B of FCC crystal by b_1. This will remain a perfect FCC structure after translation as glide of perfect dislocation moves the atoms to identical sites. Since translational movement of atoms have to pass the hump of atoms lying next to them which require more energy than to move by b_2 and then b_3 vectors to reach the specified site [Fig. 4.21(b)]. Thus the atoms from the B set leave their positions and occupy sites of C atoms. This requires less energy but motion of partial dislocation leaves the crystal imperfect with the creation of stacking fault between two partials [Fig. 4.21(c)].

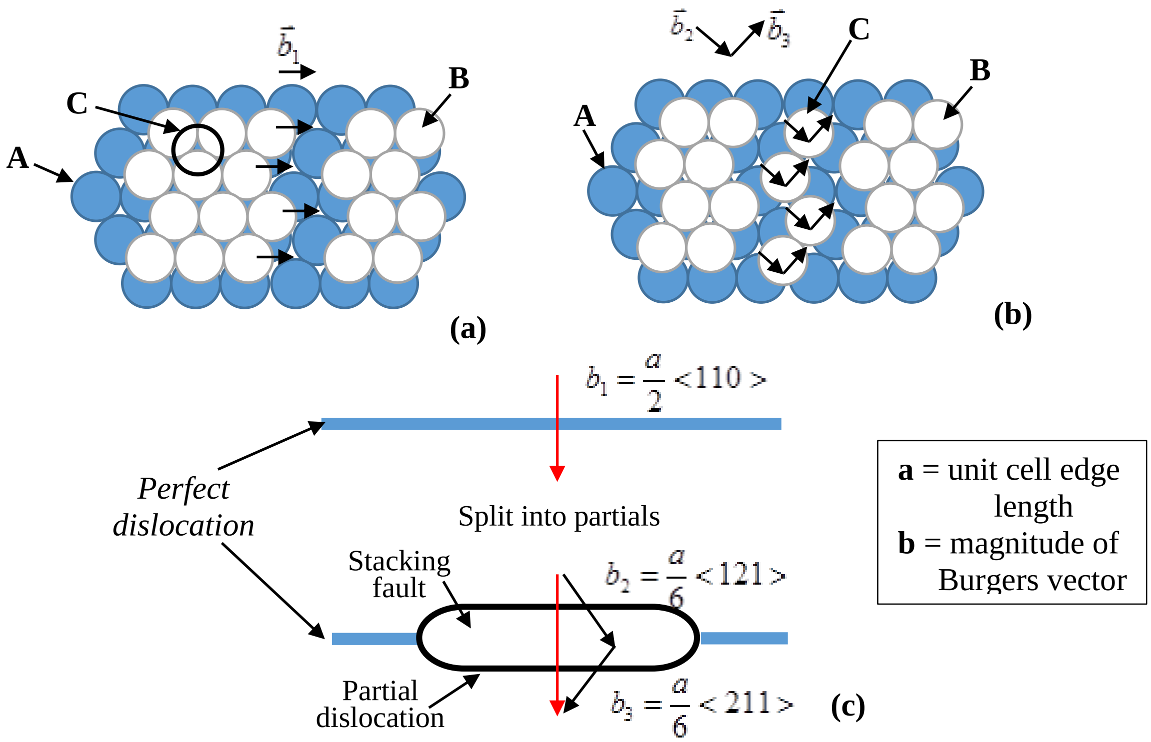

Fig. 4.21. Mechanism of splitting of perfect dislocation into partial dislocations

The energy related to dislocations is expressed by following equation:

$W_{disl} = ½\, Gb^2$ i.e. W_{disl} is proportional to b^2, where b is the burgers vector of the dislocation.

Frank's rule for dislocation reactions suggests that reaction is favourable if $b_1^2 > b_2^2 + b_3^2$

For a perfect dislocation: $\vec{b} = \frac{a}{2} < 110 >$, $b^2 = \frac{a^2}{4}\left(1^2 + 1^2 + 0^2\right) = \frac{a^2}{2}$

For Shockley partial dislocations: $\vec{b} = \frac{a}{6} < 112 >$, $b^2 = \frac{a^2}{36}\left(1^2 + 1^2 + 2^2\right) = \frac{a^2}{6}$

On comparison, $\frac{a^2}{6} + \frac{a^2}{6} < \frac{a^2}{2}$ i.e. $b_1^2 > b_2^2 + b_3^2$

The dislocation energy for partial dislocation is less than that of perfect dislocation. Thus, the partial dislocation is more favourable than the perfect dislocation. Extra energy is dissipated in creating stacking faults between two partials. Partial dislocations accompanying with stacking faults interact with each other and leads to the formation of various other defects. Fig. 4.22(a) shows various defects that occur during nanocutting in the workpiece: Stacking faults, stair rod dislocation, dislocation loop, Stacking fault tetrahedral.

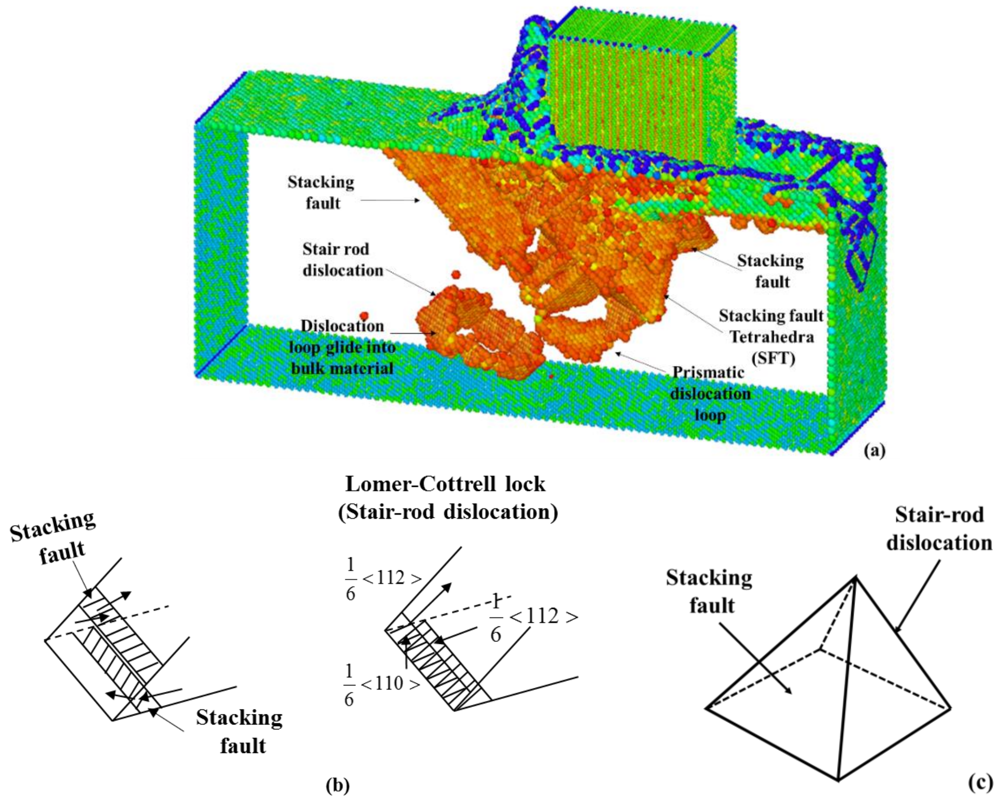

Fig. 4.22. Defects during nanocutting in CuBe

Mechanism of stair-rod dislocation formation is shown in Fig. 4.22(b). Two partial dislocations on different (111) plane when cross together they form a lock which is also known as Lomer-Cottrell barrier and give rise to stair rod dislocation. Furthermore, dislocations interactions during deformation in nanocutting lead to generation of stacking fault tetrahedra. Stacking fault tetrahedra (SFT) consists of set of stair-rod dislocations and stacking faults (SFs). Fig. 4.22(c) shows the structural arrangement of SFT.

4.5. Mechanism of diamond tool wear

During nanocutting of CuBe, interaction between tool and workpiece not only influences the surface generated but the tool also gets affected by the workpiece. Tool wear is critical for the surface generation at nanoscale as wear deteriorates the tool edge sharpness which subsequently affects the material removal mechanism and surface quality. There are two effects of tool wear:

1. a/r dynamically changes due to increase in cutting edge radius 'r'
2. Wear land on the flank face increases

   Both the effects tend to change the cutting mechanism
3. Dimensions of tool nose radius changes

   It changes the size and shape accuracy of the generated surface.

Tool wear is an undesirable problem in diamond turning not only because of the tool life but also because of its consequential effects on the machined surface quality. Degradation of the diamond tool due to wear alters the tool–workpiece contact and hence the machining conditions which can cause consequent deterioration to the quality of the machined surface. Therefore, a good understanding of the wear mechanism is essential to mitigate the wear and its after effects. Fig. 4.23 shows the possible wear mechanisms during the tool and workpiece interaction. Four basic mechanisms are possible depending on the workpiece material viz.

- Abrasion,
- Diffusion,
- Adhesion and
- Graphitization

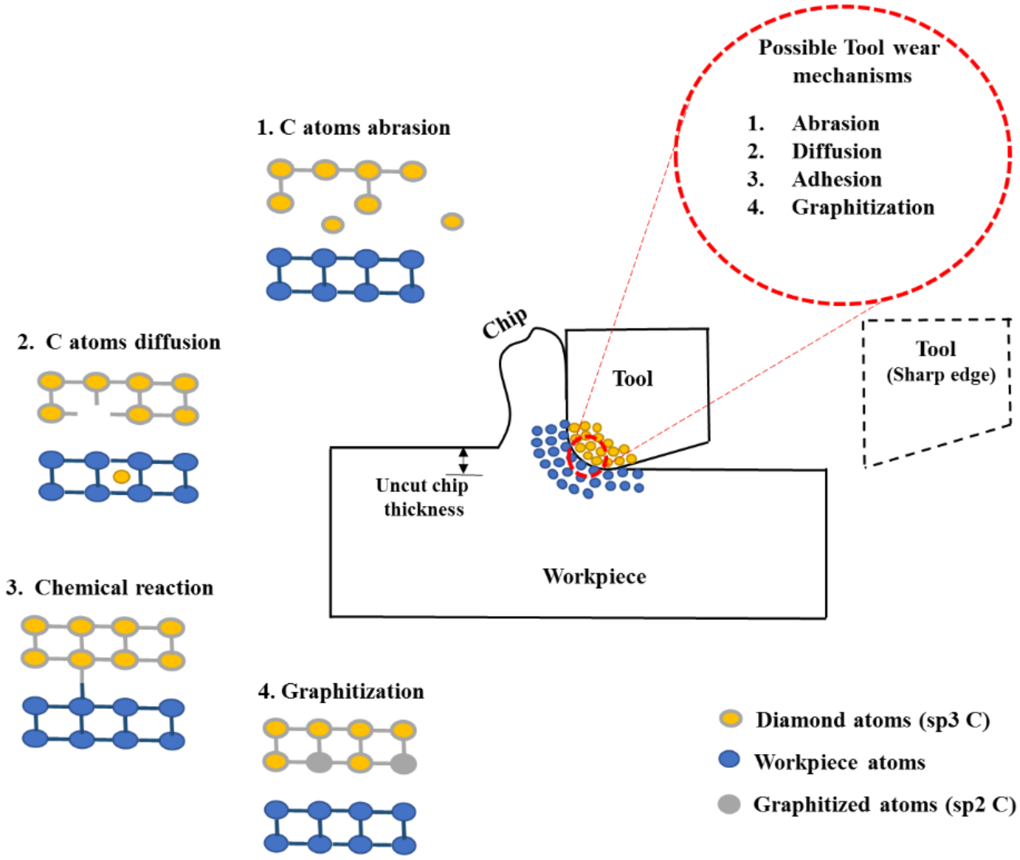

Fig. 4.23. Types of wear mechanisms in diamond tool during nanoscale cutting.

The workpiece material strongly dictates the type of wear mechanism in the diamond tool. The materials which are close to diamond in Mohs hardness scale are able to wear the tool by the abrasion process where atoms from diamond tool are unbonded by the stresses generated at the cutting edge of the tool [122]. The materials, which are chemically active in nature towards carbon atoms in the diamond tool, drive the tool wear process by chemical/thermochemical phenomenon like diffusion or at times leads to carbide formation [120]. Ferrous based materials graphitize the diamond tool and weaken the bonding forces between atoms of the diamond tool. Graphitization leads to abrupt wear in the diamond tool. Although single wear mechanism always dominates, a combination of wear mechanisms occurs during tool and workpiece interaction in nanocutting of workpiece [171,172]. Wear of the diamond tool starts initially from the edge and progresses in the flank face. Wear of tool material from the flank face increases the contact area as the machining continues. This process makes the tool to become blunt and as a result the cutting process gradually becomes inefficient. Wear rate and wear mechanism depend upon the tool edge conditions. Therefore, to understand the wear mechanism, two edge configurations of tool as shown in Fig. 4.24 were considered:

Tool and workpiece with

- Sharp edge tool and
- Blunt edge tool.

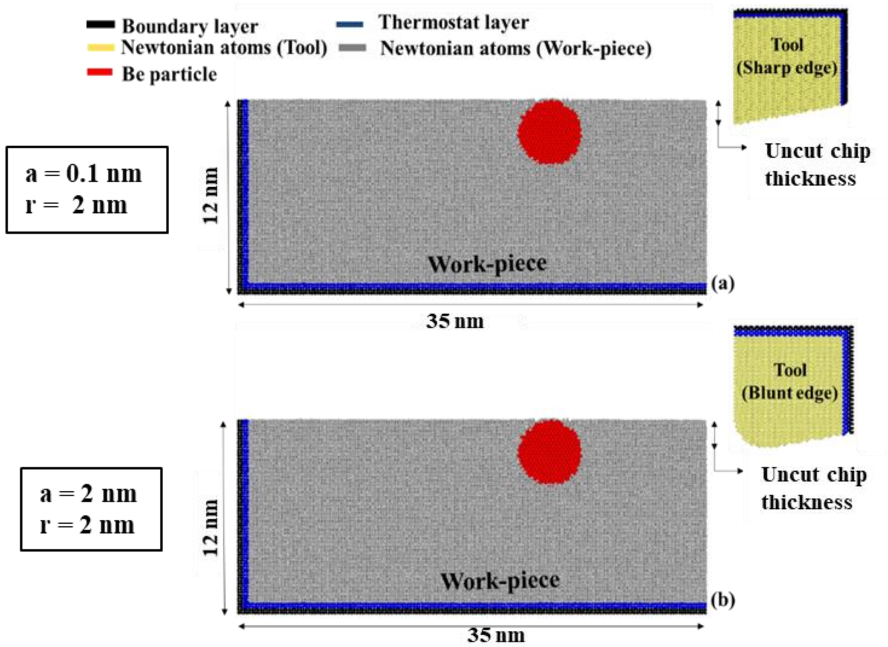

Fig. 4.24. MD model of nanoscale cutting of CuBe work-piece with diamond tool

4.5.1. Results of tool wear

During the nanoscale cutting of Cu, the tool first contacts the Cu atoms and remove them in the form of chip. As Cu is soft material, it does not cause sufficiently high stresses on the tool edge to cause any noticeable wear for this small cutting distance. The stresses generated in case of sharp edge and blunt edge diamond tools are found to be 150 GPa and 130 GPa respectively. The higher stress in case of sharp edge is due to the fact that the sharp edge acts as a stress concentrated region and even the small amount of cutting force leads to high stresses. As the tool approaches the hard particle, stresses in both the tool configurations begin to increase rapidly and reaches to the fracture limits in the sharp edge. The severe stresses on the tool are caused at the sharp tool edge during cutting as shown in Fig. 4.25(a). The stresses are so severe at the edge that, they cause failure at the atomic scale in the form of chipping on the diamond tool. The stress (σ) required to cause atomic fracture in diamond is given by [173]:

$$\sigma_t = \frac{E}{2\pi} \tag{4.1}$$

where, E is the Young's modulus of elasticity. Substituting, E for diamond as 900-1200 GPa, we get

$$\sigma_t = 140 - 180 \ \ GPa$$

The stresses obtained in the simulation also suggest that the maximum stress is of the order of 150 GPa that occurs during the interaction between the hard particle and the tool [Fig. 4.25 (a)]. Thus, it confirms with the level of stress observed in the simulation. In addition, Gogotsi et al. [174] observed that the magnitude of stress in the order of 150 GPa is sufficient to cause wear to the diamond.

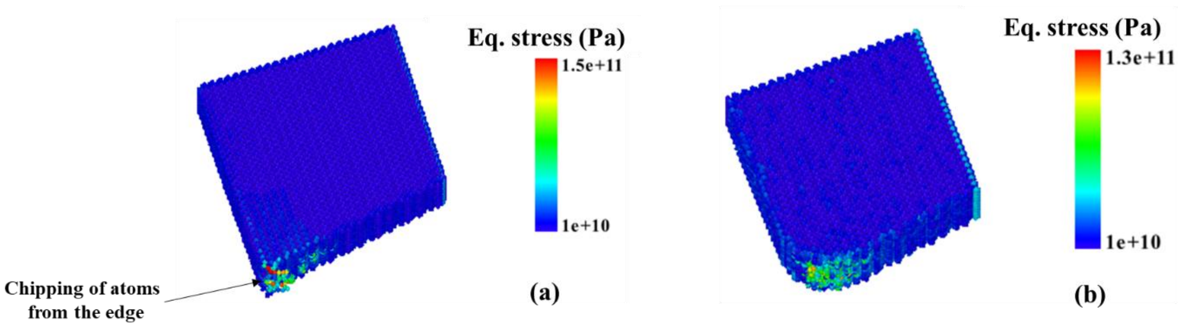

Fig. 4.25. Equivalent stresses on sharp and blunt tool at the particle location

When the stresses approach their atomic fracture limits, carbon particles are separated from the diamond tool [Fig. 4.26(a)]. Once the C atoms on the tool are removed, the tool edge gets weakened, and the removed atoms adhere on the workpiece surface. On the other hand the blunt tool edge having finite edge radius does not act as a stress concentrated region as compared to the sharp edge tool. Therefore, the stress does not reach its critical level to remove the C atoms from the diamond tool edge. However, the stresses are so severe (~130 GPa) that they can weaken the tool by deteriorating its chemical structure. Therefore, the coordination analysis was carried out for the blunt diamond tool while cutting CuBe [Fig. 4.26(b)].

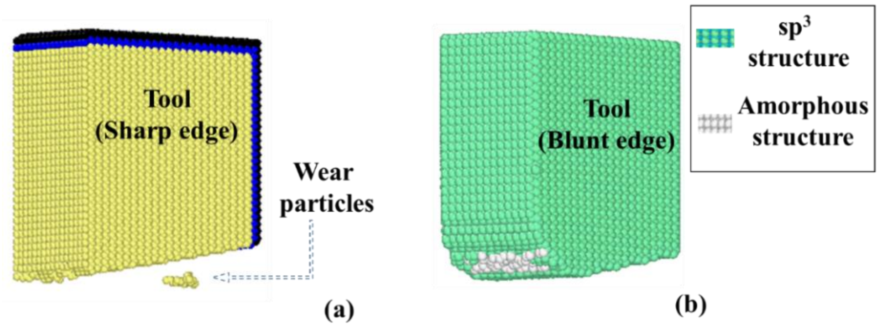

Fig. 4.26. Effect of stress on the sharp and blunt tool edge

During the cutting of Cu atoms, no structural damage occurred to the tool as the stresses were found to be lower. As it approached the Be particle, diamond structure at the tool edge converted into a non-crystalline structure characterized by white coloured atoms in Fig. 4.26(b). This phase transformation occurs due to high cutting stresses imposed by the hard particle on the tool edge. As the tool interacts more and more with the particle, the amorphous structure expands. These amorphous layers of atoms being much weaker as compared to the diamond structure, are easily abraded by the workpiece. Thus, it confirms the governing wear mechanism that involves stress induced phase transformation of diamond tool followed by its abrasion.

4.5.2. Discussion and analysis

When MD simulation was carried out for various a/r ratios with varying radii of the tool from sharp to blunt edge, radial distribution function (RDF) showed that with the decrease in a/r ratio at varying radii, the peak at the bond length for diamond decreased and got broadened which indicates that more and more atoms are transformed into amorphous phase [Fig. 4.27(a)]. Fig. 4.27(b) shows an increasing trend in amorphous atoms with the decreasing a/r ratio. The percentage change in tool wear is calculated based on the ratio of worn out atoms in the cutting edge to the total number of atoms in the cutting edge.

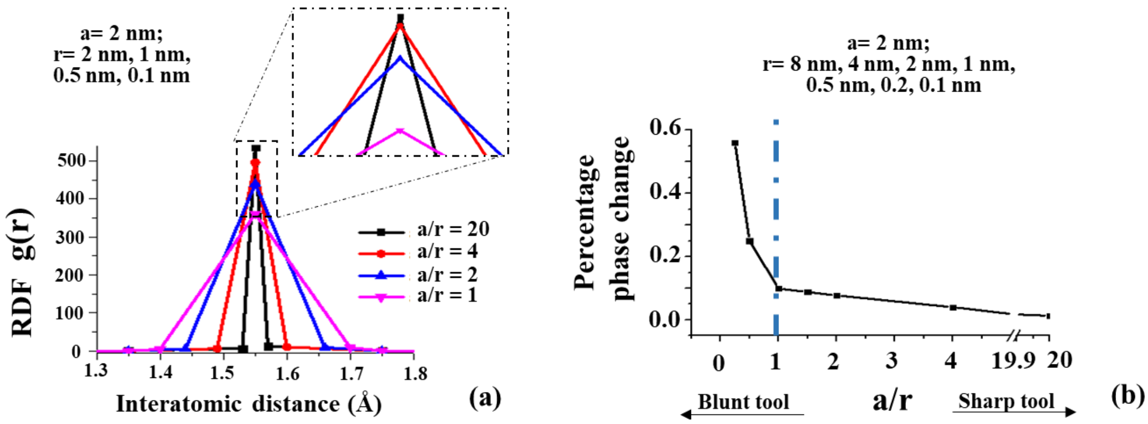

Fig. 4.27. Phase transformation of diamond tool

Fig. 4.28(a) shows the maximum stress and temperature variation for the diamond tool while machining CuBe at the precipitate location. It reveals that the stresses and temperature show a uniform change as the edge radius is varied from sharp to blunt configuration. The stresses show decreasing trend while the temperature at the tool edge radius gradually increase. The combination of the stress and temperature govern the wear mechanism as shown in Fig. 4.28(b). Initially when the tool edge is highly sharp, large stresses are developed in the tool edge which chips off the atoms from the tool edge as shown by region-III [Fig. 4.28]. As the tool wears and tool edge gets blunt shown by decreasing a/r ratio, the stress values which the tool edge is subjected to, gets decreased. In addition to the stresses, increase in the temperature takes place simultaneously, which assist in the phase change of the diamond at the tool edge. However, magnitudes of the stress and temperature are not too high, which lead to decrease in wear in region-II [Fig. 4.28(a)] and therefore governing mechanism is shown by the combination of abrasion and phase change [Fig. 4.28(b)]. When the tool edge is sufficiently worn (as represented by a/r < 1), the frictional contact leads to increase in temperature and interaction with precipitates leading to the tool stresses enough to cause phase transformation of the diamond which significantly weakens the tool edge. Thus, the wear rate grows rapidly in the region-III [Fig. 4.28(b)].

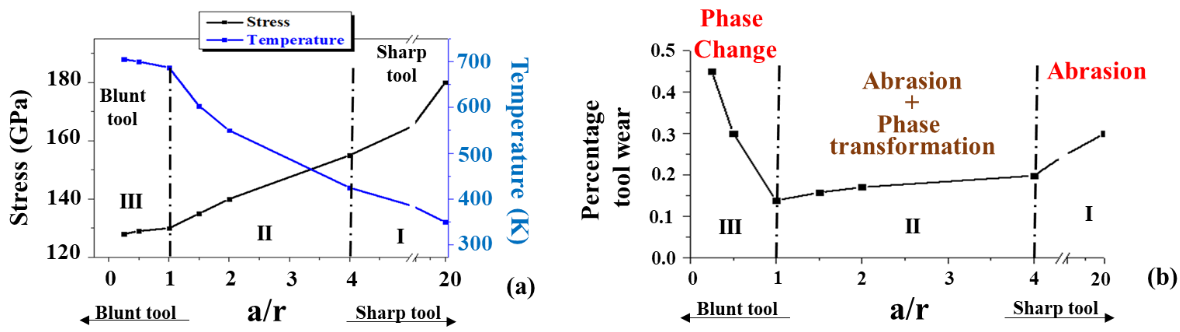

Fig. 4.28. Stress and temperature variation in tool edge and percentage change in wear

4.6. Surface Contamination

Contamination of the machined surface occurs by physical and chemical means during tool-workpiece interaction. Apart from the surface degradation, the machined surface is physically deteriorated by subsurface deformation, whereas the chemistry of the surface is affected by the tool wear. These two phenomenon occur simultaneously and affect the machined surface quality.

4.6.1. Physical contamination

Both Cu and CuBe are metallic materials and material deformation in these materials takes place due to the flow of dislocations. Fig. 4.29 shows the comparison of variation of dislocation density between Cu and in the base material of CuBe during cutting. Amount of dislocations is represented by their length. The graph is segmented into four regions. Region 1 shows a growth in dislocations as the cutting takes place in base material (i.e. Cu). The amount of dislocations in Region 2 are less for CuBe than that of Cu due to the obstruction to the dislocations flow caused by the particle. Region 3 shows a significant increase in amount of dislocations for CuBe as compared to Cu owing to large deformation which is caused by tool-particle interaction. Following the passage of the tool on the particle, the dislocation density falls for CuBe as revealed by Region 4, whereas it stays almost constant in case of Cu. The dislocations are immobile at room temperature and therefore, after machining process, they remain beneath the machined surface. This results in hardening of the machined surface layers. Experimentally researchers have shown the formation of dislocation lines and loops in diamond turned surfaces with the help of transmission electron microscopy [30–33].

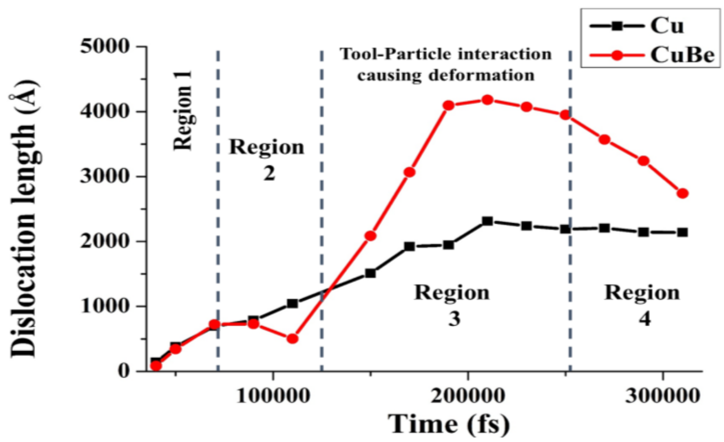

Fig. 4.29. Variation of amount of dislocations in cutting of Cu and CuBe

4.6.2. Chemical contamination

Diamond tool after wear caused by Be particle leaves behind C atoms as shown in Fig. 4.30. Be atoms in the workpiece and C atoms from the diamond tool chemically react and form beryllium carbides. C atoms abraded from diamond tool are unstable in nature and thus leads to bonding with the surface atoms of Be precipitate. Although diamond is a covalent bonded material, its atoms possess high cohesive energy, the high stresses and the temperature during cutting catalyse the bond formation between Be and C. The beryllium carbide (BeC) has a hardness of 9 on Mohs scale, which is next to diamond and thus the diamond tool is more prone to abrasion during subsequent passes in actual machining process. The chemical contamination can also affect the functional performance in tribology and optics domain.

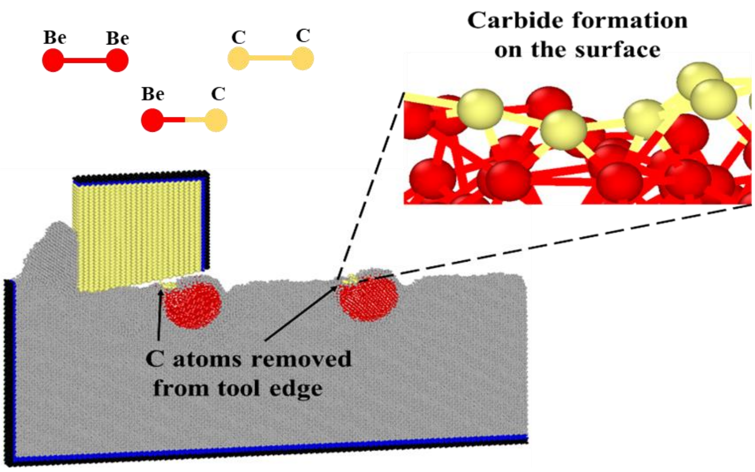

Fig. 4.30. Carbide formation on workpiece surface during nanocutting of CuBe

4.7. Significance of a/r ratio in nanocutting

Based on the MDS results, the following diagrams are presented, which signifies the effect of 'a/r' on various aspects of nanocutting of CuBe. The ratio a/r plays a significant role in nanoscale cutting of CuBe and a/r equal to 1 has been found to be the suitable ratio for the nanocutting of CuBe. In case of Cu phase [Fig. 4.31(a)], it is found that when a/r ratio is increased beyond 1, the cutting force increases which causes higher material removal. In addition, due to larger cutting action, dislocation density in the workpiece material increases, which causes surface and subsurface deformation. As a result, surface quality decreases. If it is decreased below 1, specific cutting energy gets increased which results in more tool wear. Increased tool wear leads to higher surface contamination.

In case of Be [Fig. 4.31(b)], lower a/r ratio leads to fractured precipitate which results in decreased surface quality. Moreover, phase change of the diamond tool takes place, as the a/r ratio is decreased. Subsequently, it results in tool wear and subsequent contamination.

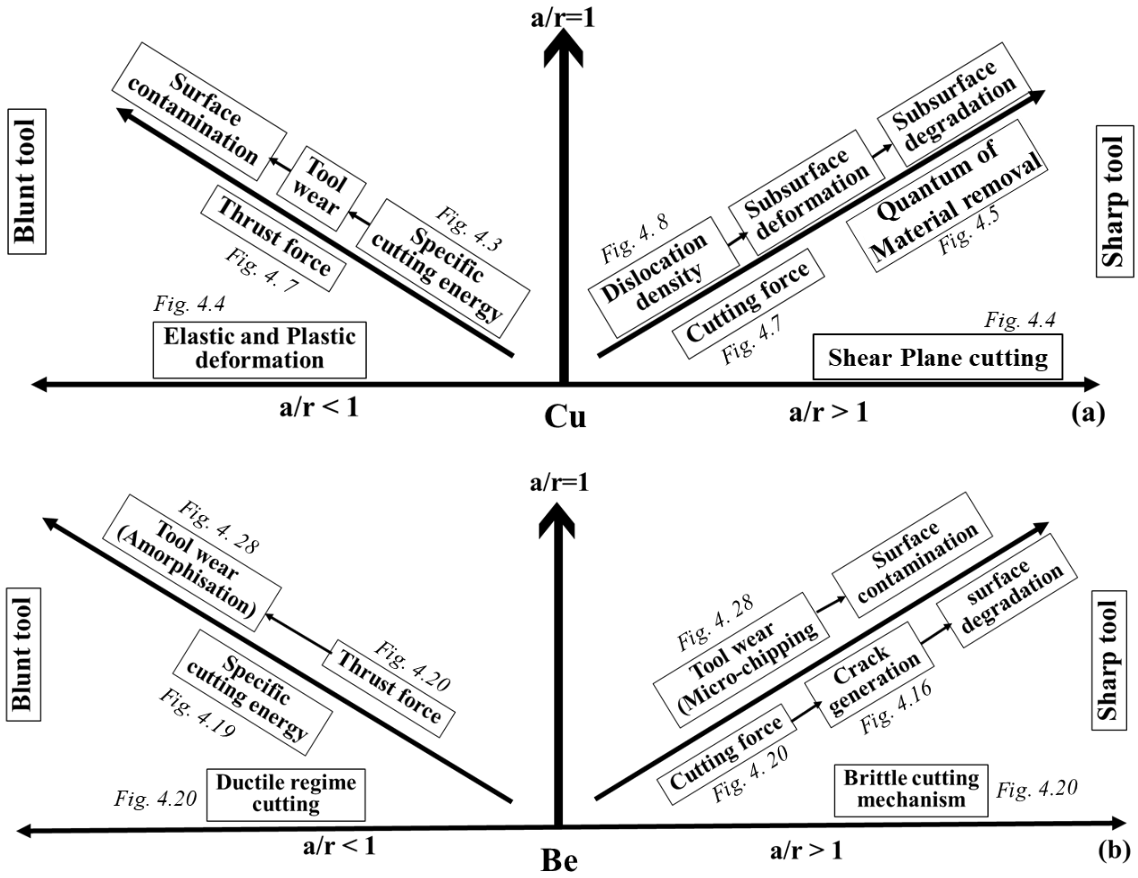

Fig. 4.31. Interaction effect diagram in nanoscale cutting of CuBe

Similarly, higher a/r ratio increases the specific cutting energy which causes intense stresses at the tool edge and subsequently, it leads to microchipping of the tool edge. The tool wear subsequently chemically contaminates the surface.

4.8. Summary

This chapter is primarily focussed on the tool and workpiece interaction especially the tool and hard Be particle interaction in the CuBe workpiece material. To elucidate the effect of Be particle on the tool and the workpiece surface, MD simulation was performed. Cu workpiece was also considered for bench marking and for elucidating the cutting behaviour of the workpiece with and without the hard particle. Following are the important findings:

1. The material removal mechanism in case of CuBe is phase dependent. In case of Cu

phase, ductile machining takes place where the governing mechanisms are: a) shearing action, (b) ploughing, and (c) elastic-plastic deformation (i.e. rubbing and burnishing) depending upon the a/r ratio. In case of hard Be phase, brittle fracture takes place at higher a/r ratio and ductile regime machining at lower a/r ratio.

2. MDS results indicate that a/r ratio equals to 1, is suitable for cutting in Cu phase and for ductile regime machining conditions in Be precipitate. The a/r ratio less than 1 in Cu phase results in higher thrust forces which causes elastic-plastic deformation and high specific cutting energy. The high specific cutting energy leads to tool wear and in turn surface contamination. The a/r ratio higher than 1 causes higher cutting forces and thus shear plane cutting takes place which leads to higher amount of material removal.
3. In case of Be phase, the a/r ratio less than 1 causes high thrust forces and specific cutting energy, which in turn leads to tool wear in the form of amorphization. The high thrust forces lead to the ductile regime cutting conditions in Be phase. For a/r ratio higher than 1, higher cutting forces takes place which in turn causes crack generation and propagation in the workpiece which indicates brittle machining of Be phase. Higher a/r ratio also results in tool wear in the form of microchipping and subsequently causes surface contamination.
4. Wear mechanism is predominantly governed by the stress and temperature generation in the tool edge. It is described with the help of a plot showing three regions. The wear mechanism while machining CuBe is: abrasion in the initial stage of time due to high stress and phase transformation at the later stage of time due to high temperature.
5. The carbon atoms removed from the tool are subsequently bonded with the workpiece material and thus contaminates the generated surface.
6. A diagram depicting various effects based on a/r ratio while nanomachining Cu and CuBe is presented.

Chapter 5

Experimental study of tool wear mechanism

5.1. Introduction

In this chapter, experiment results are analysed to examine diamond tool wear and its mechanism. Towards this, full tool life experiments were conducted and tool wear was measured at successive intervals of cutting distances. Tool wear mechanisms observed in chapter 4 are validated and established for Cu and CuBe with the help of Raman spectroscopy on the tool and on the machined surface. Tool wear coefficients for the model reported by Lane et al. [175] are determined for diamond tool and CuBe material combination from the results of MDS and experiments. An understanding of the wear mechanism for a full span of cutting will help in identifying the corrective measures to curb the tool wear and in turn to enhance the tool life. Even though the results of the MDS have already indicated the types of wear mechanism while machining CuBe, due to the scale difference between MDS and experimental study, these cannot be quantitatively correlated with each other. To understand and correlate the tool wear at experimental scale, following aspects have been investigated in this chapter:

- Tool wear experiments on Cu and CuBe for full length of cutting
- Wear characteristics of the tool and its mechanism
- Effect of hard particle on the tool
- Determination of wear coefficients for diamond and CuBe combination

5.2. Experimental methodology

Detailed experimentations on diamond turning of Cu and CuBe alloys were carried out to understand the role of hard precipitates on the tool. In the following paragraphs, the approach to the investigation and details of the experimentation carried out are presented.

5.2.1. Approach to the investigation

The approach to the investigation of diamond tool wear is schematically shown in Fig. 5.1. Schematic of diamond turning process and tool-workpiece interaction are presented in Fig. 5.1(a), where the relative motion of tool and workpiece are used to remove the desired material of the order of uncut chip thickness of few micrometers. During this process, the tool becomes worn out and its wear predominantly depends on the workpiece material.

The tool life was monitored by measuring flank wear length [Fig. 5.1(b)] as a function of increasing cutting distance. It was intermittently measured using the microscope (Make : Dino-lite digital microscope) under 200 X magnification. The tool wear pattern was measured at the end of cutting cycle with the help of scanning electron microscopy (SEM) (Make: Zeiss of 1 nm resolution) [Fig. 5.1(c)]. Wear pattern of the tool only reflects the mechanical wear; hence, laser micro-Raman spectroscopy ((Make: Horiba Jobin Yvon, France) having spot size of 1 μm and ~0.4 cm^{-1} resolution in Raman shift) was carried out on the flank wear land to investigate the occurrence of chemical wear or phase transformation [Fig. 5.1(d)]. Furthermore, the machined surface was analysed with the help of electron dispersive spectroscopy (EDS) to understand the effect of workpiece on tool wear [Fig. 5.1(e)].

The forces during diamond turning were obtained using mini-dynamometer (Model: Kistler 9256 C and Kistler Dynamometer specification: Load ~250 N max., Sampling rate = 7142 Hz, rigidity > 300 N/ μm, temperature range = 0- 70 ^{o}C, Resolution ~ 10 mN). The forces with their directions are shown in Fig. 5.1(f). The principal cutting forces act in the cutting direction; thrust forces are in the direction normal to the workpiece; and the feed forces are in lateral directions to the chip profile. The principal cutting forces are interchangeably used as cutting forces. In this chapter, cutting and thrust forces were measured to explain the cutting and tool wear behaviour in Cu and CuBe. MD simulation results analysed in previous chapter are validated with the help of experiments [Fig. 5.1 (g)].

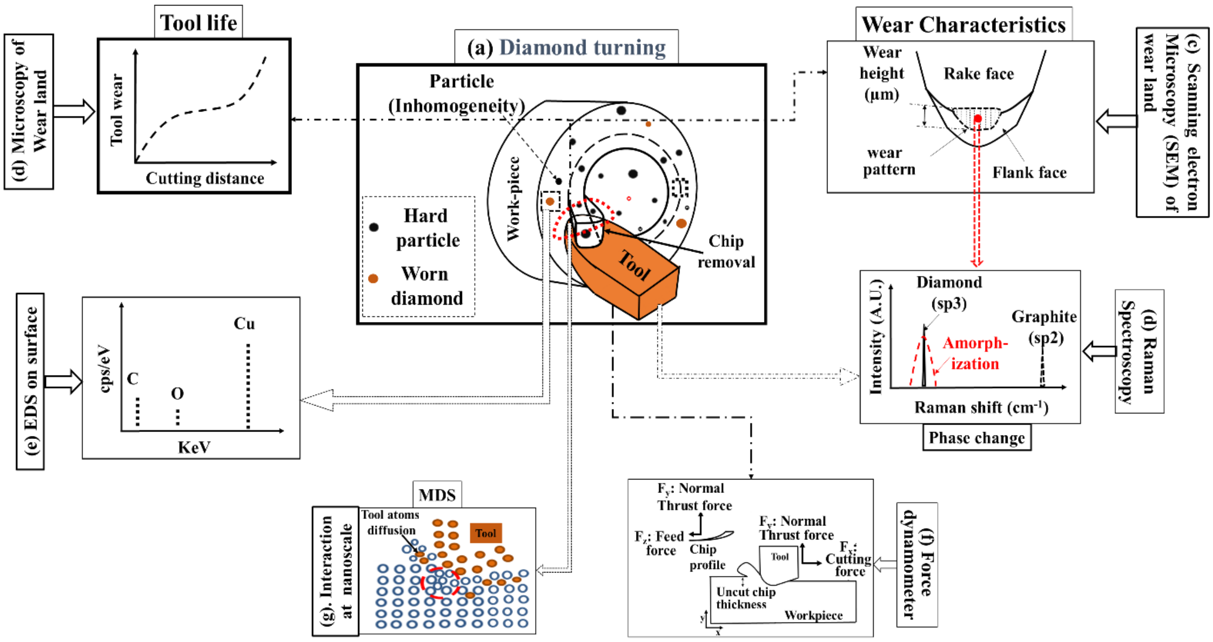

Fig. 5.1. Schematic of tool wear characterization

5.2.2. Experimental details

Ultra precision diamond turning lathe (Mikrotools UPL 420) [Fig. 5.2] was employed to perform facing operation on two materials. A controlled waviness single crystal diamond tool of 0.2 mm tool nose radius and 200 nm cutting edge sharpness was used. The cutting edge waviness of better than 0.5 µm on tools were the certified values from the tool manufacturer. Oxygen free high conductivity (OFHC) copper (Cu) and copper beryllium (CuBe) with 2% Be were selected as the two work piece materials. OFHC copper (Cu) is a soft material while CuBe is a hard material with 2% of beryllium (Be) mixed in copper. The commercially available Cu-Be (UNS C17200) was used for the experiments. CuBe contains a second gamma phase i.e. Be rich phase, which is distributed all over the Cu matrix and is responsible for higher hardness of the CuBe alloy. Characterization results of CuBe is already shown in Section 3.2.

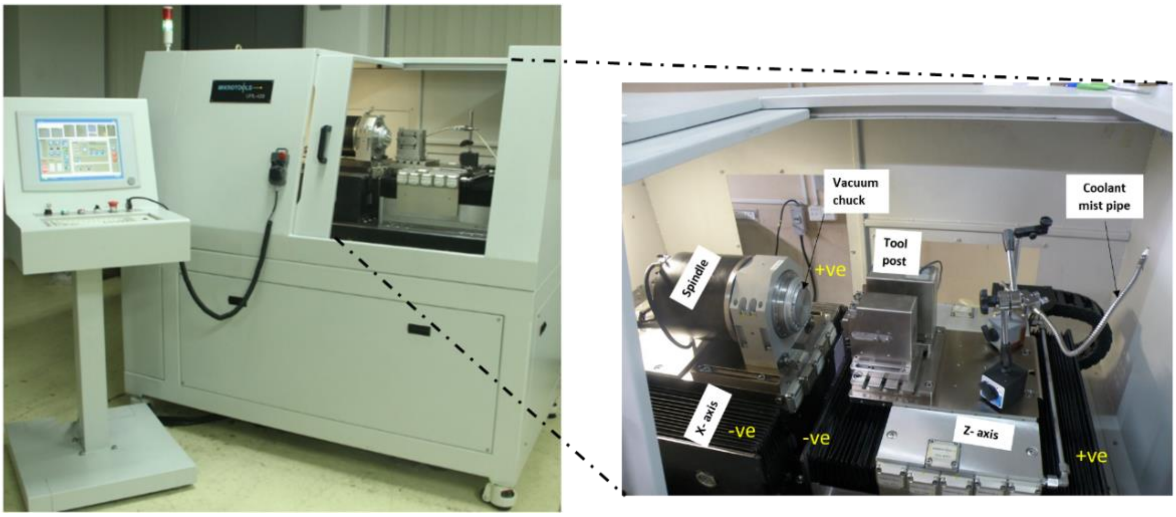

Fig. 5.2. Experimental set up

A number of specimens of diameter 18 mm and thickness 5 mm were used for the experiments. Samples were lapped on both sides and were mounted on specially designed fixture which in turn was held by vacuum chuck on the spindle. Facing operation was carried out in this study during which machining was carried out from periphery to centre of the specimen. Machining operation was performed till the chips ceased to get generated by the specified tools. In these experiments, full life spans of the tools were utilized.

During the experiments, cutting speed of 4 mm/min (spindle speed of 2000 rpm), feed rate of 2 μm/rev and depth of cut of 5 μm were used for both the materials. Three each repetition till the end of life of three each separate tools were carried out on both the workpiece materials. Based on the literature, these parameters were considered to be optimum for ultra-precision machining of Cu alloys. Table 5.1 shows the tool and cutting parameters used for performing full tool life experiments. Since study of chip morphology was not included in this study, chips were not collected and studied.

Table 5.1. Cutting parameters and tool geometry

Workpiece	Speed		Feed	Depth of Cut	coolant	
Cu	4 mm/min		2 µm/rev	5 µm	Compressed air	
CuBe						
Cutting Tool						
Edge Sharpness	Nose radius	Included angle	Waviness	Rake angle	Clearance angle	Rake and Flank plane
~200nm	0.2 mm	100º	<0.5 µm	0º	10º	(110) Rake and (100) Flank

Table 5.2. Material properties for Cu and CuBe

	Tensile strength, ultimate MPa	Tensile strength, yield MPa	Modulus of elasticity GPa	Poissons ratio	Shear modulus GPa	Hardness, Vickers HV
Cu	200-320	69.0 - 365	115	0.310	44.0	80
CuBe	1280 - 1480	965 - 1205	128	0.300	50.0	390

5.3. Results and discussions on tool wear characteristics

Results of the investigations carried out on the wear mechanisms of the diamond tools while machining both Cu and CuBe workpiece materials are presented in the following sections. The mechanisms were perceived from the imprints on the tool as well as on the machined surfaces. Further, the tool life, wear pattern, phase change in diamond and tool-workpiece material interaction occurring during machining of Cu and CuBe were also investigated.

5.3.1. Tool life

The diamond tool used on Cu covered a cutting distance of ~20 km, whereas on CuBe, it covered ~8 km approximately before the chips ceased to form. All the tools covered nearly the similar cutting distance for Cu and CuBe. To have a comparison, tool wear was calculated at same distances for Cu and CuBe (i.e. 20 km for Cu and 8 km for CuBe). Flank wear was considered as a measure of tool wear and Fig. 5.3 shows the increase in flank wear length of the tool while machining Cu and CuBe with respect to the cutting distance.

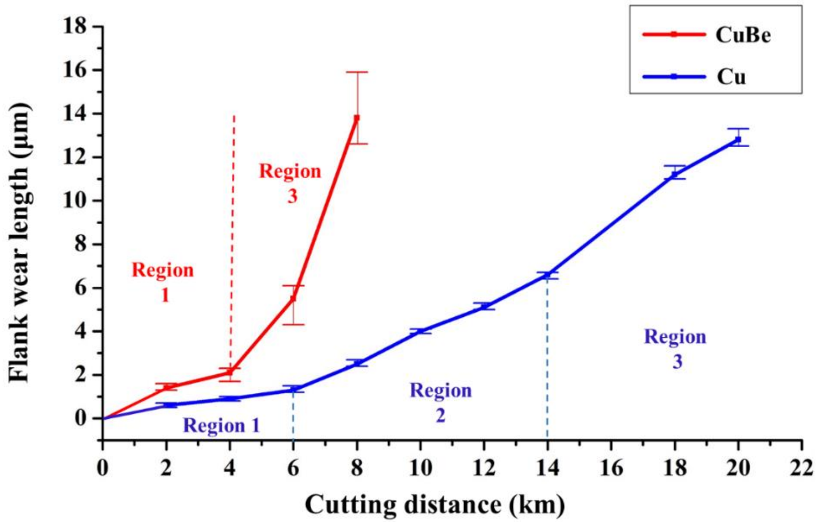

Fig. 5.3. Flank wear length variation with respect to cutting distance on Cu and CuBe

Experimental data and the outcome of the experiments in terms of tool life and tool wear are shown in Table 5.3.

Table 5.3. Life and flank wear values for each tool used to diamond turn Cu and CuBe

Material	Tool	Tested tool life (in km)	Tool wear (μm)
Cu	#1	20	12.5
	#2		12.8
	#3		13.3
CuBe	#1	8	15.9
	#2		13.8
	#3		12.6

Values of the intermediate curve were compared for both Cu and CuBe. Both the workpiece materials show an increase in tool wear rate with the cutting distance. Tool wear plot for Cu clearly shows three distinct regions. Region 1 shows a very little flank wear length of 1.3 μm for a cutting distance up to 6 km. Slope of the wear values remains almost constant. Region 2 shows a constant slope with change in flank wear length from 1.3 to 6.7 μm in the cutting span from 6 to 14 km. Region 3 indicates a higher slope than the Region 2 before the chips cease to form. It shows an increase in flank wear from 6.7 to 12.8 μm during the cutting distance from 14 to 20 km. The deviation in flank wear lengths for three repetitions is the lowest at the Region 1 and is maximum at the Region 3. The maximum percentage change of 4 % in the results of the tool wear curve for Cu was noticed at the end of the cutting, where the maximum flank wear length was noticed.

Tool used on CuBe showed a different wear trend. The wear rate observed in case of CuBe is quite high. Three repetitions of the facing trials show a lot of variation in the wear magnitudes, the maximum being 26 %. From the wear curve for CuBe, it is apparent that only the Region 1 and Region 3 are prevalent, and the steady-state region defined by Region 2, is completely absent. Initially, flank wear land of 2.1 μm in Region 1 for a cutting distance of 4 km is noticed. The wear rate subsequently increases significantly to ~13.8 μm in the cutting distance from 4 to 8 km. Large flank wear land leads to a larger tool-workpiece contact area, thereby, increasing the wear rate further.

On comparing both the curves, it is observed that the slope of the wear curves in the region 3 for CuBe is very high (3), as compared to that in the case of Cu (0.66), in the same region. Thus, it can be concluded that the excessive catastrophic wear takes place on the cutting edge of the diamond tool during machining of CuBe. The life of the tool used while machining on CuBe is found to be ~40% of the tool life in case of Cu.

As average hardness of CuBe (~360 HV) is approximately 3.5 times higher than that of Cu (~105 HV), the tool wear rate is also higher in case of CuBe as characterized by the flank wear land length. A large difference in the tool wear values for all the repetitions in case of CuBe is due to the fact that the interaction between hard particles and the diamond tool causes a variation in tool wear as the particles are of various sizes with different distribution and are at different depths.

It is obvious from the results that once a certain amount of wear land is formed while machining CuBe, further interaction of tool flank face and hard particle causes rapid wear owing to the increased tool particle interaction.

5.3.2. Tool wear pattern

SEM images of worn out tools were taken to investigate tool wear characteristics. Fig. 5.4(a) and (b) show the wear pattern and give indication about the types of wear mechanisms. To understand any chemical interplay between the tool and workpiece, Raman spectrums for both tools (used on Cu and CuBe respectively) were carried out and shown in Fig. 5.4(c) and (d). It is noticed that no obvious wear is seen on the rake face of the tool, but only flank wear was found to be dominant. The flank wear land results in loss of clearance angle, causing increased friction, which in turn increases the wear rate and decreases the tool life.

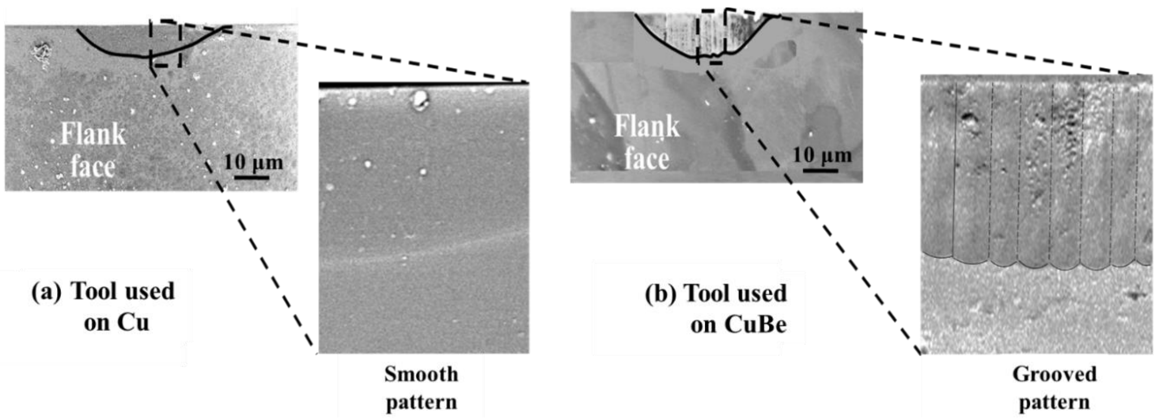

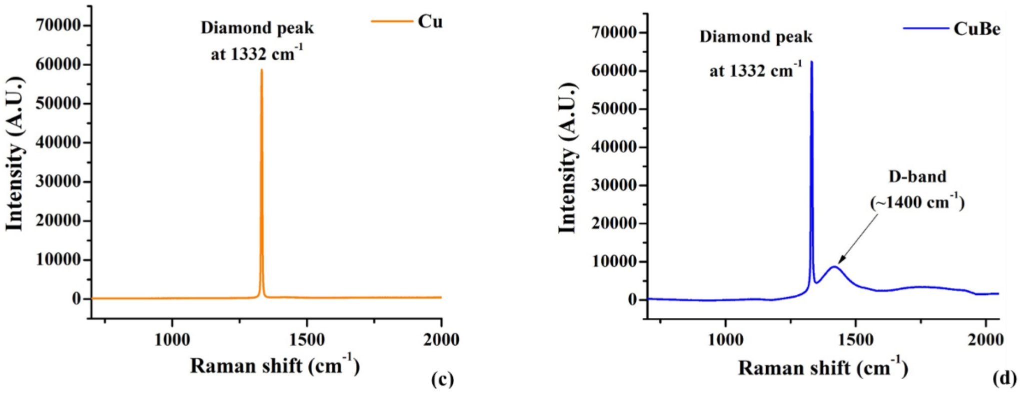

Fig. 5.4. SEM and Raman spectroscopy results on flank wear region

Based on this result, it is obvious that unlike the known (conventional) tool life curve having primary, secondary and tertiary regions, the tool used for machining CuBe exhibits only two regions. Due to this, making decision to terminate the usage of tool for further reconditioning becomes difficult.

In case of tool used on Cu, a highly smooth wear land is noticed on the flank face as shown in Fig. 5.4(a). The wear land is uniform and is symmetrical about the tool tip centre. As the tool wear rate is gradual and the observed wear land is smooth, it suggests that atom by atom attrition has taken place during machining of Cu. Thus, the type of wear observed while machining of Cu is attritious wear. Raman spectrum shows that only the sp3 peak at 1332 cm^{-1} is significant, which indicates that there are no additional phases other than the diamond present on the tool.

In case of CuBe, wear land similar to Cu is formed. It is also observed to be uniform and symmetrical. However, upon a close examination, it shows formation of some microgrooves on the wear land in the direction of cutting [Fig. 5.4(b)]. It is noticed that the pitch of the microgrooves is equal to the feed rate per revolution. Higher hardness of CuBe is responsible for the creation of microgrooves on the tool’s flank surface. This phenomenon is noticed especially in case of machining of hard materials. Zhang et al. [176] described similar type of groove formation on the flank face while diamond turning on reaction-bonded silicon carbide with feed rates of 2 and 5 μm/rev. Similar phenomenon was also noticed by Li et al. [177] and Yan et al. [98].

Raman spectroscopy on the flank surfaces of the diamond tools show that two phases are present on the worn-out region as shown in Fig. 5.4(d): One represents diamond i.e. sp3 peak (1332 cm^{-1}) and the second one occurs at 1350-1420 cm^{-1}, which denotes structural alteration in the diamond on the worn-out surface. The broad peak that occurs at around 1350-1420 cm^{-1} denotes D-band. The D-band is a disordered state of graphite, which reflects the degradation of atomic structure of diamond as reported by Hodkiewicz (2010) [178]. The disordered structure in the tool edge is transpired as a result of the impacts caused by the hard particles as this particular peak was not observed in the case of Cu. Structural disorder at the cutting edge weakens the diamond tool and the subsequent abrasion becomes easier. Therefore, the wear mechanism in the case of CuBe can be established as phase transformation of diamond followed by the abrasive wear.

Fig. 5.5(a) shows the schematic of tool and workpiece interaction during cutting and their engagement leading to along the tool nose profile. Though the engagement between tool and workpiece is calculated to be ~44.72 μm [Fig. 5.5(b)], the flank wear width comes out at the termination of cutting is ~80 μm in case of CuBe. This increase in flank wear width is explained with the help of schematic as shown in Fig. 5.5(c-h). Fig. 5.5(c) and (f) shows the schematic of cutting when the diamond tool is sharp and tool nose is round and maximum uncut chip thickness is achieved. As the tool wear takes place, tool edge gets blunt and round nose engaged with the workpiece gets flattened. Due to this, the chip thickness reduces and the contact area of the tool gets increased as shown in Fig. 5.5(d) and (g). As the tool wear out more, the flat portion of the tool nose increases further and tool becomes so blunt that the chip formation does not take place [see Fig. 5.5(e) and (h)].

The tool workpiece interaction in diamond turning causes two effect on the tool: (1) it degrades the tool edge radius which decreases the a/r ratio during machining; (2) It causes the wear on the flank face of the tool. Both of these effects tend to affect the cutting mechanism. With a decrease in a/r ratio, shearing region in the chip profile diminishes, ploughing region gets shifted and the sliding region gets enlarged. Similarly, with an increase in flank wear, sliding region increases, and shearing region contracts.

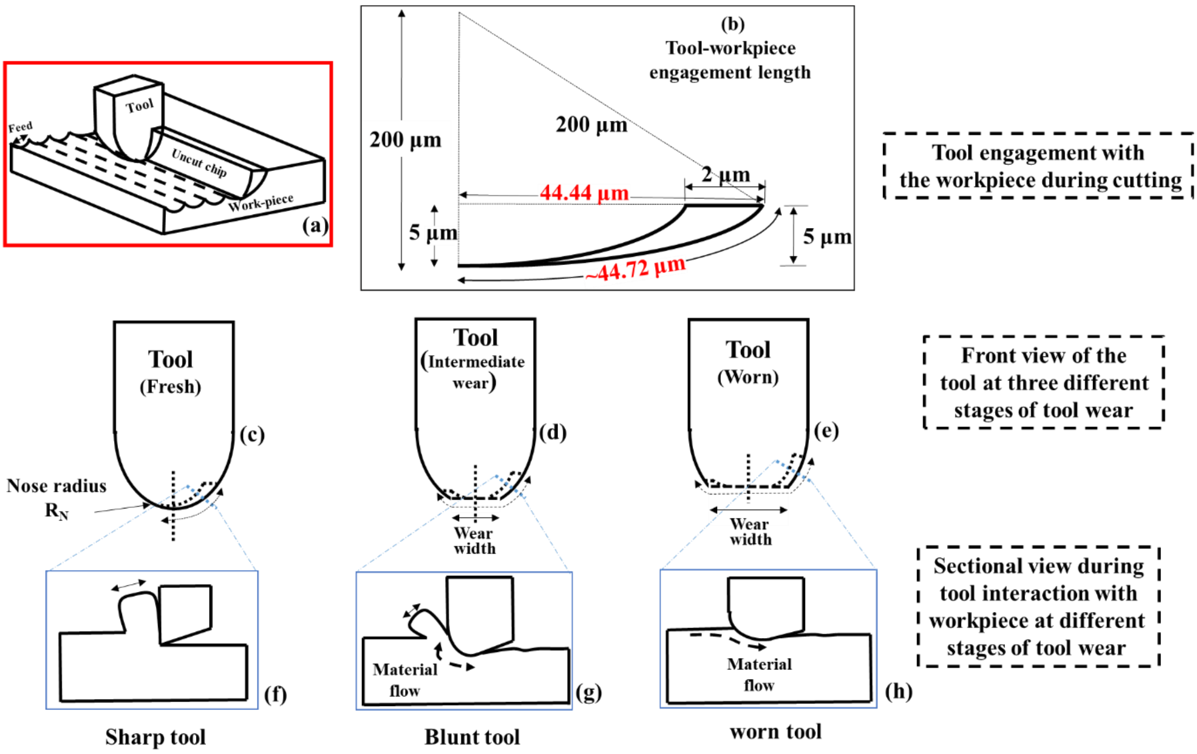

Fig. 5.5. Variation stages of tool wear

5.4. Discussion on tool wear mechanism

5.4.1. Wear mechanism of diamond tool

The earlier study carried out by Wada et al. [123] on diamond turning of homogeneous and heterogeneous materials showed that attritious wear mechanism occurs in homogeneous material (Al) leading to smooth wear pattern, while microfracture of the tool occurs in machining heterogeneous material (Nylon with filler material). Uddin et al. [125] observed a smooth wear pattern in case of homogeneous machining of single crystal Si. They used different crystallographic orientations of single crystal diamond tool for machining and observed similar patterns of tool wear on the flank surface.

Durazo-Cardenas et al. [179] explained that there exists three stages of tool wear while machining Si with the diamond tool: (i) initial attritious wear, followed by (ii) steady wear, which is followed by (iii) rapid wear. In the present study, the Cu workpiece, which is a homogeneous material like Si and Al, attritious wear mechanism occurs in three stages. However, in case of CuBe, only two stages of tool wear occur, which is a heterogeneous material: (i) initial attritious wear, followed by (ii) accelerated wear.

To understand the wear mechanism during full span of cutting, Raman spectroscopy on the Cu and CuBe machined surfaces was carried out and the results are shown in Fig. 5.6 and Fig. 5.7(a-d) respectively. In case of Cu, a small amount of sp^3 C is observed on the machined surfaces as shown at peak 1332 cm^{-1} [Fig. 5.6] which in turn indicates that diamond particles due to tool wear are present on the machined surface. In comparison to CuBe, machined Cu surface reflects very small peak which shows that only attritious wear mechanism governs the tool wear in Cu.

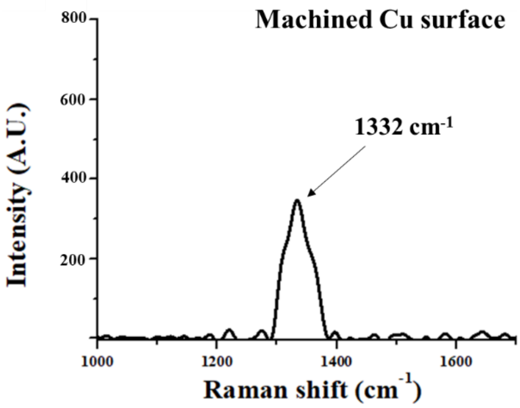

Fig. 5.6. Raman spectrum of the machined Cu surface

In the initial stages of cutting, when the tool edge is sharp, the machined surface reveals a single peak corresponding to 1332 cm^{-1} [Fig. 5.7(a)]. This indicates that sharp edge is chipped off leaving a few clusters of atoms in the form of sp3 structure on the machined surface. Hung et al. [5] also observed that the hard Be inclusions caused microchipping which consequently reduced the machinability of CuBe. As the machining progresses, tool wear takes place and sharp edge of the tool becomes blunt. This leads to wear by phase transformation as revealed by another peak emerging at 1400 cm^{-1} corresponding to degenerated layer [Fig. 5.7(b)]. This peak at 1400 cm^{-1} increases with the cutting distance and becomes dominant at later stages of cutting [Fig. 5.7(c) and (d)]. Therefore, it indicates that the phase transformation of the diamond tool in later stages of cutting is the governing mechanism of tool wear.

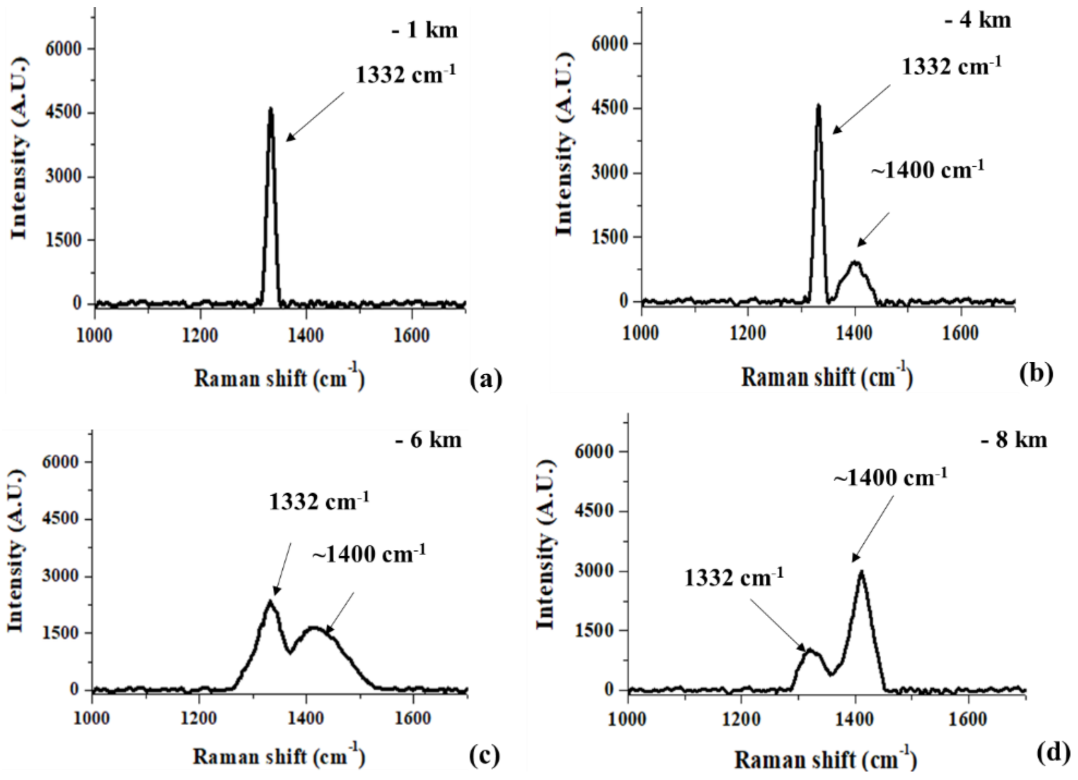

Fig. 5.7. Results of Raman spectroscopy on the machined surface

5.4.2. Influence of hard particles on tool wear

To understand the effect of hard particles on tool wear, EDS was performed on the machined surfaces. To understand the influence of tool and workpiece interaction at different locations containing Cu and Be rich phases, the results of EDS were examined carefully. During machining, wear of diamond tool results into a loss of tool material, which subsequently adheres or diffuses into the machined surface. It is observed here that the worn-out tool material adheres only on the locations of hard particles on the machined surfaces. EDS spectrum at three locations on the machined Cu surface is plotted as shown in [Fig. 5.8(a)]. Since the tool wear rate is quite small, concentration of C is too less to be detected in the spectrum at these locations. Only Cu peak is observed in the spectrum as the workpiece is 99.95% Cu (OFHC Cu).

In CuBe machined surface [Fig. 5.8(b)], at locations of Cu rich phase, only Cu is the primary element observed in the spectrum and no traces of C are found out (i.e. at location 4). However, at the location of the second phase hard particles, C exists in high atomic percentage (i.e. 15-20 % at locations 5 and 6). Since Be is reactive to C, it is likely that the formation of BeC has taken place. BeC is harder than Be (i.e. 9 on Mohs scale of hardness), therefore, the interaction of tool with BeC could cause more wear on the tool flank face. Similar observations were evident during MD simulation in Chapter 4. This phenomenon could be one of the reasons for the rapid increase of wear rate of the tool used on CuBe [Fig. 5.3].

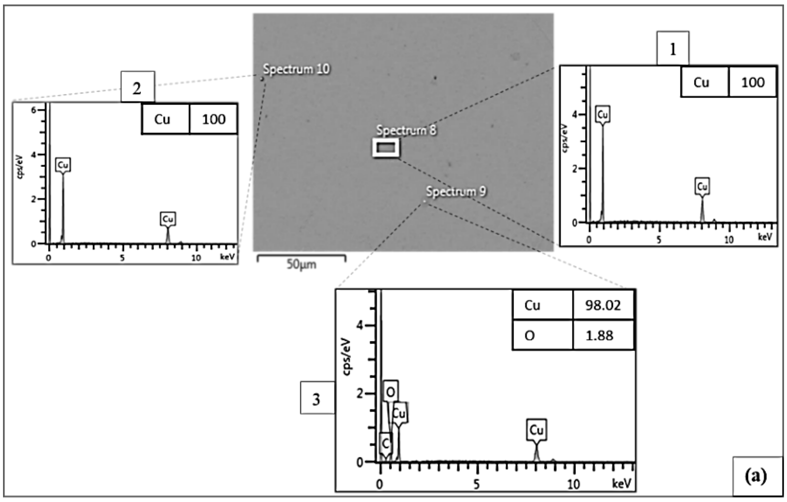

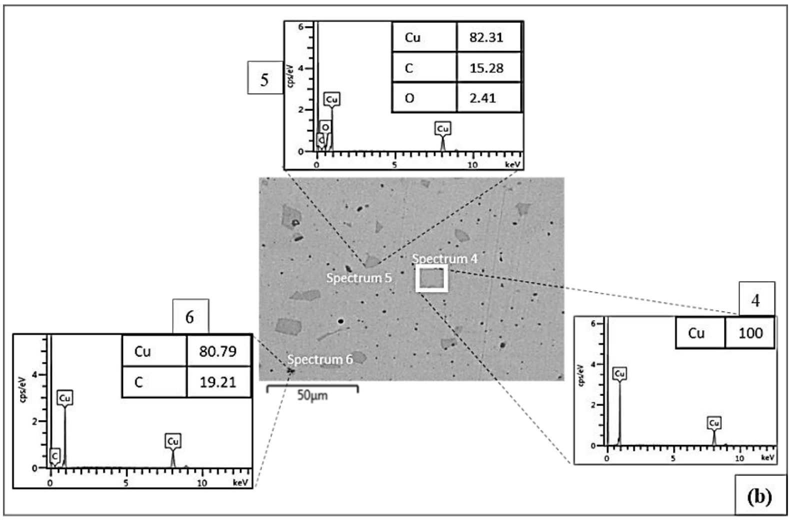

Fig. 5.8. EDS of the diamond turned Cu and CuBe surface

There is a significant difference in the concentration of C near the location of Be rich phase in CuBe. In case of Cu, there is undetectable amount of C as only Cu is visible, while there is 15-

20% of C present at hard particle locations in CuBe. In the EDS spectrum, at the hard particle locations, particularly in CuBe, accelerated the tool wear and consequent adhering of wear fragments on the location of hard particles in the machined surfaces is observed. This could be because of the hardness difference that is observed between the Be rich phase and Cu rich phase. The oxygen percentage shown in the spectrum is expected from the oxidation of Cu and Be as both are prone to oxidation (i.e. at location 6).

In the EDS spectrum, at the hard precipitate locations, particularly in CuBe, accelerated the tool wear and consequent adhering of wear fragments on the location of hard precipitates in the machined surfaces is observed. This phenomenon was also observed in the MDS. Moreover, the percentage of Carbon present at various cutting instances show wide variation [Fig. 5.9]. Initially when the chipping of the tool edge takes place, C percentage is found to be higher (~13%) than it is in the middle stage (~7%) where the tool wear rate is low. At the end of tool life, where the rapid wear takes place, the C percentage on the work surface increases to ~22%. Higher percentage of C at the end of the cutting process occurs due to the accelerated tool wear in the later phase of cutting.

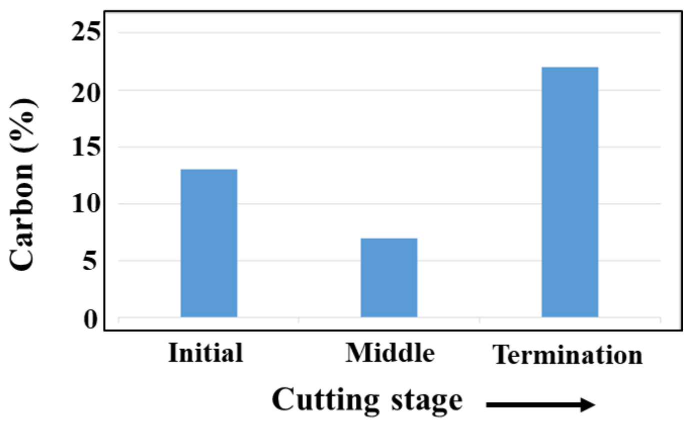

Fig. 5.9. Carbon percentage on machined surface at different cutting stages

5.4.3. Force variation with tool wear

To analyse the reasons for possible phase transformation on the tool, cutting forces viz. principal cutting forces and thrust forces were measured during the diamond turning of Cu and CuBe alloy. For measurement of forces, force dynamometer was placed under the cutting tool and forces were recorded by the data acquisition unit attached to the dynamometer sensor as shown by a schematic in Fig. 5.10.

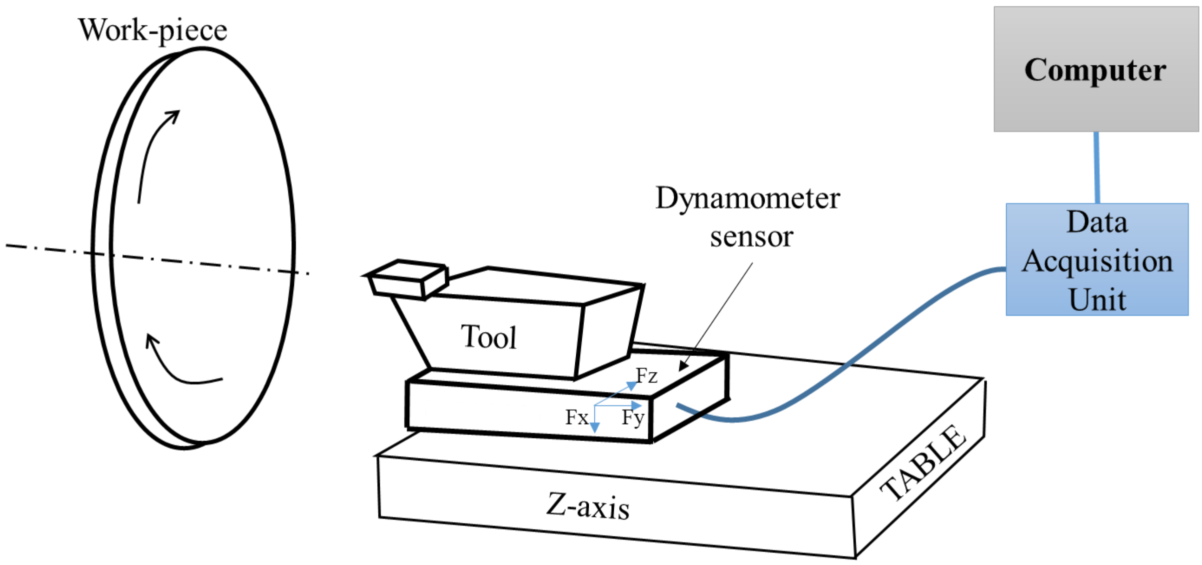

Fig. 5.10. Schematic of actual set-up with force dynamometer

Typical cutting forces plots for Cu and CuBe during initial, intermediate and final stages of tool wear are shown in Fig. 5.11(a-e) and Fig. 5.13(a-e), respectively. In addition, forces plot with respect to cutting distance for Cu and CuBe are shown in Fig. 5.12 and Fig. 5.14 respectively.

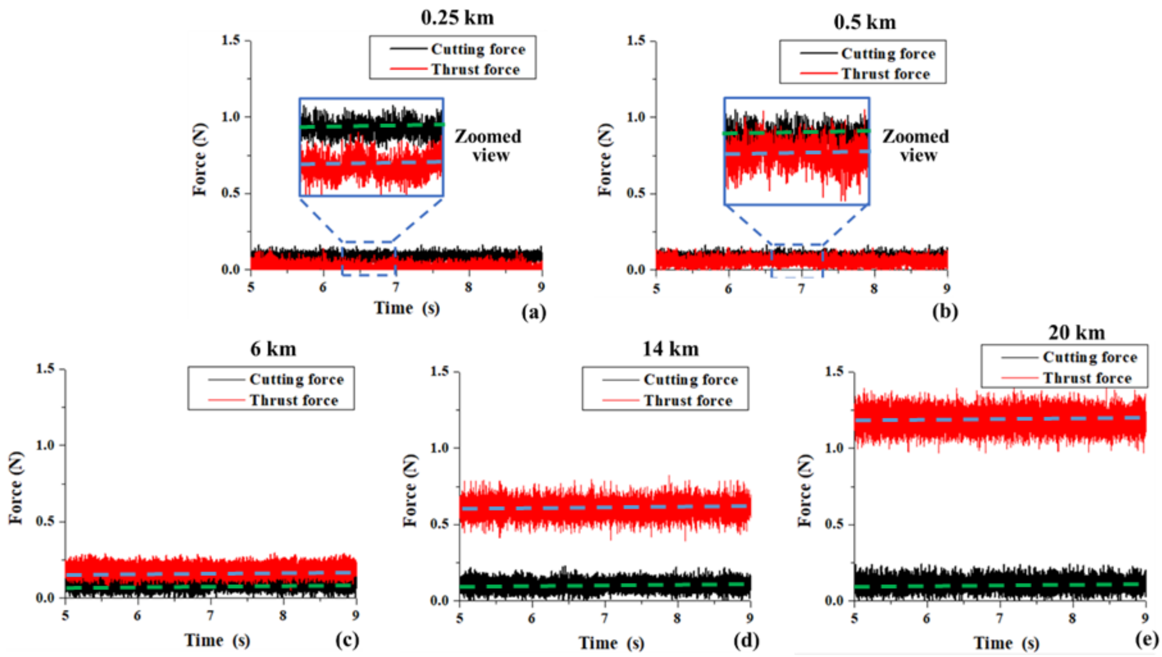

Fig. 5.11. Cutting and thrust forces during machining of Cu

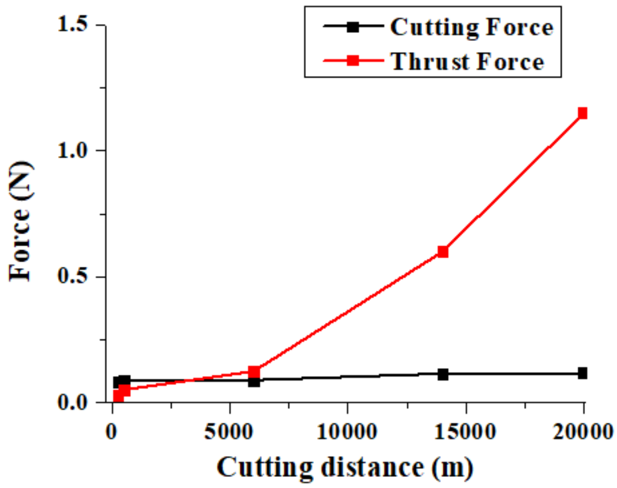

Fig. 5.12. Variation of cutting and thrust forces with the cutting distance in Cu

During diamond turning of Cu, the thrust forces vary as compared to the principal cutting forces. In the initial stages for cutting distance up to 0.5 km, where no significant wear has taken place, the thrust force (~ 0.052 N) is found to be lower in magnitude as compared to the cutting force (~ 0.087 N). This is due to the fact that the sharp cutting edge in the beginning stages experiences higher load on the rake face. As the cutting distance increases to 6 km, the corresponding flank wear length of ~1.3 µm, thrust forces (~ 0.125 N) show slightly higher amplitude than the cutting forces (~ 0.09 N).

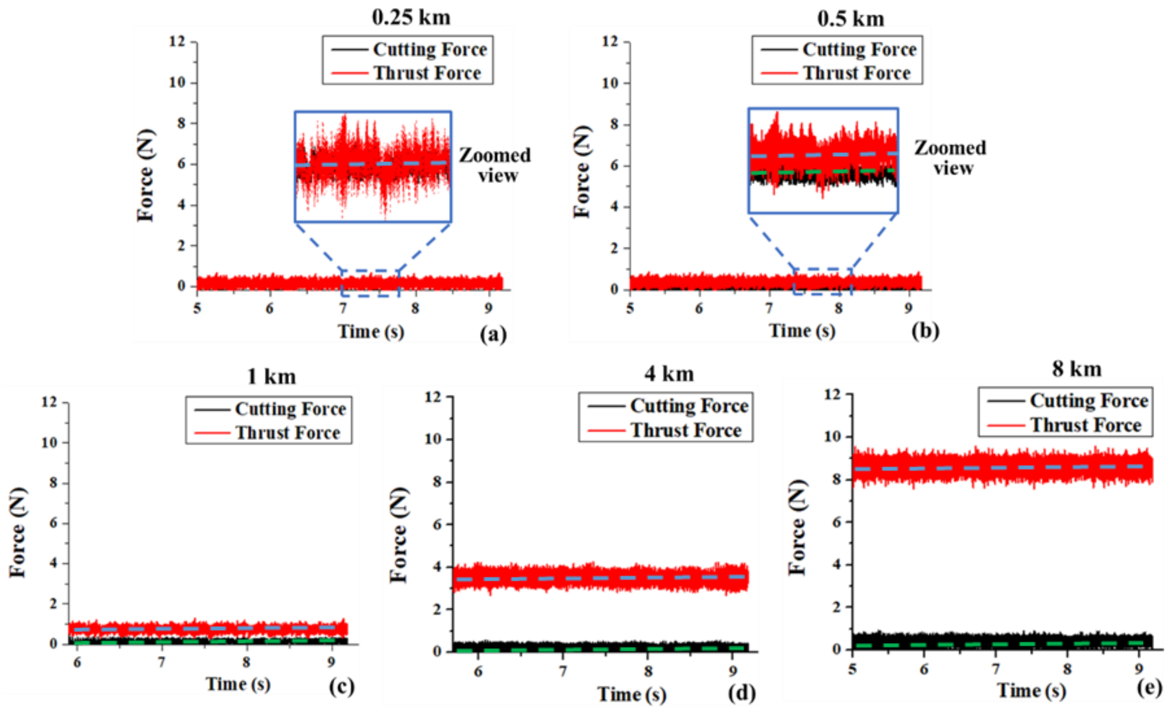

Fig. 5.13. Cutting and thrust forces during machining of CuBe

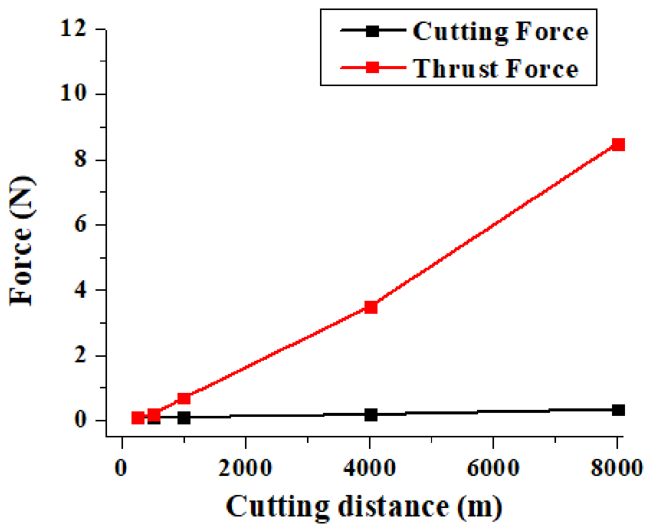

Fig. 5.14. Variation of cutting and thrust forces with the cutting distance in CuBe

This is due to the fact that an increasing wear area has a tendency to receive higher reaction force from the workpiece material beneath the tool flank face. At the end of the cutting, for a flank wear length of ~12.8 μm, thrust forces (~ 1.15 N) are observed to be much higher than the cutting forces (~ 0.113 N) due to large flank wear area.

In case of CuBe, the thrust forces (~ 0.11 N) are comparable to the principal cutting forces (~ 0.13 N) in the initial phases of cutting for a cutting distances of 0.5 km. A large thrust force is observed due to the fact that higher hardness of CuBe causes higher normal reaction on the tool. As the cutting distances increases up to 1 km, the thrust forces (~ 0.7 N) significantly increase, whereas the cutting forces remain approximately the same (~ 0.12 N). For a cutting distance of 4 km and the flank wear length of ~2 μm, the thrust forces increase to ~ 3.5 N.

At the final stages of cutting distance of 8 km corresponding to flank wear length of ~13.8 μm, the thrust forces while machining CuBe reach as high as to ~8.5 N. On comparing the forces of Cu and CuBe, it is observed that the magnitude of the forces is large in case of CuBe. In addition, the thrust force is quite significant in case of CuBe over the entire cutting distance whereas, in case of Cu, the principal cutting force is marginally higher at the initial stage and later the thrust force becomes dominant. While for Cu, the previous researches also showed attrition as dominant wear mechanism [180], the tool wear mechanism in cutting of CuBe needs further explanation. In diamond turning, chip profile varies from zero to some maximum value of uncut chip thickness depending upon the feed rate [Fig. 5.15].

For the parameters used in the current study, maximum uncut chip thickness is calculated to be ~ 0.447 μm. From the schematic, it is realized that the cutting edge radius (r) changes as the tool wear occurs while the maximum uncut chip thickness (a) remains constant. The value of the cutting edge radius (r) is 200 nm in the beginning of cutting and 1.82 μm at the end, that means the a/r ratio in the beginning is ~2.24 and ~0.245 at the end. The cutting process continues till the chip formation takes place. The chip forms until the a/r ratio approaches to ~ 0.25 as revealed by previous researches [76,181].

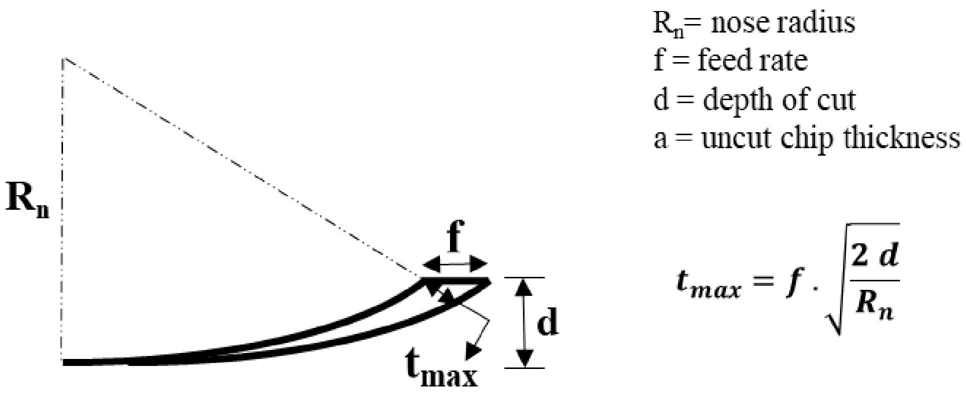

Fig. 5.15. Maximum uncut chip thickness along the chip profile

These forces, when act in a very small cutting zone, leads to large amount of stresses which in turn causes tool wear. In addition, there exists a high interface temperature in conjunction with large stresses. Some of the earlier studies suggest that the temperature during diamond turning rises to 1000 K [182] [183]. Some of the studies have reported temperature in the range of 600-800 K [113] [129]. Nevertheless, MD simulations carried out for different a/r ratio varying from 0.25 to 20 in Chapter 4 suggest that high stresses (~ of the order of 150 GPa) and temperature (~ of the order of 650 K) are the primary causes of tool wear.

The high temperature provides the conducive atmosphere to transform the diamond (sp^3 phase) to another phase (amorphous) on the tool surface, with sufficiently high stresses. Therefore, it is transpired that the tool wear mechanism in CuBe, which takes place by phase transformation depends on stress as well as temperature during the diamond turning process, which is reported through the results of MDS [Fig. 4.28 (a) and (b)].

5.5. Determination of tool wear constants from a known wear model

The tool wear in diamond turning of CuBe involves chemical phase transformation which suggests that the wear behaviour can be very well described by the Arrhenius equation based model. Calculation of constants in tool wear expression will lead to the determination of extent of interactions between diamond and CuBe. Literature reports these tool wear constants for diamond tool and iron workpiece material combinations [175].

In the formulation, while the tool wear is known experimentally with respect to cutting distance, stresses and temperature are difficult to find out experimentally. The stress and temperature values are taken from MDS carried out in Chapter 4. However, the MDS was carried out at various a/r ratios which do not indicate cutting distances specifically. Since the stress and temperature values are computed for different a/r ratio through simulation, the flank wear lengths obtained experimentally are plotted with respect to a/r ratio. It will enable to calculate the coefficients from the wear formulation.

As the edge radius is not measured experimentally at intermittent cutting distances during cutting operation, first the tool edge radius is determined with the corresponding cutting distance or tool wear. It is assumed that the tool wear and edge radius varies proportionally during cutting. Since the initial edge sharpness and wear for whole cutting span is known, intermediate edge radii corresponding to any tool wear can be computed assuming it is linear. Fig. 5.16 (a) and (b) show the AFM results of cutting edge radius of fresh and worn tool after usage. For a fresh tool, it is 200 nm and for a worn tool, it is measured to be 1.82 μm. The wear values at these two points are known from the results of diamond turning experiments carried out in section 5.3.1.

The edge radius increases proportionally to tool flank wear and here it is assumed to be linear, which can be expressed as: $r = r_o + kW$; where, r_o is edge sharpness of fresh tool, k is constant or slope of proportionality and W is flank wear length in microns. k can be expresses as: $k = (r_f - r_o) / (w_f - w_o)$; r_f and w_f are final edge radius of worn tool and flank wear length at the end of cutting (i.e. w_f =13.8 μm) respectively.

K is found out to be 0.117. The edge radius for each wear value can be obtained from the plot shown in Fig. 5.16(c) which was generated through two end conditions of cutting edge radius and flank wear respectively.

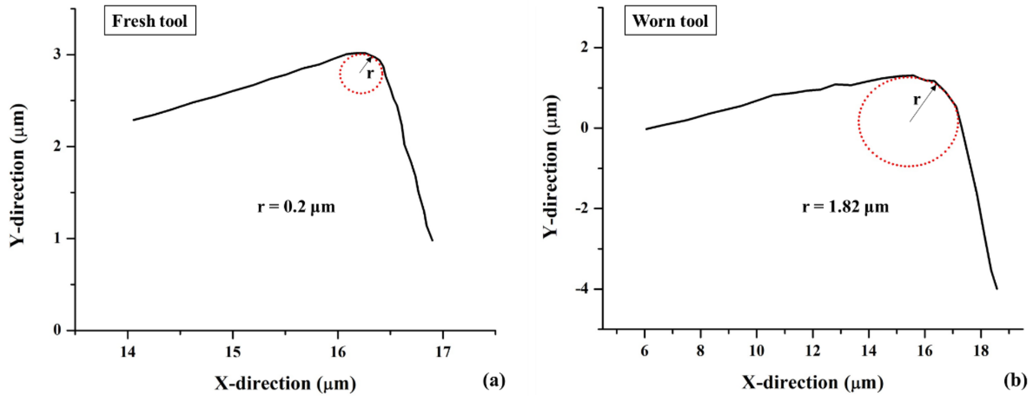

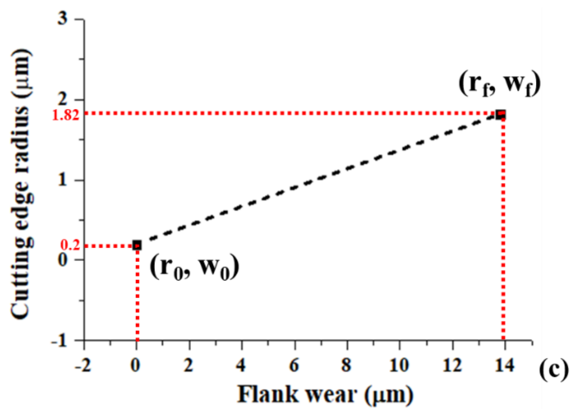

Fig. 5.16. Measurement of cutting edge radius

The flow chart for the determination of tool wear constants is shown in Fig. 5.17. The edge sharpness is determined at certain cutting distances. Based on the values of computed cutting edge sharpness ‘r’ and constant uncut chip thickness ‘a’, a/r can be calculated for each intermittent cutting distances.

Subsequently, flank wear is plotted with respect to a/r ratio as shown in Fig. 5.18. This is done in order to calculate the stress and temperature at certain a/r ratios, which were calculated from simulation results conducted in Chapter 4. To calculate the wear coefficients, following formulation is used [175]:

$$\frac{dW}{ds} = A.\sigma_{eq}\,.\;exp\left(\frac{-B}{T}\right) \tag{5.1}$$

Where, A and B are constants, σ_{eq} is equivalent stress, v_c is cutting speed. s is cutting distance and T is interface temperature. The values of the constants A and B are calculated from the MDS data of stress and temperature.

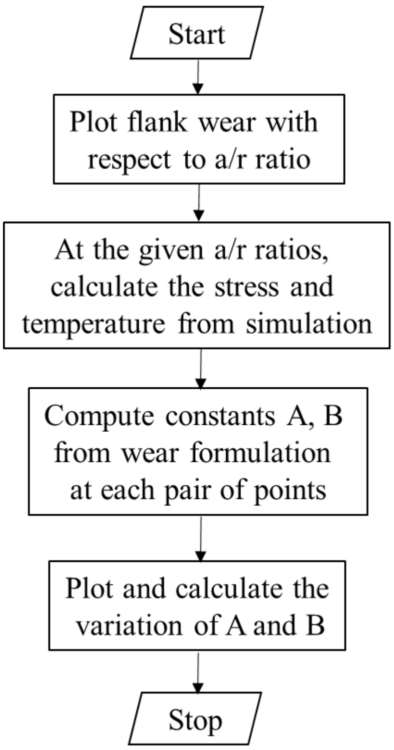

Fig. 5.17. Flowchart for quantifying the wear model constants for full span of tool life

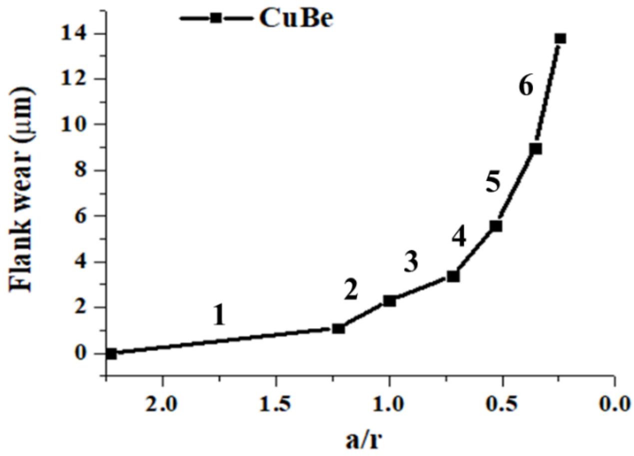

Fig. 5.18. Variation of tool flank wear with respect to a/r

Since the tool edge in the beginning was sharp (i.e. edge radius ~200 nm) and at the end of tool life, it got blunt (i.e. flank wear length ~14 µm and edge radius ~1.82 µm), MD simulations data were utilized with different computed cutting edge sharpness values from sharp to blunt edge to calculate stresses and temperature. The wear plot is divided into 6 intervals with 7 points. For each pair on wear (i.e. 6 intervals for 7 points), the constants were calculated and they are plotted as shown in Fig. 5.19.

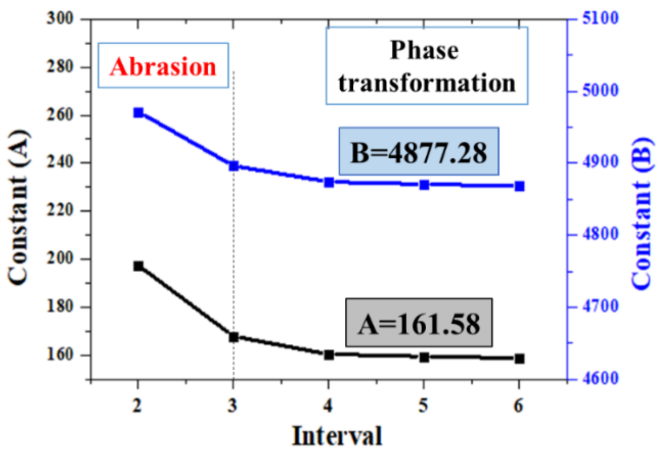

Fig. 5.19. Variation of A and B

The wear constants are plotted with respect to the interval. 1st interval is not shown as there is no initial wear for a fresh tool. It is observed that both the constants do not vary much beyond the interval 3. There is less than 6 % variation beyond interval 3, however, before interval 3, there is a variation of more than 20%. This is due to the fact that the wear model, from which the constants are evaluated, is based upon Arrhenius equation which describes chemical interaction. The present study on tool wear reveals that in the initial stages there is abrasion of diamond which is a mechanical interaction, whereas, in later stages, there is phase transformation of the diamond which is a chemical interaction. The average values of A and B are found out to be ~161.58 GPa^{-1} and ~4877.28 K respectively. B describes the activation energy E_a as $B = E_a/R$; where, R is universal gas constant. The activation energy E_a comes out to be 40.55 KJ/mol.

Table 5.4 lists the wear constants and activation energy for diamond turned CuBe and iron (Fe). The available values for A and B for Diamond-Fe combination are 310 and 3006.976 K (i.e. E_a =25 KJ/mol) respectively [175], which is a worst combination of tool and workpiece in terms of tool wear. This shows that the activation energy decides the extent of tool wear. Lesser is activation energy, more tool wear is likely. The constant 'A' gives the frequency of interactions which lead to tool wear. Therefore, higher the value of A, more will be the tool wear. These constants can be used to predict the wear rate while machining CuBe with a single crystal diamond tool and can be used for many applications including tool path compensation technique.

Table 5.4. Wear constants and activation energy for diamond turned CuBe and Fe

Material	A	B	E_a (KJ/mol)
CuBe	161.58	4877.28	40.55
Fe	310	3006.976	25

5.6. Summary

Tool wear has been one of the critical issues since the ultraprecision diamond turning came into prominence as it reduces not only the machining efficiency but also degrades the quality of machined surfaces. Wear mechanisms play a major role in tool life and in turn machining cost and efficiency. CuBe is an extensively used alloy and it causes extensive wear on the tool edge. Therefore, after investigating the tool wear mechanisms for nanocutting of CuBe by single crystal diamond tool based on different characterization techniques, following conclusions are drawn:

1. In case of Cu, attritious wear mechanism is dominant while in case of CuBe, abrasive wear by the micro-chipping at the tool edge in the initial phase (i.e. region 1 of tool life) and phase transformation in the tool edge during the second region of machining (i.e. region 2 of tool life) is the governing wear mechanism.
2. Smooth wear pattern and micro-grooved pattern while machining Cu and CuBe respectively are noticed on the flank wear land.
3. Hard precipitates in CuBe affect the tool wear rate during machining of CuBe. Tool wear is observed to be significantly higher in case of CuBe machining. Tool life on CuBe is found to be 40 % of the tool life in case of Cu.
4. The magnitude of average cutting force on Cu and CuBe are comparable whereas thrust force on CuBe is much higher in case of CuBe. In both cases of Cu and CuBe, thrust force increases with cutting distance.
5. The constants of a tool wear model i.e. A and B, are determined for diamond tool and CuBe combination during diamond turning.

6. Unlike the known (conventional) tool life curve having primary, secondary and tertiary regions, the tool used for machining CuBe exhibits only two regions. Due to this, making decision to terminate the usage of tool for further reconditioning becomes difficult.

The consequences of tool wear are reflected on the machined surface in the form of degradation in surface finish, cutting forces, surface contamination and various other surface properties. To study these aspects, experimental study on the diamond turned Cu and Cue section is carried out in Chapter 6.

Chapter 6

Analysis of roughness, lay pattern and chemical contamination of diamond turned surface

6.1. Introduction

The quality of surface generated during diamond turning process is influenced by a number of factors which include tool geometry, feed rate, depth of cut, cutting speed, machine tool vibrations, spindle error motions, work material properties and tool-workpiece relative vibrations [184]. These are generally categorized under process and material factors. The process factors include the cutting parameters viz. cutting speed, feed rate, depth of cut and tool geometry. This also comprises of tool and workpiece vibrations. Whereas the material factors consist of material anisotropy, material inhomogeneities and the crystallographic orientation of the workpiece materials. A better understanding of these factors and their interaction which influence the surface generation, is essential for high quality surface generation and for better tool life. Tool quality is a major influencing parameter in the course of diamond turning, which gets deteriorated with the machining process and in turn affects the quality of the generated surface. The tool and workpiece interaction while machining CuBe affects the surface quality in terms of surface roughness and morphology of the machined surface. With the increase in cutting distance, owing to deteriorating tool edge condition, the machined surface undergoes physical, chemical and metallurgical transformations.

This chapter presents the details of the experimental study and the analysis of diamond turned CuBe surfaces generated for a full span of cutting tool life. Since CuBe is a heterogeneous material, presence of hard particles affect the cutting mechanism as well. Hence, in order to observe the material removal mechanism, its effect on the generated surface as well as the effect of hard particle on the surface quality, Molecular Dynamic Simulation (MDS), and to verify the MDS results to possible extent, experiments of nanoscale cutting of Cu and CuBe with diamond tools were conducted. Generated surface quality gets gradually degraded both physically and chemically during the entire cutting process for a full life span of diamond tool. The chapter is divided into various sections and is presented in the following sequence.

- The methodology for the experimentation and characterization.
- Mechanism of surface generation and cutting mechanism.
- FFT spectrum of the surface roughness profile to analyse the tool workpiece interaction.
- MD simulation study results to reveal the effect of hard particle on lay pattern.
- Surface contamination characterized by EDS, Raman and X-ray photoelectron spectroscopy.
- Characterizing for mechanical and optical properties of diamond turned surface.

6.2. Approach to the investigation on diamond turned surface

Fig. 6.1 shows schematically the influence of tool and workpiece interactions on the surface quality during diamond turning.

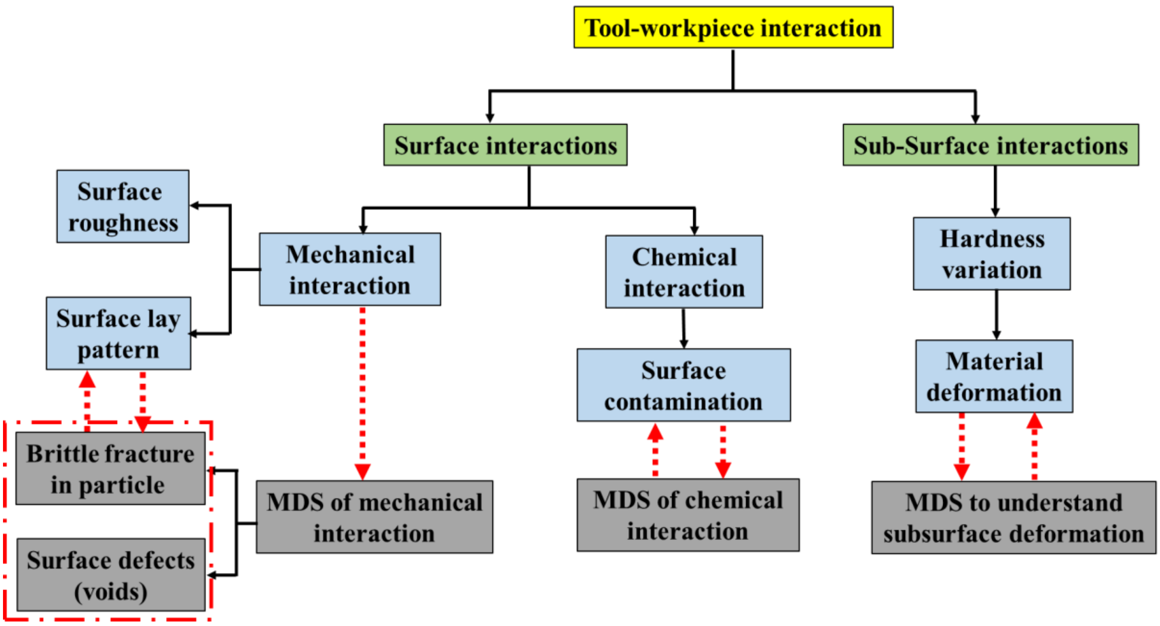

Fig. 6.1. Schematic of tool-workpiece interaction effects on the surface quality

Tool and workpiece interaction affects the surface as well as subsurface. During the cutting process, tool and workpiece interact mechanically as well as chemically on the work surface. Mechanical interaction leads to the material removal which in turn results in surface generation. The generated surface morphology is composed of surface lay pattern and defects. Surface morphology is dependent on the choice of workpiece material and its interaction with the tool as a function of tool edge condition. The tool edge sharpness varies during the course of the cutting process which also affects the tool and workpiece interaction. In addition, there are chemical interactions that occur on the surface. During the cutting process, as the tool wears, the wear particles tend to contaminate the machined surface and may affect the surface properties due to alteration of chemical characteristics on the surface. Besides the surface interactions, there are subsurface phenomenon which take place during the cutting process. These subsurface phenomenon occur due to material deformation underneath the machined surface. This deformation in turn leads to variation in hardness. All these interaction effects may lead to the degradation in the functional performance of the diamond surface. Since all these phenomenon are taking place at nanoscale, therefore, the mechanisms of mechanical, chemical and subsurface interactions are explained by Molecular dynamics simulation.

Comparative experiments of diamond turning on Cu and CuBe workpiece materials for entire span of tool life are performed as described in Section 5.2.2 and simulations at nanoscale are carried out to understand tool and workpiece interaction on surface as well as subsurface. There are basically four aspects related to the investigation on diamond turned surface:

1) Experimental investigation on the mechanical interactions of tool and workpiece and their effect on surface quality in terms of surface roughness and surface morphology which includes lay pattern and surface defects

2) Experimental investigation on the chemical interactions between the tool and the machined surface that cause surface contamination
3) Experimental investigation on the subsurface deformation that causes increase in hardness of subsurface layers
4) Mechanism of mechanical, chemical and subsurface interactions by MD simulations to investigate the underlying mechanisms

Experiments on Cu and CuBe workpiece materials were performed to study the achieved surface quality for a full span of tool life. To investigate the effect of physical interaction on the surface, surface profiler (Contact surface profiler of Taylor Hobson Make with 0.8 nm vertical resolution), FFT, optical microscopy (Make: Dino-lite digital microscope of 200 X magnification), and Scanning electron microscopic (SEM) (Make: Zeiss of 1 nm resolution), techniques were used. On the other hand, to investigate the compositional/chemical changes on the surface, Raman spectroscopy (Make : Horiba Jobin Yvon, France) having spot size of 1 μm and ~0.4 cm-1 resolution in Raman shift), and X-ray photo spectroscopy (Make: ULVAC; Model: PHIPHI5000, Versa Probe II ; Specs: X-ray beam diameter: < 10 μm to 200 μm ; Ion beam energies: 5eV to 5keV) techniques were used.

Fig. 6.2 shows the schematics of the investigation carried out on the surface generation. The schematic of the diamond turning process is presented in Fig. 6.2(a), where the tool and workpiece move relative to each other and work material corresponding to few microns feed and depth of cut is removed as chip. The relative motion of tool and workpiece in the specified path generate the desired surface; and the quality of the machined surface depends on various factors like process parameters, machine tool condition, cutting tool inaccuracies, workpiece material properties and interaction between tool and workpiece etc.

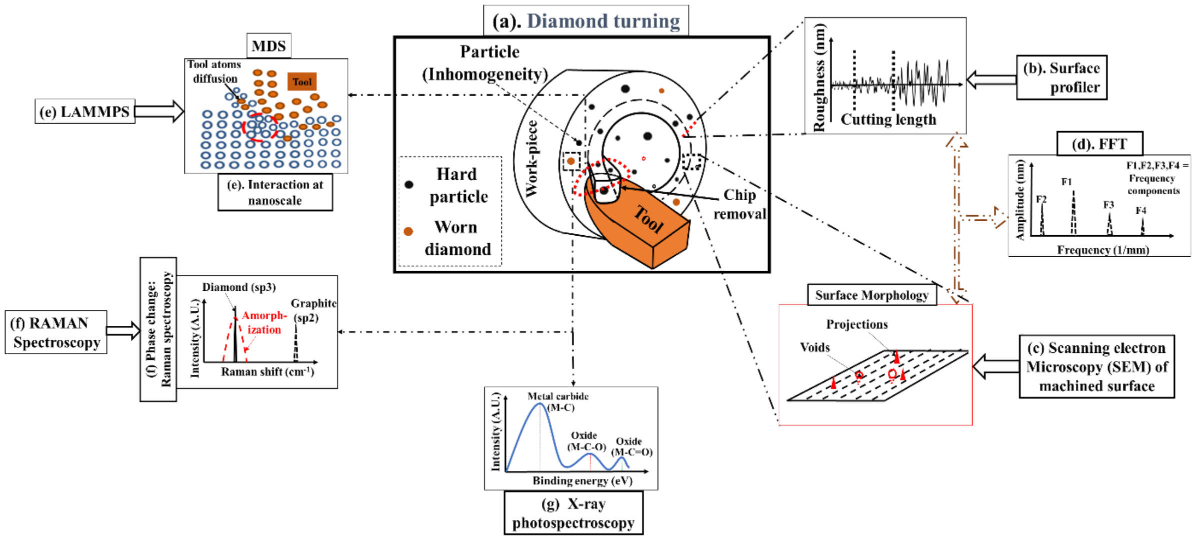

Fig. 6.2. Schematic of surface characterization techniques

For a given set of process parameters and machine tool, the effect of tool and work material combination on the surface quality needs to be studied and understood. Since machining of Cu and CuBe workpiece materials with the diamond tool are studied here, the factor which affects the surface quality is mainly inhomogeneities present in the workpiece in the form of hard particles. To address the issue of surface quality, surface roughness was measured with the help of roughness profiler [Fig. 6.2(b)] and SEM was performed to examine the surface morphology [Fig. 6.2(c)]. On the machined surface, FFT spectrum analysis was carried out with the help of MATLAB [Fig. 6.2(d)] to understand the behavior of surface profile with respect to cutting distance. MD simulation was conducted to analyze the behavior of hard particles on the machined surface as well as the cutting process [Fig. 6.2(e)]. Furthermore, surface contamination in the form of transfer of tool material to the machined surfaces in different forms was analyzed with the help of Laser micro-Raman spectroscopy [Fig. 6.2(f)]. In addition, XPS was carried out on the machined surfaces to observe the chemical contamination as well as the bonding states of tool and workpiece materials [Fig. 6.2(g)]. Prior to XPS operation, the samples were cleaned properly and subsequently sputtered with Argon ions at 300 eV, 10 mA for 600 s to eliminate any atmospheric pollutants on the surfaces present. The methodology is similar as mentioned in Section 5.2.2. Surface characterization and analysis were carried out on the same experimental samples used for studying tool wear.

6.3. Mechanism of surface generation: Results and Discussion

The presence of inhomogeneities in the Be particles affects the machining process mechanically/physically as well as chemically. Accordingly, this section is divided into two sub-sections: (i) mechanical and (ii) chemical interaction of tool-workpiece as described below:

6.3.1. Mechanical interaction between the tool and workpiece

The mechanical effect of the tool on the workpiece surface primarily appears as the surface roughness and morphological effects on the surface in terms of physical defects like surface lay pattern, voids and cracks. The simultaneous effect on the tool manifests as wear on its flank surface.

6.3.1.1. Variation of surface roughness with respect to cutting distance

Fig. 6.3(a) shows the variation of average surface roughness values with respect to cutting distance for both Cu and CuBe respectively. Life of each diamond tool was different for these two materials and hence traversed unequal cutting distance i.e. 20 km for Cu and 8 km for CuBe. The tools were used even after they have crossed the secondary region in the tool wear graph and ceased to be useful for further cutting. Average roughness values (Ra) of the machined surfaces of both the materials were found to be varying nonlinearly as the cutting distance is increased. However, there was a significant variation in the trends of surface roughness of both the materials. It is observed that the behaviour of surface roughness plot for both Cu and CuBe is similar to that of their tool wear behaviour. Thus, surface finish degradation is dependent on the tool edge condition.

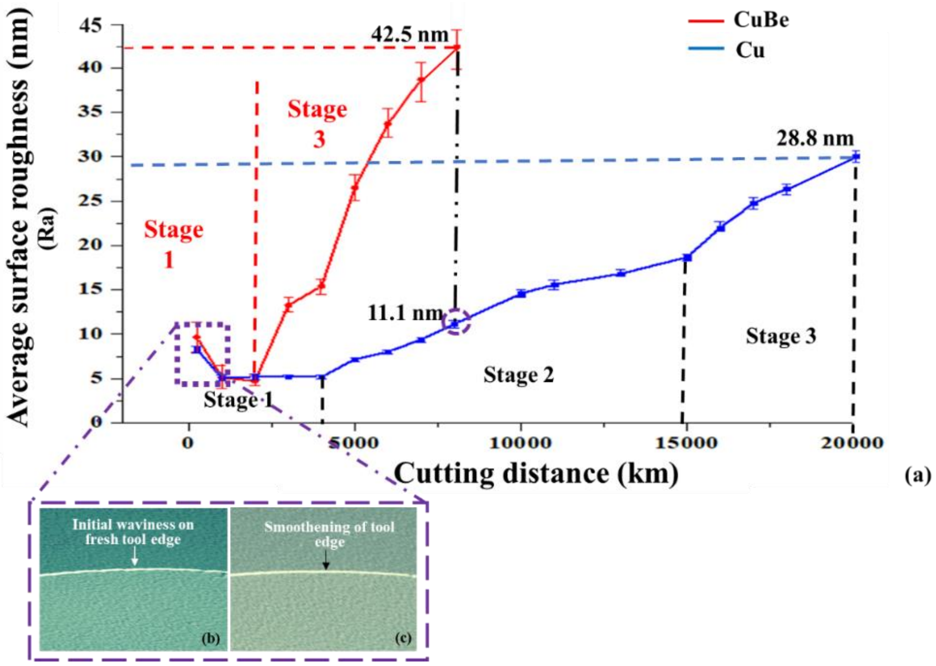

Fig. 6.3. Variation of surface roughness with cutting distance

In case of Cu, surface roughness plot shows three distinct stages: Stage 1 shows decrease in surface roughness values; stage 2 displays gradual increase of surface roughness; and stage 3 involves rapid increase in surface roughness. In the stage 1, improvement in surface roughness takes place up to a cutting distance of approximately 4 km. First surface roughness value decreases till the cutting distance of 500 m and then gets stabilised up to a cutting distance of 4 km. In the stage 2, the roughness plot shows an increasing slope at an almost constant rate up to a distance of approximately 15 km. The constant rate of increase in surface roughness value occurs due to the gradual wear of the tool with respect to increasing cutting distance. At the end of stage 3, when chips cease to form, increase in surface roughness was significantly higher. At the end of the cutting cycle, the surface roughness obtained was 28.8 nm which is approx. 5 times more than the best surface finish value achieved with this tool. This is due to continuous and rapid degradation of the tool. On the other hand, diamond turned CuBe surface has shown a rapid change in surface roughness value curve than that of Cu surface. Surface roughness improves from 10 nm to 4 nm up to the cutting distance of 2 km in stage 1 and then increases abruptly. Stage 2 is not marked for CuBe as there is abrupt increase in the roughness value slope. Surface roughness obtained at the end of cutting cycle is 42.5 nm which is observed to be approximately 8 times of the best surface finish value achieved with this tool.

Upon examination of both the plots together, the initial improvement in surface roughness values of both Cu and CuBe is attributed to the smoothening of cutting edge inaccuracies present in the form of micro irregularities as highlighted in Fig. 6.3(b) and (c).

Fresh edge of the tool contains some irregularities due to manufacturing limitations for the diamond tool which are chipped off or gradually removed during machining. In case of Cu, these irregularities are gradually removed from the diamond tool by atom by atom attrition during the interaction with the workpiece. As it happens gradually, the distance covered in Cu for edge smoothening is more as compared to CuBe where the initial waviness irregularities are chipped off owing to its higher hardness. The comparison of both the curves shows that there is a very close match of surface roughness till the cutting distance of 2 km, where the initial improvement in surface roughness has taken place. Subsequently, it is observed that the CuBe workpiece has shown a rapid increase in surface roughness value. Further in Cu, stage 1 is sustained for longer cutting distance in comparison to CuBe. Surface roughness in case of CuBe at the cutting distance corresponding to its tool life is approximately 4 times higher than that of Cu after covering the same cutting distance. It is also observed that the maximum percentage variation of surface roughness values for three machining trials at the end of cutting was more in case of diamond turning on CuBe as compared to that of Cu. In case of CuBe, it is ~12.5 %, whereas, in Cu, it is ~9%. Higher variation in case of CuBe is due to the heterogeneous nature of CuBe workpiece.

The cutting process in CuBe is disrupted by the presence of the hard particles which leads to sudden impact loads on the tool edge. This tool gets worn out quickly which in turn affects the surface finish significantly. Once tool edge becomes blunt and wear land increases, particles start interfering more and more with the tool. The worn out tool subsequently increases the surface roughness value rapidly as marked by stage 3. In comparison, it is seen that when the cutting process is terminated there is an increase of ~48 % in surface roughness as compared to Cu.

6.3.1.2 Characteristics of Cu and CuBe machined surface

Since there is a substantial difference in surface roughness, it is anticipated that there would be a significant difference in the surface morphology of both the materials. Therefore, SEM results of the surface morphology shown in Fig. 6.4(a) and (b) were analysed. Diamond turned Cu surface results into the smooth surface as shown in Fig. 6.4(a). This shows a deterministic pattern on the machined Cu surface. As diamond turning is a deterministic process, it is obvious that the machined surface is generated with a lay pattern which is dominated by feed marks. The generated surface is smooth which signifies that the ductile cutting has taken place while machining homogeneous Cu workpiece.

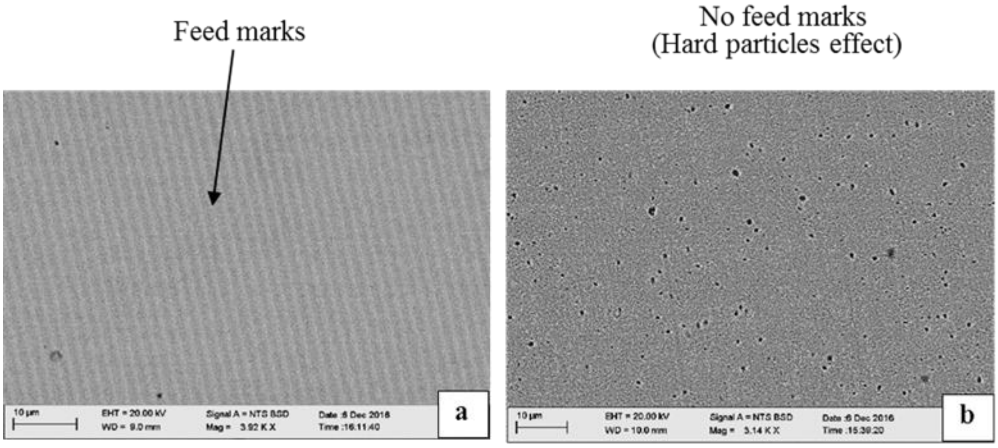

Fig. 6.4. SEM image of Cu and CuBe diamond turned surface

However, the diamond turning of CuBe workpiece reveals different results. It is noticed that the CuBe machined surface is devoid of any lay pattern as shown in Fig. 6.4(b). The presence of particles has modified the lay pattern in CuBe workpiece. The generated surface is dominated by the voids created due to the dislodgements of hard particles. Material removal in OFHC Cu takes place through only ductile cutting. Whereas it occurs in CuBe through (i) ductile machining in Cu (ii) either dislodgements or brittle machining of hard precipitates. MD results for both Cu and CuBe in Chapter 4 has confirmed this aspect. The behaviour of the hard particle during machining and its influence on the surface generation depends on the size, position and distribution of the particle with reference to cutting plane and the cutting depth. Fig. 6.5(a) shows the machined CuBe surface at initial stage of cutting where a lot of dislodgements of the precipitates occur on the surface

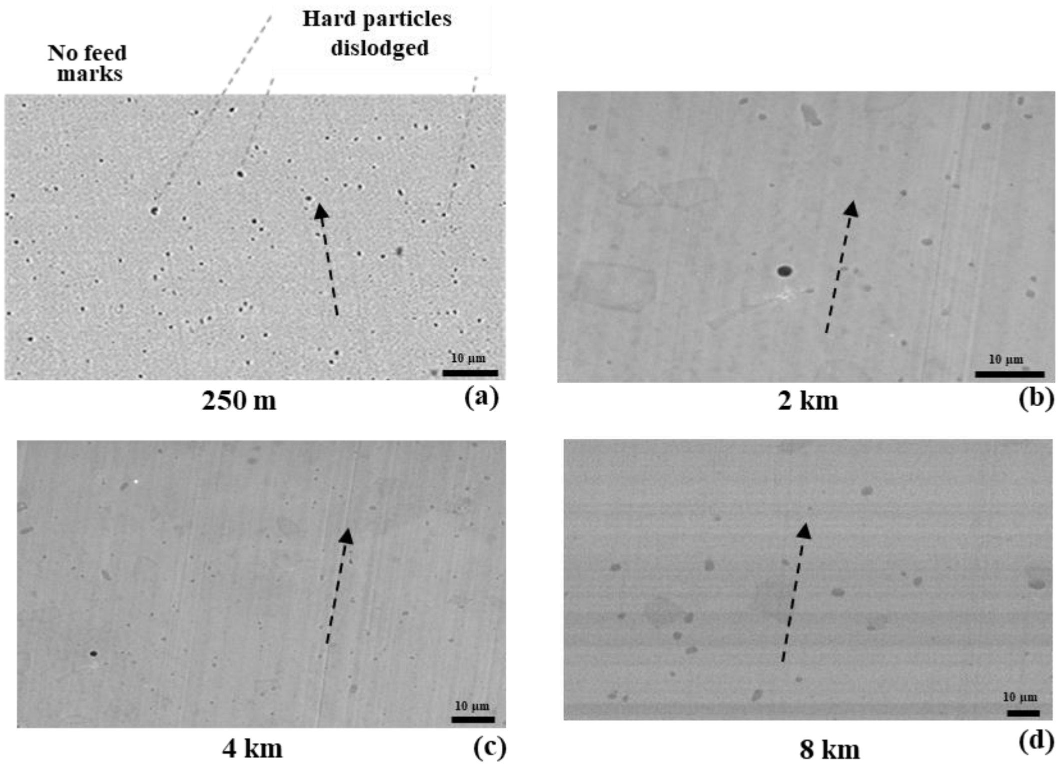

Fig. 6.5. Suppression of deterministic lay pattern

. Initially the tool edge is sharp and many of the precipitates appear to be bigger than the edge radius value. When the precipitate size is large as compared to the cutting edge radius and when it interferes with the cutting plane, it is dislodged from the surface without being suppressed. Similarly, when the particles are not interfering the cutting plane, (either above or below the cutting plane), they do not create voids. As the tool wear starts, tool gets blunt and the flank wear land presses the precipitates into the workpiece [Fig. 6.5(b) and (c)]. Thus the number of dislodgements become lesser and lesser as tool wear grows [Fig. 6.5(d)].

Material removal takes place through ductile cutting in Cu rich phase while Be rich phase or the hard precipitate from base material or only the projected portion of the particle cluster is removed due to its interference with the tool. When the tool interferes with the hard particle, cracks are generated in the particle. This represents the ductile to brittle transition as the tool cuts from base material to the location of hard particle. The machining of the hard precipitate show brittle machining where cracks are generated on the precipitate after machining [Fig. 6.6(a) and (b)]. Similar phenomenon was observed with the help of MDS when the tool performs cutting action on the precipitate in Chapter 4 [Fig. 4.15]. The cracks are formed and propagated beneath and ahead of the tool during machining of Be precipitate.

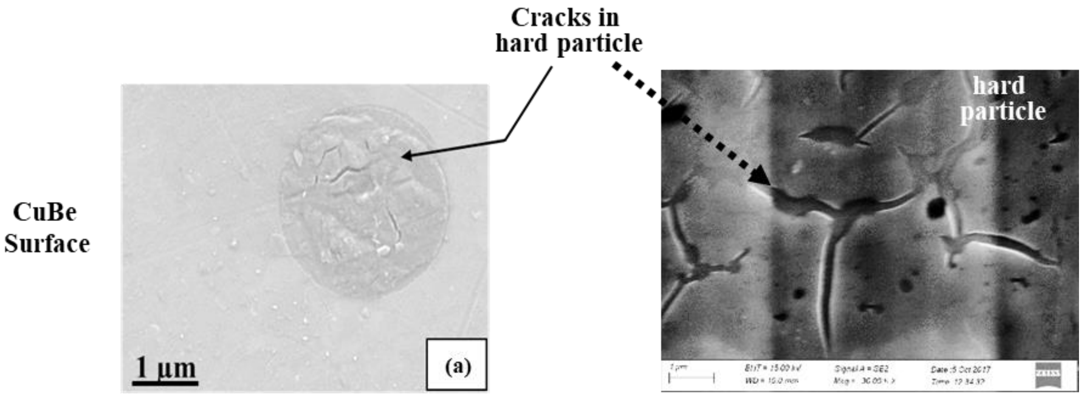

Fig. 6.6. Machined surface of CuBe and hard precipitate

6.3.1.3. Analysis of FFT spectrum of machined surface

Surfaces of both the materials show significant variation in their texture, FFT was carried out and results were analyzed to explain the nature of both the machined surfaces. Typical FFT plot of the diamond turned surface roughness profile reflects three types of frequency components [185]: Process related, material related vibrations, and tool-workpiece vibrations as shown in Fig. 6.7. Fig. 6.8(a) and (b) show the FFT spectrum performed on the diamond turned Cu and CuBe surface roughness profiles. In Fig. 6.8(a), the FFT for OFHC Cu with 2 µm/rev feed, the fundamental peak at 500 Hz (1000 µm /2 µm/rev = 500 Hz) is initially found to be increasing in its amplitude (3.7 nm in the beginning, 7.8 nm in the middle and 8 nm in the end of cutting distance). One of the significant reasons for the increasing amplitude is that initially the micro irregularities on the cutting edge are more prominent and subsequently due to smoothening of the cutting edge, feed domination becomes prominent. Some more peaks are noticed in the frequency range of 200-300 Hz indicating the tool-workpiece vibrations induced by the gradual increase in tool wear with the increase in cutting distance. Similar effect due to these vibrations was also outlined by Lee and Cheung [186]. These low-frequency peaks keep on increasing gradually till the cutting process terminates.

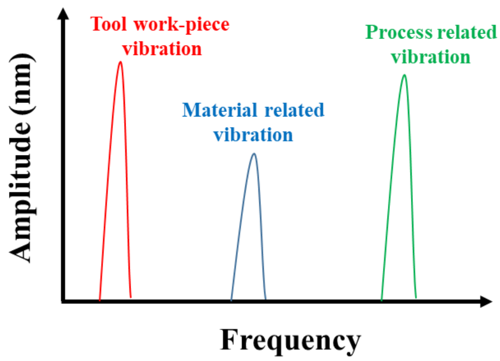

Fig. 6.7. Typical FFT plot for diamond turned surface roughness profile

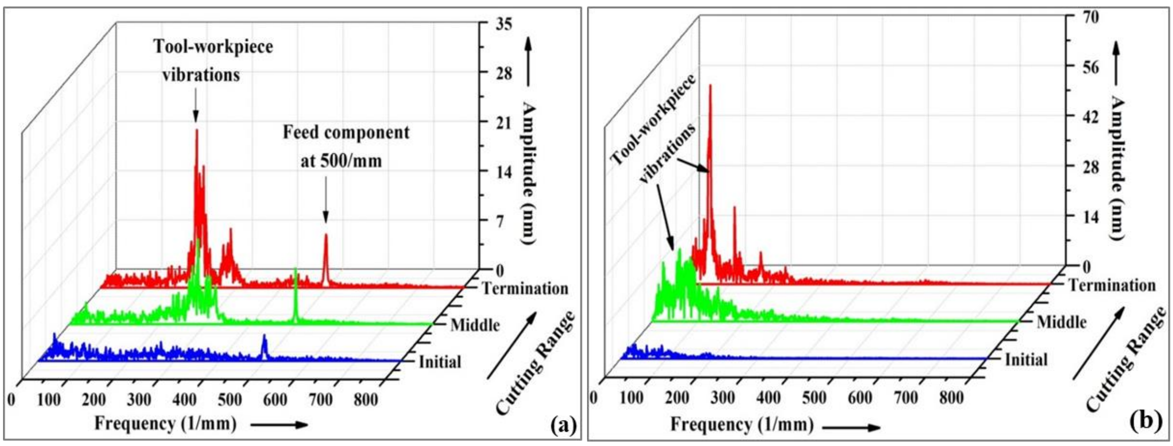

Fig. 6.8. FFT spectrum of the surface finish profile for Cu and CuBe

In contrast, diamond turned CuBe roughness profiles reveal the entirely different dominating frequency components on the machined surface profiles as shown in Fig. 6.8(b). In case of FFT for CuBe, the peak corresponding to the employed feed i.e. 500 Hz is not noticed and only low-frequency components are found to be dominating. These low-frequency components grow significantly with increasing cutting distance. Material inhomogeneity due to the presence of hard precipitates shifts the fundamental frequency, i.e. frequency corresponding to feed rate at 500 Hz, to lower frequency regions in the range of 0-50 Hz. In other words, tool-workpiece vibrations due to hard precipitates interaction with the cutting tool dominate over process characteristics. These low-frequency amplitudes increase with the increase in tool wear (or cutting distance) as a result of increased chattering because of increased length of the flank face. There is no sign of fundamental frequency components in the FFT spectrum of any of surface roughness profiles from beginning to end of the machining process. Thus, it is also indicated by FFT spectrum that the feed marks are suppressed during diamond turning of CuBe.

6.3.2. Analysis of mechanical interaction of tool-workpiece by MD simulation

Machined surface quality depends on the cutting mechanism and the tool wear induced surface degradation. Cutting mechanism determines the physical surface quality. Since the single point diamond turning includes nanoscale cutting zone and makes it difficult to analyze through experimental techniques, MD simulation provides the deep insights by revealing atom to atom interactions between the tool and workpiece. Here, simulation was carried out at two configurations of tool edge namely, sharp and blunt tool edge. The effect of cutting is observed on the surface. It is revealed that while cutting with a sharp tool, a void is generated as shown in Fig. 6.9(a) because of the tangential force to the particle. Fig. 6.9(c) shows that a high tangential force exists for the sharp tool cutting the CuBe workpiece. When a blunt cutting edge is used, the particle gets suppressed due to higher normal reaction caused by the particle on the tool [Fig. 6.9(b)]. Fig. 6.9(c) and (d) show the results of cutting and thrust forces variation with the help of MDS.

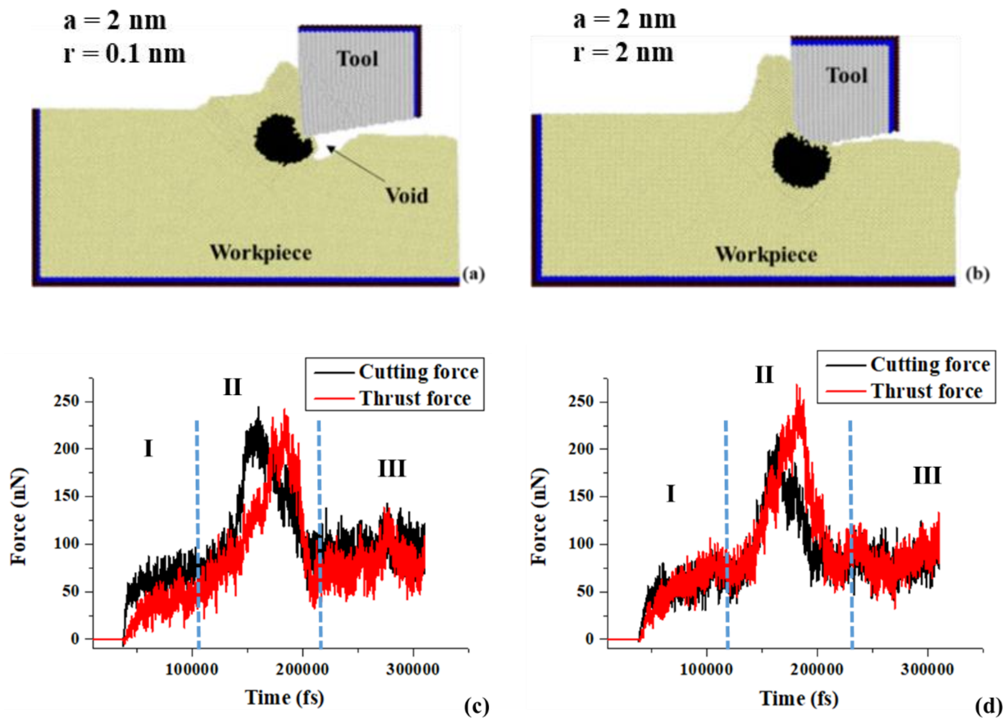

Fig. 6.9. Surface defects as revealed by MDS of nanocutting

Both the graphs are divided into three regions: Region I represents the forces for the tool cutting workpiece before the particle, Region 2 shows the forces at the particle location and Region 3 indicates the forces during cutting after tool passage through the particle. The region 2 is of interest due to the fact that the tool encounters the particle. It shows that for a sharp cutting edge, the cutting and thrust forces at the hard particle location gets increased significantly. Since the cutting forces are high, the tool tends to force the hard particle tangentially, which in turn creates a void on the generated surface. It was also seen in the experimental results shown in Fig. 6.5(a). Whereas, for a blunt tool with a round cutting edge, both the forces increase, however the thrust force is more in comparison to the cutting forces [Fig. 6.9(d)]. This increase in thrust force tends to suppress the particle instead of cutting through it. Thus, as the tool gets blunt, the tendency to create voids by the tool gets decreased. This phenomenon was also seen in Fig. 6.5(b-d), where the number of particle dislodgements were significantly reduced.

The CuBe nanocutting simulation has been done to observe the effect of the particle on cutting. When the tool cuts along the particle, it neither gets suppressed nor dislodged. As the Be particle is hard and brittle, it suffers crack formation [Fig. 4.15]. With the tool movement, the crack propagates ahead and beneath the tool. This crack formation reveals that as the tool travels from Cu rich phase to Be rich phase, ductile to brittle transition of cutting mechanism takes place. SEM results in Fig. 6.6 reveals the same.

From the examination and analysis of the machined surfaces, it is clearly seen that a fresh tool (sharp tool) generates surface with void and as the tool usage increases, it generates surfaces with lesser voids. Hence for application like tribology, it is recommended to use sharp tools to have higher bearing ratio, whereas for optical applications, generation of surfaces with used tool is preferred.

6.3.2.1. MD simulation of the effect of hard particle on lay pattern

Fig. 6.10(a) and (b) show the MD model before cutting the particle and after cutting it respectively with sectional views to observe the effect of the particle on the feed marks present on the surface. Fig. 6.10(a) shows the feed marks which were modelled on the surface, prior to cutting. The particle is present at the chip profile region from where the material is to be removed. When the tool encounters the particle at its location, it is subjected to a lateral force which cause the levelling of the previously generated feed marks. Thus it tends to change the surface lay pattern from deterministic to random as it was also examined in the SEM examination of the machined surfaces in Fig. 6.5. Fig. 6.10(b) shows the effect of cutting hard particle on the lay pattern. At the particle location, the cutting action show deviation in the path of surface generation. It is observed that the lay pattern is suppressed with the lateral force caused by the particle on the tool in the lateral direction. This causes the random surface without lay pattern as evidenced in Fig. 6.5(b). This phenomenon causes the absence of frequency component associated with feed marks in the FFT spectrum of CuBe [see Fig. 6.8(b)]. The presence of a hard particle in the workpiece changes the lay pattern from deterministic to near random. Fig. 6.10(c) shows the forces plot for the lateral directions.

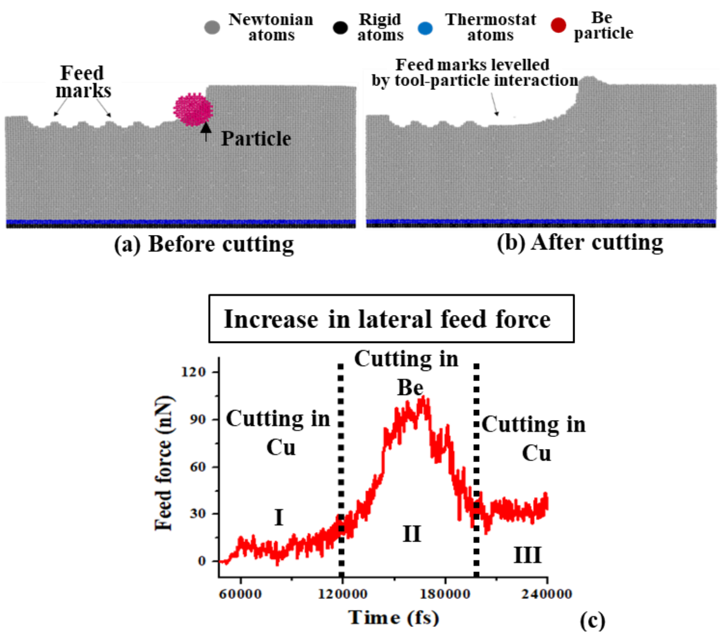

Fig. 6.10. Lay pattern before and after cutting and change in forces by MDS

The force plot has been divided into three zones: Zone I represents initial cutting phase where the tool cuts along the homogeneous material; Zone II represents the phase where tool cuts along the hard particle; and Zone III again shows the cutting through the homogeneous material. In Zone I, the tool cuts only in Cu and the lateral force component rises and then stabilise around certain value. As the tool encounters Be particle, the lateral force starts increasing suddenly and reach to its peak value at the location of hard particle as shown by Zone II. It is observed that the increase in lateral force is highest while cutting at the particle location. As the tool advances, these cutting forces show decreasing trend. In Zone III, the tool moves past the particle and it again starts cutting in Cu where forces fluctuate around a constant value.

In case of Cu, since the cutting process is uniform, a well-defined lay pattern characterized by the feed marks is obtained owing to the deterministic nature of the cutting process. The force on the tool comes from the cutting action necessary to remove the material volume quantified by feed rate and depth of cut. However, in case of CuBe, the particle presence in the workpiece material interferes with the tool along its flank face provide higher cutting load as well as thrust load.

Load increase in the lateral direction i.e. lateral/feed force is observed to be highest, when the particle is encountered. Since increase in lateral force is approximately more than 10 times, it will create workpiece induced vibration on the tool in lateral direction which is the dominating factor for diminishing the deterministic lay pattern on the CuBe machined surface.

Schematically, Fig. 6.11 (a) and (b) show the effect of lateral force on the lay pattern of diamond turned Cu and CuBe. In case of Cu, the machined surface is characterized by well defined feed marks, whereas, the machined CuBe surface is devoid of any well defined feed marks. Lateral movement of the tool suppresses the lay pattern generated in previous cut and transforms the surface lay pattern from deterministic to random.

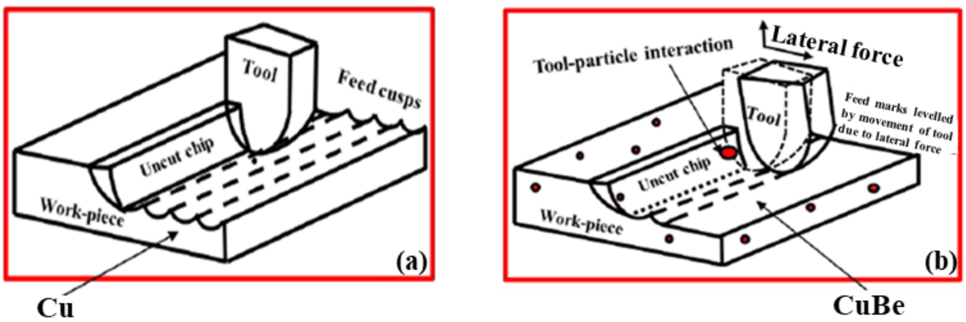

Fig. 6.11. Schematic of surface lay pattern while diamond turning of Cu and CuBe

Fig. 6.12 (a) and (b) show the variation of tangential cutting and lateral forces (feed forces in actual cutting) while carrying out the diamond turning on Cu and CuBe work-pieces. The experimental values of the forces resembles qualitatively with MDS results. For Cu, the value of both the forces is very small as it is a ductile material. However, the tangential cutting forces show higher magnitude than the feed force [Fig. 6.12(a)]. In case of CuBe, the magnitude of the thrust force is much higher than the cutting force. It is due to the precipitate interaction with the tool during machining. Higher lateral feed forces result in tool displacement which causes elimination of previous cutting marks. In addition, higher thrust forces also causes high amplitude of force induced vibrations.

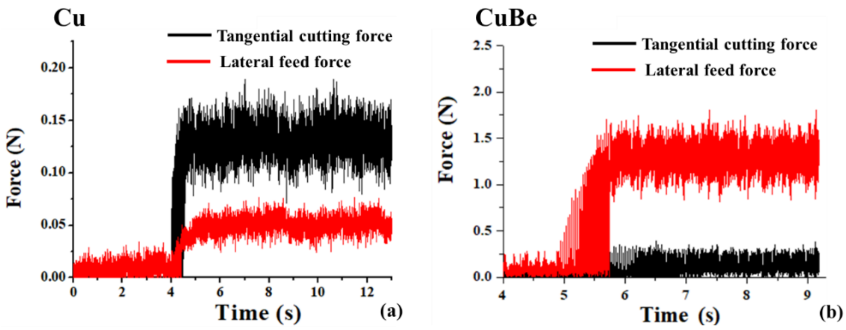

Fig. 6.12. Experimental forces for Cu at 8 km and CuBe at 4 km of cutting distances

6.3.3. Surface Contamination of diamond turned Cu and CuBe workpieces

During the physical interactions between diamond tool and workpiece, there are chemical interactions which take place during diamond machining of Cu and CuBe workpiece materials. Chemical interactions, in the form of transfer of materials from tool to workpiece due to tool wear with increasing cutting distance, take place. Raman spectrum was carried out to detect the phases of the diamond that are present on the machined surface. Furthermore, XPS characterization was performed to study the transfer of foreign materials into the workpiece material and their bonding states. Bonding states of worn out particles depend on the type of bonds they form with the parent material.

6.3.3.1. Electron dispersive spectroscopy of Cu and CuBe surfaces

Preliminary analysis of machined Cu and CuBe surface through EDS after diamond machining shows that there occurs transfer of tool material into the workpiece surface. Fig. 6.13(a) and (b) show the elemental spectrum in case of Cu and CuBe surface after diamond turning.

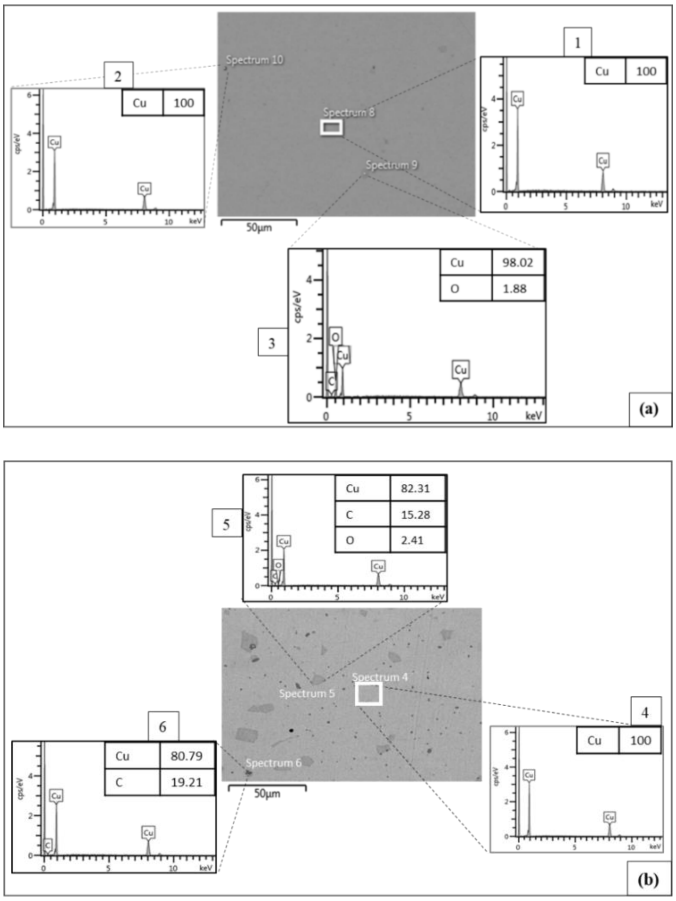

Fig. 6.13. EDS of the diamond turned Cu and CuBe surface

It is observed that the EDS spectrum of machined Cu surface does not encounter C owing to very less transfer of tool material into the workpiece. Also Cu is non-reactive to C, therefore chemical interaction does not take place. However, CuBe with hard Be precipitates is observed with presence of C at certain locations where the Be rich phase exists [Fig. 6.13(b)]. Since Be is reactive to C, the C from tool material combines with Be and contaminates the workpiece surface. This reaction is further detrimental as it creates harder spots which can cause rapid wear of the tool.

Similarly, physical contamination of surface by microchipped diamond particles is seen on the surface. This was also observed with the help of MD simulation in Chapter 4, where the sharp edge of the tool gets chipped off by the sudden impact caused by the particle during machining.

6.3.3.2. Raman Spectroscopy of machined Cu and CuBe surfaces

The C atoms removed as a result of diamond tool wear gets transferred to the machined surface. These atoms are then diffused into the machined surface depending on the reactivity of both the materials. Cu being a soft metal wears the diamond tool gradually and it is also less reactive to diamond, therefore, very weak and broad spectrum at 1332 cm^{-1} is observed on the machined surface through Raman spectrum. In case of CuBe, it is reflected on the machined surface with a broad peak at 1332 cm^{-1} as shown in Fig. 6.14.

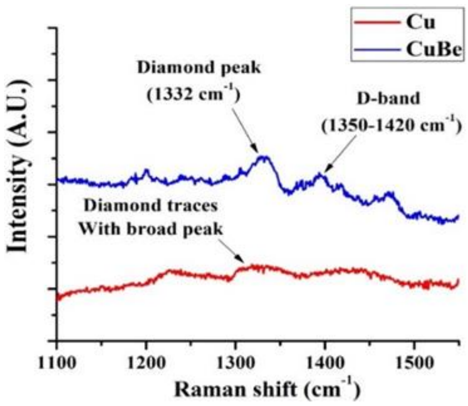

Fig. 6.14. Raman spectrum of Diamond turned Cu and CuBe machined surface

The broad peak represents the state of amorphization of the diamond. It shows another peak near to 1350-1400 cm^{-1} which shows D-band peak of worn diamond particles. The D-band peak represents a disordered state of graphite which reflects the degradation of atomic structure of diamond and contains a mixture of sp^3 and sp^2 bonding as reported by Hodkiewicz (2010)

[178]**.** The broad peak at 1332 cm^{-1} appears due to C adhesion on the top surface layers which suggest that the machined surface is contaminated by the chemical interaction between C and surface elements.

Raman spectrum reveals that C atoms removed from the diamond tool are transferred to the machined surface, however, their bonding states on the machined surface are not known. To understand the chemistry between tool wear particles and workpiece material, XPS was performed.

6.3.3.3. X-ray Photo Spectroscopy (XPS) of machined Cu and CuBe surfaces

To examine the surface further for the chemical contamination in terms of bonding states of contaminants, XPS results on the diamond turned Cu and CuBe surfaces were analyzed. Fig. 6.15(a) for carbon spectrum shows the presence of a peak at the binding energy of ~ 284.8 eV representing (C-C) form, ~ 286 eV representing (C-O) state. However, C-C peak at 284.8 (sp^3 C) is more dominant than that of the C-O peak which signifies that contamination of the surface takes place primarily by virtue of diamond particles abraded from CuBe workpiece and simultaneously through the oxidation of C atoms of worn diamond on the machined surface. Fig. 6.15(b) showing the XPS for oxygen spectrum indicates that C-O and Cu-O are present as peaks with binding energies of 532.5 and 530.5 eV respectively. Since the temperature at the narrow deformation zone in diamond turning approaches to ~1000 K [122], it causes the oxidation of both C atoms from the wear particles and workpiece simultaneously. The chemical interaction of tool and workpiece are dictated by the Gibbs free energy (ΔG) of the chemical reactions occurring in the small cutting zone. Larger the negative value of Gibbs free energy, more favourable the reaction is. Following reactions take place during diamond and copper interaction in the presence of atmospheric oxygen at 1000 K [183]:

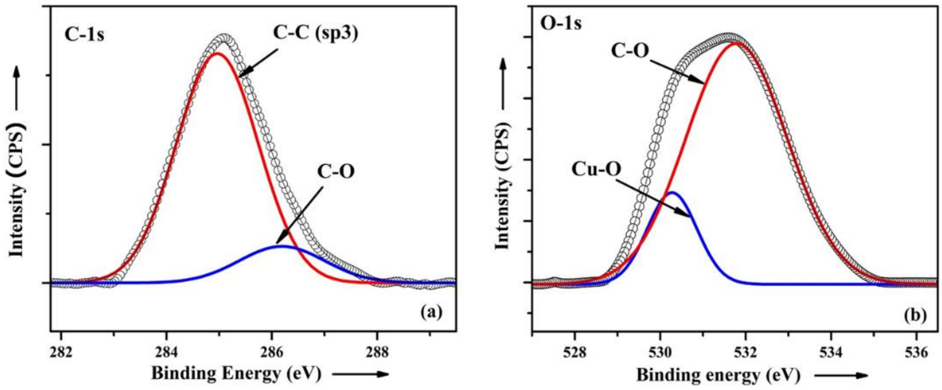

Fig. 6.15. XPS of CuBe machined surface having carbon and oxygen spectrum

(i) $C + O_2 = CO_2$, $\Delta G \approx -100$ Kcal/mol; (ii) $2C + O_2 = 2CO$, $\Delta G \approx -90$ Kcal/mol;

(iii) $2Cu + O_2 = 2CuO$, $\Delta G \approx -55$ Kcal/mol; (iv) $4Cu + O_2 = 2Cu_2O$, $\Delta G \approx -40$ Kcal/mol;

At 1000K, ΔG shows lowest values for the formation of CO_2 and CO that suggests the oxidation of worn out diamond atoms in the cutting zone. It happens faster than the oxidation of Cu atoms as ΔG for oxidation of Cu is lesser. As the cutting operation continues, more and more diamond atoms oxidize and subsequently contaminate the surface by the intermixing of oxides in the machined surface layers.

Similarly, XPS spectrums were obtained for Cu surface as shown in Fig. 6.16(a) & (b). Cu shows multiple peaks in both Carbon and Oxygen spectrum which manifest various oxidation states of carbon and copper. The C-C peak at 284.8 eV is not observed in the C-1s spectrum of Cu [Fig. 6.16(a)] which signifies that abrasion of diamond particles is not caused as the OFHC Cu is a homogeneous material. However, C-O and C=O peaks at about 286 eV and 288 eV respectively are observed on the Cu surface and indicate that oxidation of both the tool atoms and workpiece take place and contaminate the surface. Simultaneously, in the O-1s spectrum of Cu [Fig. 6.16(b)], different oxidation states of Cu and C are noticed which reveals that oxidation of Cu and C atoms dominates more in machining Cu. In both the plots of Cu, oxides of carbon are found to be dominant owing to a larger negative value of Gibbs free energy. Subsequently, these oxides of C and Cu get mixed with the surface and contaminate the layers of the surface.

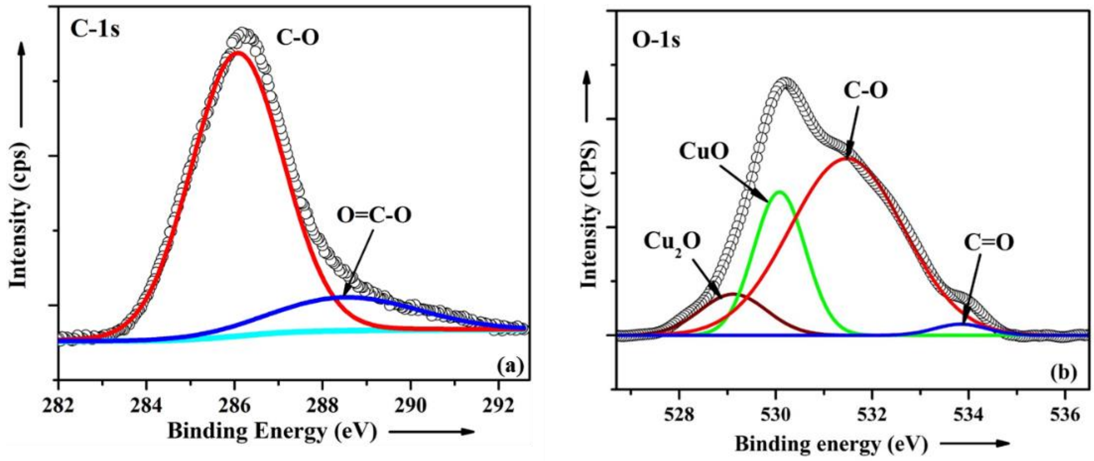

Fig. 6.16. XPS of Cu machined surface having Carbon and Oxygen spectrum

Considering the contamination mechanism in both the materials from XPS results, it can be inferred that in case of CuBe the contamination happens due to the absorption of abraded diamond particles as well as oxides of the C atoms from the tool. Whereas, in case of Cu, it is the oxides of C atoms which are diffused on the machined surface layers. Simultaneously, both the materials reveal the formation of oxides of Cu which suggest that there could be a formation of Cu-O-C complex. Shimada et al. (2000) drew the similar inference of complex formation while machining Cu with the diamond tool [183].

6.4. Effect of surface contamination on performance

The mechanical interplay between diamond tool and CuBe workpiece affects various desired properties on the surface which in turn influence the functional performance. Some of them are: Chemical contamination, surface hardness and optical properties.

6.4.1. Chemical contamination

Fig. 6.17(a) shows the variation of elements along with the depth under the machined surface. It is observed that the Cu shows increasing trend while the C and O shows decreasing trend as the specimen is etched and characterized with XPS. C from the tool varies in magnitude at different instances of cutting [Fig. 6.17(b)]. In the initial phase of cutting, when the tool chipping takes place, the C concentration on the surface and subsequent layers is found to be more than that of the middle phase where the tool wear is low. In the last phase of cutting, tool wear is rapid, therefore, the concentration of the C is higher. It indicates that the tool wear results in diffusion of C particles into the surface and thereby affecting the chemistry of the machined surface. This chemically altered layer may influence the optical as well as tribological properties of the surface.

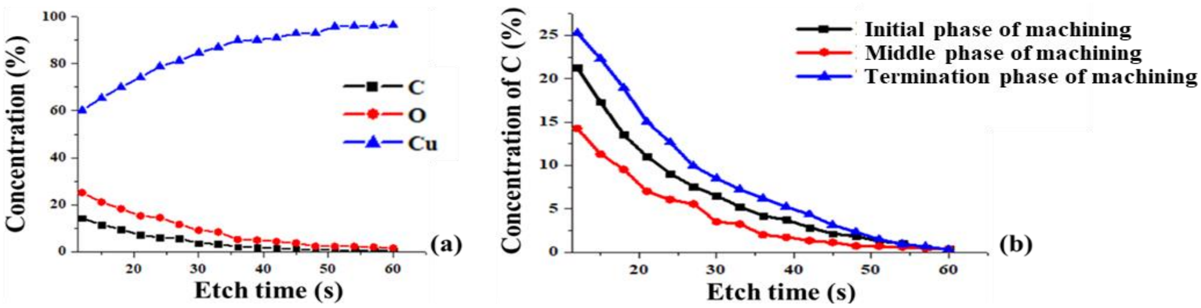

Fig. 6.17. Variation of C, O and Cu along the depth beneath the machined CuBe surface

6.4.2. Effect on the mechanical properties

Nanoindentation tests were carried out to notice the hardness variation at increasing depth of indentation. Fig. 6.18(a) shows the load variation with respect to various depths. Based on the slope of the unloading curve of the load-displacement graph, the values of the hardness and elastic modulus were calculated and plotted for various depths of indentation [Fig. 6.18(b) and (c). It is observed that the hardness and the elastic modulus values of surface layer are higher than in the bulk of the material. It is due to the fact that the dislocations formation and their restriction by the hard precipitate induces work hardening on the surface and it led to the increase in hardness and elastic modulus on the top surface layers. The influence is found to be dominant up to 100 nm. Similar to the chemically altered layer, mechanically deformed layer can influence tribological and mechanical performance of the surface.

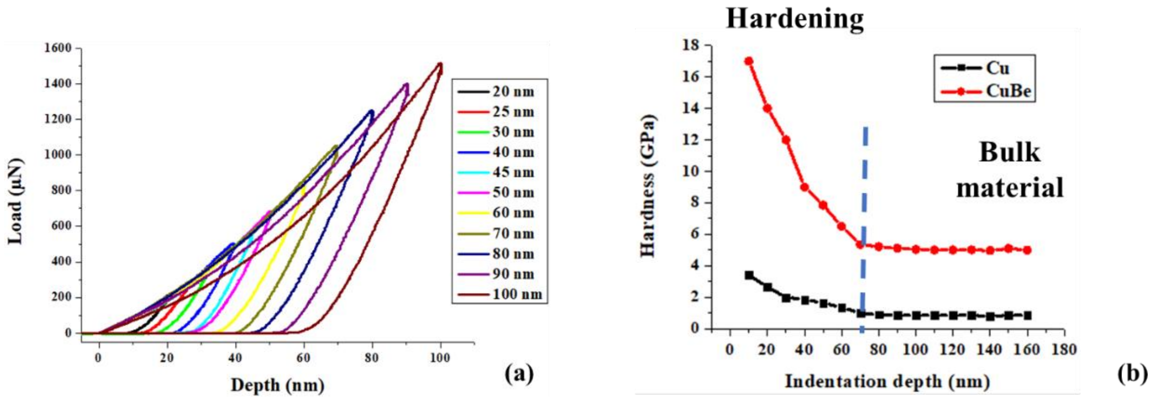

Fig. 6.18. Load versus depth curves for nanoindentation in CuBe

6.4.3. Effect on the optical properties of CuBe

It is observed from the Fig. 6.19 that the optical reflectivity of the machined surface varies as the cutting distance increases. Fig. 6.19 (a) show optical reflectivity of the CuBe machined surfaces at various cutting distances. Initially when the tool is sharp (at cutting distance ~ 250 m), the surface generation is poor due to the initial waviness of the tool as well as the voids caused on the surface. Optical reflectivity comes out to be ~ 60 % up to a wavelength of 1000 nm and then drops suddenly. As the tool wear takes place, the surface finish improves and the presence of voids become less with the blunt edge causing suppression of hard precipitates. This increases the optical reflectance as shown at cutting distances of 1 and 3 km.

Optical reflectivity lies in 75-85 % up to a wavelength of 700 nm, which covers the infra-red region. However, in the visible region, the reflectivity drops significantly from 75 % to 40 %. When the tool wears significantly, the surface finish is considerably degraded which eventually results in drop in reflectivity (i.e. less than 50 %) [Fig. 6.5]. Therefore, mid tool life span of diamond tool is more suitable for machining CuBe for optical applications. However due to the presence of voids and projection of particles, the applicability of CuBe for optical applications is reduced compared to Cu.

In case of Cu, machined surface shows the optical reflectivity higher than 70 % in the wavelength of 500 nm and above. It remains above 70 % for cutting from the beginning to 12 km of cutting distance for a wavelength range of more than 500 nm, which represents the visible region. Once the surface finish degrades after 12 km of cutting distance, optical reflectivity drops below 50 %. Thus, it can be deduced that diamond turned CuBe surface is suitable in the infra-red [Fig. 6.19(a)]. On the other hand, diamond turned Cu surface is suitable in the visible as well as in the infra-red region [Fig. 6.19(b)].

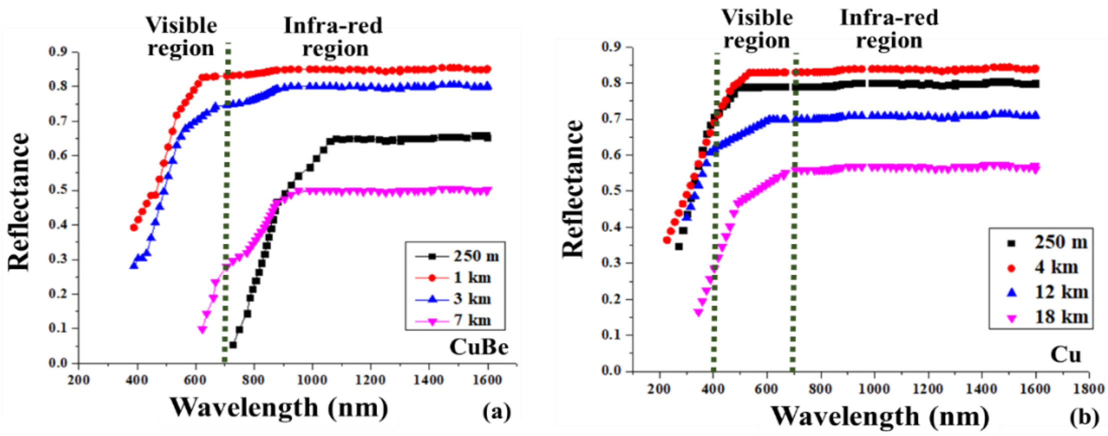

Fig. 6.19. Variation of reflectance with respect to wavelength

6.5. Interpretation of the mechanisms in tool-workpiece interaction

All the mechanisms related to material removal, tool wear and surface quality explained in this study during ultraprecision diamond turning of Cu and CuBe are presented with the help of a schematic shown in Fig. 6.20(a) and (b) respectively.

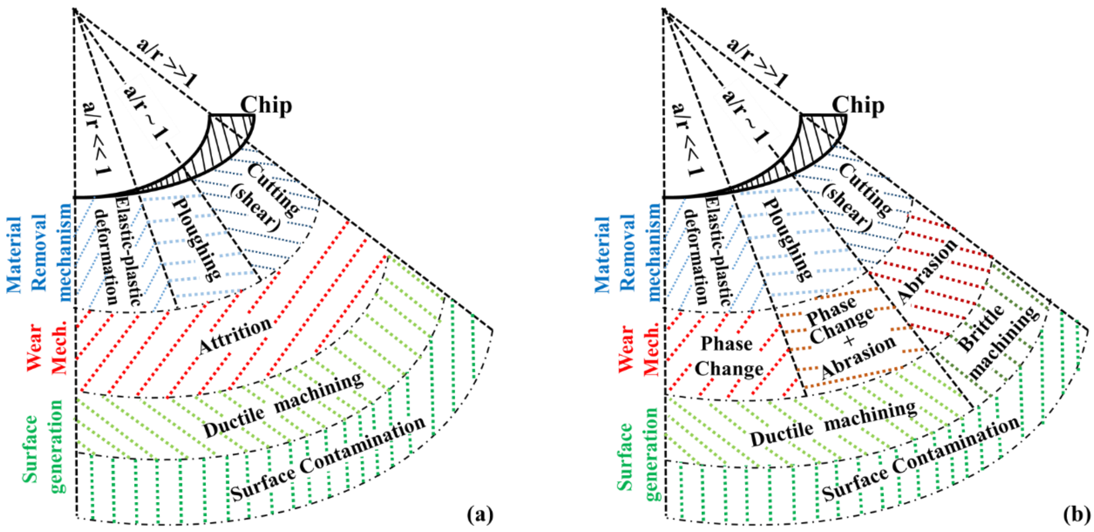

Fig. 6.20. Interaction effect diagram for diamond turning of Cu and CuBe respectively

The chip region is divided into three zones based on the a/r ratio and the mechanisms of material removal, tool wear and surface generation are highlighted for bothe Cu and CuBe. In case of Cu, when the a/r ratio is greater than 1, cutting ocurs through shearing action. As the a/r comes down to 1, ploughing action takes place and for a/r<<1 sliding mechanism dominates. As Cu is a soft material, wear mechanism takes place by attrition and the resulting work surface is generated by ductile machining mode at every a/r ratio.

For CuBe at a/r>=1, material removal mechanism through shear cutting, wear mechanism in the form of abrasion and surface generation in Be phase by brittle mode machining with surface contamination take place Fig. 6.20(b). In case of a/r ~ 1, material removal through ploughing, wear mechanism in the form of phase transformation and abrasion, ductile mode machining are achieved. In case of a/r<<1, only sliding with elastic plastic deformation, phase transformation on the tool, and consequent surface contamination take place. While the MDS is used for studying the mechanisms of material removal, tool wear and surface quality, experiments are carried out for investigating tool wear and surface generation. Experimental results confirm the results obtained by MDS for tool wear mechanism, surface contamination and transformed lay pattern.

6.6. Summary

This chapter describes the effect of tool-workpiece interaction on the machined surface quality based on the analysis with the help different surface characterization techniques. Following conclusions are drawn from this chapter:

1. There is a significant difference in surface roughness values of Cu and CuBe at different instances of cutting during the entire lifespan of the tool. The maximum difference in the average roughness values of diamond turned Cu and CuBe surface is observed to be ~48 % at the end of cutting owing to large surface roughness in CuBe.
2. Hard particles in CuBe affect the quality of the machined surface. Smooth surface obtained in case of Cu workpiece represent ductile cutting, whereas CuBe surface reveals dislodgements of hard particles and fractured surface at the hard particle location which denote the ductile to brittle transition as the tool cuts from the base material to the hard particle.
3. While machined Cu surface shows well defined deterministic lay pattern characterized by feed marks, CuBe is subjected to suppression of feed marks which results in near random lay pattern at the employed cutting parameters. The same phenomenon is described by FFT spectrum for the Cu and CuBe workpieces.
4. MD simulation results reveal that hard particle increases the lateral forces while machining CuBe and it plays a role in suppressing the lay pattern leading to the surface which is near random pattern.
5. Diamond turned CuBe surface is chemically contaminated by the tool material in the form of diamond (sp3) and oxides of C and Cu in the form (C-O), (Cu-O) respectively whereas Cu machined surface is contaminated by C-O, C=O, and Cu-O.

6. The physical and chemical contamination does not occur only on the surface but it has diffusive effect beneath the surface. The C concentration penetrates beneath the surface which decays exponentially. Similarly, hardness variation takes place owing to deformation occurring on the workpiece top layers.
7. Diamond turning of CuBe is suitable for infrared optics applications whereas diamond turning of Cu is suitable for visible as well as infrared optics.
8. Mid tool life span of diamond tool is more suitable for machining CuBe for optical applications. For tribological applications, it is recommended to use sharp tools to have higher bearing ratio.
9. Based on results of the investigations, interaction effect diagrams for both Cu and CuBe in diamond turning are presented.

Chapter 7

Conclusions and Future scope

7.1. Conclusions

In the present work, investigation of the tool and workpiece interaction in diamond turning of CuBe is carried out. There are predominantly three aspects of the study: (1) cutting mechanism; (2) study of tool wear and its mechanism; (3) investigation of the surface quality. The study on Cu was performed for the benchmarking purposes. Following are the main conclusions which are drawn from the present study.

1. Interatomic potential for Cu-Be is developed and the values of potential function parameters are: D =0.0563 eV, α= 5.042 Å^{-1} and r_o = 2.065 Å.
2. The material removal mechanism in case of CuBe is phase dependent. MDS results show that in case of Cu phase, ductile regime machining takes place where the governing mechanisms are: a) shearing action, (b) ploughing, and (c) elastic-plastic deformation (i.e. rubbing and burnishing) depending upon the a/r ratio. In case of hard Be phase, brittle fracture takes place at higher a/r ratio and ductile regime machining at lower a/r ratio. For machining CuBe, a/r ratio equals to 1 is found to be the optimum value to get ductile mode machining.
3. While machining CuBe, wear mechanism is predominantly governed by the stress and temperature generation in the tool edge. Experimental as well as MDS results reveal that the wear mechanism is: abrasion in the form of chipping in initial phase due to high stress and phase transformation in the later phase due to high temperature.
4. While machining CuBe, higher stress and temperature at the cutting zone create the amorphous layer on diamond tool and number of amorphous atoms increase as more

and more interaction of the diamond tool and the Be precipitate takes place. The wear mechanism is thus observed to be the phase transformation of the diamond tool followed by severe wear.

5. For the same cutting conditions, the cutting distance covered on Cu is ~20 km and on CuBe, it is ~8 km before the complete failure of the diamond tool. It shows that diamond tool life in machining of CuBe is 40% of that of Cu.
6. Unlike the known (conventional) tool life curve having primary, secondary and tertiary regions, the tool used for machining CuBe exhibits only two regions. Owing to this, making of decision to terminate the usage of tool for further reconditioning becomes difficult.
7. Tool wear coefficients, A and B for the known tool wear model are determined for CuBe and Diamond combination and their values are: A= 161.58 GPa^{-1}; B= 4877.28 K.
8. Hard precipitates in CuBe affect the quality of the machined surface. Experimental results of SEM reveals that smooth surface obtained in case of machined Cu workpiece represent ductile cutting, whereas CuBe surface reveal dislodgements of hard precipitates and fractured surface at the hard precipitate location. This denotes the ductile to brittle transition as the tool travels from base material to hard precipitate.
9. Experimental as well as simulation results reveal that while the machined Cu surface shows well defined deterministic lay pattern characterized by feed marks, CuBe is devoid of any feed marks and exhibits suppressed deterministic lay pattern.
10. The carbon atoms removed from the tool are subsequently bonded with the workpiece material and thus contaminates the generated surface. These C atoms form carbides with Be atoms.

11. SEM and Raman spectroscopic analysis of the worn flanks of the diamond tool shows a smooth wear pattern while machining Cu but shows a micro-grooved pattern while machining CuBe. Therefore, the wear mechanism on Cu appears to be attritious wear while on CuBe, it involves sp^3 phase transformation followed by severe abrasive wear.
12. There is significant difference in surface roughness values of Cu and CuBe at different instances of cutting during the life span of the tool. Maximum difference of ~48 % increase in the surface roughness value is observed at the end of cutting in CuBe when compared to Cu.
13. Diamond turned CuBe surface is chemically contaminated by the tool material in the form of diamond (sp^3) and oxides of C and Cu in the form (C-O), (Cu-O) respectively whereas Cu machined surface is contaminated by C-O, C=O and Cu-O. This necessitates secondary process or cleaning of CuBe surfaces.
14. Diamond turned CuBe surfaces are suitable for applications in IR optics region whereas diamond turned Cu is suitable for applications in visible and IR optics.
15. Based on the results of MDS, interaction effects of diamond tool and Cu as well as CuBe are presented for various a/r ratios as diagrams. Similarly based on the results of MDS and experiments, interaction effect diagrams are presented for Cu and CuBe.

From the present work, following **scientific contributions** are made:

- The mechanisms of surface generation and wear mechanisms are identified in diamond turning of CuBe.
    - Wear mechanism: Phase transformation in the form of Amorphization is identified as a wear mechanism
    - Surface generation: Near Random lay pattern as a result of suppression of deterministic lay pattern in CuBe machined surface.
- Interatomic potential function parameters are developed for Cu-Be.

- The constants of a tool wear model i.e. A and B, are determined for diamond tool and CuBe combination in diamond turning.

7.2. Recommendations for future work

Based on this work, various opportunities for commercial, technological and scientific developments are projected, some of which are highlighted in the following sections:

- **Multiscale Simulation of diamond turning**

Since MD simulation provides a very small characteristic length scale to analyse the cutting phenomenon, it does not investigate the effect on the bulk material. Therefore, multiscale modelling of diamond turning is possibly a research area which could be investigated for higher length scales of cutting.

- **Effects of coolant and coatings**

Due to the limitations of time and the lack of potential functions in MDS, the effect of coolant during nanometric cutting of Cu and CuBe was not studied in the current work. The presence of a coolant will certainly influence the tribo-chemistry of the diamond tool and studying its effect will help develop an understanding of the appropriate measures for the mitigation of tool wear.

- **Tool wear control**

The present work has identified the wear mechanism of diamond tool while machining CuBe, which is transformation of diamond to amorphous structure. Since the tool wear mechanism is known, the future studies can be attempted to control the tool wear by providing solutions to reduce the rate of phase change.

- **Surface contamination**

The current study explains the surface contamination due to tool wear and its subsequent effect on optical and mechanical properties. As tool wear particles are absorbed on the surface layers, it may also affect the tribological, electrical and magnetic properties. The investigation of the influence on the surface properties of diamond turned materials is an open ended opportunity.

- **Study of chip morphology**

The current study does not involve the investigation of chip morphology during machining. It is expected that the heterogeneous nature of the workpiece material may affect the chip morphology. The coexistence of ductile cutting as well as crack generation during diamond turning of CuBe may change the nature of chip formation. Thus, there is a scope for further investigations in understanding the chip morphology in diamond turning of CuBe.

References

1) Balasubramaniam R, Sarepaka R V, Subbiah S. Diamond Turn Machining: Theory and Practice. CRC Press; 2017.

2) Goel S, Luo XC, Agrawal A, Reuben RL. Diamond machining of silicon: A review of advances in molecular dynamics simulation. Int J Mach Tools Manuf 2015;88:131–64.

3) Taniguchi N. Current status in, and future trends of, ultraprecision machining and ultrafine materials processing. CIRP Ann 1983;32:573–82.

4) Arnold JB, Morris TO, Sladky RE, Steger PJ. Machinability studies of infrared window materials and metals. Opt Eng 1977;16:164324.

5) Hung NP, Zhong ZW, Lee KK, Chai CF. Precision grinding and facing of copper-beryllium alloys. Precis Eng 1999;23:293–304.

6) Brinksmeier E, Preuss W. Micro-machining. Philos Trans R Soc A Math Phys Eng Sci 2012;370:3973–92.

7) Brehm PD. Single Point Diamond Machining As An Optical Manufacturing Process. International Society for Optics and Photonics 1983;406:92–8.

8) Gerth HL. Introduction to precision machining of metal optics. International Society for Optics and Photonics 1982;315:225–30.

9) Paper K. The Role of Precision Engineering in Manufacturing. CIRP Annals 1987;36(2):495-501.

10) Mckeown PA, Keown PAM. Ultra-precision diamond machining of advanced technology components. Material and manufacturing process 1986;1(1):107-32.

11) Arnold JB, Steger PJ, Saito TT. Tool feed influence on the machinability of CO2 laser optics. Applied optics 1975;14:1777–82.

12) Johnson FE, Saito TT. Applications of Diamond Turning to Infrared Optical Systems. Opt Eng 1977;16(4):387–92.

13) Michael J. Production Aspects Of Single Point Diamond Turning. International Society for Optics and Photonics 1984;508:12-20.

14) Saito TT, Reichelt W, Livermore L, Livermore L, Lawrence AEC. Diamond Turning of Optics : The Past, Past, the Present, and and the Exciting Future. Opt Eng 1978;17(6):570-3.

15) Johnson FE, Saito TT. Applications of diamond turning to infrared optical systems. International Society for Optics and Photonics 1976;93:104–12.

16) Evans CJ. Precision engineering: an evolutionary perspective. Phil Trans R Soc A 2012;370:3835–51.

17) Davies MA, Evans CJ, Vohra RR, Bergner BC, Patterson SR. Application of precision diamond machining to the manufacture of microphotonics components. International Society for Optics and Photonics 2003; 5183:94-109.

18) Chiu WM, Lee WB. Development of ultra-precision machining technology. Fifth Int. Conf. Fact. 2000 - Technol. Exploit. Process, 1997:486–90.

19) Ikawa N, Donaldson RR, Komanduri R, König W, McKeown PA, Moriwaki T. Ultraprecision metal cutting—the past, the present and the future. CIRP Ann 1991;40:587–94.

20) Saito TT. Machining of optics : an introduction. Applied optics 1975;14(8):1773–6.

21) Bryan JB, Donaldson RR, McClure ER, Whelan HA, Clouser RW. Diamond turning of parabolic mirrors. International Society for Optics and Photonics 1974;39:39–45.

22) Barkman WE. The Linear Motor Slide Drive System. International Society for Optics and Photonics 1978;159:25-32.

23) Benjamin RJ. Diamond turning at a large optical manufacturer. Opt Eng 1978;17(6):574-6.

24) Bryan JB. Design and construction of an ultraprecision 84 inch diamond turning machine. Precis Eng 1979;1:13–7.

25) Casstevens, John M., and C. E. Daugherty. Diamond turning optical surfaces on electroless nickel. International Society for Optics and Photonics 1978;159:109–13.

26) Thompson DC, Chrislock JL, Newton LE. Development of an inexpensive, high-accuracy diamond turning machine. Precis Eng 1982;4:73–7.

27) Patterson SR, Magrab EB. Design and testing of a fast tool servo for diamond turning. Precis Eng 1985;7:123–8.

28) Kanai A, Miyashita M, Hoshi T. Nanometer Positioning Characteristics of Closed Looped Differential Hydro-or Aerostatic Actuator. CIRP Ann 1983;32:287–9.

29) Donaldson RR, Patterson SR. Design and construction of a large, vertical axis diamond turning machine. International Society for Optics and Photonics 1983;433:62–8.

30) Donaldson RR, Maddux AS. Design of a high-performance slide and drive system for a small precision machining research lathe. CIRP Ann 1984;33:243-48.

31) Burleson RR. The Evolution Of Precision Computerized Numerical Controls (CNC). International Society for Optics and Photonics 1983:433:94–6.

32) Arnold JB, Steger PJ, Morris TO. Machinability aspects of diamond-turned metal optics. International Society for Optics and Photonics 1976;65:108–18.

33) Bennett JM. Measurement of the rms roughness, autocovariance function and other statistical properties of optical surfaces using a FECO scanning interferometer. Appl Opt 1976;15:2705–21.

34) Bennett JM, Decker DL. Surface characterization of diamond-turned metal optics. International Society for Optics and Photonics 1981;288:534–45.

35) Stover JC. Surface characteristics of machined optics. International Society for Optics and Photonics 1976;93:90–6.

36) Shagam RN, Sladky RE, Wyant JC. Optical figure inspection of diamond-turned metal mirrors. Opt Eng 1977;16(4):375-80.

37) Brodmann R, Gerstorfer O, Thurn G. Optical roughness measuring instrument for fine-machined surfaces. Opt Eng 1985;24(3):408-13.

38) Taylor JS, Syn CK, Saito TT, Donaldson RR. Surface finish measurements of diamond-turned electroless-nickel-plated mirrors. Opt Eng 1986;25:10-13.

39) Chaloux LE. Part Fixturing For Diamond Machining. International Society for Optics and Photonics 1984; 508:109-12.

40) Hannah PR. The Ultra-Precision Optical Element Fabrication - Machines. International Society for Optics and Photonics 1983;433:104–6.

41) Cooke F, Frank AM, Bryan JB, Clouser RW. Quick fast off-axis parabolas. Appl Opt 1978;17:671–3.

42) Miller DM, Hauver GH, Culverhouse JN, Greenwell EN. Description of a unique machine tool permitting achievement of< 15-A rms diamond-turned surfaces. Opt Eng 1979;18:55-66.

43) Fuchs BA, Hed PP, Baker PC. Fine diamond turning of KDP crystals. Appl Opt 1986;25:1733–5.

44) Baker PC, Sonderman JB, Saitot TT. Finishing of precision generated metal optical components. International Society for Optics and Photonics 1976;65:42–8.

45) Jeanmichel C, Prevost M. Diamond Turning With Moore Machine For Infra-Red Applications. Machining And Results. International Society for Optics and Photonics 1986; 645:36–45.

46) Ikawa N, Donaldson RR, Komanduri R, König W, Aachen TH, McKeown PA, et al. Ultraprecision Metal Cutting — The Past, the Present and the Future. CIRP Ann 1991;40:587–94.

47) Lucca DA, Rhorer RL, Komanduri R. Energy dissipation in the ultraprecision machining of copper. CIRP Ann 1991;40:69–72.

48) Zhang FZ, Chen LJ. Ultra-Precision Cutting for ZKN7 Glass. CIRP Ann 2000;49:17–20.

49) Moriwaki T, Okuda K, College KT. Machinability of Copper in Ultra-Precision Micro Diamond Cutting. CIRP Annals 1989;38:115–8.

50) Ikawa N, Shimada S, Tanaka H. Minimum thickness of cut in micromachining. Nanotechnology 1999;3:6–9.

51) Kim J-D, Kim DS. Theoretical analysis of micro-cutting characteristics in ultra-precision machining. J Mater Process Technol 1995;49:387–98.

52) Shimada S, Ikawa N, Tanaka H, Ohmori G, Uchikoshi J, Yoshinaga H. Feasibility Study on Ultimate Accuracy in Microcutting Using Molecular Dynamics Simulation. CIRP Ann - Manuf Technol 1993;42:91–4.

53) Yuan ZJ, Zhou M, Dong S. Effect of diamond tool sharpness on minimum cutting thickness and cutting surface integrity in ultraprecision machining. J Mater Process Technol 1996;62:327–30.

54) Furukawa Y, Moronuki N. Effect of Material Properties on Ultra Precise Cutting Processes. CIRP Ann - Manuf Technol 1988;37:113–6.

55) Lucca DA, Rhorer RL, Komanduri R. Energy Dissipation in the Ultraprecision Machining of Copper. CIRP Ann - Manuf Technol 1991;40:69–72.

56) Taminiau D, Dautzenberg JH. Bluntness of the tool and process forces in high-precision cutting. CIRP Ann 1991;40:65–8.

57) Lucca DA, Seo YW, Rhorer RL, Donaldson RR. Aspects of Surface Generation in Orthogonal Ultraprecision Machining. CIRP Ann - Manuf Technol 1994;43:43–6.

58) Komanduri R, Chandrasekaran N, Raff LM. Effect of tool geometry in nanometric cutting: A molecular dynamics simulation approach. Wear 1998;219:84–97.

59) Bifano TG, Dow T a., Scattergood RO. Ductile-Regime Grinding: A New Technology for Machining Brittle Materials. J Eng Ind 1991;113:184.

60) Blake PN, Scattergood R. Ductile-Regime Machining of Germanium and Silicon. Journal of the American ceramic society 1990;57:949–57.

61) Blackley WS, Scattergood RO. Ductile-regime machining model for diamond turning of brittle materials. Precis Eng 1991;13:95–103.

62) Blackley WS, Scattergood RO. Chip Topography for Ductile- Regime Machining of Germanium. J Eng Ind 1994;116:263–6.

63) Nakasuji T, Kodera S, Hara S, Ikawa N. Diamond Turning of Brittle Materials for Optical Components. CIRP Ann - Manuf Technol 1990;39:89–92.

64) Shimada S, Ikawa N, Inamura T, Takezawa N, Ohmori H, Sata T. Brittle-Ductile Transition Phenomena in Microindentation and Micromachining. CIRP Ann - Manuf Technol 1995;44:523–6.

65) Leung T., Lee W., Lu X. Diamond turning of silicon substrates in ductile-regime. J Mater Process Technol 1998;73:42–8.

66) Liang Y, Moronuki N, Furukawa Y. Calculations of the effect of material anisotropy on microcutting processes. Precision engineering 1994;16(2):132-8.

67) Lee WB, Kong H. Prediction of microcutting force variation in ultra- precision machining. Precision engineering 1990;12(1):25-8.

68) Moronuki N, Liang Y, Furukawa Y. Experiments on the effect of material properties on microcutting processes. Precision engineering 1994;16(2):124–31.

69) Sato M, Yamazaki T, Shimizu Y, Takabayashi T. A study on the microcutting of aluminum single crystals. JSME Int Journal Ser 3, Vib Control Eng Eng Ind 1991;34:540–5.

70) Zhang JJ, Sun T, Hartmaier A, Yan YD. Atomistic simulation of the influence of nanomachining-induced deformation on subsequent nanoindentation. Comput Mater Sci 2012;59:14–21.

71) Zhu P, Fang F. Study of the minimum depth of material removal in nanoscale mechanical machining of single crystalline copper. Comput Mater Sci 2016;118:192–202.

72) Pei QX, Lu C, Lee HP, Zhang YW. Study of materials deformation in nanometric cutting by large-scale molecular dynamics simulations. Nanoscale Res Lett 2009;4:444–51.

73) Ye YY, Biswas R, Morris JR, Bastawros A, Chandra A. Molecular dynamics simulation of nanoscale machining of copper. Nanotechnology 2003;14:390–6.

74) Wang Q, Bai Q, Chen J, Sun Y, Guo Y, Liang Y. Subsurface defects structural evolution in nano-cutting of single crystal copper. Appl Surf Sci 2015;344:38–46.

75) Li J, Fang Q, Liu B, Liu Y. The effects of pore and second-phase particle on the mechanical properties of machining copper matrix from molecular dynamic simulation. Appl Surf Sci 2016;384:419–31.

76) Hosseini SV, Vahdati M. Modeling the effect of tool edge radius on contact zone in nanomachining. Comput Mater Sci 2012;65:29–36.

77) Syn CK, Taylor JS, Donaldson RR. Diamond tool wear vs. cutting distance on electroless nickel mirrors. International Society for Optics and Photonics 1987;676:128-142.

78) Sugano T, Takeuchi K, Goto T, Yoshida Y, Ikawa N. Diamond Turning of an Aluminum Alloy for Mirror. CIRP Ann - Manuf Technol 1987;36:17–20.

79) McKeown PA. Ultra-precision diamond machining of advanced technology components. Adv Manuf Process 1986;1:107–32.

80) Asai S, Kobayashi A. Observations of chip producing behaviour in ultra-precision diamond machining and study on mirror-like surface generating mechanism. Precision Engineering 1990;12(3):137–43.

81) Myler JK. The influence of Machine Tool Vibration on the Surface Texture of Diamond Turned Components. Proc.SPIE 1987; 732:196-210.

82) Puttick KE, Whitmore LC, Zhdan P, Gee AE, Chao CL. Energy scaling transitions in machining of silicon by diamond. Tribol Int 1995;28:349–55.

83) To S, Lee WB, Chan CY. Ultraprecision diamond turning of aluminium single crystals. J Mater Process Technol 1997;63:157–62.

84) Cheung C., Lee W. Characterisation of nanosurface generation in single-point diamond turning. Int J Mach Tools Manuf 2001;41:851–75.

85) Revel P, Khanfir H. Surface characterization of aluminum alloys after diamond turning. J Mater Process Technol 2006;178(1-3):154–61.

86) Zhang SJ, To S, Cheung CF, Wang HT. Dynamic characteristics of an aerostatic bearing spindle and its influence on surface topography in ultra-precision diamond turning. Int J Mach Tools Manuf 2012;62:1–12.

87) Lee WB, Cheung CF, To S. Multi-Scale Modeling of Surface Topography in Single-Point Diamond Turning. Key Eng Mater 2007;340–341:1009–16.

88) Kim DS, Chang IC, Kim SW. Microscopic topographical analysis of tool vibration effects on diamond turned optical surfaces. Precis Eng 2002;26:168–74.

89) Lee WB, Cheung CF. Dynamic surface topography model for the prediction of ano-surface generation in ultra-precision machining. Int J Mech Sci 2001;43:961–91.

90) Liu K, Melkote SN. Effect of plastic side flow on surface roughness in micro-turning process. Int J Mach Tools Manuf 2006;46:1778–85.

91) To S, Cheung CF, Lee WB. Influence of material swelling on surface roughness in diamond turning of single crystals. Mater Sci Technol 2001;17:102–8.

92) Kong MC, Lee WB, Cheung CF, To S. A study of materials swelling and recovery in single-point diamond turning of ductile materials. J Mater Process Technol 2006;180:210–5.

93) Cheung CF, To S, Lee WB. Anisotropy of surface roughness in diamond turning of brittle single crystals. Materials and Manufacturing Processes 2002;17(2):251-67.

94) Cheung CF, Lee WB. Multi-spectrum analysis of surface roughness formation in ultra-precision machining. Precis Eng 2000;24:77–87.

95) Lee WB, Cheung CF, To S. Materials induced vibration in ultra-precision machining. J Mater Process Technol 1999;89–90:318–25.

96) Wang H, To S, Chan CY, Cheung CF, Lee WB. A theoretical and experimental investigation of the tool-tip vibration and its influence upon surface generation in single-point diamond turning. Int J Mach Tools Manuf 2010;50:241–52.

97) Zhang G, To S, Zhang S. Relationships of tool wear characteristics to cutting mechanics, chip formation, and surface quality in ultra-precision fly cutting. Int J Adv Manuf Technol 2016;83:133–44.

98) Yan J, Syoji K, Tamaki J. Some observations on the wear of diamond tools in ultra-precision cutting of single-crystal silicon. Wear 2003;255:1380–7.

99) Han XS, Lin B, Yu SY, Wang SX. Investigation of tool geometry in nanometric cutting by molecular dynamics simulation. J Mater Process Technol 2002;129:105–8.

100) Yingfei G, Jiuhua X, Hui Y. Diamond tools wear and their applicability when ultra-precision turning of SiCp/2009Al matrix composite. Wear 2010;269:699–708.

101) Zareena AR, Veldhuis SC. Tool wear mechanisms and tool life enhancement in ultra-precision machining of titanium. J Mater Process Technol 2012;212:560–70.

102) Zong WJ, Sun T, Li D, Cheng K, Liang YC. XPS analysis of the groove wearing marks on flank face of diamond tool in nanometric cutting of silicon wafer. Int J Mach Tools Manuf 2008;48:1678–87.

103) Zong WJ, Li ZQ, Sun T, Li D, Cheng K. Analysis for the wear resistance anisotropy of diamond cutting tools in theory and experiment. J Mater Process Technol 2010;210:858–67.

104) Yue X, Xu M, Du W, Chu C. Effect of cutting edge radius on surface roughness in diamond tool turning of transparent MgAl2O4 spinel ceramic. Opt Mater (Amst) 2017;71:129–35.

105) He CL, Zong WJ, Sun T. Origins for the size effect of surface roughness in diamond turning. Int J Mach Tools Manuf 2016;106:22–42.

106) Chen J, Zhao Q. A model for predicting surface roughness in single-point diamond turning. Meas J Int Meas Confed 2015;69:20–30.

107) Zeqin L, Sujuan W, Xindu C, Suet T, Ziqiang Y, Junhui L. Modeling and prediction of surface topography with three tool-work vibration components in single-point diamond turning. Int J Adv Manuf Technol 2018;98:1627–39.

108) Zhang SJ, To S, Wang SJ, Zhu ZW. A review of surface roughness generation in ultra-precision machining. Int J Mach Tools Manuf 2015;91:76–95.

109) Mukaida M, Yan J. Ductile machining of single-crystal silicon for microlens arrays by ultraprecision diamond turning using a slow tool servo. Int J Mach Tools Manuf 2017;115:2–14.

110) Rahman MA, Amrun MR, Rahman M, Kumar AS. Variation of surface generation mechanisms in ultra-precision machining due to relative tool sharpness (RTS) and material properties. Int J Mach Tools Manuf 2017;115:15–28.

111) Tauhiduzzaman M, Veldhuis SC. Effect of material microstructure and tool geometry on surface generation in single point diamond turning. Precis Eng 2014;38:481–91.

112) Zhou M, Ngoi BKA. Factors affecting form accuracy in diamond turning of optical components. J Mater Process Technol 2003;138:586–9.

113) Ueda T, Sato M, Nakayama K. The Temperature of a Single Crystal Diamond Tool in Turning. CIRP Ann - Manuf Technol 1998;47:41–4.

114) Uddin MS. Effect of crystallographic orientation on wear of diamond tools in nanoscale ductile cutting of silicon. Chapter 2 in PhD Thesis 2004:7–24.

115) Asai S, Taguchi Y, Horio K, Kasai T, Kobayashi A. Measuring the Very Small Cutting-Edge Radius for a Diamond Tool Using a New Kind of SEM Having Two Detectors. CIRP Annals 1990; 39(1):85-88.

116) Obata K. Single-crystal diamond cutting tool for ultra-precision processing. Sei Tech Rev 2016;82:82–8.

117) Yuan ZJ, He JC, Yao YX. The optimum crystal plane of natural diamond tool for precision machining. CIRP annals. 1992;41(1):605-8.

118) Hurt HH, Showman GA. Wear test of a preselected diamond tool. International Society for Optics and Photonics 1987; 676:116–27.

119) Yeo SH, Zhou M, Ngoi KA, Yap SP. Investigation of cutting temperature and tool wear in diamond cutting of glasses. Mater Manuf Process 1999;14:875–85.

120) Paul E, Evans CJ, Mangamelli A, McGlauflin ML, Polvani RS. Chemical aspects of tool wear in single point diamond turning. Precis Eng 1996;18:4–19.

121) Lin Z-C, Lai W-L, Lin HY, Liu CR. Residual stresses with different tool flank wear lengths in the ultra-precision machining of NiP alloys. J Mater Process Technol 1997;65:116–26.

122) Evans C, Bryan JB. Cryogenic Diamond Turning of Stainless Steel. CIRP Ann - Manuf Technol 1991;40:571–5.

123) Wada R, Kodama H, Nakamura K, Mizutani Y, Shimura Y, Takenaka N. Wear characteristics of single crystal diamond tool. CIRP Ann 1980;29:47–52.

124) Zhou M, Ngoi BKA, Yusoff MN, Wang XJ. Tool wear and surface finish in diamond cutting of optical glass. J Mater Process Technol 2006;174:29–33.

125) Uddin MS, Seah KHW, Li XP, Rahman M, Liy K. Effect of crystallographic orientation on wear of diamond tools for nano-scale ductile cutting of silicon. Wear 2004;257:751–9.

126) Yan J, Zhang Z, Kuriyagawa T. Mechanism for material removal in diamond turning of reaction-bonded silicon carbide. Int J Mach Tools Manuf 2009;49:366–74.

127) Li XP, He T, Rahman M. Tool wear characteristics and their effects on nanoscale ductile mode cutting of silicon wafer. Wear 2005;259:1207–14.

128) Shimada S, Tanaka H, Higuchi M, Yamaguchi T, Honda S, Obata K. Thermochemical wear mechanism of diamond tool in machining of ferrous metals. CIRP Ann 2004;53:57–60.

129) Goel S, Luo X, Reuben RL. Molecular dynamics simulation model for the quantitative assessment of tool wear during single point diamond turning of cubic silicon carbide. Comput Mater Sci 2012;51:402–8.

130) Brinksmeier E, Preuss W, Riemer O, Rentsch R. Cutting forces, tool wear and surface finish in high speed diamond machining. Precis Eng 2017;49:293–304.

131) Kumar J, Negi VS, Chattopadhyay KD, Sarepaka RG V., Sinha RK. Thermal effects in single point diamond turning: Analysis, modeling and experimental study. Meas J Int Meas Confed 2017;102:96–105.

132) Heidari M, Yan J. Ultraprecision surface flattening of porous silicon by diamond turning. Precis Eng 2017;49:262–77.

133) Arnold JB, Morris TO, Sladky RE, Steger PJ. Machinability studies of infrared window materials and metals. Adv. Precis. Mach. Opt., vol. 93, International Society for Optics and Photonics; 1976, p. 96–103.

134) Mehfuz R, Ali MY. Surface Roughness Analysis of Beryllium-Copper Alloy in Micro End Milling. Proc. 7th Int. Conf. Mech. Eng. December), Dhaka, Bangladesh, ICME07-AM-07, 2007.

135) Sudhakar K V, Cisneros JC, Cervantes H, Pineda CG. Machining characteristics and fracture morphologies in a copper-beryllium (Cu-2Be) alloy. J Mater Eng Perform 2006;15:117–21.

136) Alder BJ, Wainwright TE. Phase Transition for a Hard Sphere System. J Chem Phys 1957;27:1208–9.

137) Belak JF, Stowers IF. A molecular dynamics model of the orthogonal cutting process. Lawrence Livermore National Lab., CA (USA); 1990.

138) Komanduri R, Chandrasekaran N, Raff LM. Orientation Effects in Nanometric Cutting of Single Crystal Materials: An MD Simulation Approach. CIRP Ann - Manuf Technol 1999;48:67–72.

139) Komanduri R, Chandrasekaran N, Raff LM. M.D. simulation of nanometric cutting of single crystal aluminum-effect of crystal orientation and direction of cutting. Wear 2000;242:60–88.

140) Komanduri R, Raff LM. A review on the molecular dynamics simulation of machining at the atomic scale. Proc Inst Mech Eng Part B J Eng Manuf 2001;215:1639–72.

141) Komanduri R, Chandrasekaran N, Raff LM. MD simulation of exit failure in nanometric cutting. Mater Sci Eng A 2001;311:1–12.

142) Komanduri R, Chandrasekaran N, Raff LM. MD simulation of indentation and scratching of single crystal aluminum. Wear 2000;240:113–43.

143) Komanduri R, Chandrasekaran N, Raff LM. Molecular dynamics simulation of atomic-scale friction. Phys Rev B 2000;61:14007.

144) Komanduri R, Chandrasekaran N, Raff LM. Effect of tool geometry in nanometric cutting: a molecular dynamics simulation approach. Wear 1998;219:84–97.

145) Komanduri R, Chandrasekaran N, Raff LM. Molecular dynamics simulation of the nanometric cutting of silicon. Philosophical Magazine B 2001;81(12):1989-2019.

146) Pei QX, Lu C, Fang FZ, Wu H. Nanometric cutting of copper: A molecular dynamics study. Comput Mater Sci 2006;37:434–41.

147) Pei QX, Lu C, Lee HP. Large scale molecular dynamics study of nanometric machining of copper. Comput Mater Sci 2007;41:177–85.

148) Lucca D, Chou P, Hocken RJ. Effect of Tool Edge Geometry on the Nanometric Cutting of Ge. CIRP Ann - Manuf Technol 1998;47:475–8.

149) Cai MB, Li XP, Rahman M, Tay AAO. Crack initiation in relation to the tool edge radius and cutting conditions in nanoscale cutting of silicon. Int J Mach Tools Manuf 2007;47:562–9.

150) Crone WC. Compositional variation and precipitate structures of copper–beryllium single crystals grown by the Bridgman technique. J Cryst Growth 2000;218:381–9.

151) Jarosaw Meller. Molecular Dynamics. Encycl Life Sci 2001:1–8.

152) Davim JP, Jackson MJ. Nano and micromachining. Wiley Online Library; 2009.

153) Lennard-jones AJE, Dent BM. On the forces between atoms and ions.—II. Proc R Soc London Ser A, Contain Pap a Math Phys Character 1926;112:230–4.

154) Morse PM. Diatomic molecules according to the wave mechanics. II. Vibrational levels. Phys Rev 1929;34:57–64.

155) Foiles SM, Baskes MI, Daw MS. Embedded-atom-method functions for the fcc metals Cu, Ag, Au, Ni, Pd, Pt, and their alloys. Phys Rev B 1986;33:7983.

156) Erhart P, Albe K. Analytical potential for atomistic simulations of silicon, carbon, and silicon carbide. Physical Review B 2005:71(3): 035211.

157) Ding X, Rahman M. A study of the performance of cutting polycrystalline Al 6061 T6 with single crystalline diamond micro-tools. Precis Eng 2012;36:593–603

158) Inamura T, Takezawa N. Atomic-Scale Cutting in a computer using crystal models of copper and diamond. CIRP annals 1992;41:121–4.

159) Romanowski S, Bartczak WM, Wesołkowski R. Density functional calculations of the hydrogen adsorption on transition metals and their alloys. An application to catalysis. Langmuir 1999;15:5773–80.

160) https://www.webelements.com/copper/crystal_structure.html (last accsessed on 19/04/2019)

161) Schwarzenberger DR. Accurate determination of the lattice parameters of beryllium. Philos Mag 1959;4:1242–6.

162) Spreiter Q, Walter M. Classical Molecular Dynamics Simulation with the Velocity Verlet Algorithm at Strong External Magnetic Fields. J Comput Phys 1999;152:102–19.

163) Plimpton S. Fast Parallel Algorithms for Short-Range Molecular Dynamics. J Comput Phys 1995;117:1–19.

164) Stukowski A. Visualization and analysis of atomistic simulation data with OVITO–the Open Visualization Tool. Model Simul Mater Sci Eng 2009;18:15012.

165) Bergeon N, Guenin G, Esnouf C. Study of the Faults Stackings in the γ (fcc)-ε (hcp) Martensitic Transformation. Le J Phys IV 1997;7:C5-125.

166) To S, Lee WB. Deformation behaviour of aluminium single crystals in ultraprecision diamond turning. Mater Process Technol 2001;113:296–300.

167) Yan J, Asami T, Harada H, Kuriyagawa T. Fundamental investigation of subsurface damage in single crystalline silicon caused by diamond machining. Precis Eng 2009;33:378–86.

168) Puttick KE, Whitmore LC, Chao CL, Gee AE. Transmission electron microscopy of nanomachined silicon crystals. Philos Mag A Phys Condens Matter, Struct Defects Mech Prop 1994;69:91–103.

169) Shibata T, Ono A, Kurihara K, Makino E, Ikeda M. Cross-section transmission electron microscope observations of diamond-turned single-crystal Si surfaces. Appl Phys Lett 1994;65:2553–5.

170) Berry J, Provatas N, Rottler J, Sinclair CW. Defect stability in phase-field crystal models: Stacking faults and partial dislocations. Phys Rev B 2012;86:224112.

171) Zhang SJ, To S, Zhang GQ. Diamond tool wear in ultra-precision machining. Int J Adv Manuf Technol 2017;88:613–41.

172) Mir A, Luo X, Cheng K, Cox A. Investigation of influence of tool rake angle in single point diamond turning of silicon. Int J Adv Manuf Technol 2017:94(5-8):2343-55.

173) Taniguchi N. Nanotechnology: integrated processing systems for ultra-precision and ultra-fine products. Oxford University Press, USA; 1996.

174) Gogotsi YG, Kailer A, Nickel KG. Pressure-induced phase transformations in diamond. J Appl Phys 1998;84:1299–304.

175) Lane BM, Dow TA, Scattergood R. Thermo-chemical wear model and worn tool shapes for single-crystal diamond tools cutting steel. Wear 2013;300:216–24.

176) Zhang Z, Yan J, Kuriyagawa T. Study on tool wear characteristics in diamond turning of reaction-bonded silicon carbide. Int J Adv Manuf Technol 2011;57:117–25.

177) Li XP, He T, Rahman M. Tool wear characteristics and their effects on nanoscale ductile mode cutting of silicon wafer. Wear 2005;259:1207–14.

178) Hodkiewicz J. Characterizing carbon materials with Raman spectroscopy. Thermo Sci Appl Note 2010;51946.

179) Durazo-Cardenas I, Shore P, Luo X, Jacklin T, Impey SA, Cox A. 3D characterisation of tool wear whilst diamond turning silicon. Wear 2007;262:340–9.

180) Maekawa K, Itoh A. Friction and tool wear in nano-scale machining-a molecular dynamics approach. Wear 1995;188:115–22.

181) Woon KS, Rahman M, Fang FZ, Neo KS, Liu K. Investigations of tool edge radius effect in micromachining: A FEM simulation approach. J Mater Process Technol 2008;195:204–11.

182) Zou L, Dong G, Zhou M. Investigation on frictional wear of single crystal diamond against ferrous metals. Int J Refract Met Hard Mater 2013;41:174–9.

183) Shimada S, Inamura T, Higuchi M, Tanaka H, Ikawa N. Suppression of Tool Wear in Diamond Turning of Copper under Reduced Oxygen Atmosphere. CIRP Ann - Manuf Technol 2000;49:21–4.

184) Sata T, Li M, Takata S, Hiraoka H, Li CQ, Xing XZ, et al. Analysis of surface roughness generation in turning operation and its applications. CIRP Ann Technol 1985;34:473–6.

185) Khan GS, Sarepaka RG V, Chattopadhyay KD, Jain PK, Bajpai RP. Characterization of nanoscale roughness in single point diamond turned optical surfaces using power spectral density analysis. Indian J Eng Mater Sci 2004;11:25–30.

186) Lee WB, Cheung BCF. Surface generation in ultra-precision diamond turning: Modelling and Practices. vol. 12. John Wiley & Sons; 2003.